Models of Intermittent Particle Flow

Gregory Page

THÈSE DE DOCTORAT
DE SORBONNE UNIVERSITÉ

Spécialité : Physique

École doctorale n°564 : Physique en Île-de-France

réalisée

au Laboratoire de Physique Théorique de la Matière Condensée

sous la direction de Julian TALBOT

présentée par

Gregory PAGE

pour obtenir le grade de :

DOCTEUR DE SORBONNE UNIVERSITÉ

Sujet de la thèse :

Models of Intermittent Particle Flow

---

soutenue le 16 / 10 / 2020

devant le jury composé de :

M.	**KELLAY Hamid**	**Rapporteur**
M.	**HIDALGO Raul**	**Rapporteur**
Mme.	**APPERT-ROLLAND Cécile**	**Examinateur**
M.	**JOYCE Michael**	**Examinateur**
M.	**MARIN Alvaro**	**Examinateur**
M.	**VIOT Pascal**	**Invité**
M.	**TALBOT Julian**	**Directeur de thèse**

Remerciements

These past three years have created so many connections, which like threads in a tapestry, weaved together to form this glorious, improbable, ensemble. While it's impossible to do it proper justice with only a few words, I will nonetheless try...

Thank you to my supervisor, Julian, for the opportunity, for encouraging, and supporting me!

Thank you Pascal and Charles for the many stimulating discussions, and your help.

Thank you Jacques Resing and Carl Dettmann for your ideas and advice.

Thank you Bertrand Delamotte and the LPTMC lab for accepting me and for affording me many opportunities.

Thank you my fellow PhD and Postdocs for discussions and activities in equal measure :
Antony, Maxime, Marc, Mathias and Léopold

Thank you to the Language department for the teaching position, and the Tedx conference team (especially Jennifer!).

Thank you Pacôme Delva for the Python teaching position.

Thank you to my friends: Mathieu 'Otter' Moog, Amir , Michele, Valentina , Julia, Leyla, Barbara, and Twinny, for the adventures.

Thank you to my housemates and fellow global pandemic lockdown survivors !
Mélody, Jo, Valentin, Guillaume, France and Maureen.

Thank you Olivier Plaisant et Les divertissements and l'ensemble Vocale, as well as les Ondes Plurielles.
hâte de rejouer bientôt avec vous.

Thank you all fellow Tango dancers for many Milongas.
Hasta pronto.

Thank you Ellena, for existing,
sempre no meu coração.

And finally, to my Parents, Thank you.
Where would I be without you ?

Thank you all for the memories.

Here's to many years of more.

[List of Publications]

Part I

- ***G. Page, J. Resing, P. Viot and J. Talbot***, "Optimizing the throughput of particulate streams subject to blocking", Journal of Statistical Mechanics: Theory and Experiment **2018**. (2018)
Status: *Published*

- ***C. Barré, G. Page, J. Talbot and P. Viot***, "Stochastic models of multi-channel particulate transport with blockage ", Journal of Physics: Condensed Matter **30**. (2018)
Status: *Published*

- ***C. Barré, G. Page, J. Talbot and P. Viot***, "Recurrence dynamics of particulate transport with reversible blockage: From a single channel to a bundle of coupled channels", Phys. Rev. E **99**, 042119. (2019)
Status: *Published*

Part II

- ***G.Page, C. Barré, P. Viot & J. Talbot*** , "Metastable arches in Constricted Channels"
Status: *In progress*

Part III

- ***G.Page, C. Antoine, C. P. Dettmann, & J. Talbot***, "The Iris Billiard: Critical Geometries for Global Chaos", Chaos: An Interdisciplinary Journal of Nonlinear Science (2020)
Status: *Submitted: Pending Review*

CONTENTS

CHAPTER
1

GENERAL INTRODUCTION

Particle flows underlie many phenomena, at multiple length scales, such as pedestrian and vehicular traffic, granular and macromolecular transport, and gaseous motion. It is often desirable to predict and control how they depend on the characteristics of their confining space. This thesis will study different models of particulate flow: those that exchange matter and energy with an external environment, and those that don't. The exchange with an external environment may be manifested by particle arrival and exit, or by the presence stochasticity. Properties of the system, such as temperature, constituent particle size, softness, the confining geometry or its capacity, will be modified to study the various conditions for which the flow may be irreversibly stopped, continuously varied, or made intermittent. Intermittency can be initially understood as an irregular change of state with time, the presence and consequences of which, are described in the next section.

1.1 Motivation

Pedestrian traffic is a part of everyday life. It can be modelled as confined particulate flow [1–4], where each particle is acted on by forces from other particles, and the confining boundary. These account for a mixture of individualistic and 'herding' behaviours often attributed to social contagion. The interparticle forces may be a mixture of repulsive 'psychological' and 'overlap' (space exclusion) forces. Frictional forces that depend on the relative velocity of collision and overlap may also impede tangential motion. In escape panic, the presence of constrictions may lead to a buildup of pressure between people, with life or death consequences [5]. Experiments simulating pedestrian evacuation drills have provided evidence of intermittent flow [6] due to clogging and bursting phenomena. The characteristic exponential size distribution of the bursts imply a constant probability of arrest. These systems also display paradoxical 'slower is faster' effects [6], after an initial transient time, and for a period before the end [7]. A simplified phenomenological model [8], suggests that the effect arises from competition between linear and non-linear forces. Finally, empirical results on pedestrian flows in both normal and panic situations shows that the geometric boundaries enclosing the flow not only influence the capacity of the space under consideration, but also influence the time-gap distribution of exiting pedestrians [9]. These ideas are also applicable to minimising vehicular traffic congestion, by suppressing fluctuations. The characteristics of the passages through which traffic flows may be modified through the use of traffic-controlling measures, such as intelligent speed limits, on-ramp controls or driver-assistance systems. Industrial estimates of the potential market of these applications exceed US $1 billion a year [10].

At a smaller scale, granular matter is one of the most manipulated types of material [11]. For example, the pharmaceutical industry relies heavily on the processing of powders and pills. In agriculture and the food processing industry, sugar, salt and seeds are three obvious examples of granular materials which are transported

and manipulated in bulk. The reliance of so many industries upon the transportation and storage of granular matter accentuates the importance of understanding how it behaves under manipulation. Tumblers are, perhaps the most common granular processing devices, used for mixing [12]. These are hollow rotating vessels that are partially filled with granular material, producing a circulating flow. Tumblers exhibit many behaviours, including avalanche, slumping, rolling, cascading and centrifuging [13]. Snapshots at every half (or quarter) rotation of tumbler flow show chaotic motion, as applied to half filled circular, elliptical and square tumblers [14]. Early studies of linear discharge of granular matter from silos showed that significant changes in the flow over a well chosen range of opening diameter [15]. Later it was realised that the clogging phenomena result from the formation of arches spanning the orifice [16–18]. Ref [19] observed that intermittent flow regimes precede clogging events in work studying the flow of colloidal suspensions through small orifices. Particle jamming has been long appreciated as an underlying mechanism for unpredictable behaviours in the fields of mechanical and chemical engineering. There are estimations that 40% [20, 21] of the capacity of many industrial plants is wasted because of problems related to the transport of these materials. Even a modest improvement in the understanding of granular matter flows has the potential to yield significant economic benefits, and more importantly, better coffee machines. Driven granular matter, where the constituents are rendered motile by, for example, gravity or a global vibration of the container, can exhibit both solid-like and liquid-like phases. The description of the latter has been the subject of much debate [11] because of marked deviations from established fluid flow principles, resulting from bridging and jamming phenomena caused by forces between particles neighbouring each other and the enclosing walls [22].

Colloidal systems display similar jamming, or blocking, phenomena. Examples include: filtration processes [23], the transit of macromolecules through artificial or biological channels [24] [25] and many other instances in the wider field of nanofluidics [26] [27]. Biological microswimmers produce dipolar fluid flows by the combined action of their flagella and the cell body on the fluid. These are described as either ‘pusher’ or ‘puller’ stresslets in the far field domain, which corresponds to the flagella being located behind or in front of the cell body respectively [28]. Such groups of swimming micro-organisms undergo a complex interplay with the surrounding fluid, which in turn can reorient and advect them. These may be related to geometrical induced turbulence for mixing processes as observed in micro-fluidic channels [29].

Our aim is to understand the effects of geometrical confinement on flows, and how it fundamentally changes dynamical properties by the limitation of the configuration space accessible to the flow’s components. Ref [30] has also shown that as the channel width shrinks toward the diameter of the particles, the magnitude of any hydrodynamic effect caused by the presence of a medium becomes comparable to the entropic effect. The chaotic dynamics of many, finitely sized, elastic, microscopic particles, has, historically formed the basis of explaining fluid motion [31]. This description, in the low density limit, led in 1872, to the famous non-linear Boltzmann equation [32]. In 1905 the Lorentz gas was introduced to describe the evolution of a dilute electron gas in a metal [33], where the heavier atoms were assumed to be fixed. Like Boltzmann, Lorentz assumed that the particles could be modelled by elastic spheres. The Lorentz gas consists of a point particle freely moving except for reflections from an infinite collection of scatterers, and remains one of the iconic models of chaotic diffusion, for both random and periodic scatterer configurations. Apart from its unbounded domain, the Lorentz gas presents dynamics identical to $2D$ mathematical billiards [34], which provide an understanding of the fundamental role the confining geometry plays in causing non-linear intermittent phenomena. Billiards provide a deep insight into the foundations of statistical physics [34] such as the limits of ergodicity [35, 36], and may also help to explain phenomena observed in Tokamak physics [37–39]. Furthermore, the correspondence principle [40] demands that classical phase structures must have an equivalent in the semi-classical (short wavelength) regime [41].

1.2 Dynamical systems

The various models studied in this thesis all fall under the umbrella of ‘dynamical systems’. In the following, we introduce some basic ideas to help appreciate the differences between the models studied. Dynamical systems evolve with time, in some dynamical space, that is fully determined by a given interaction and the initial condi-

tions. One way to describe the motion of the system is by a smoothly evolving function that is the solution of the following equation of motion,

$$\partial_t \mathbf{x^d}(t) = f(\mathbf{x^d}(t)). \tag{1.1}$$

$f : \mathrm{R}^d \to \mathrm{R}^d$ assigns a rule of evolution, $f(\mathbf{x}(\mathbf{t}))$, to each d-dimensional vector $\mathbf{x^d}(\mathbf{t})$, whose variables may be chosen to describe some physical system at time $t \in \mathbb{R}$. The vector components, $[x^1(t), x^2(t), x^3(t)...x^d(t)]$, form the system's state space, whose time evolution is a trajectory or orbit. The number of variables chosen to represent the physical system, d, denotes the number of degrees of freedom, associated with the dynamical system, and so the dimension of its state space. When the state space is continuous we refer to it as the phase space. Projecting the trajectory onto a discrete partition of the phase space at discrete instants of time, replaces t with $n \in \mathrm{Z}$. We therefore go from the motion of differential equations to difference equations by assigning a mapping $\mathbf{T} : \mathrm{R}^d \to \mathrm{R}^d$ such that:

$$\mathbf{x^d}_{n+1} = \mathbf{T} \circ \mathbf{x^d}_n. \tag{1.2}$$

In addition to it being possible to express the time evolution laws in continuously or iteratively, the state space on which the laws acts may be also discrete or continuous. An ideal coin toss might be modelled by the evolution of a state occupying one element by a state space consisting of only $d = 2$ states, heads and tails, $[\pi_H(t), \pi_T(t)]$, where $\pi_i(t) = 0.5 \ \ \forall i \in [H, T]$ is the probability that the system is in either state at time t. In the context of probability, this set of all possible outcomes is referred to as the sample space S, and a single realisation of an experiment is an event. Once the dynamical evolution law is known, it must be applied many times to determine the entirety of the future accessible states.

Dynamical systems are strictly deterministic if, having specified an initial state $\mathbf{x_0}$, the trajectory may be uniquely determined n steps in the future as $\mathbf{x_n} = \mathbf{T^n} \circ \mathbf{x_0} \ \ n \in \mathbb{Z}$. They are stochastic if there is a probability distribution of outcomes (e.g. for every initial state, the ideal coin toss has two outcomes with equal probability). Initially we will consider simple deterministic versus stochastic systems. We then examine a deterministic billiard that displays chaotic behaviour. Dynamical chaos may be characterised in terms of either individual trajectories or trajectory ensembles. Almost all chaotic trajectories are complicated in the sense that they are unpredictable from observations of any preceding motion [42].

A final, yet important, distinction to make when classifying dynamical systems depends on the preservation of the state/phase space volume. They may be categorised as:

- **Dissipative systems** The volume of the state/phase space contracts with increasing time. These are normally characterised by the presence of attracting sets within the phase space.
- **Conservative systems** The state/phase space constrains the motion, and its volume does not vary in time. As a result, these systems do not possess, what are normally understood as, 'attractors'. Non-integrable Hamiltonian systems contain coexisting periodic, quasiperiodic and chaotic orbits.

Dissipative systems contain an approximation [42] of a complicated interaction with some heat bath, that inevitably leads to random noise, from the fluctuation-dissipation theorem. Conservative systems are therefore necessarily closed, i.e. decoupled from the environment, for both matter and energy exchange, consistent with the absence of any random parameters or noise in the evolution laws.

1.3 Thesis overview

This thesis presents and analyses three distinct model dynamical systems, with the guiding thread of identifying various conditions of intermittent flow.

1. 1D models of particulate flow through single and multiple coupled and uncoupled channel bundles, with a limited carrying capacity. Different rules of blocking are used, and the transient and steady state dynamics are analytically and numerically studied.

2. Finite sized, soft particles driven through a 2D channel with a single or double constriction, are studied using overdamped Brownian dynamics simulation. Special conditions for intermittency, related to the formation of metastable structures, are observed. The geometrical origin of the effects are further explored and characterised in the near-ballistic regime.

3. The Iris Billiard, consisting of a freely moving point particle confined by a unit circle enclosing a central scattering ellipse in 2D is investigated numerically. When the ellipse degenerates to a circle, the system is integrable, otherwise it displays mixed dynamics. Recurrence analysis of the chaotic regime is applied to identify critical geometries that signal whether a transition to global chaos is possible. The transition can be associated with a symbolic intermittency *via* a simple partition of the billiard's state space.

Part I

Stochastic models of blocking phenomena

CHAPTER
2

INTRODUCTION

Particle transport in confined channel geometries is a non-equilibrium phenomenon that may arise for various reasons: pressure differences at each end of the channel, contact with a reservoir full of chemically distinct particles, external driving forces acting on the system's components, or the particulate components being active. The most interesting and relevant observable characteristic of this sort of channel based system is its flux, i.e. its particulate throughput. The flux's behaviour depends on both the inter-particle interaction and the properties of the confining space.

The first part of this thesis considers flows of particles through 1D channels that are characterised by a limited carrying capacity, applicable over a range of length scales [43]. Carrying capacities present an impediment to transport. Once a channel's capacity is reached, it becomes blocked, i.e. the flow is stopped, no more particles may enter or exit. The blockage is reversible if the flow resumes after a finite amount of time and, given a constant entering flux, a steady state with alternating open and blocked states will eventually be reached [44]. In the absence of blockage, increasing the intensity of incoming particles leads to a proportionate increase in the throughput, or rate of exiting particles. When the system is subject to blockage, increasing the input intensity increases the probability of blockage, which therefore disrupts the throughput. Thus, it is expected that, under certain conditions, the throughput will be maximised for some finite intensity of entering particles.

Flux constraints often occur when it is necessary to overcome some 'limiting final step' before fully passing through the system in question. For example, when one must pay for items in a shop by passing by a checkout before leaving. If too many people arrive at once, a queue forms. Queuing theory has long been used to analyse service operations performed on units arriving according to a given distribution [45, 46]. Traditional applications of this branch of mathematics include industrial engineering, telecommunications and traffic flow. More recently, queuing theory has been used in biophysics to model enzymatic servers [47] and will be applied here in Chapter 4.

Bundles of parallel particle conveying channels, each of limited capacity and therefore subject to blockage, will also be considered. If the blockage is irreversible, the failure of one channel results in an increased load on the remaining open channels. This can trigger a cascade, ultimately leading to a complete breakdown of the system [48–50]. An analogous phenomenon of multiple failures can be observed in the exertion of an external force on textile fibres. The fibre bundle model (FBM) [51–54] consists of a number of parallel threads subjected to an applied load. If the load on a single thread exceeds its threshold, the thread breaks and the global load is then redistributed over the remaining intact threads [55], with the attendant possibility of the material tearing. Self-healing materials[56] are examples of multilayer network structures which have local finite storage capacities. When an overload occurs in a node of the network, this leads to a local failure and the network is able to rebuild a new local node. To describe these phenomena, Manfredi et al. [57] proposed a stochastic model showing that the

Figure 2.1: A fragile stone forest bridge

optimal performance is reached via complex trade-offs between physical parameters. This feature can be viewed as analogous to the 'slower-is-faster' phenomenon[58], also present in pedestrian traffic flows[59, 60]. Further examples include blackouts in power distribution networks that are generally preceded by a cascade of failures resulting from local overloads[61]. Earthquakes[62, 63], vehicular traffic jams [64], network traffic jams[65–68], material fractures[69, 70] and internet attacks (DoS) [71] all exhibit similar features.

2.1 Scenarios of controlled particle flux

2.1.1 Unstable forest bridge at crossroads

A couple explore a path in a mountain forest. They encounter a wide, rapid creek, with a single stone arch as a bridge to the other side. Sensing that the arch would collapse under too much weight, they carefully cross one after the other. The time before re-embarking together on the other side of the bridge is longer than it would have been for a lone walker. In the 'irreversible' scenario, the couple, in a rush, attempt to walk the bridge together, and fall off. This passage has a carrying capacity, $N = 2$, that must not be reached to ensure the normal functioning of the passage.

Much later, two lone walkers, following separate paths meet at the same bridge, within a small enough time interval, Δt, to impede each other's passage. Not being in a rush, after crossing they choose to take time to discuss about the weather and share a drink before parting ways, all of which results in a longer shared time of passage than would have been had Δt been sufficiently large to allow each to pass without impediment.

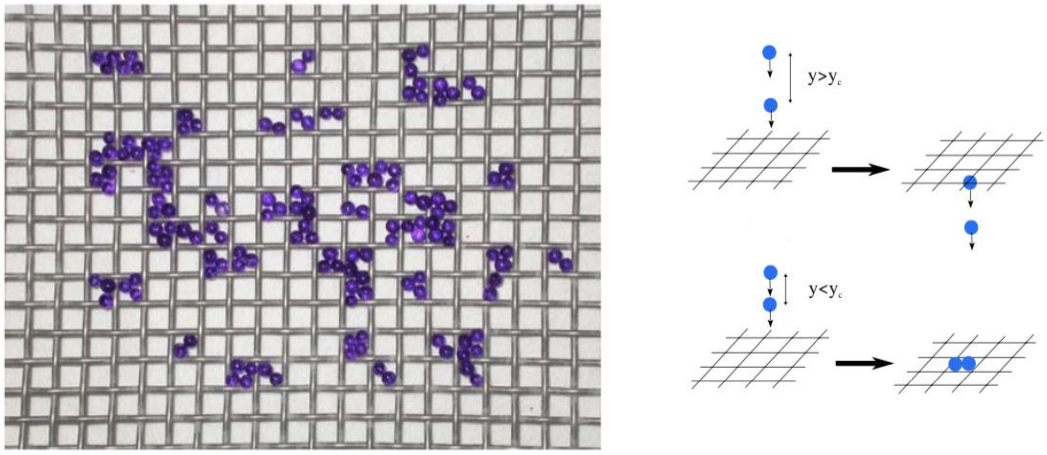

Figure 2.2: (a) A view of the arches formed by dry grains, all with the same characteristics, of a sieve at the end of a filtration test [72]. (b) A model of filtration. In the first (top) scenario, the particles arrive with enough space between them to pass the filter. Whereas in the second scenario (bottom) they arrive close enough to each other to create a blockage at the filter.

2.1.2 Granular filtration

One of the main blockage phenomena found in a range of physical situations, whether in everyday life, engineering or the environment, is filtration. A flow of a heterogeneous mixture in suspension passes through a sieve, a porous structure that allows certain particles to be filtered out. Filtration is widely used to purify fluids or to separate particle species in microfluidics, nanofluidics or chromatography. Filtration is a technique that can be used in the fields of food processing, pharmaceuticals. It can also be found directly in nature, for example: when fine sediments accumulate in gravel bed streams, in wastewater treatment using sand [73] or in aquaculture, where the water is filtered by oysters or other bivalves [74]. Filtration can be done via two different processes, screening or absorption both of which block objects whose size is smaller than the pore[75–77]. Blocking phenomena were experimentally explored by Roussel et al. with a flow of monodisperse glass beads suspended in a viscoelastic gel [72] through a sieve. This was studied by analysing the fraction of balls retained as a function of the ratio between their diameter and mesh size as well as the density of balls in the gel. This fraction was found to be non-zero even for values of particle diameter smaller than the pore width, as shown in Fig 2.2a. A simple interpretation of this phenomenon comes by recognising that, if two particles arrive with a separation less than a critical value y_c, then they block the mesh. Assuming that all balls fall at the same speed, we can then define a critical time, τ, which must separate their arrival, below which they will block.

This type of blockage is also found in granular flows of a two-dimensional hopper flow [78] or in granular material inside narrow vertical tubes [79], for example an hourglass [80]. The latter experiment consists of flowing granular material along narrow tubes that extract and reinsert the material at a constant ratio.

2.1.3 Ion microchannels

Many biological processes involve blocking phenomena, which determine whether bacteria, or ions, pass through channels that have specific shapes, asymmetries or irregularities. Channels across cell membranes allow the

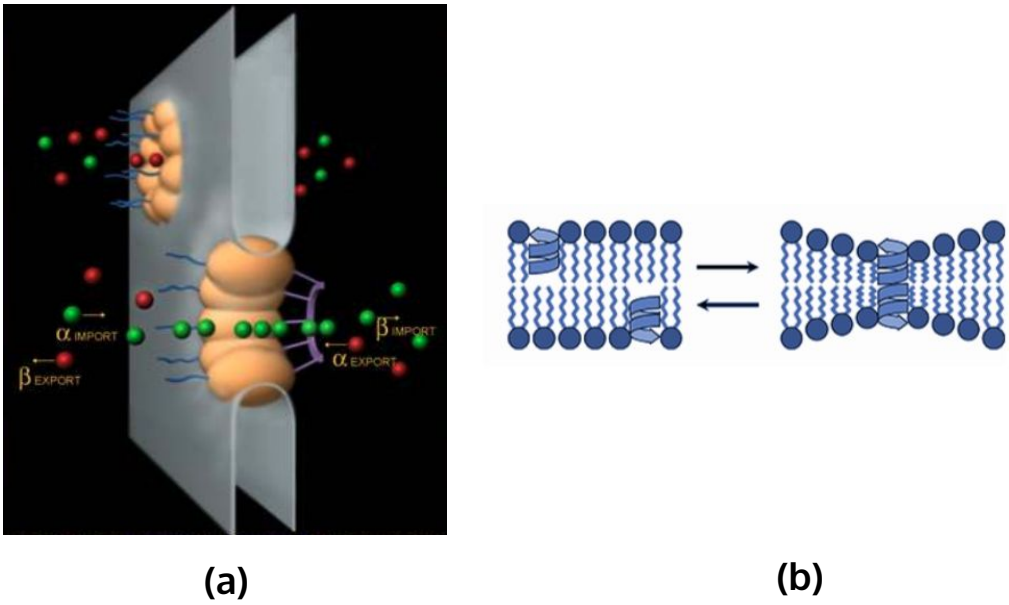

Figure 2.3: (a) 3D image of nuclear pores embedded in a nuclear envelope [81], that transport matter between cytoplasm and the nucleus. Entering particles are depicted in green, and exiting particles in red. (b) Channel creation in a bilipid layer by gramicidine.

transport of ions, but are sometimes blocked by drugs or toxins [82, 83]. Macromolecules bidirectionally flow through the pores of the cell nuclei [81]; entering and exiting molecules being unable to pass through a particular pore simultaneously. Fig. 2.3a illustrates these nuclear pores. At times, the limited capacity of the pores restricts the flow of one type of molecule. In [81] it is shown that at low density the flow alternates very quickly, and molecules enter and exit in an alternating manner without producing blockage; at higher density the times of change of direction increase, causing some particles to be blocked.
Gramicidin is a mixture of antibiotics, the activity of which consists in the creation of channels in the bilipid membrane, thereby increasing the permeability of the target bacteria [84], as shown in Fig. 2.3b. These channels selectively transport ions and water in single pathways.

2.1.4 Internet attacks (DoS)

Some internet attacks are carried out by saturating a server, rendering it unavailable. These are known as denial of service (DoS) attacks [71], and come in different forms. The physical network may be overcrowded by requests, saturating the network flow: which can be understood as a high density case. Alternatively, the server saturates well before the network capacities. The type of attack that fits the models studied here best is the flooding of a computer server, which induces an overload preventing proper function or even saturating the server [85–87]. In these situations, blocking is caused by a bombardment of data that arrives at a server too quickly. It is the characteristics of the server that most influence the system failure (the density of requests before an attack can be low).

2.2 Previous models studied

To provide context of the results presented in Chapters 3 and 4, previously developed models of stochastic $1D$ particle flow, and their characteristics are examined.

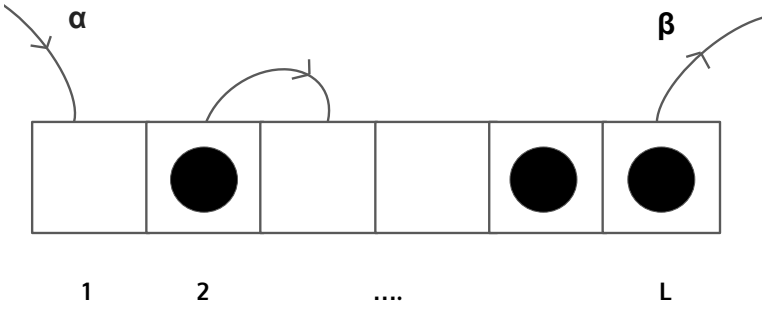

Figure 2.4: A TASEP model of L sites. The arrows represent transition probabilities. A particle hops to the next cell, at rate one to the right, iff it's empty. Site 1, if already empty, receives incoming particles at a rate α. Site L expels particles at a rate β, if already occupied.

2.2.1 TASEP

A first approach to modelling high density flux is by considering the interplay between stochastic forces and steric exclusion effects [88]. The totally asymmetric simple exclusion process (TASEP) [89, 90] provides a theoretical approach to out-of-equilibrium blocking phenomena. The simplest model is a finite set of regularly spaced sites, where particles can randomly jump from left to right [91], under the condition that a particle cannot transition to an already occupied site. It is necessary to choose an evolution principle, i.e. the order in which the particles advance. There are several types in the literature: in the input order, with a random order at each time step [92, 93], or a random order kept throughout the simulation [89, 94], etc. Once the particle has been chosen, it passes to an adjacent site on the right if it is empty. Particles enter the system with a probability $\alpha \in [0,1]$ and exit, through site L, with a probability $\beta \in [0,1]$.

It is possible to draw a phase diagram according to the input and output flow [95, 96]. There are three phases: low density (LD), high density (HD) and maximum current (MC). The low-density phase is well understood, since the input rate, α, is very low compared to the output rate β. The high-density phase corresponds to $\beta > \alpha$. Between these two phases there is a first order phase transition, i.e. there is a discontinuity in density. The third and final maximum current phase is in the region where both α and β are high. In this phase, the limiting factor is the chain size. For transport models this phase transition is particularly important for many of the applications seen earlier in the general introduction.

This model and its derivatives also provide a quantitative description of car and pedestrian traffic [97, 98], which may be rendered more complex through the addition of, for example, traffic lights [99, 100]. Some models consider bidirectional TASEP flows [101–104]. There are also microscopic applications of this model to study the movement of ribosomes in RNA [88], and protein synthesis has also been modelled via TASEP [105]. Collective movements similar to those observed in car traffic are visible at almost all levels in biological systems [106].

2.2.2 Non-Markovian models of blocking

In 2013 Gabrielli et al [107] introduced and solved a stochastic model describing this type of clogging in a canal. The original idea was to study what happens when two cars pass each other on a small road that allows only the passage of one car at a time. A single valued transit time was used, which accounts for the physical time of passage through a channel, and would well-represent closed loop conveyor systems with homogeneous servers [108] such as found in industrial engineering. Previous work [107, 109] studied various properties of interest,

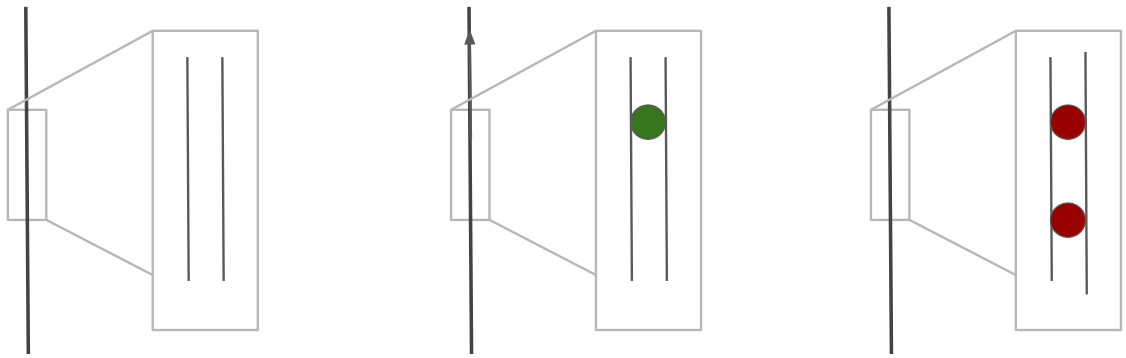

Figure 2.5: A $1D$, $N = 2$ channel. Left: When empty. Middle: Occupied by one transiting particle. Right: Overloaded by two simultaneously present particles.

such as the survival probability at time t, mean blockage time, exiting particle flux, and the total number of exiting particles can be calculated exactly. The original model considered one channel with capacity $N = 2$, i.e., two particles must be simultaneously present in the channel to block the system. Fig 2.5 illustrates the single channel which, when empty, carries one particle, and is blocked by two particles. While, every 1D channel model in this thesis will model an independent particle arrival, the nature of the transit time will be varied. Particles enter at random times according to a Poisson process of intensity λ and exit, if no blockage occurs, after a fixed transit time τ. If the blockage is irreversible, the mean total number of exiting particles can be continually increased by reducing the intensity to values approaching zero [109]. This, of course, requires an ever-increasing amount of time. Subsequently, several generalisations were studied, including a higher blocking threshold ($N > 2$) [110], an inhomogeneous entering flux [111], and multiple channels [112, 113]. The work presented here considers the problem of maximising the final quantity of the total number particles that exit the system in a given finite time. Sections 3.3 and 3.4 study the case where the blockage is irreversible and reversible, respectively. In the latter case, the system is reactivated after a constant waiting time, τ_b, which gives rise to a transient regime leading to a steady state [114].

2.3 Part I overview

The blocking phenomena under consideration may be caused by either ‘extrinsic’ or ‘intrinsic’ mechanisms. The former refers to the situation where the number of particles present somehow exceeds the channel carrying capacity, and will be the focus of the first part of this thesis. A model based on this phenomenology successfully accounted for experimental data [115, 116]. These results provide an effective tool for optimising particle transport in channels and for other applications, such as self-healing materials. The latter mechanism arises from collective effects such as encountered in filtration processes. In this case, while isolated particles can pass through a mesh hole, clogging occurs when two or more particles arrive in near concurrence, causing one to impede the other. This effect, due to the delicate and often non-linear interplay between the spatio-temporal closeness of the particles and the confining geometry, could be seen as setting the capacity of a channel to greater than one.

Chapter 3 revisits the already published stochastic model of blocking phenomena with single-valued transit times, described in Section 2.2.2. Conditions for the optimisation of the steady state and time-dependent flux are studied for both single and multi-channel systems. When the blockages are of finite duration, the system reaches a steady state with an exiting flux that is reduced compared to the incoming. For many of the applications in the previous section, the throughput of serviced jobs is a crucial quantity.

Chapter 4 modifies the original $1D$ channel model, such that both the transit time and deblocking time (where applicable) follow a Poisson distribution, rendering the system 'memoryless'. This feature allows the time evolution of the model to be described by a set of differential equations, for which exact solutions can, in principle, be obtained.

CHAPTER
3

NON-MARKOVIAN MODELS OF BLOCKING

This chapter revisits the already published model of single channel blocking phenomena, discussed in Section 2.2.2. The following introduces key concepts that will be repeatedly used to describe the Poisson process driven particle arrival.

3.1 Key concepts

3.1.1 Random variables

A 'random variable', $X(t)$, is either a number or vector whose value is the result of a random phenomenon. A stochastic dynamical process is a family of random variables indexed by a set T, representing different events in time such that $X(t)_{t\in T} \in \mathbb{R}$. The process is defined on a probability space (Ω, S, P), where each $\omega \in \Omega$ governs the realisation of the process. We now define a 'counting process' $\{X(t), t \geq 0\} \in \mathbb{N}$ that keeps count of the number of random events that have occurred until time t. The variable representing the counting process is also a random variable that is monotonically increasing in t. $X(t) - X(s)$ represents the number of events in the time interval $(s,t], s < t$.

3.1.2 Poisson process

Poisson processes, $\{X(t),\ t \geq 0\}$, are counting processes that describe many real processes that occur in large populations. Poisson processes possess the additional properties that the number of events counting in disjoint time intervals are independent, and that the mean number of event occurrences within the time interval, λ, is stationary over all time. The probability of i events occurring in the time interval $(0,t]$ is:

$$p(i,t) = \mathbb{P}\{X(t) = i\} = \frac{(\lambda t)^i}{i!} e^{-\lambda t},\ \ i \in \mathbb{N} \tag{3.1}$$

The only changes in the process are unit jumps upwards, whose inter-event time intervals are independant, exponentially distributed variables with mean $1/\lambda$ and variance $1/\lambda^2$, $\lambda > 0$.

the following conditional probability transition probability is given as:

$$\mathbb{P}\{X_n = k | X_{n-1} = j\} = \frac{\lambda^{k-j}}{(k-j)!} e^{-\lambda}, \tag{3.2}$$

where $k > j$.

3.2 Presentation of model

A stream of particles enter the channel, of capacity N, according to a homogeneous Poisson process with the following density function:

$$\psi(t) = \lambda e^{\lambda t}, \tag{3.3}$$

of intensity, λ. The probability that i particles enter the channel in the time interval $(0,t)$ is given by Eq.(3.1.2). Any particle within the channel that is not blocked transits the system over a single time, τ. If N particles are simultaneously present, the channel blocks (Fig.2.5 illustrates for the case $N=2$), and ejects the blocking particles after a time $\tau_b > \tau$. The following section will first consider the case where the channel blocks irreversibly, i.e. $\tau_b \to \infty$.

3.3 Single channel with irreversible blockage

The average number of particles that exit in the time interval $(0,t_s)$ can be computed by integrating the exiting particle flux,

$$m(t_s) = \int_1^{t_s} j(t)dt \tag{3.4}$$

The lower limit of the integral is $t = \tau = 1$, as no particle can exit before this time (assuming that the channel is empty at $t = 0$.) For $t_s \to \infty$:

$$m(\infty) = \tilde{j}(u=0) = \frac{1}{e^{\lambda}-1}, \tag{3.5}$$

where $\tilde{j}(u) = \int_0^{\infty} e^{-ut} j(t)dt$ is the Laplace transform of the time dependent flux. The number of exiting particles tends to infinity as $\lambda \to 0$ and to zero as $\lambda \to \infty$. The dynamics of the sysmtem is studied for finite t_s. In this case there is clearly a finite entering intensity that optimises the total number of exiting particles. If the intensity is too small, blocking is unlikely as only a few particles enter, whereas if λ is too large more particles are injected but blocking is highly probable. The explicit equation for the time dependent flux [109] is given by:

$$j(t) = e^{-\lambda t} \sum_{k=1}^{\lfloor t \rfloor} \frac{\lambda^k (t-k)^{k-1}}{(k-1)!}. \tag{3.6}$$

Substituting this in Eq.(3.4) gives:

$$m(t_s) = \sum_{k=1}^{\lfloor t_s \rfloor} \exp(-\lambda k) \left[1 - \frac{\Gamma(k, \lambda(t_s-k))}{(k-1)!} \right] = \sum_{k=1}^{\lfloor t_s \rfloor} \exp(-\lambda k) \frac{\gamma(k, \lambda(t_s-k))}{(k-1)!}, \tag{3.7}$$

where $\Gamma(k,x)$ and $\gamma(k,x)$ are the upper and lower incomplete gamma functions respectively. The results shown in Fig. 3.1 demonstrate that the expected number of exiting particles displays a maximum, at finite intensity for a finite stopping time, t_s. The value of λ that maximizes the output increases as t_s decreases and that the maximum sharpens as t_s increases. The explicit expression for the intensity that maximizes the output is a piece-wise function. For $1 \leq t_s \leq 2$,

$$m(t_s) = e^{-\lambda} - e^{-\lambda t_s}. \tag{3.8}$$

It is easy to show that a maximum occurs for

$$\lambda = \frac{\ln(t_s)}{t_s - 1}, \tag{3.9}$$

which returns $\lambda = \ln(2)$ when $t_s = 2$. For $2 \leq t_s \leq 3$:

$$m(t_s) = e^{-\lambda} - e^{-\lambda t_s} + e^{-2\lambda} - e^{-\lambda t_s}(1 + \lambda(t_s - 2)). \tag{3.10}$$

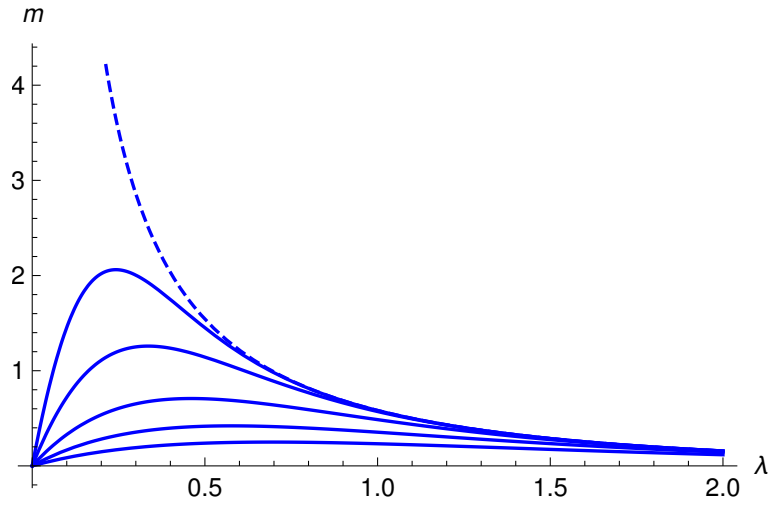

Figure 3.1: Average number of exiting particles as a function of the intensity for different stopping times, $t_s = 32, 16, 8, 4, 2, 1.5$ top to bottom. The dashed line shows the long-time limit, Eq.(3.5).

$m(t)$ being a piece-wise continuous function, it may be readily confirmed that for $t_s = 2$, the value is the same as that given by Eq.(3.8). There is no analytic expression of the value of λ that maximizes this expression for $t > 2$, but numerical solutions are, however, straightforward. Moreover, for large t_s, which corresponds to small intensity, λ, an asymptotic solution may be obtained. By using the Laplace's method[109], $j(t)$ if found to decay as :

$$j(t) \simeq \lambda e^{-\lambda^2 t}. \tag{3.11}$$

Integrating Eq.(3.11), one obtains that $m(t_s)$ is given by:

$$m(t_s) \simeq \frac{1}{\lambda}(1 - e^{-\lambda^2 t_s}). \tag{3.12}$$

Differentiating Eq.(3.12) with respect of λ, one obtains a maximum of $m(t_s)$ when :

$$\lambda \simeq \frac{C}{\sqrt{t_s}}. \tag{3.13}$$

Where C is a constant. The limitation of the flux route is that it does not allow us to calculate higher moments of the exiting particle distribution, but only the mean value. To go further, we therefore introduce the function $f(m,t)$ giving the probability that m particles have exited at time t, regardless of the state of the channel (open or closed) at time t (the joint probabilities that m particles have exited at time t and the channel is still open are discussed in Appendix A). The equations describing the evolution of these functions are as follows:

$$\frac{df(0,t)}{dt} = -\lambda e^{-\lambda} q_s(0,t-1) \tag{3.14}$$

$$\frac{df(1,t)}{dt} = \lambda e^{-\lambda} q_s(0,t-1) - \lambda e^{-2\lambda} q_s(1,t-2) \tag{3.15}$$

$$\frac{df(n,t)}{dt} = \lambda e^{-2\lambda} q_s(n-1,t-2) - \lambda e^{-2\lambda} q_s(n,t-2),\ n > 1, \tag{3.16}$$

where $q_s(n,t)$ is the joint probability that n particles have entered the channel and that the channel is still open [109]. The loss term for the evolution of $f(0,t)$ is the result of a particle exiting the channel at time t that had previously entered the channel at $t-1$. This term is also the gain term for the evolution of $f(1,t)$. For $n > 1$ the gain term consists of the entry of a particle at $t-1$ that exits at t. For this to be possible the channel must have been

open at $t-2$ with $n-1$ particles entering in the interval $(0,t-2)$, which occurs with probability $q_s(n-1,t-2)$, and no particle must enter in the intervals $(t-2,t-1)$ and $(t-1,t)$ giving rise to the factor of $e^{-2\lambda}$. The loss term is similar except that n particles must have entered in the interval $(0,t-2)$ with an additional particle entering at $t-1$ and exiting at t. The gain term for $n=1$ is slightly different as the particle entering the channel at $t-1$ is the first one, so the channel is certainly empty at this time. The telescopic structure of equations (3.14), (3.15) and (3.16) is consistent with the conservation of probability, $\sum_{n=0}^{\infty} df(n,t)/dt = 0$. We obtain the complete solution by introducing the generating function:

$$G_f(x,t) = \sum_{n=0}^{\infty} z^n f(n,t). \tag{3.17}$$

Taking the time derivative and substituting the above expressions for $f(n,t)$ we obtain

$$\frac{\partial G_f(z,t)}{\partial t} = \lambda(z-1)(e^{-\lambda}q_s(0,t-1) + e^{-2\lambda}(G(z,t-2) - q_s(0,t-2))), \tag{3.18}$$

where $G(z,t) = \sum_{n=0}^{\infty} z^n q_s(n,t)$. Taking the Laplace transform and using the initial condition $G_f(z,0) = 1$ we finally obtain

$$\tilde{G}_f(z,u) = \frac{u+\lambda-\lambda e^{-(u+\lambda)}}{u(u+\lambda-\lambda z e^{-(u+\lambda)})}. \tag{3.19}$$

The individual functions can be recovered from

$$\tilde{f}(n,u) = \frac{1}{n!}\frac{\partial^n \tilde{G}_f(z,u)}{\partial z^n}\bigg|_{z=0}. \tag{3.20}$$

The first two are

$$f(0,t) = 1 + (e^{-\lambda t} - e^{-\lambda})\theta(t-1) \tag{3.21}$$

and

$$f(1,t) = ((e^{-\lambda t}(1+\lambda(t-2)) - e^{-2\lambda})\theta(t-2) - (e^{-\lambda t} - e^{-\lambda})\theta(t-1), \tag{3.22}$$

where $\theta(t)$ is the Heaviside function. These results can also be obtained by direct solution of Eqs. (3.14) and (3.15), respectively. The first two moments are

$$\langle \tilde{m}(u) \rangle = \frac{\partial \tilde{G}_f(u,z)}{\partial z}\bigg|_{z=1} = \frac{\lambda e^{-(u+\lambda)}}{u(u+\lambda-\lambda e^{-(u+\lambda)})}, \tag{3.23}$$

and

$$\begin{aligned} \langle \tilde{m}^2(u) \rangle &= \frac{\partial^2 \tilde{G}_f(u,z)}{\partial z^2}\bigg|_{z=1} + \frac{\partial \tilde{G}_f(u,z)}{\partial z}\bigg|_{z=1} \\ &= \frac{\lambda e^{-(u+\lambda)}(\lambda+(u+\lambda)e^{-(u+\lambda)})}{u(\lambda-(u+\lambda)e^{-(u+\lambda)})^2}. \end{aligned} \tag{3.24}$$

from which the first and second moments at infinite time may be obtained as

$$\langle m \rangle = \lim_{u\to 0} u\langle \tilde{m}(u) \rangle = \frac{1}{e^{\lambda}-1} \tag{3.25}$$

and

$$\langle m^2 \rangle = \lim_{u\to 0} u\langle \tilde{m}^2(u) \rangle = \frac{1+e^{\lambda}}{(1-e^{\lambda})^2}, \tag{3.26}$$

giving for the variance

$$\langle m^2 \rangle - \langle m \rangle^2 = \frac{e^{\lambda}}{(e^{\lambda}-1)^2}. \tag{3.27}$$

At small intensity, this behaves as λ^{-2}, while for large intensity it approaches zero as $e^{-\lambda}$. In order to obtain the variance of m at time t, we have to invert $\langle m^2(u)\rangle$ and $\langle m(u)\rangle$. By using Eq.(3.23), one has

$$\langle m(u)\rangle = \frac{e^{-(u+\lambda)}}{1-e^{-(u+\lambda)}}\left[\frac{1}{u}-\frac{1}{u+\lambda-\lambda e^{-(u+\lambda)}}\right] \tag{3.28}$$

$$= \sum_{n\geq 1} e^{-n(u+\lambda)}\left[\frac{1}{u}-\sum_{k\geq 0}\frac{(\lambda e^{-(u+\lambda)})^k}{(u+\lambda)^{k+1}}\right], \tag{3.29}$$

which gives

$$\langle m(t)\rangle = \sum_{n\geq 1}\left(e^{-\lambda n}\theta(t-n) - e^{-\lambda t}\sum_{k=0}\frac{\lambda^k (t-k-n)^k\theta(t-k-n)}{k!}\right). \tag{3.30}$$

This expression corresponds to that obtained from the survival probability [44]. Similarly, by using Eq.(A.18), one obtains

$$\langle m^2(u)\rangle = \frac{e^{-(u+\lambda)}(1+e^{-(u+\lambda)})}{(1-e^{-(u+\lambda)})^2}\left[\frac{1}{u}-\frac{1}{u+\lambda-\lambda e^{-(u+\lambda)}}\right] - 2\frac{\lambda e^{-2(u+\lambda)}}{1-e^{-(u+\lambda)}}\frac{1}{(u+\lambda-\lambda e^{-(u+\lambda)})^2}. \tag{3.31}$$

By using the identity $\frac{1}{(1-a)^2} = \sum_{n=0}(n+1)a^n$, one has

$$\langle m^2(u)\rangle = \sum_{n=0}(n+1)(1+e^{-(u+\lambda)})e^{-(n+1)(u+\lambda)}\left[\frac{1}{u}-\sum_{k=0}\frac{(\lambda e^{-(u+\lambda)})^k}{(u+\lambda)^{k+1}}\right] - 2\sum_{n=0}\lambda e^{-(n+2)(u+\lambda)}\sum_{k=0}(k+1)\frac{(\lambda e^{-(u+\lambda)})^k}{(u+\lambda)^{k+1}}. \tag{3.32}$$

This can be inverted to give the second moment as a function of time:

$$\begin{aligned}\langle m^2(t)\rangle = &\sum_{n\geq 0}(1+n)e^{-(2+n)\lambda}\Big(\theta(t-n-2)+e^{\lambda}\theta(t-n-1)\Big)\\ &-\sum_{n\geq 0}\sum_{k\geq 0}\frac{e^{-t\lambda}(1+n)\lambda^k}{k!}\Big((t-n-k-2)^k\theta(t-n-k-2)+(t-n-k-1)^k\theta(t-n-k-1)\Big)\\ &-\sum_{n\geq 0}\sum_{k\geq 0}\frac{2e^{-k\lambda-(2+n)\lambda-(t-n-k-2)\lambda}\lambda^{k+1}}{(k+1)!}(1+k)(t-n-k-2)^{1+k}\theta(t-n-k-2).\end{aligned} \tag{3.33}$$

Numerical results for the second moment and the variance as a function of λ are shown in Figs. 3.2 a & b, respectively. Like the first moment (Fig. 3.1), the second moment displays a maximum at a finite value of λ. The family of curves at different stopping times approaches the long-time limit, Eq.(3.26) as time increases. The variance also displays a maximum as a function of intensity, see Fig. 3.2b, but the location of the maximum for a given stopping time is displaced to a higher value of the intensity. The time dependent variance for different values of λ is shown in Fig. 3.3a. Finally, Fig. 3.3b shows the value of λ that maximises the mean and variance as a function of the stopping time. We observe that the intensity that maximises the mean number of exiting particles is a strictly decreasing function of the stopping time. The intensity that maximises the variance of the number of exiting particles, however, has a non-trivial behaviour. It is the same that maximises the intensity for $1 \leq t_s \leq 2$, but it then increases to a maximum value for $t_s \approx 3$ and then decreases. For $t_s > 2$, the variance is maximised at a higher value of λ than that which maximises the mean number.

3.4 Reversible single channel model

Reversible blockages, in single file channel flow [114], are now considered. During a blockage, the N particles are retained in the channel, and no more may enter. After the single valued deblocking time, τ_b the channel instantaneously releases all N particles, thereby resetting to the empty state, allowing new particles to enter. The dynamics is therefore described by a recurring cycle of alternating open and closed states, that ultimately leads to

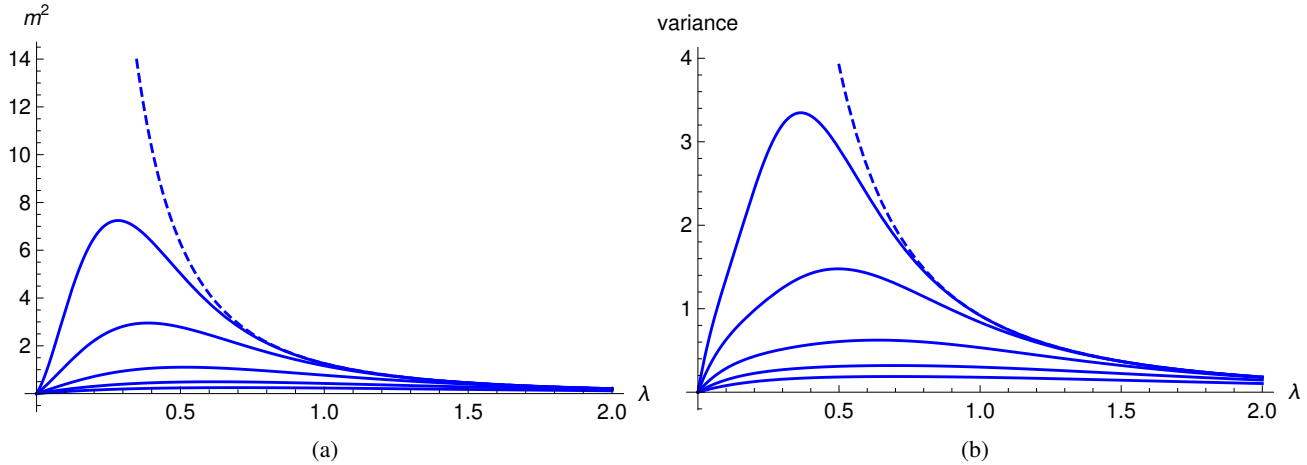

Figure 3.2: (a) Second moment of the number of exiting particles as a function of the intensity for different stopping times, $t_s = 20, 10, 5, 3, 2$ top to bottom. The dashed line shows the long time limit, Eq.(3.26). (b) Variance of the number of exiting particles as a function of the intensity for different stopping times, $t_s = 10, 6, 4, 2, 1.5$ top to bottom. The dashed line shows the long time limit, Eq.(3.27).

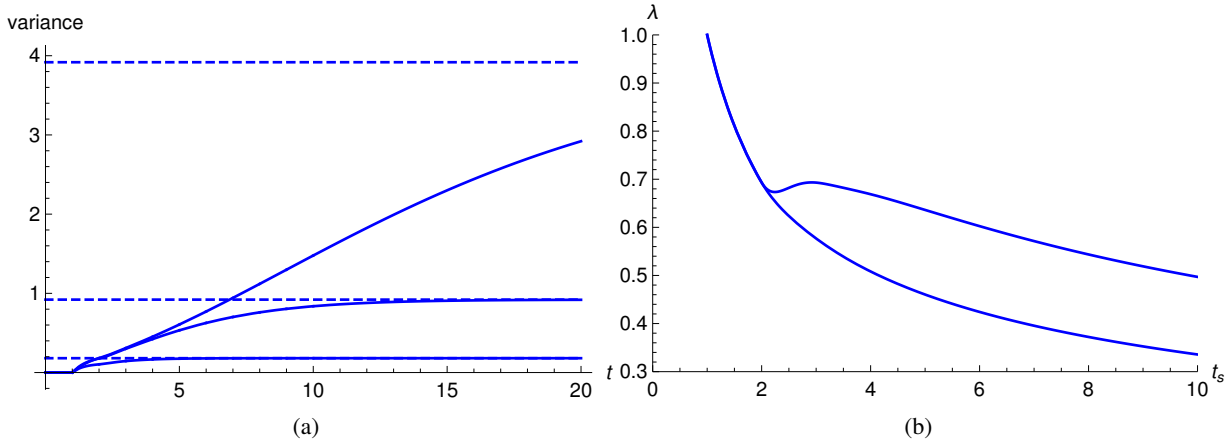

Figure 3.3: (a)Variance of the number of exiting particles as a function of time for different intensities, $\lambda = 0.1, 0.5, 1, 2$. The dashed lines show the long time limit, Eq.(b) Intensity that maximizes the variance (upper curve) and mean of number of exiting particles as a function of the stopping time.

a stationary state. In an average steady state recurrence cycle, the channel is open for an average time, $\langle t \rangle$, and blocked for a fixed time τ_b. The stationary probability that the system is open is therefore:

$$p_o(\lambda) = \frac{\langle t \rangle}{\langle t \rangle + \tau_b}, \tag{3.34}$$

where the denominator represents the total mean recurrence time. The stationary output flux is then given by the ratio of the mean number of particles released during one cycle to the cycle period,

$$j(\lambda) = \frac{\langle m \rangle + N}{\langle t \rangle + \tau_b}. \tag{3.35}$$

$\langle m \rangle$ is the mean number of output particles between two successive blockages. By equating the number of entering particles in one period to those exiting we obtain the following 'number balance'

$$\langle m \rangle + N = \lambda \langle t \rangle. \tag{3.36}$$

Finally, from the above three equations we deduce that:

$$j(\lambda) = \lambda p_o(\lambda). \tag{3.37}$$

The latter relation does not depend on the existence of a cycle, as it is the result of number conservation. The output flux is equal to the entering one minus the part that is rejected when the channel is in the closed state. By taking the limit $\lambda\tau \ll 1$, the mean blockage time and the mean number of exiting particles between blockages behave asymptotically as $\langle t \rangle \gg \tau_b$ and $\langle m \rangle \gg N$, respectively. Therefore, for a given τ_b, the probability that the channel is open is close to unity and the flux $j(\lambda) \simeq \lambda$. Blockages rarely occur at low λ. In this limit, the mean blockage time can be estimated by noting that a blockage occurs when a batch of particles enters in a finite duration τ, leading to $\langle t \rangle = \tau \frac{(N-1)!}{(\lambda\tau)^N}$ [110]. Expanding $p_o(\lambda)$ to first order gives

$$p_o(\lambda) \simeq \frac{1}{1 + \frac{(\lambda\tau)^N \tau_b}{(N-1!)\tau}}. \tag{3.38}$$

When $\lambda\tau \gg 1$, blockages are very frequent, and both the mean number of exiting particles between blockages, $\langle m \rangle$, and mean time between blockages, $\langle t \rangle$, approach zero. The resulting flux consists entirely of successive releases of the blocked particles, $j(\lambda) = N/\tau_b$ and $p_o(\lambda) \simeq 0$. In this limit, $\langle t \rangle$ corresponds to the time necessary for N particles to enter an empty channel, N/λ. The open probability and the flux in this high intensity limit are therefore:

$$p_o(\lambda) \simeq \frac{N}{N + \lambda\tau_b}, \tag{3.39}$$

and

$$j(\lambda) \simeq \frac{N\lambda}{N + \lambda\tau_b}. \tag{3.40}$$

3.4.1 Solvable models: $N \leq 3$

For small capacities, $N \in [1,2,3]$, the time evolution of the process can be expressed by analytically tractable differential or integro-differential equations [114]. For larger values of N, the time evolution cannot be solved by any known means.

We first consider $N = 1$, which corresponds to a stochastic switch. The transit time, τ, is an irrelevant variable because no particle can exit the channel without having already blocked it. For $N > 1$, it is possible for particles to pass through the channel without causing a blockage. Let $p_o(t)$ denote the probability that the channel is open at time t. Its time evolution obeys:

$$\frac{dp_o(t)}{dt} = -\lambda p_o(t) + \lambda p_o(t - \tau_b). \tag{3.41}$$

The loss term corresponds to the entrance of a particle at time t, while the channel is open, causing the channel to block. The gain term corresponds to the exit of a particle that became blocked at time $t-\tau_b$, with the subsequent reopening of the channel at time t. The mean output flux at time t is given by:

$$j(t) = \lambda p_o(t-\tau_b), \tag{3.42}$$

which corresponds to the release of a blocked particle that entered at $t-\tau_b$. Applying the time Laplace transform, $\tilde{f}(u) = \int_0^\infty dt e^{-ut} f(t)$, to Eqs.(3.41) and (3.42) gives,

$$\tilde{p}_o(u) = \frac{1}{\lambda + u - \lambda e^{-u\tau_b}}, \tag{3.43}$$

and,

$$\tilde{j}(u) = \frac{\lambda e^{-u\tau_b}}{\lambda + u - \lambda e^{-u\tau_b}}. \tag{3.44}$$

Expanding the denominator of Eq.(3.43) in terms of $\lambda e^{-u\tau_b}/(\lambda+u)$, allows one to easily invert the Laplace transform, term by term, giving,

$$p_o(t) = \sum_{n=0}^{\infty} \frac{[\lambda(t-n\tau_b)]^n}{n!} e^{-\lambda(t-n\tau_b)} \theta(t-n\tau_b), \tag{3.45}$$

where $\theta(t)$ is the Heaviside function. The stationary open probability, $p_o(\lambda)$, and flux, $j(\lambda)$, can be obtained from Eqs.(3.43) and (3.44) by using $\tilde{f}(u) \simeq \frac{f(\lambda)}{u}$,

$$p_o(\lambda) = \frac{1}{1+\lambda\tau_b}, \tag{3.46}$$

and

$$j(\lambda) = \frac{\lambda}{1+\lambda\tau_b}. \tag{3.47}$$

These results can be easily inferred from Eqs. (3.34) and (3.35) by setting $\langle m \rangle = 0$ and $\langle t \rangle = 1/\lambda$. The exiting particle flux is controlled by the incoming flux, λ and the time of blockage, τ_b.

We now consider the $N=2$ model, i.e. blockage occurs when two particles are simultaneously in the channel, for which exact results have already been obtained [114]. Here we propose an alternative, simpler derivation using the state probabilities of the channel. Let $p_0(t)$, $p_1(t)$ denote the probability that an open channel contains zero or one particle respectively, and $p_2(t)$ be the probability that it contains two particles and is therefore blocked. The time evolution of the process is given by:

$$\frac{dp_0}{dt} = -\lambda p_0(t) + \lambda e^{-\lambda\tau} p_0(t-\tau) + \lambda p_1(t-\tau_b), \tag{3.48}$$

$$\frac{dp_1}{dt} = -\lambda e^{-\lambda\tau} p_0(t-\tau) - \lambda p_1(t) + \lambda p_0(t), \tag{3.49}$$

$$\frac{dp_2}{dt} = -\lambda p_1(t-\tau_b) + \lambda p_1(t), \tag{3.50}$$

with the following initial conditions:

$$p_0(0) = 1,\ p_1(0) = p_2(0) = 0. \tag{3.51}$$

In Eq.(3.48), the loss term corresponds to the entrance of a particle in the empty channel at time t. The two gain terms $\lambda e^{-\lambda\tau} p_0(t-\tau)$ and $\lambda p_1(t-\tau_b)$ correspond to a particle exiting the channel at time t and a channel release (with a blockage occurring at time $t-\tau_b$), respectively. In Eq.(3.49), the two loss terms describe either a particle exiting the occupied channel at time t or a particle entering the occupied channel. The gain term corresponds to a

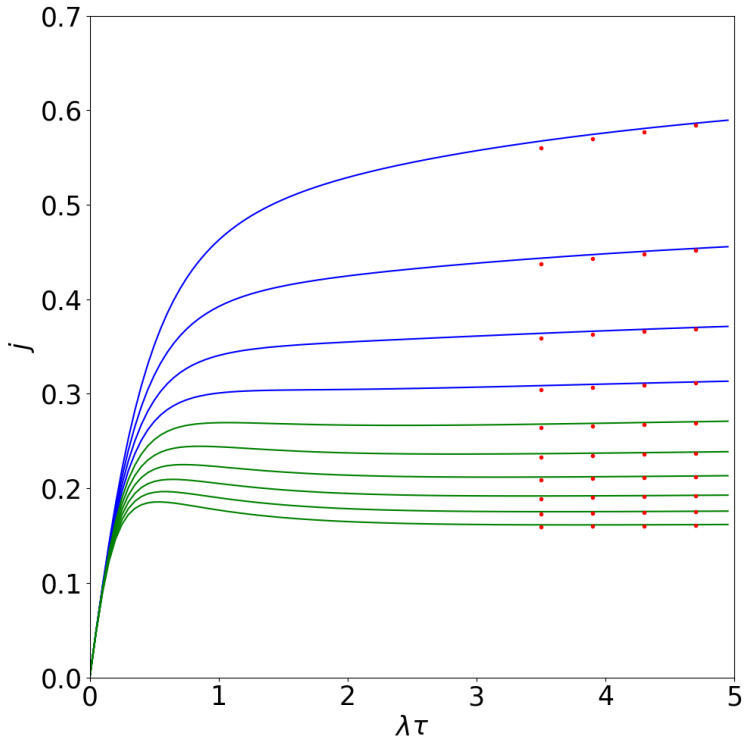

Figure 3.4: Exiting flux, $j(\lambda)$, versus λ for $N = 2$ and $\tau_b = 3,4.\cdots,12$ from top to bottom. The blue curves show cases where the flux increases monotonically with λ. The green curves show cases where the flux displays a maximum at a finite value of λ. The dotted lines correspond to the asymptotic values of the flux, Eq.(3.40).

particle entering a free channel. In Eq.(3.50), the loss term corresponds to a channel release and the gain term to a particle entering a channel with one particle already inside. Summing the three equations verifies that the total probability is conserved: $p_0(t)+p_1(t)+p_2(t)=1$. Taking the Laplace transform of Eqs.(3.48-3.50) gives:

$$\left[u+\lambda(1-e^{-\tau(u+\lambda)})\right]\tilde{p}_0(u)-\lambda e^{-u\tau_b}\tilde{p}_1(u)=1, \tag{3.52}$$

$$-\lambda(1-e^{-\tau(u+\lambda)})\tilde{p}_0(u)+(\lambda+u)\tilde{p}_1(u)=0, \tag{3.53}$$

$$-\lambda(1-e^{-u\tau_b})\tilde{p}_1(u)+u\tilde{p}_2(u)=0. \tag{3.54}$$

These simultaneous equations may be solved to give

$$\tilde{p}_0(u)=\frac{u+\lambda}{\Delta}, \tag{3.55}$$

$$\tilde{p}_1(u)=\frac{\lambda}{\Delta}(1-e^{-\tau(u+\lambda)}), \tag{3.56}$$

$$\tilde{p}_2(u)=\frac{\lambda^2}{u\Delta}(1-e^{-u\tau_b})(1-e^{-\tau(u+\lambda)}), \tag{3.57}$$

where

$$\Delta=(u+\lambda)^2-\lambda(\lambda+u)e^{-\tau(u+\lambda)}-\lambda^2e^{-u\tau_b}(1-e^{-\tau(u+\lambda)}). \tag{3.58}$$

The mean exiting flux $j(t)$ is the sum of two contributions: the exit of a particle from an open channel and the release of two particles from a closed channel. $j(t)$ is therefore given by

$$j(t)=\lambda e^{-\lambda\tau}p_0(t-\tau)+2\lambda p_1(t-\tau_b). \tag{3.59}$$

By using Eqs.(3.55),(3.56), the Laplace transform of the output flux $\tilde{j}(u)$ is

$$\tilde{j}(u) = \frac{\lambda}{\Delta}[(u+\lambda)e^{-(u+\lambda)\tau} + 2\lambda e^{-u\tau_b}(1-e^{-\tau(u+\lambda)})]. \tag{3.60}$$

As expected, we recover the results of Ref.[114] and the time-dependent mean flux can be obtained by a Laplace inversion of Eq.(3.60). The key quantities we focus on are the stationary probability $p_o(\lambda)$ that the system is open and the mean flux $j(\lambda)$. $p_o(\lambda)$ is the sum of the two stationary probabilities p_0 and p_1, each obtained by evaluating $\lim_{u\to 0} u\tilde{p}_i(u)$ with $i = 0, 1$:

$$p_o(\lambda) = \frac{2-e^{-\lambda\tau}}{2+\lambda\tau_b-(1+\lambda\tau_b)e^{-\lambda\tau}}, \tag{3.61}$$

and

$$j(\lambda) = \lambda\frac{2-e^{-\lambda\tau}}{2+\lambda\tau_b-(1+\lambda\tau_b)e^{-\lambda\tau}}. \tag{3.62}$$

Figure 3.4 displays $j(\lambda)$ versus $\lambda\tau$ for different integer values of τ_b from 3 to 12. The dashed lines correspond to the asymptotic values of the exiting flux $\lim_{\lambda->\infty} j(\lambda) = \frac{2}{\tau_b}$. One first observes that the stationary flux reaches the asymptotic values more rapidly as τ_b increases. Moreover, $j(\lambda)$ displays a maximum when τ_b is larger than 7. It is possible to obtain the exact value of τ_b for which the flux $j(\lambda)$ displays a maximum at a finite value of λ[117] by solving $\frac{\partial j(\lambda)}{\partial\lambda} = 0$. A real solution for λ exists if $\tau_b > 6.2$. Note that for $N = 1$ the flux is always a monotonically increasing function of λ.

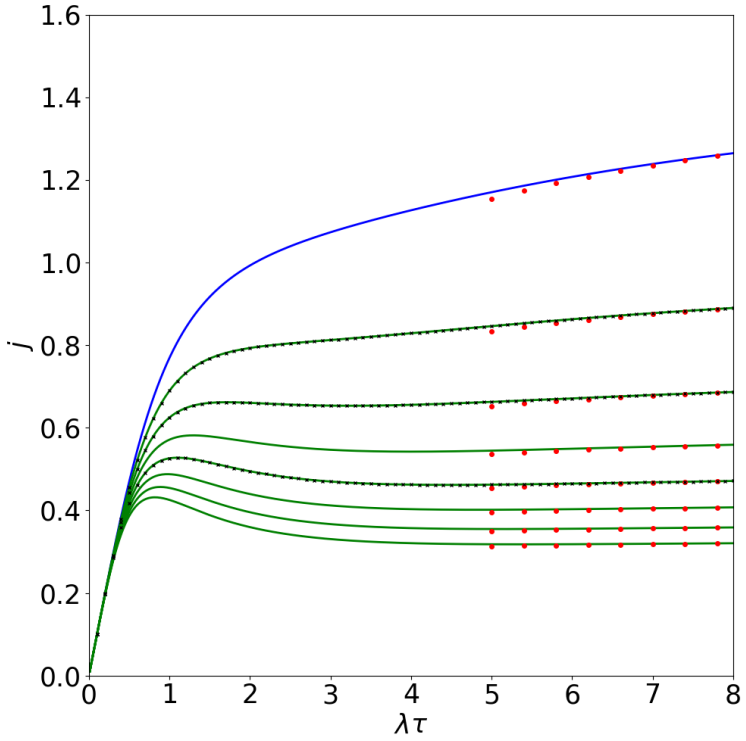

Figure 3.5: Exiting flux, $j(\lambda)$ versus λ for $N = 3$ and $\tau_b = 2, 3, \cdots, 9$ from top to bottom. The blue curves indicate cases where the flux increases monotonically with λ. The green curves indicate the cases where the fluxes display a maximum at a finite value of λ. The black crosses show simulation results for $\tau_b = 3, 4, 6$, which perfectly match with the exact results. The dotted lines indicate the asymptotic values of the flux, Eq.(3.40).

For $N = 3$, the complete kinetic description of the model is cumbersome so we restrict our attention to the stationary quantities for which analytical expressions have been obtained [110]. In particular, the mean time to blockage starting from an empty channel is given by

$$\lambda\langle t\rangle = \frac{2e^{\nu}\sinh(g\nu) + ge^{\lambda\tau}}{-g - 2\sinh(g\nu)e^{-\nu} + e^{\nu}\left(\sinh(g\nu) + g\cosh(g\nu)\right)} + 1 \tag{3.63}$$

for $\lambda\tau > 2\ln(2)$ and

$$\lambda\langle t\rangle = \frac{2e^{\nu}\sin(g\nu) + ge^{\lambda\tau}}{-g - 2\sin(g\nu)e^{-\nu} + e^{\nu}\left(\sin(g\nu) + g\cos(g\nu)\right)} + 1 \tag{3.64}$$

for $\lambda\tau < 2\ln(2)$, where $g = \sqrt{|1-4e^{-\lambda\tau}|}$ and $\nu = \frac{\lambda\tau}{2}$. The two stationary quantities $p_o(\lambda)$ and $j(\lambda)$ are obtained by inserting this result in Eqs.(3.34) and(3.35). Fig. 3.5 displays $j(\lambda)$ as a function of $\lambda\tau$ for different values of τ_b. There are several differences compared with the $N = 2$ model. First, a maximum exiting flux occurs if the blockage time $\tau_b > 3.6$, which is significantly smaller for $N = 2$ ($\tau_b > 6.2$). Second, the asymptotic values are reached at a lower value of λ, and finally, the intensity of λ at which $j(\lambda)$ is maximum is also shifted towards larger intensity.

3.4.2 Steady state simulation results: $N > 3$

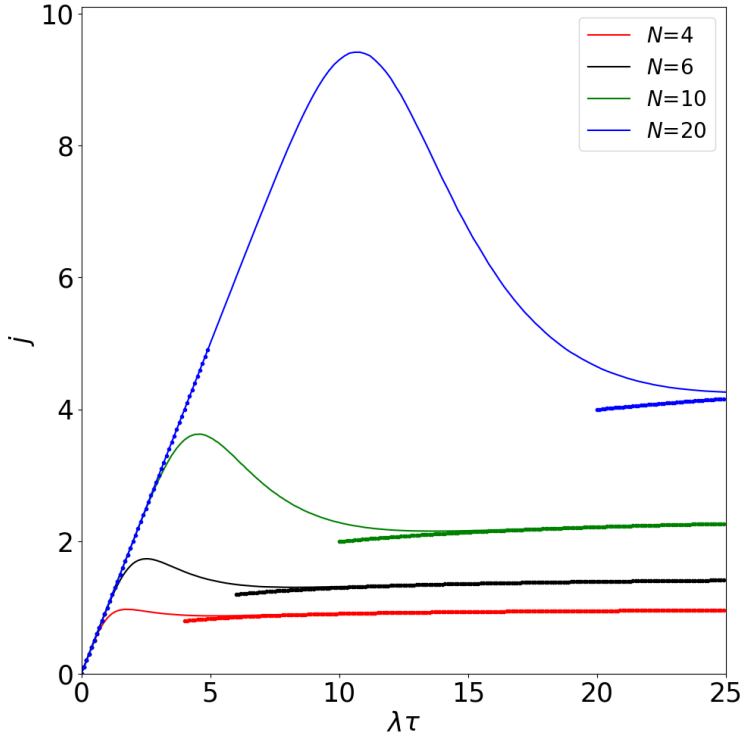

Figure 3.6: Exiting particle flux, $j(\lambda)$, versus λ for $N = 4, 6, 10, 20$ and $\tau_b = 4$. Dotted curves correspond to the asymptotic values at low and high intensity.

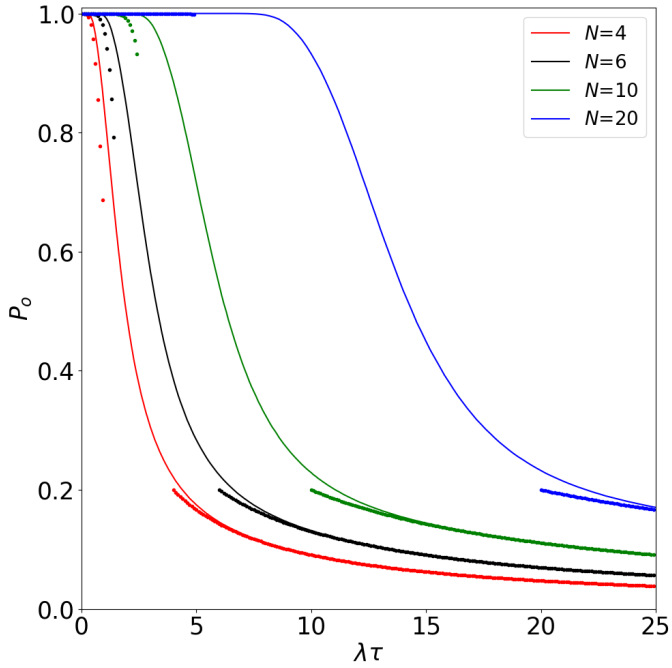

Figure 3.8: Open probability p_o versus $\lambda\tau$ for $N = 4, 6, 10$ and $\tau_b = 4$. Dotted curves correspond to the asymptotic values at low and high intensity.

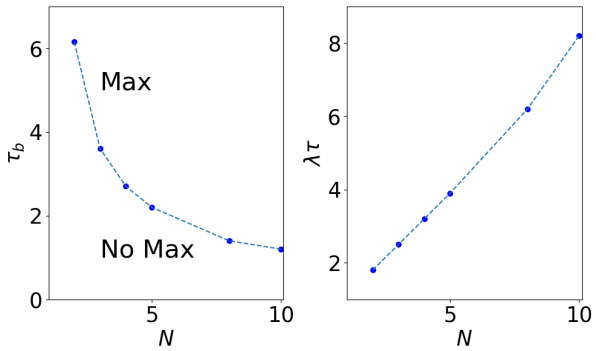

Figure 3.7: (left) Critical values of τ_b as a function of N above which the steady state flux of a single channel displays a maximum at finite λ. (right) The corresponding values of $\lambda\tau$.

As a result of strong time correlations between the transiting particles, it was not possible to obtain analytic solutions for $N > 3$. We therefore used numerical simulations to investigate these cases. To benchmark our code, we compared the simulation results for the stationary flux for $N = 3$ with the exact expressions for three different values of τ_b. In Fig. 3.5 we observe perfect agreement between the analytical expressions and the simulation results. Figure 3.6 displays the stationary exiting flux as a function of the intensity for different values of N and $\tau_b = 4$. At low intensity, the flux increases linearly, and at high intensity the asymptotic behaviour of the simulation results is well-described by Eq.(3.40). The behaviour in the intermediate region is due to complex dynamics that alternates between blockages and sequences of uninterrupted transport. For $N > 3$, the stationary flux, $j(\lambda)$, may display a maximum at finite $\lambda\tau$, whose amplitude increases with N. The stationary flux also exhibits a minimum which is always smaller than the asymptotic value, N/τ_b.

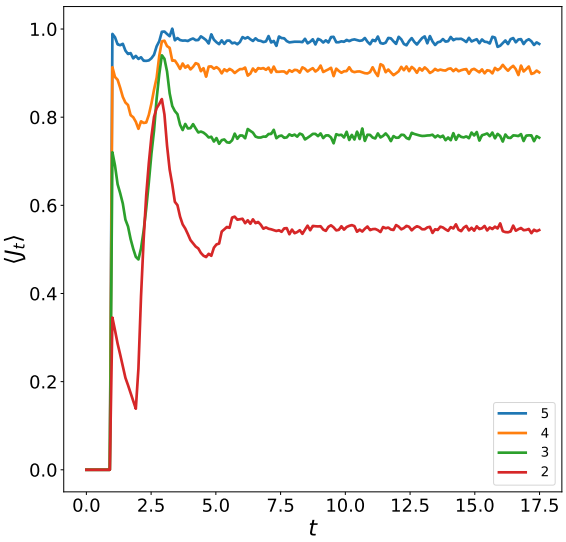

(a) $\tau = 1, \tau_b = 2, \lambda = 1$

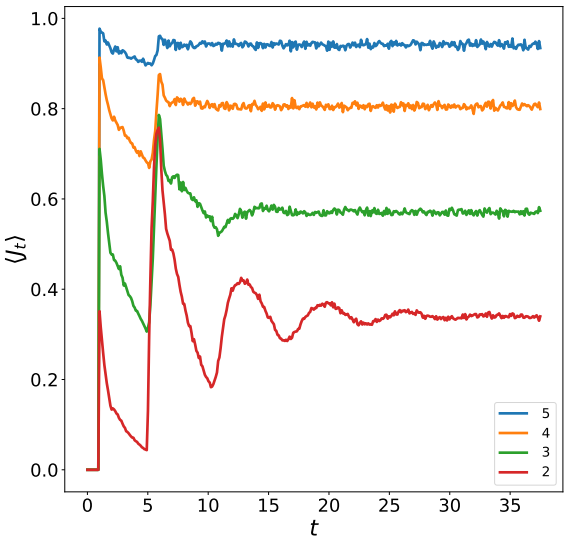

(b) $\tau = 1, \tau_b = 5, \lambda = 1$

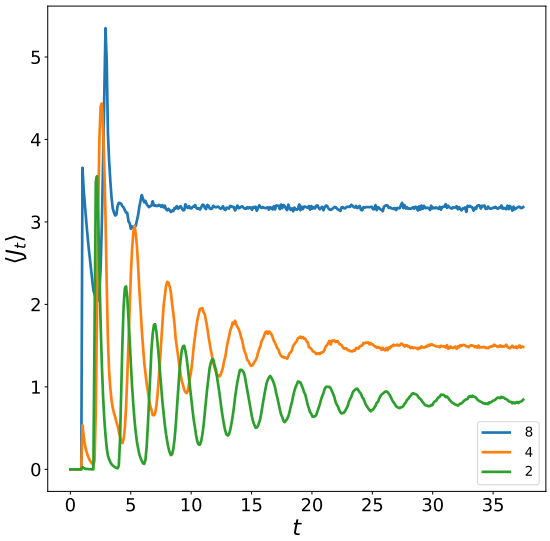

(c) $\tau = 1, \tau_b = 2, \lambda = 5$

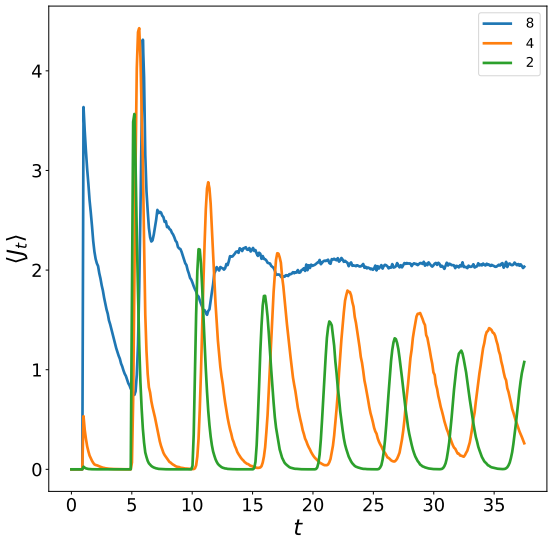

(d) $\tau = 1, \tau_b = 5, \lambda = 5$

Figure 3.9: Numerically obtained transient average flux through system for different N (shown in legend). Results were obtained using the Gillespie algorithm.

We performed a systematic study of the behaviour of the exiting flux as a function of λ, τ_b and N. The flux always displays a maximum when τ_b exceeds a threshold value. Figure 3.7 shows that the critical value of τ_b decreases rapidly with N, showing that the feature observed in Fig. 3.4 is very general and occurs for smaller values of τ_b when N increases. For τ_b below the critical value, the stationary flux is a monotonically increasing function of $\lambda\tau$. The right panel of Fig. 3.7 shows the values of $\lambda\tau$ corresponding to the critical values of τ_b. The behaviour of the open probability $p_o(\lambda)$, shown in Fig. 3.8, is consistent with Eq.(3.37).

In particular, a plateau whose length increases in proportion to N (roughly as $N/2$), is observed. This corresponds

to the situation where blockage events are rare and the output flux is close to λ.

3.4.3 Single channel time-dependent flux

Figure 3.9 show simulation outputs for the time-dependant average flux, with a transit time $\tau = 1$, and a deblocking time of $\tau_b = 2,5$ respectively from a single channel for different values of N and $\lambda = 1,5$. As the channel capacity increases, the time dependent flux presents fewer oscillations, and tends towards a higher steady state value that depends on the intensity of the entering stream. Furthermore, increasing the value of τ_b, for a given value of intensity increases the spacing between flux oscillations.

3.5 Bundle model

We now consider a bundle of N_c identical channels. Each channel has the same properties as the single channel model, i.e. blockage occurs when N particles are present in a channel at the same time. In the following we assume that the total intensity, $\Lambda = \lambda N_c$, is constant and is equally distributed over the open channels. Thus, after k blockages the intensity on each of these open $N_c - k$ channels is

$$\lambda_k = \lambda \frac{N_c}{N_c - k}. \tag{3.65}$$

Since a blocked channel releases all particles after finite time τ_b, the system's mean output flux evolves towards a non-zero stationary value. The bundle has two states: open, in which at least one of the constituent channels is open and closed, if all the constituent channels are blocked. If a particle arrives while the bundle is in the latter state, it is rejected.

Equations (3.34,3.35,3.36) cannot be applied to the channel bundle in the steady state, as it does not cycle between closed and empty states for finite intensity, Λ. In the limit of very large intensities, however, we have

$$P_o(\Lambda) \sim \frac{1}{\Lambda} \tag{3.66}$$

and

$$\lim_{\Lambda\to\infty} \langle M \rangle = 0 \tag{3.67}$$

where $\langle M \rangle$ is the mean number of exiting particles that are not the due to blockage releases, and

$$\lim_{\Lambda\to\infty} J(\Lambda) = \frac{NN_c}{\tau_b}. \tag{3.68}$$

In this limit the intensity is so high that all channels block instantaneously and simultaneously and the blocked particles are released after a time τ_b. The exiting flux is entirely the result of these releases. The analogue of Eq.(3.37),

$$J(\Lambda) = \Lambda P_o(\Lambda), \tag{3.69}$$

is valid for arbitrary intensity since, as for the single channel case, it is result of the conservation of particle number.

3.5.1 Exact solution: $N = 1$

When $N > 1$ a particle may traverse the channel in a time, τ, without causing a blockage. In comparison, the $N = 1$ model is singular as no unimpeded transit is possible: each entering particle causes a blockage that lasts for a fixed time, τ_b. The variable, τ, is thus absent in this model. Despite the relative simplicity of the $N = 1$ model, its dynamics cannot be written as a system of differential equations for the state probabilities $P(i,t)$, where i denotes the number of blocked channels at time t. However, in the stationary state, by applying detailed balance (known as the 'rate up - rate down' principle in queuing theory), we have:

$$\Lambda P(i) = (i+1)\frac{P(i+1)}{\tau_b} \tag{3.70}$$

Solving the difference equation and applying conservation of the total probability leads to

$$P(k) = \frac{(\Lambda\tau_b)^k}{k!\sum_{n=0}^{N_c}\frac{(\Lambda\tau_b)^n}{n!}},\ k \in [0,N_c] \tag{3.71}$$

The stationary exiting flux is given by Eq.(3.69) with

$$P_o = 1 - P(N_c) = 1 - \frac{(\Lambda\tau_b)^{N_c}}{N_c!\sum_{n=0}^{N_c}\frac{(\Lambda\tau_b)^n}{n!}} \tag{3.72}$$

The result can be written in the form

$$J(\Lambda) = \Lambda\left(1 - \frac{(\Lambda\tau_b)^{N_c}}{e^{\Lambda\tau_b}\Gamma(1+N_c,\Lambda\tau_b)}\right), \tag{3.73}$$

where $\Gamma(n,x)$ is the incomplete gamma function. The asymptotic behaviour at small intensity, Λ is

$$J = \Lambda\left[1 - \frac{(\Lambda\tau_b)^{N_c}}{N_c!} + O((\Lambda\tau_b)^{N_c+1})\right], \tag{3.74}$$

whereas at large intensity the flux behaves as,

$$J = \frac{N_c}{\tau_b}\left[1 - \frac{1}{\Lambda\tau_b} + O\left(\frac{1}{(\Lambda\tau_b)^2}\right)\right], \tag{3.75}$$

whose leading term is in accordance with Eq.(3.68). For all values of N_c, $J(\Lambda)$ is always a monotonically increasing function of Λ. The expression for $P(N_c)$ is Erlang's first formula [118, 119] for a stochastic queuing process with N_c servers with exponential entry and service time distributions under the condition that when all servers are busy an arrival is rejected. Both models are 'birth-and-death' processes that have the *same* stationary solution. Their transient regimes, however, are significantly different.

3.5.2 Simulation results: $N > 1$

For the multichannel models, no exact solution can be obtained for $N > 1$. Therefore we have performed numerical simulations to obtain the stationary exiting flux, J and the stationary probability that at least one channel is open, P_o for bundles composed of different numbers of channels with increasing capacity N and for $\tau_b = 4\tau$. All quantities were investigated as a function of the mean incoming flux Λ. As discussed in the previous section, the stationary flux rapidly displays a maximum at a finite value of $\lambda\tau$ when $N > 1$.

Figure 3.10 shows J as a function of $\Lambda\tau$ for $N_c = 2, 10$ and for $N = 2, 3, 4, 6, 10$. When $\Lambda\tau \ll 1$, the rate of incoming particles is very small and the finite capacity of the channel is rarely reached, meaning that blockage events are scarce. The stationary exiting flux is therefore equal to the input flux, $J \simeq \Lambda$. This behaviour is observed

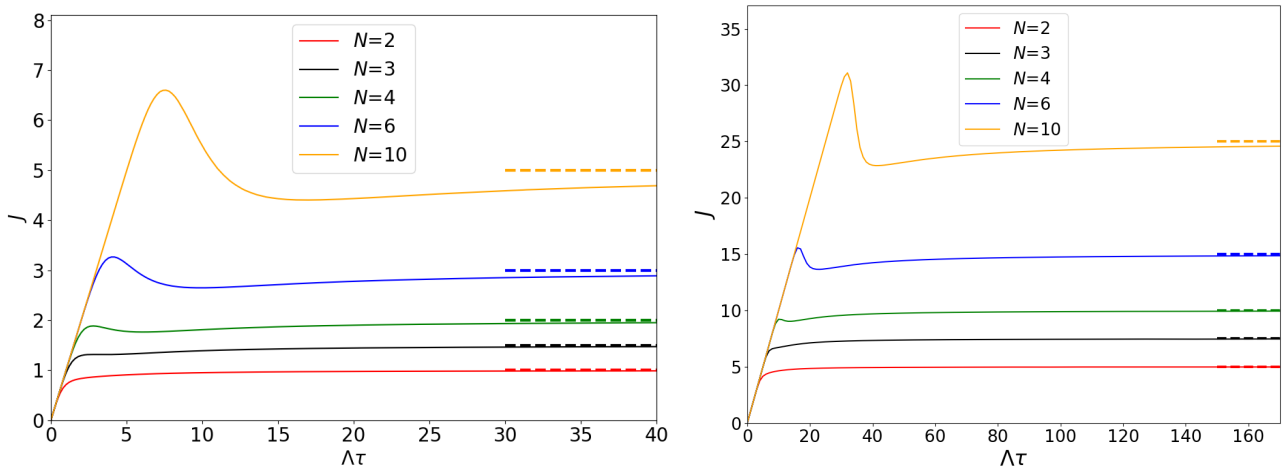

Figure 3.10: $J(\Lambda)$ versus $\Lambda\tau$ for $N = 2,3,4,6,10$ and $\tau_b = 4$, for (left) $N_c = 2$, and (right) $N_c = 10$. The dashed lines correspond to the asymptotic values, Eq.(3.68).

for a larger range of $\Lambda\tau$ for larger values of N and N_c . Figure 3.11a shows the rescaled flux J/N_c versus the rescaled intensity, Λ/N_c for different values of N_c. In the low intensity regime J is equal to Λ and displays a finite discontinuity at Λ_c. At high intensities the curve evolves towards an asymptotic and the best fit is given by

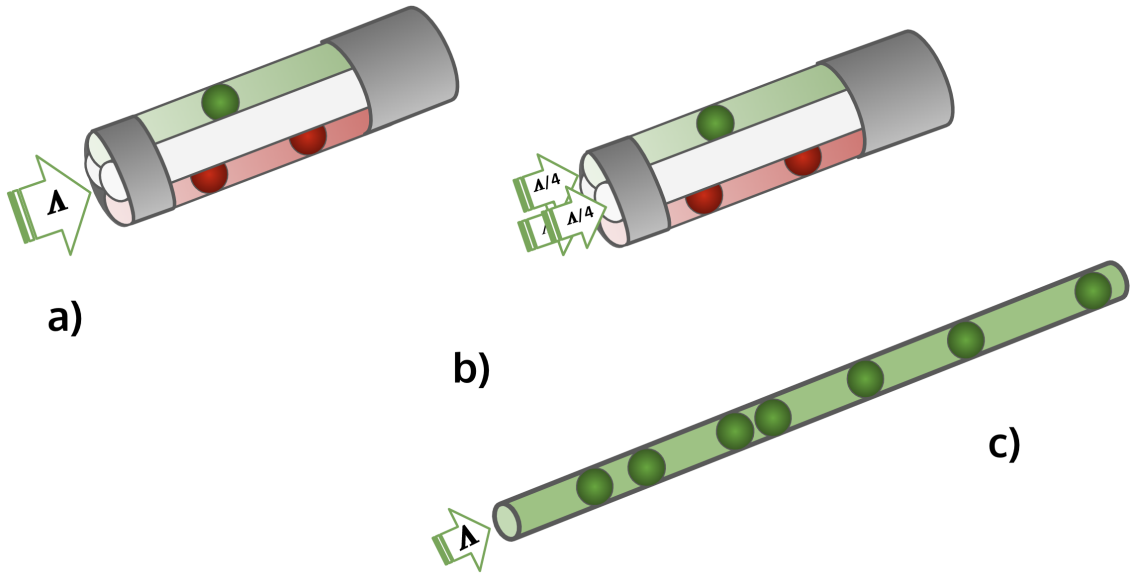

Figure 3.12: (a) Four coupled low capacity (LC) channels, each with capacity $N = 2$, sharing the input particle flux of intensity, Λ. If one channel is blocked, the flux is evenly redistributed between the remaining open channels; (b) Four independent LC channels, each of capacity $N = 2$, where each channel recieves a flux of particles at intensity, $\Lambda/4$. If one channel is blocked, its incoming particles are simply rejected and not redirected to the remaining open channels. (c) One high capacity (HC) channel. While blocked, incoming particles are simply rejected. The first scenario compares systems (b) and (c). For a fair comparison in the case shown, the HC threshold should equal $N_{HC} = N_c * N = 8$. The second scenario compares systems (a) and (b).

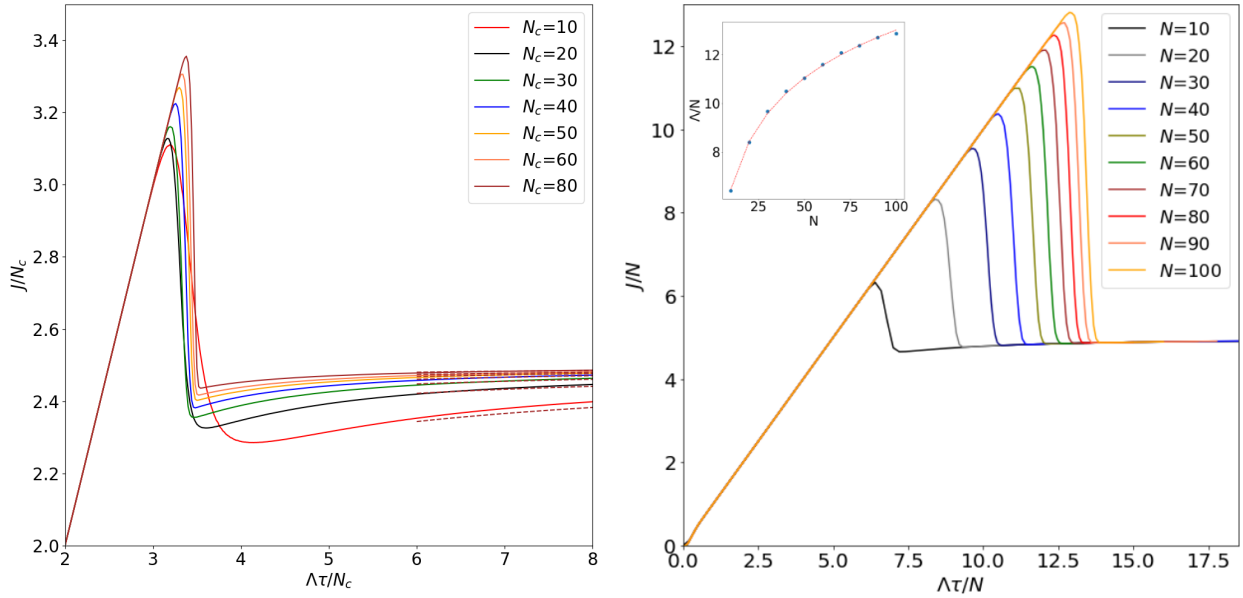

(a) $N = 10$. Many N_c.

(b) $N_c = 20$, Many$N$.

Figure 3.11: Left: Exiting flux of a channel bundle composed of N_c channels each with $N = 10$: J/N_c versus $\Lambda\tau/N_c$ for different values of N_c and $\tau_b = 4$. The dashed curves show the asymptotic behaviour. Right: J/N versus $\Lambda\tau/N$ for different values of N and $\tau_b = 4$. The dashed curves correspond to the asymptotic behaviours. The inset shows the value of Λ that maximises the exiting flux as a function of N and the red dashed line shows the logarithmic fit, of form $2.73\log(0.89N) + 0.65$.

$$J \simeq \frac{N_c N}{\tau_b}\left(1 - \frac{3N}{2\Lambda\tau_b}\right). \tag{3.76}$$

We observe an abrupt change of kinetic behaviour: Below the critical value Λ_c, almost all particles cross the bundle without triggering a significant number of blockages, whereas for larger Λ, all channels are closed and the stationary flux is essentially given by the release of blocked particles.

Fig. 3.11b shows the rescaled flux J/N versus the rescaled intensity, Λ/N for different values of N for a given $N_c = 10$. At a low input intensity, the exiting flux J is equal to Λ until it reaches a maximum close to a critical value that closely follows a logarithmic law, as shown in the inset of Fig. 3.11a. For higher values of input intensity the rescaled exiting flux, for all values of N, rapidly collapses to a single curve whose best fit is again given by Eq.(3.76).

3.6 Flux optimization

Here we compare the stationary flux of a bundle of coupled channels with that of a bundle of uncoupled channels and one 'high capacity' (HC) channel. Fig. 3.12 illustrates the configurations compared. The transport efficiency is measured by the difference in output flux, ΔJ. The systems are chosen so that in the limits of low and high input flux intensity, $\Delta J = 0$. In the low intensity limit, since blocking events are rare, the exiting flux is equal the input flux Λ, irrespective of the configuration. In the high intensity limit, Eqs.(3.39) and (3.68) demonstrate that the exiting fluxes of the single high capacity, bundled uncoupled or coupled channels are also be equal. Since the stationary flux of a bundle of coupled channels displays non-trivial behaviour with increasing N_c and N, we therefore expect non-trivial behaviour of ΔJ.

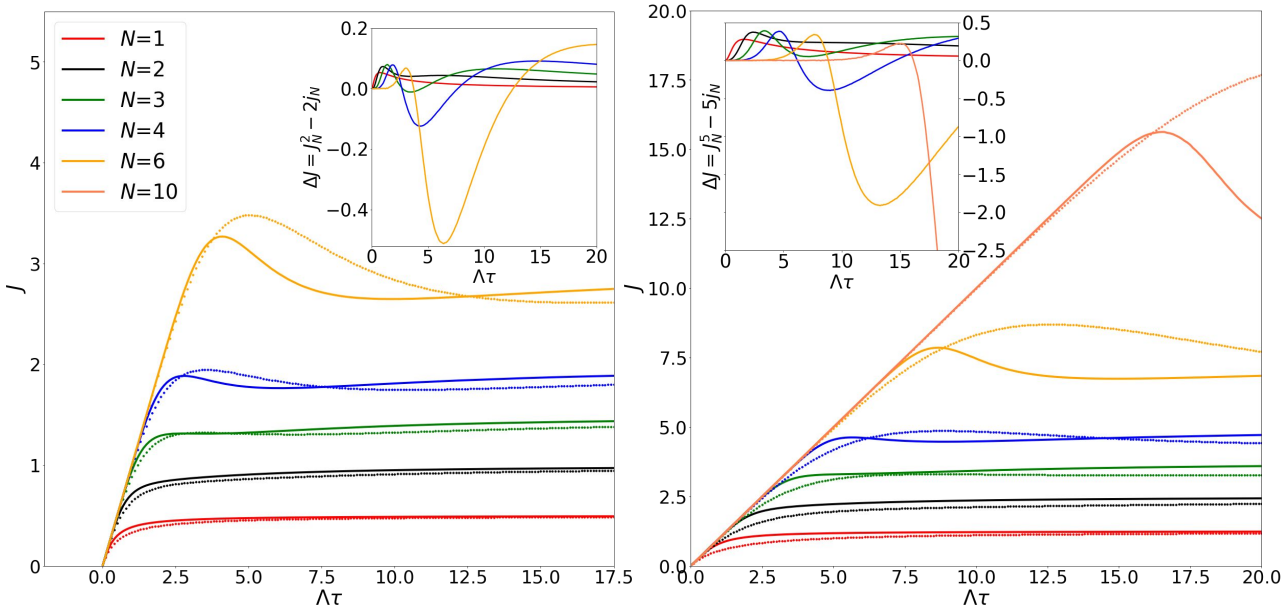

Figure 3.13: Total exiting flux from the coupled (lines) and uncoupled (dotted) channel configurations. From Left to right, $N_c = 2,5$, $\tau_b = 4$. The insets show the difference between the two.

3.6.1 Coupled versus uncoupled channels

We first compare a channel bundle composed of N_c channels, each of capacity N. The entering flux, Λ, is equally distributed over the coupled open channels. In contrast, the N_c independent channels, each of capacity N, each receive an incoming flux of intensity, Λ/N_c. The difference in the output flux of the two configurations is defined as:

$$\Delta J = J_N^{N_c}(\Lambda) - N_c j_N(\Lambda/N_c). \tag{3.77}$$

Simulation results comparing the output flux of each configuration for $N_c = 2,5$, $\tau_b = 4$, are shown in Fig. 3.13. The differences are shown in the inset of the figure. At low intensity, for all configurations, the output flux is approximately equal for each setup, and linearly increases with Λ until a critical value, which itself is a monotonically increasing function of N.

The behaviour for $N = 1$ can be understood quantitatively using the results of Sec. 3.5.1 and Eq.(3.47). At low intensity, the flux difference is

$$\Delta J = \frac{\Lambda^2 \tau_b}{N_c} + O(\Lambda^3), \tag{3.78}$$

and at high density we find

$$\Delta J \simeq \frac{N_c(N_c-1)}{\Lambda \tau_b^2} \tag{3.79}$$

and confirmed that $\Delta J > 0$ for $0 < \Lambda < \infty$. We conclude that the coupled channels are always more efficient than the uncoupled ones. The difference is maximised for a finite value of Λ. For all $N > 1$, we note the appearance of two maxima in the flux difference with an intervening minimum. The increased complexity is due to the presence of two characteristic times: the transit time τ and the blockage time τ_b (while the $N = 1$ system has only the latter).

Fig. 3.14 shows the flux difference between the bundle configurations at $Nc = 2$, $N = 2$, as a function of intensity of entering flux, Λ, for different values of τ_b. For $\tau_b > 2$ the behaviour is more complex after the first maximum, with the appearance of a minimum followed by a second maximum before tending towards zero.

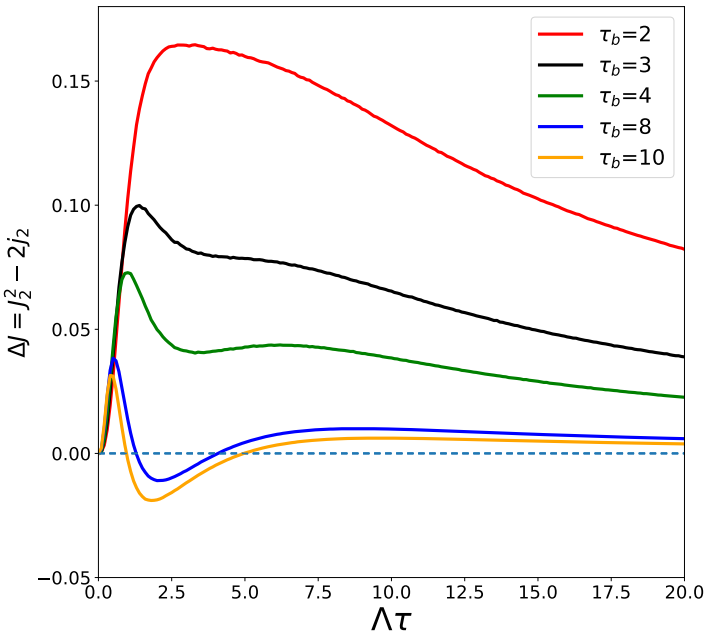

Figure 3.14: Difference in the output flux between $N_c = 2$ coupled and uncoupled channels, with $N = 2$ as a function of intensity, Λ, for different values of τ_b.

3.6.2 Single HC channel verses coupled LC channels

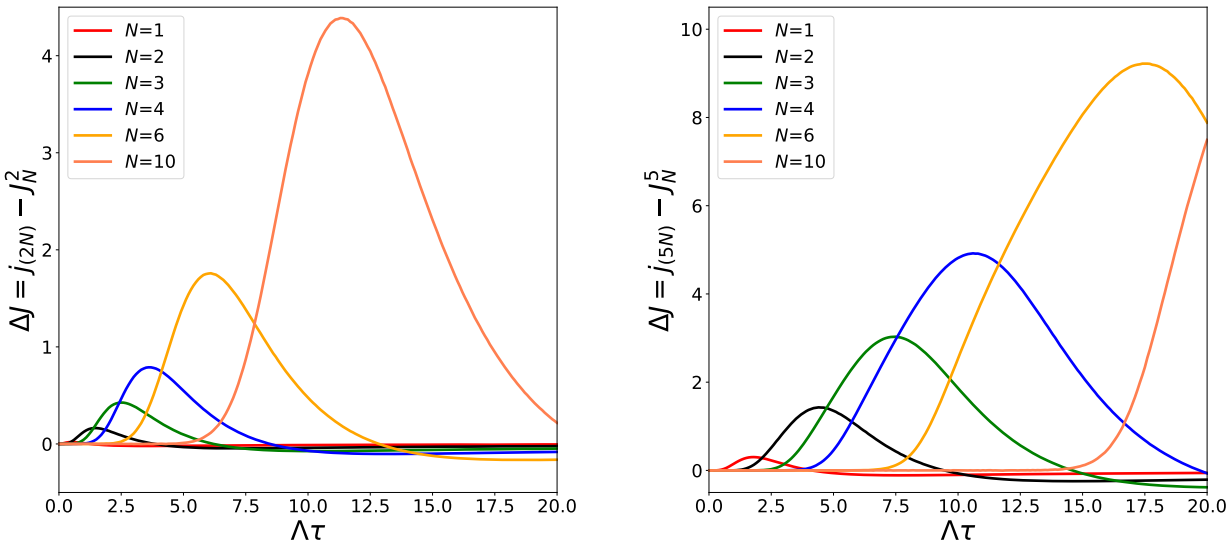

Figure 3.15: Single HC channel, versus coupled LC channels. From top to bottom, $N_c = 2, 5$. All curves display a single maximum followed by a single minimum, before tending to zero at high intensity.

The transport efficiency of a single 'high capacity' (HC) channel is now compared with a bundle of several coupled channels, of a proportionately reduced capacity. Figure 3.15 shows the difference in the output stationary state flux between a single HC channel and a bundle of $N_c = 2,5$ coupled LC channels, with different capacities. The flux difference in this case is

$$\Delta J = j_{N_c N}(\Lambda) - J_N^{N_c}(\Lambda). \tag{3.80}$$

For all N, the flux difference displays a minimum, followed by a maximum, before tending towards zero for increasing intensity. The amplitudes of the maxima are always greater than those of the minima.

The next chapter will present an extension of the $1D$ model of blockage studied.

CHAPTER
4

MARKOV MODELS OF BLOCKING

This chapter extends the $1D$ channel model previously introduced in Chapter 3 by now taking the transit and deblocking times, τ and τ_b, as exponentially distributed random variables with mean μ and μ^* respectively. This generalisation permits a distribution of service and deblocking times, which increases the range of applicability to real physical scenarios, despite allowing for the possibility of non-physical events manifesting as both transit and deblockage in zero time. The definition of all the system's transition rates as stochastic variables renders the system 'memoryless', the properties and consequences of which shall be examined in the next section.

4.1 Markov processes

Markov processes are random processes whose future state is purely determined by the current one. Poisson processes, defined in Section 3.1.2 are a special type of continuous time Markov processes. The next section introduces Markov chains, that will form the foundation of the extension of the model presented in Chapter 3.

4.1.1 Markov chains & Markov property

A Markov chain is a Markov process that may be either discrete or continuous in time, t, and occurs within a countable sample space of size N, $\mathbb{S} = \{\pi_0(t), \pi_1(t), ...\pi_N(t)\}$. In the discrete case, this process, for n successive events, may be succinctly denoted as :

$$X = (X(n))_{n\in\mathbb{Z}} = (X(0), X(1), X(2)...), \;\; X_n \in \mathbb{S} \;\; \forall n, \tag{4.1}$$

whose lack of memory, in the order 1[1] case, is expressed by:

$$\mathbb{P}(X_{n+1} = x_{n+1} | X_n = x_n, ...X_0 = x_0) = \mathbb{P}(X_{n+1} = x_{n+1} | X_n = x_n). \tag{4.2}$$

i.e. given a current state of the system and the time step, no information about the future is obtained by gathering information of past states.

[1] The order n case accounts for the past n states

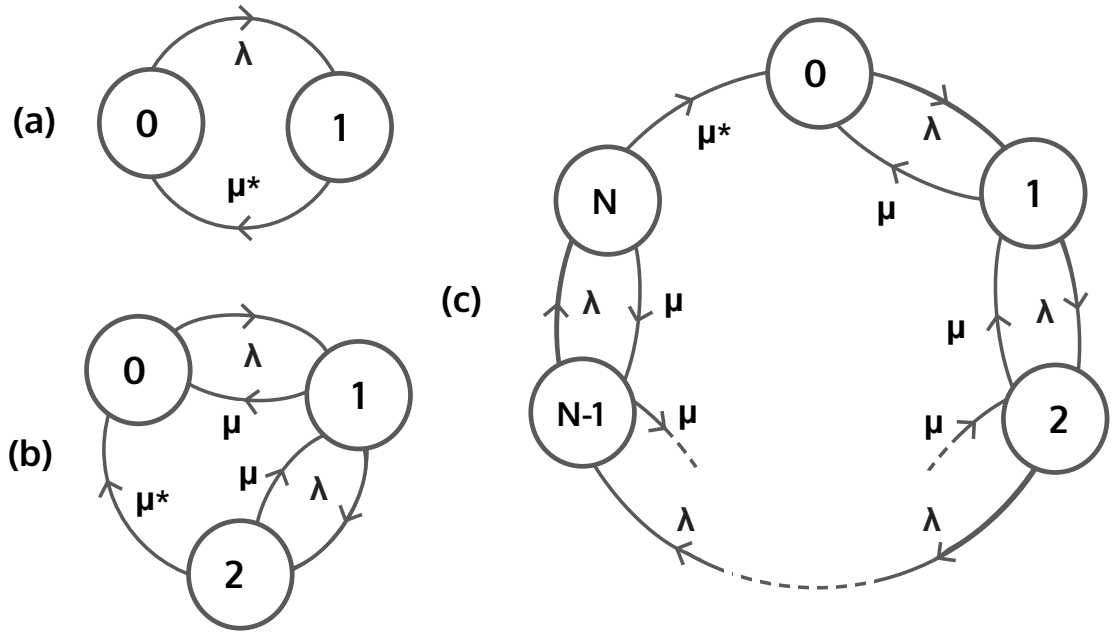

Figure 4.1: Circular $N+1$ state Markov chain systems. (a) $N=1$, (b) $N=2$, which corresponds to the system shown in Fig 2.5, (c) $\forall N \in \mathbb{Z}^+$. The transition rates correspond to the FIFO queueing discipline.

4.1.2 Markov dynamics

To fully characterise the dynamics of a Markov chain we require an initial probability distribution, which can be described as a state vector $\mathbf{P} = [\pi_0(0), \pi_1(0), ...\pi_N(0)]$ where $\pi_k(0),\ 0 \leq k \leq N$ is the probability that the system is in state k at time $t = 0$. N denotes the countable number of possible states within $\mathbb{S}$:

$$\mathbb{P}(X_0 = x_0) = \mathbf{P}(\mathbf{x_0}) \quad \forall x_0 \in \mathbb{S}. \tag{4.3}$$

and an $N \times N$ transition probability matrix, from state $x_n = i$ to $x_{n+1} = j$ expressed by Eq. 4.1.1 as:

$$p_{ij} = \mathbb{P}(X_{n+1} = j | X_n = i), \quad i, j \in \mathbb{S} \times \mathbb{S}. \tag{4.4}$$

From these, the total probabilistic dynamics may be recurrently computed.

A Markov process is termed 'homogeneous' if its transition probabilities do not change with time. In what follows, we will study uniquely these processes. The probability distribution at time $n+1$, $\mathbf{P}(\mathbf{j})$ relative to the system's probability distribution at time n, $\mathbf{P}(\mathbf{i})$, is written as:

$$\mathbf{P}(j) = \mathbb{P}(X_{n+1} = j) = \sum_{i \in \mathbb{S}} \mathbb{P}(X_n = i)\mathbb{P}(X_{n+1} = j | X_n = i) = \sum_{i \in \mathbb{S}} \mathbf{P}(\mathbf{i}) p_{ij} \tag{4.5}$$

The dynamics of the finite state space Markov chains studied will be represented as oriented graphs. Each node within the graph represents a state, and for all pairs of states (i, j), an edge going from one to the other represents a transition probability $p_{ij} > 0$, and so takes its value. See Fig. 4.1

4.2 Queuing theory

Much of what follows will be presented in the framework of queuing theory, which define a system in terms of three parameters: *clients*, i.e. people, objects, particles, that request a service, *servers*, components of the system

in question that respond to the request, and *service*, which is the action required to respond to the request. A client can use a service if it's not occupied, and once a service has been carried out, the server then becomes available for the next client. Every model is defined by three factors: the arrival process, the service mechanism, and the queuing discipline. Kendall notation $a/b/s/c$ is employed [120] where:

- a: The time distribution of arriving demands of service.
- b: The service time distribution.
- s: The number of servers.
- c: The system size (i.e. the number of objects that may be accommodated while awaiting service).

The fourth parameter, c may be omitted if there is no capacity restriction. If $c = s$, the model is termed a 'loss' system as there is no waiting room. The arrival and service time distribution may be described by:

- M: exponential distribution
- D: deterministic (i.e. constant service time) as studied in Chapter 3.
- G: 'General distribution'

Further characteristics include the client and service behaviour: If a client arrives to find all servers occupied, it may either wait, or leave. And finally, the service behaviour, may serve the clients one by one, according to their order of arrival, randomly, or by priority. The most frequently used is the discipline of 'first in, first out' (FIFO) [2], and will be often considered in the following sections.

4.2.1 $M/M/1$ model

This is the most well known and widely studied, queuing model. It consists of a single server, with client arrival following a Poisson process of intensity λ, and an average exponential service time $1/\mu$. If $\lambda/\mu > 1$, the rate of client arrival is greater than their departure, and an indefinitely long queue forms. In this case the system does not have a stationary distribution. The server follows the 'first in first out' (FIFO) discipline. The time evolution of the system's state probabilities is described by the following differential equations:

$$\dot{\pi}_0 = -\lambda \pi_0(t) + \mu \pi_1(t) \tag{4.6}$$

$$\dot{\pi}_n = -(\lambda + \mu)\pi_n(t) - \mu \pi_{n+1}(t) + \lambda \pi_{n-1}(t) \tag{4.7}$$

The stationary probability that k clients are simultaneously in the system is simply given by:

$$\pi_k = \pi_0 \left(\frac{\lambda}{\mu}\right)^k, \tag{4.8}$$

where:

$$\pi_0 = \left(1 = \sum_{k=1}^{\infty} \left(\frac{\lambda^k}{\mu}\right)\right) = 1 - \frac{\lambda}{\mu}. \tag{4.9}$$

[2] In the mundane example of supermarket checkouts, this discipline is clearly not followed due to the distinction between 'normal and self checkouts' or the option to pay by cash or card.

4.2.2 $M/M/N/N$ model

We consider the system where service demands arrive following the Poisson process of intensity λ , and the service time has an exponential distribution with mean $1/\mu$. There are $s = N$ servers, and no waiting room. The finite state space is defined by the number of demands of service present within the system. Unlike the previous model examined, the servers do not follow the FIFO discipline.

Let π_k be the probability that, at an arbitrary time while in the stationary state, there are $k \in [0,N]$ clients in the system. The corresponding set of balance equations is then given by:

$$\lambda \pi_0 = \mu \pi_1, \tag{4.10}$$

$$\lambda \pi_{k-1} + (k+1)\mu \pi_{k+1} = (\lambda + k\mu)\pi_k, \quad 1 \leq k \leq N-1, \tag{4.11}$$

$$\lambda \pi_{N-1} = N\mu \pi_N \tag{4.12}$$

the above three expressions are equivalent, by the application of both the rate up = rate down principle, and recursion, to:

$$\pi_k = \frac{\lambda}{k\mu}\pi_{k-1} = \frac{\lambda^2}{k(k-1)\mu^2} = \ldots = \frac{1}{k!}\left(\frac{\lambda}{\mu}\right)^k \pi_0, \quad 1 \leq k \leq N. \tag{4.13}$$

applying the normalisation condition $\sum_{k=0}^{N} \pi_k = 1$, the probability distribution for k service demands to the system is:

$$\pi_k = \frac{1}{k!}\left(\frac{\lambda}{\mu}\right)^k \pi_0 = \frac{\frac{1}{k!}\left(\frac{\lambda}{\mu}\right)^k}{\sum_{i=0}^{k} \frac{1}{i!}\left(\frac{\lambda}{\mu}\right)^i}, \quad 0 \leq k \leq N. \tag{4.14}$$

Service demands that arrive while all servers are being used are blocked. Since the probability that there are k demands of service immediately before an arrival equals the probability that there are k service demands at an arbitrary time, given by Eq. 4.2.2. Therefore the blocking probability is:

$$\pi_N = \frac{\frac{1}{N!}(\frac{\lambda}{\mu})^N}{\sum_{i=0}^{N} \frac{1}{i!}(\frac{\lambda}{\mu})^i}. \tag{4.15}$$

This is the Erlang loss formula, first derived in 1917 [121].

4.2.3 Other models

A further generalisation is to consider group arrivals or services [122–124]. The batch service is denoted M/M(a,b)/1, where a is the size of the arriving group, and b is the maximum capacity of the server. The service starts when clients enter the system such that $b \geq a \geq 1$. Group arrivals are used to model many physical applications [125, 126], and group service applies to the management of transport systems with limited capacities, such as elevators [127]. Models with heterogeneous servers, i.e. where each server can have a different service time, have also been studied [128, 129].

4.3 Single channel model

We consider a channel that blocks when N particles are simultaneously present, represented by the circular Markov chain in Fig. 4.1 c. Particles enter the channel according to a Poisson process, defined in Section 3.1.2, with a constant intensity λ. Particle exit is also modelled as Poisson process with a constant rate μ. The channel remains open if it contains fewer than N particles. In the open state, any particle that is present exits the channel at a rate μ, independent of the time already spent inside. However, when N particles are simultaneously present, a blockage occurs with the consequence that all incoming particles are rejected until the channel reopens after a time given by an exponentially distributed blockage time with rate $\mu^* < \mu$. When the channel reopens all the trapped particles are instantaneously ejected. The models introduced here can be viewed as an extension of the, previously seen, approaches developed in queuing theory[46, 130], and encompass situations characterised by both temporary or permanent blockages.

4.3.1 Non-FIFO model

The stochastic dynamics is described by using $N+1$ state probabilities, $\pi(0,t), \pi(1,t), \cdots, \pi(N-1,t)$ and $\pi(N,t)$ which correspond to $0, 1, \cdots, N-1$ and N particles in the channel, respectively. $\mathbf{P(t)} = (\pi(\mathbf{0},\mathbf{t}), \pi(\mathbf{1},\mathbf{t}), \cdots, \pi(\mathbf{N-1},\mathbf{t}), \pi(\mathbf{N},\mathbf{t}))$ denotes the state vector. The time evolution of the process is described by:

$$\frac{d\mathbf{P(t)}}{dt} = \mathbf{P(t)} \cdot \mathbf{Q_{N+1}} \tag{4.16}$$

where $\mathbf{Q_{N+1}}$ is the $(N+1) \times (N+1)$ transition matrix that gives the dynamical rule of evolution,

$$\mathbf{Q_{N+1}} = \begin{pmatrix} -\lambda & \lambda & & & & 0 \\ \mu & -(\lambda+\mu) & \lambda & & & \\ & \ddots & \ddots & \ddots & & \\ & & (N-1)\mu & -(\lambda+(N-1)\mu) & \lambda & \\ \mu^* & & & 0 & -\mu^* & \end{pmatrix}. \tag{4.17}$$

Except for the first and last columns, every state has two gain terms and two loss terms: The two loss terms correspond to a channel with i particles (with $0 < i < N$), where a particle enters at time t (with a rate λ) or where a particle exits (at rate μ). The two gain terms correspond to the entrance of a particle (with a rate λ) in a channel with $i-1$ particles, and to the exit of a particle (at rate μ) from a channel with $i+1$ particles. As the discipline employed in this model in non-FIFO, increasing the number of attendant particles, under the blocking limit, therefore increases the probability that one will exit. The description is completed by considering the two boundary situations: for an empty channel, there is one loss term corresponding to a particle entrance and two gain terms: the first corresponds to a particle exit from an empty channel and the second to the release of a blocked channel (with N particles). Conversely, for a blocked channel, one has a single loss term corresponding to a release at rate μ^* and a gain term corresponding to a particle entering a channel containing $N-1$ particles.

The time evolution of $\mathbf{P(t)}$ is supplemented by the conservation of the total probability, $\sum_{i=0}^{N-1} \pi(i,t) + \pi(N,t) = 1$. Consequently, the sum of each row of the transition matrix is equal to 0, which leads to a zero eigenvalue of the matrix. The steady-state probabilities of the circular processes are explicitly calculated in Adan and Resing [130]. In the steady state, i.e. $\dot{\mathbf{P}} = \mathbf{0}$, the probabilities are given by $\pi_N = C_N \lambda^N$ and, for $k = 1, 2, \ldots, N$,

$$\pi_{N-k} = C_N \mu^* \sum_{j=1}^{k} \left(\lambda^{N-j} \mu^{j-1} \prod_{i=1}^{j-1} [N-k+i] \right), \tag{4.18}$$

where C_N is a normalization constant so that $\sum_{i=0}^{N} \pi_i = 1$, given as:

$$C_N = \left(\lambda^N + \mu^* \sum_{j=0}^{N-1} \frac{N!}{(j+1)(N-j-1)!} \mu^j \lambda^{N-1-j} \right)^{-1}. \tag{4.19}$$

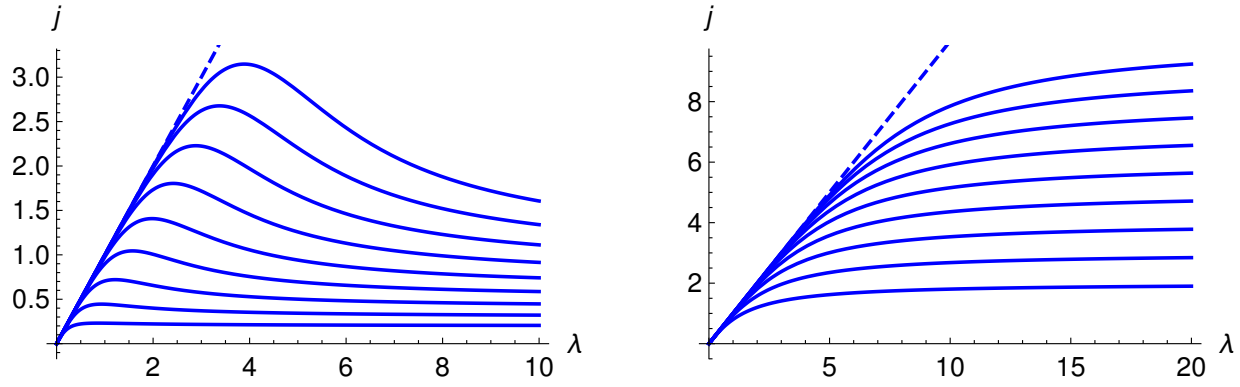

Figure 4.2: (a) Steady state throughput, j, Eq. (4.22), as a function of the intensity, λ, for $\mu = 1, \mu^* = 0.1$ and $N = 2,3,...,10$ bottom to top. The dashed line shows the behaviour in the limit of small intensity, $j = \lambda$. The limiting value at large intensity is given by $N\mu^*$. (b) Steady state throughput of the $M/M/N/N$ queue as a function of the intensity, λ, for $\mu = 1$. The limiting value at large intensity is given by $N\mu$.

Following the analysis presented by Cohen [131] we find the following formula for the mean first passage time from the empty state 0 to the blocked state with N particles. Appendix A contains the full calculation.

$$\nu_{0,N} = \frac{1}{\lambda}\sum_{m=0}^{N-1} m! \sum_{k=0}^{m} \frac{1}{k!}\left(\frac{\lambda}{\mu}\right)^{k-m}. \tag{4.20}$$

The throughput can be calculated by noting that state $k \in [0,N]$ contributes $k\mu\pi_k(t)$ particles per unit time, which is the rate of exiting particles $k\mu$ multiplied by the probability that the channel is in state k. There is an additional contribution from the blocked state whose N particles are simultaneously ejected at the rate μ^*, which adds $N\mu^*\pi_N(t)$. The general expression of the time dependent throughput is the sum of these contributions

$$j_N(\lambda,t) = k\mu \sum_{k=1}^{N-1} \pi_k(t) + N\mu^*\pi_N(t). \tag{4.21}$$

In the stationary state, j can be expressed as

$$j = \lambda(1-\pi(N)), \tag{4.22}$$

i.e. the incoming flux multiplied by the probability that the channel is open. From $\pi_N = C_N\lambda^N$ and Eq. (4.19) we also find the following explicit expression

$$j_N(\lambda) = \frac{\lambda}{\left[\mu^* \sum_{j=0}^{N-1} \frac{N!}{(j+1)(N-j-1)!}\mu^j\lambda^{-(j+1)}\right]^{-1} + 1}. \tag{4.23}$$

In the large intensity limit, the throughput may be written as:

$$j_N(\lambda \to \infty) = N\mu^*, \tag{4.24}$$

which corresponds to the situation where no particle can cross the channel without blockage. The flux is given by the number of particles trapped in each blockage, N, times the rate of the channel release, μ^*. At low intensity the throughput is given by

$$j_N(\lambda) = \lambda - \frac{\lambda^{N+1}}{(N-1)!\mu^{N-1}\mu^*} + O(\lambda^{N+2}). \tag{4.25}$$

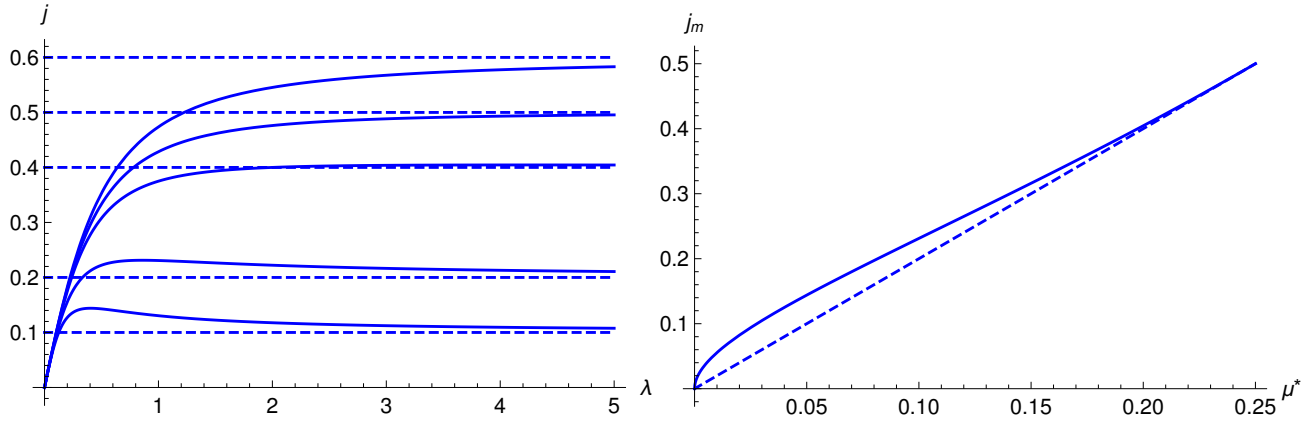

(a) $N = 2$. Steady state throughput

(b) $N = 2$. Maximum throughput

Figure 4.3: Left: $N = 2$. Steady state throughput, j as a function of intensity, λ for $\mu = 1, \mu^* = 0.3, 0.25, 0.2, 0.1, 0.05$ top to bottom. The dashed lines show the limiting value, $2\mu^*$. Global maxima are evident for certain values of μ^* (see text). Right: $j_{\max}$, as a function of μ^* ($\mu = 1$). The dashed lines shows the limiting value, $2\mu^*$.

In this limit almost all particles cross the channel, which corresponds to the leading term λ. The decrease of the flux corresponding to the term of order λ^{N+1} is due to the rare events where the channel is blocked and is given by $\frac{\lambda}{\mu^*\tau}$, where τ is the mean time of blockage at low intensity[132], $\tau = (N-1)!\frac{\mu^{N-1}}{\lambda^N}$. The outgoing flux as a function of the intensity is shown for several values of N and for $\mu = 1, \mu^* = 0.1$ in Fig. 4.2. One notes the initial linear regime corresponds to no loss of the incoming flux, which increases in importance with increasing N. This is followed by a maximum throughput at a finite intensity. We compare our model with the $M/M/N/N$ queue [130], introduced in Section 4.2.2, i.e. one with exponentially distributed arrival and service times with rates λ and μ, respectively, N servers and no waiting line [46]. The Markov chain of this model is similar to Fig. 4.1 except that there is no direct transition from state N to state 0. Instead there is a transition from state N to state $N-1$ with rate $N\mu$. An arriving unit is lost to the system if all N servers are busy. The probability of this event is given by the Erlang loss formula, introuced in Section 4.2.2:

$$\pi_N = \frac{\frac{1}{N!}(\frac{\lambda}{\mu})^N}{\sum_{i=0}^{N}\frac{1}{i!}(\frac{\lambda}{\mu})^i}. \tag{4.26}$$

The throughput, given by substituting this probability in Eq. (4.22), always increases monotonically towards the maximum value $N\mu$ as λ increases: See Fig. 4.2. In the following we examine in more detail the behaviour of the systems $N = 2$ and 3. For simplicity, and without loss of generality, we will set $\mu = 1$, which is equivalent to taking the unit of time as μ^{-1}.

4.3.2 N=2

The explicit equations describing the evolution of the three state probabilities, with $\mu = 1$, are;

$$\begin{aligned}
\dot{\pi_0} &= -\lambda\pi_0(t) + \mu\pi_1(t) + \mu^*\pi_2(t),\\
\dot{\pi_1} &= \lambda\pi_0(t) - (\mu+\lambda)\pi_2(t),\\
\dot{\pi_2} &= \lambda\pi_1(t) - \mu^*\pi_2(t).
\end{aligned} \tag{4.27}$$

and the time dependent throughput is

$$j(\lambda,t) = \mu\pi_1(t) + 2\mu^*\pi_2(t). \tag{4.28}$$

As the system evolves towards a steady state the throughput approaches a constant value. In the steady state, the stationary probabilities are

$$[\pi_0, \pi_1, \pi_2] = C_2[(\lambda+\mu)\mu^*, \lambda\mu^*, \lambda^2]. \tag{4.29}$$

with $C_2 = ((2\lambda+\mu)\mu^* + \lambda^2)^{-1}$. As expected Eq. (4.21) and Eq. (4.22) yield the same result for the steady state throughput:

$$j(\lambda) = \lambda \frac{2\lambda+\mu}{\lambda^2/\mu^* + 2\lambda + \mu} \tag{4.30}$$

Figure 4.3a displays the steady state throughput as a function of the intensity, λ. The limiting values of the steady state throughput at small and large intensity are

$$j(\lambda) = \lambda - \frac{\lambda^3}{\mu\mu^*} + O(\lambda^4), \tag{4.31}$$

$$\lim_{\lambda\to\infty} j(\lambda) = 2\mu^*. \tag{4.32}$$

We search for a non-trivial maximum throughput at finite λ by seeking solutions of $dj/d\lambda = 0$ which requires $4\lambda\mu\mu^* + \mu^2\mu^* - \lambda^2(\mu - 4\mu^*) = 0$. The solutions can be written as

$$\frac{\lambda}{\mu} = \frac{\sqrt{r}+2r}{1-4r} \geq 0, \tag{4.33}$$

where $r = \mu^*/\mu$. Thus, solutions exist for $r < r_c = 1/4$. If $r > 1/4$ there is no maximum at finite λ. If $r < 1/4$ the maximum throughput is given by

$$j_{\max} = \frac{\mu\sqrt{r}}{2(1-\sqrt{r})} = \frac{\mu^*}{2(1-\sqrt{r})\sqrt{r}} \tag{4.34}$$

Figure 4.3b shows that this approaches the limiting value $2\mu^*$ as $\mu \to 1/4$. To obtain the the mean time to first blockage. From Eq. (4.20) we have

$$\nu_{0,2} = \frac{2}{\lambda} + \frac{\mu}{\lambda^2}. \tag{4.35}$$

Following [44] we note that in the steady state there is an alternation of open and blocked states with average times of $\nu_{0,2}$ and $1/\mu^*$, respectively whose sum defines a cycle with period $1/\mu^* + \nu_{0,2}$. This provides an alternative route to the probability that the system is in the blocked state, $\pi_{(1,0)}$ which is the fraction of the cycle spent in the blocked state: $\pi_2 = (1/\mu^*)/((1/\mu^*) + \nu_{0,2}) = \lambda^2/((\mu+2\lambda)\mu^* + \lambda^2)$, as obtained previously. To obtain the kinetic behaviour, the system of equations in Eq. (4.27) may be solved analytically. The eigenvalues of the matrix Q_3 are 0 (associated with the conservation of the total probability), and two real negative values $\gamma_{1,2}$ given by

$$\gamma_{1,2} = -\frac{\mu + \mu^* + 2\lambda \pm \beta}{2} \tag{4.36}$$

where $\beta = \sqrt{(\mu-\mu^*)^2 + 4\lambda(\mu-\mu^*)}$. The probabilities are therefore given by

$$\pi_i(t) = \pi_i + a_i e^{\gamma_1 t} + b_i e^{\gamma_2 t}, \tag{4.37}$$

where π are the stationary values and a_i and b_i are determined by the initial conditions for $i = 0, 1, 2$. One easily obtains that

$$\begin{aligned}
a_0 &= \frac{\gamma_2}{\beta}(1-\pi_0) + \frac{\lambda}{\beta}, & b_0 &= -\frac{\gamma_1}{\beta}(1-\pi_0) - \frac{\lambda}{\beta} \\
a_1 &= -\frac{\gamma_2}{\beta}\pi_1 - \frac{\lambda}{\beta}, & b_1 &= \frac{\gamma_1}{\beta}\pi_1 + \frac{\lambda}{\beta} \\
a_2 &= -\frac{\gamma_2}{\beta}\pi_2 & b_2 &= \frac{\gamma_1}{\beta}\pi_2.
\end{aligned} \tag{4.38}$$

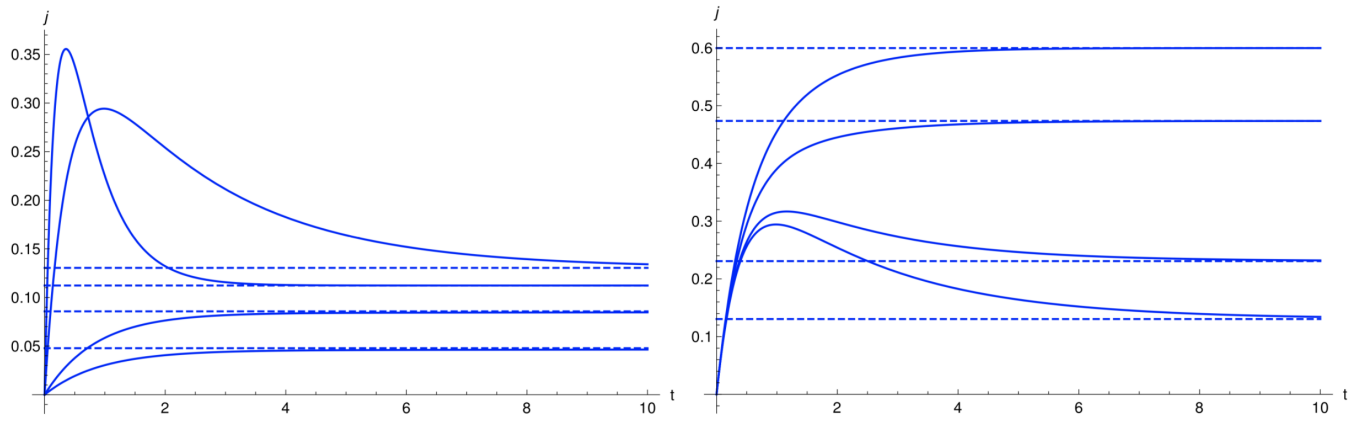

Figure 4.4: Time evolution of j for $N = 2$. Left: $\mu^* = 0.05$, λ = 3, 1, 0.1, 0.05, top to bottom. Right: $\lambda = 1$, $\mu^* = 0.05, 0.1, 0.3, 0.5$ bottom to top. The dashed lines show the steady state value, Eq. (5.4).

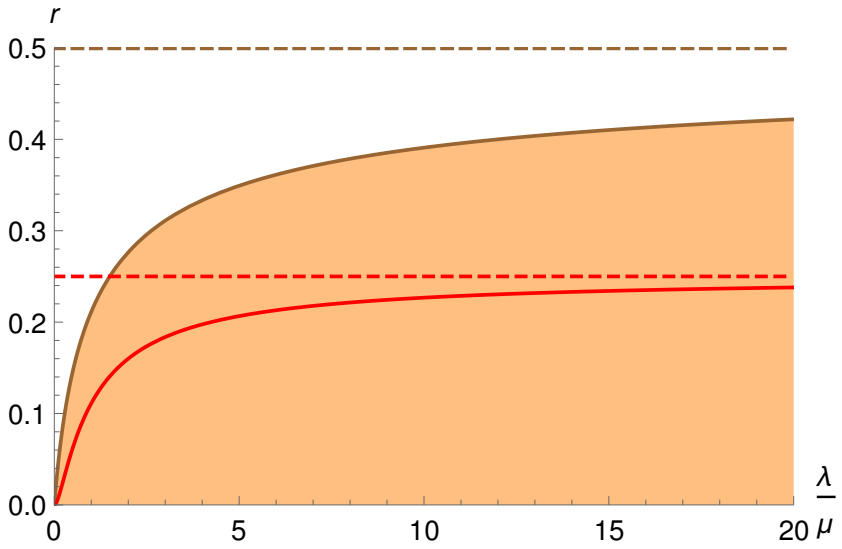

Figure 4.5: State diagram for $N = 2$. The shaded region bounded by the upper solid line, Eq. (4.41), corresponds to the parameter space in which a maximum throughput occurs at a finite time given by Eq. (4.40). No maximum at any time occurs if $r > 1/2$ (upper dashed line). The solid, red line, Eq. (4.33), corresponds to the intensity that maximizes the steady state throughput for a given value of $r = \mu^*/\mu$. No maximum occurs for finite λ if $r > 1/4$ (lower dashed line).

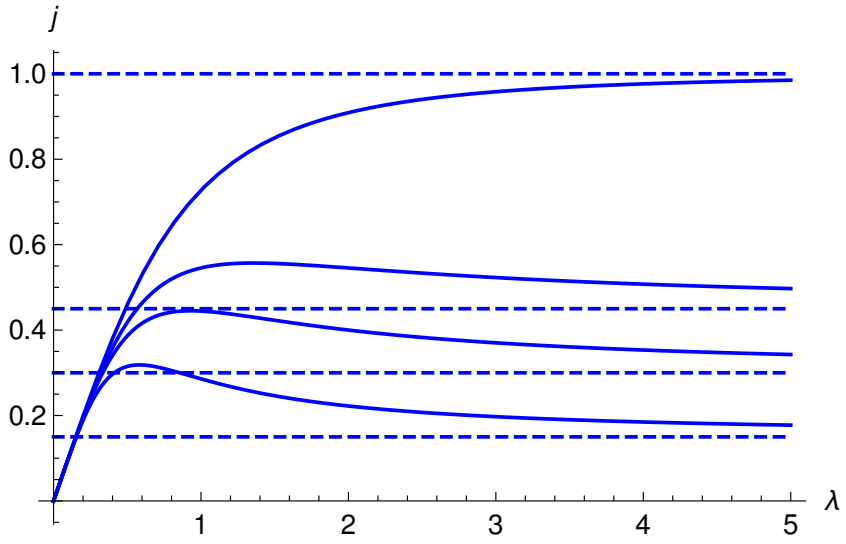

Figure 4.6: $N = 3$. Steady state throughput, j, as a function of λ for $\mu = 1, \mu^* = 0.3333, 0.15, 0.1, 0.05$ top to bottom. The dashed lines show the limiting value, $3\mu^*$.

Figure 4.4 illustrates the behaviour of the time dependent throughput for different parameter values. We note two distinct behaviours: either the throughput increases monotonically to the steady state value, or it displays a maximum at a finite time before decreasing to the steady state value. Applying Eq.(4.28) returns

$$\frac{\partial j(t)}{\partial t} = \gamma_1(\mu a_1 + 2\mu^* a_2)e^{\gamma_1 t} + \gamma_2(\mu b_1 + 2\mu^* b_2)e^{\gamma_2 t} \tag{4.39}$$

The solution for $\frac{\partial j(t)}{\partial t} = 0$ is given by

$$t_{\max} = \frac{1}{\beta}\ln\left(\frac{\mu^*(\mu+2\lambda)+\gamma_1\mu}{\mu^*(\mu+2\lambda)+\gamma_2\mu}\right). \tag{4.40}$$

For a solution to exist the argument of the logarithm must be finite and positive. Setting the denominator equal to zero thus gives the boundary of the set of parameter values at which $j(t)$ displays a maximum:

$$\mu_b^*(\lambda) = \frac{\mu}{2}\left(1 - \sqrt{\frac{\mu}{2\lambda+\mu}}\right), \tag{4.41}$$

It is the limiting value of μ^*, for a given value of λ, at which the non-trivial maxima of the time dependent throughput exists. We note that if $r > 1/2$ no maximum at finite time exists; rather the throughput approaches the steady state value from below. The kinetic and steady state behaviours are shown in Fig. 4.5.

4.3.3 N=3

The master equations describing the evolution of the four state probabilities are;

$$\begin{aligned}
\dot{\pi}_0 &= -\lambda\pi_0(t) + \mu\pi_1(t) + \mu^*\pi_3(t),\\
\dot{\pi}_1 &= \lambda\pi_0(t) - (\mu+\lambda)\pi_1(t) + 2\mu\pi_2(t),\\
\dot{\pi}_2 &= \lambda\pi_1(t) - (2\mu+\lambda)\pi_2(t),\\
\dot{\pi}_3 &= \lambda\pi_2(t) - \mu^*\pi_3(t).
\end{aligned} \tag{4.42}$$

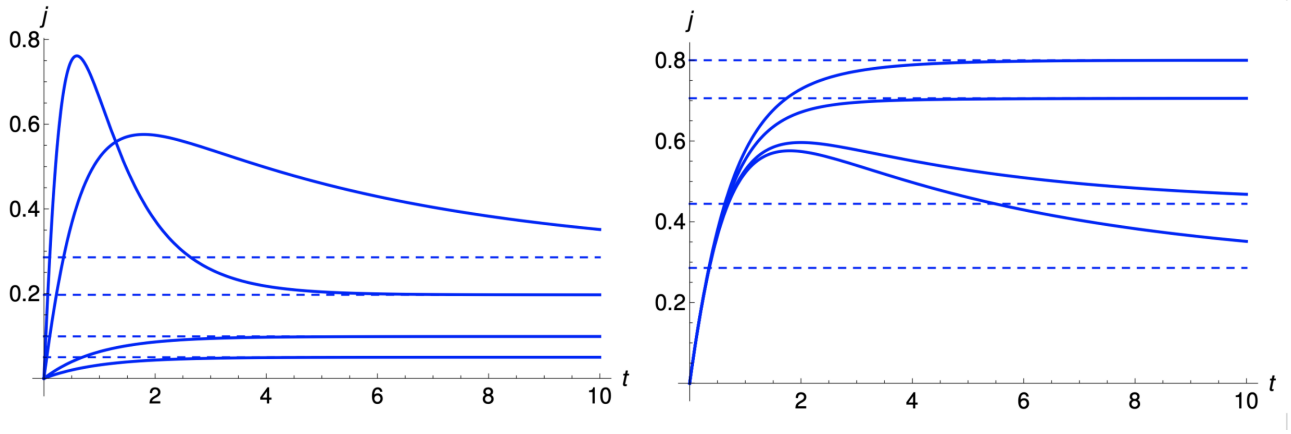

Figure 4.7: $N = 3$. Time evolution of $j(t)$. Left: $\mu^* = 0.05$ fixed, for $\lambda = 3, 1, 0.1, 0.05$, top to bottom. Right: $\lambda = 1$ fixed; $\mu^* = 0.05, .1, 0.3, 0.5$, bottom to top. The dashed lines show the steady state value, Eq. (4.45).

And the time dependent throughput is;

$$j(\lambda, t) = \mu\pi_1(t) + 2\mu\pi_2(t) + 3\mu^*\pi_3(t). \tag{4.43}$$

The steady state probabilities are given by:

$$[\pi_0, \pi_1, \pi_2, \pi_3] = C_3[(\lambda^2 + \lambda\mu + 2\mu^2)\mu^*, \lambda(\lambda + 2\mu)\mu^*, \lambda^2\mu^*, \lambda^3]. \tag{4.44}$$

with $C_3 = (\lambda^3 + 3\mu^*\lambda^2 + 3\mu\mu^*\lambda + 2\mu^2\mu^*)^{-1}$, and the system's throughput is

$$j(\lambda) = \lambda(1 - \pi_{(1,0)}) = \frac{\lambda(3\lambda^2 + 3\lambda\mu + 2\mu^2)\mu^*}{\lambda^3 + 3\mu^*\lambda^2 + 3\mu\mu^*\lambda + 2\mu^2\mu^*} \tag{4.45}$$

with the limiting values at small and large intensities are

$$j(\lambda) = \lambda - \frac{\lambda^4}{2\mu^2\mu^*} + O(\lambda^5), \tag{4.46}$$

$$\lim_{\lambda\to\infty} j(\lambda) = 3\mu^*, \tag{4.47}$$

respectively. Some examples are shown in Fig. 4.6. For $r < r_c = 1/3$ there is a maximum throughput at finite intensity. To explore the transient behaviour, we solved Eqs. (4.42) numerically. Some results are shown in Fig. 4.7. The same two distinct behaviours, as remarked for $N = 2$, are present. No maximum at finite time is observed if $\mu^* > 0.75$.

We have studied the optimisation of the throughput of a stream of particles subject to blocking using a circular Markov chain model. The sojourn time of a particle contained in an open channel is exponentially distributed with rate μ. If N particles are simultaneously present the channel is blocked and all newly arriving particles are rejected. After an exponentially distributed blockage time with rate μ^* all particles forming the blockage simultaneously exit the channel. We presented general expressions for the steady state probabilities and throughput. For $N = 2$ we showed that the steady state throughput assumes a maximum value at finite intensity if $\mu^*/\mu < 1/4$. The time dependent throughput may also display a maximum if $\mu^*/\mu < 1/2$. We showed that this behaviour is qualitatively different from the well-known $M/M/N/N$ queue whose steady state throughput always increases monotonically with the intensity of entering particles.

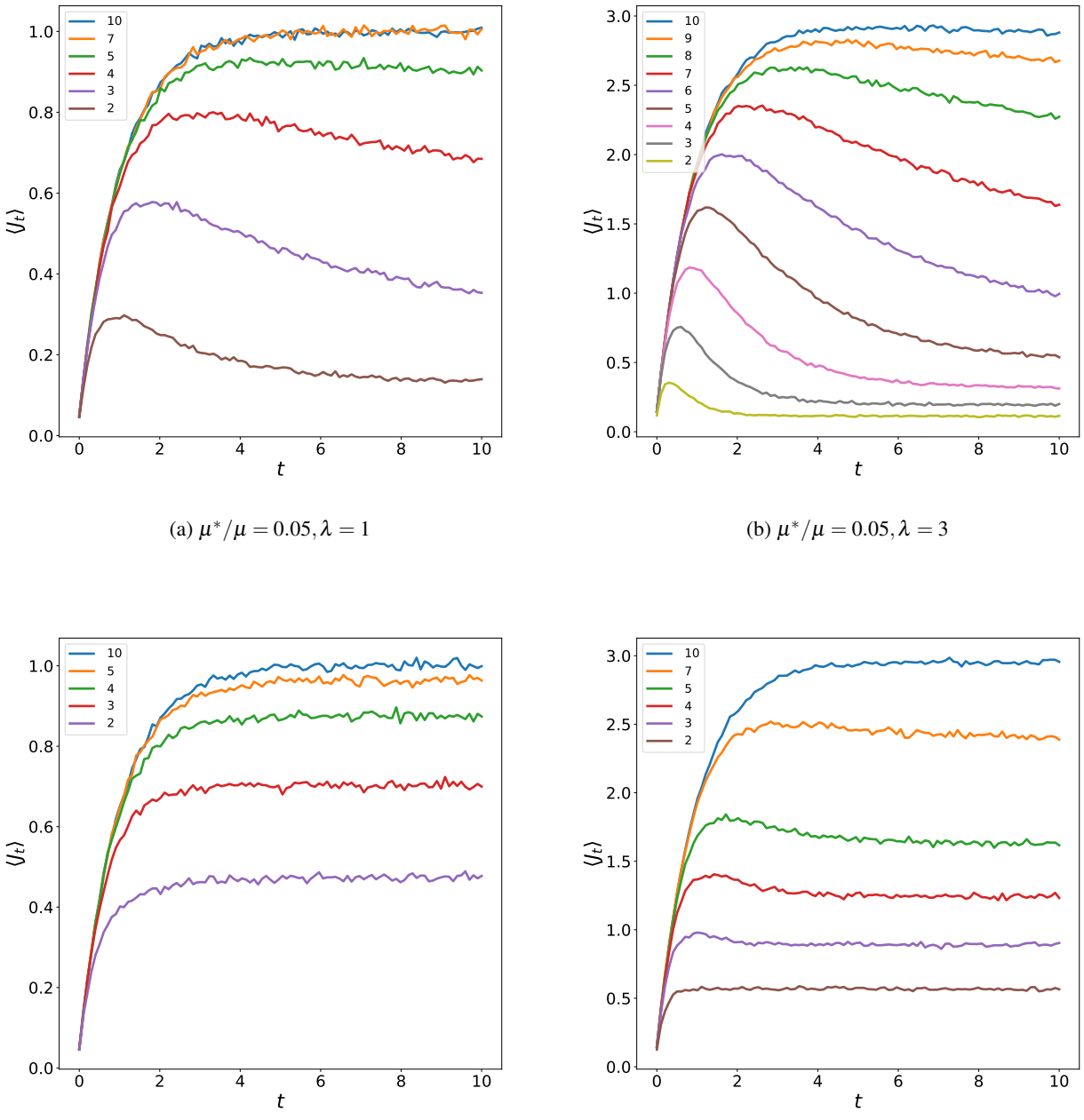

(a) $\mu^*/\mu = 0.05, \lambda = 1$

(b) $\mu^*/\mu = 0.05, \lambda = 3$

(c) $\mu^*/\mu = 0.3, \lambda = 1$

(d) $\mu^*/\mu = 0.3, \lambda = 3$

Figure 4.8: Numerically obtained transient average flux through a single non-FIFO Markovian channel for different N (shown in legend). Results were obtained using the Gillespie algorithm.

Non-FIFO single channel time dependent flux

Fig 4.8 display simulation results of the transient, non-FIFO, mean flux, for a range of configurations well beyond those analytically considered. Unlike the results already seen for the non-Markovian case, in Fig 3.9, the Markovian time dependant average flux does not undergo the same degree of oscillation. However, depending on the parameters chosen, the time dependant flux may or may not present a maximum before settling to its equilibrium value. As for the Non-Markovian case, however, increasing the channel capacity causes the average transient flux

to match the incoming flow intensity.

4.3.4 FIFO model

The single channel model is revisited and is the same in every respect, except that it now employs the 'first in first out' (FIFO) queuing discipline to determine the egress of any transiting particles within. As before, the stochastic dynamics is described by using $N+1$ state probabilities, $\pi(0,t),\pi(1,t),\cdots,\pi(N-1,t)$ and $\pi(N,t)$ which correspond to $0,1,\cdots,N-1$ and N particles in the channel, respectively. As before, $\mathbf{P(t)} = (\pi(\mathbf{0},\mathbf{t}),\pi(\mathbf{1},\mathbf{t}),\cdots,\pi(\mathbf{N}-\mathbf{1},\mathbf{t}),\pi(\mathbf{N},\mathbf{t}))$ denotes the $(N+!)$ state vector, so that the time evolution of the process is described by:

$$\frac{d\mathbf{P(t)}}{dt} = \mathbf{P(t)}\cdot\mathbf{Q_{N+1}}. \tag{4.48}$$

$\mathbf{Q_{N+1}}$ is the $(N+1)\times(N+1)$ matrix,

$$\mathbf{Q_{N+1}} = \begin{pmatrix} -\lambda & \lambda & 0 & \dots & 0 & 0 \\ \mu & -(\lambda+\mu) & \lambda & \dots & 0 & 0 \\ \vdots & \vdots & \vdots & \ddots & \vdots & \vdots \\ 0 & \dots & \mu & -(\lambda+\mu) & \lambda & 0 \\ 0 & \dots & 0 & \mu & -(\lambda+\mu) & \lambda \\ \mu^* & \dots & \dots & 0 & 0 & -\mu^* \end{pmatrix}. \tag{4.49}$$

The change of state i, in all but the first and last columns, contains two gain terms and two loss terms. The former correspond to the entrance of a particle (at rate λ) in a channel with $i-1$ particles, and to the exit of a particle (at rate μ) from a channel with $i+1$ particles. The two loss terms correspond to a channel with i particles ($0<i<N$) where a particle enters at time t (at rate λ) or where a particle exits (at rate μ). Although in the non-FIFO model the state $k\in[0,N]$ contributed $k\mu\pi_k(t)$ particles per unit time, here they only contribute $\mu\pi_k(t)$ per unit time. As before, the description is completed by including the previously omitted boundary situations: the empty channel has a loss term corresponding to a particle entrance and two gain terms. The first term corresponds to a particle exit from an empty channel and the second to the release of a blocked channel (with N particles). A blocked channel has a single loss term corresponding to a release with rate μ^* and a gain term corresponding to a particle entering the channel while in the $(N-1)^{th}$ state.

The time evolution of $P(t)$ is again supplemented by the conservation of total probability, $\sum_{i=0}^{N}\pi(i,t)=1$, leading the sum of each row of the transition matrix to be equal to 0. The channel throughput is given by

$$j(t) = \mu\sum_{k=1}^{N-1}\pi(k,t) + N\mu^*\pi(N,t). \tag{4.50}$$

This is again different to the original single channel throughput expression given by Eq. (4.21), due to the application of the FIFO discipline. The second term remains unchanged, and describes the re-opening of a blocked channel that instantaneously releases N particles. The expression for stationary state, j, remains unchanged from the expression given by Eq. (4.22).

Figure 4.9 shows the stationary flux with respect to λ for $N=2,3,4,6$ (shown bottom to top). For $\mu^*=0.5$, at low intensity λ, the flux increases linearly with λ since blockage events are improbable, and finally saturates at high intensity. The flux is a monotonically increasing function of λ. The dashed lines correspond to the limit $j=N\mu^*$. For $\mu^*=0.1$, j displays a global maximum for a finite value of λ for $N=2,3,4,6$. One can show the critical value of μ^*, for which the asymptotic behaviour changes, is $\mu^*/\mu = 0.25, 0.22, 0.187, 0.139$ for $N=2,3,4,6$, respectively. To solve Eq.(4.48), one notes that the process belongs to the class of circular Markov chains [130, 133] for which a solution can be obtained for the stationary state. After some calculations, the blocking probability

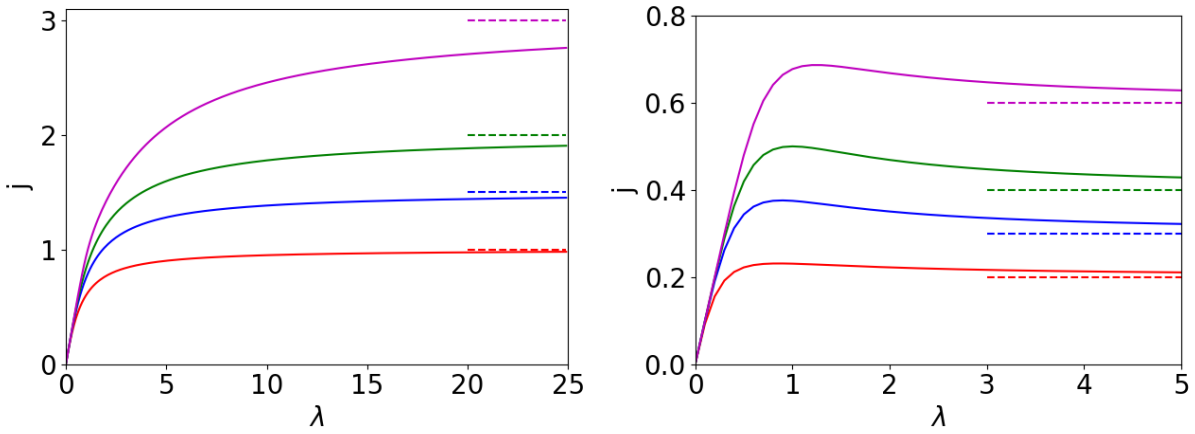

Figure 4.9: Single channel stationary flux, j, from Eq.(4.52), as a function of λ for $N = 2,3,4,6$ (from bottom to top) with $\mu = 1$ and for two values of μ^*: (left) $\mu^* = 1/2$ and (right) $\mu^* = 0.1$. The dashed lines show the limiting value, $N\mu^*$.

is found as

$$\pi(N) = \frac{1}{1 + \frac{\mu^*}{\lambda}\sum_{i=1}^{N}(N+1-i)\left(\frac{\mu}{\lambda}\right)^{i-1}}, \tag{4.51}$$

and by using Eq.(4.22), the stationary flux of exiting particles, j, reads:

$$j = \frac{\mu^*\sum_{i=1}^{N}(N+1-i)\left(\frac{\mu}{\lambda}\right)^{i-1}}{1 + \frac{\mu^*}{\lambda}\sum_{i=1}^{N}(N+1-i)\left(\frac{\mu}{\lambda}\right)^{i-1}}. \tag{4.52}$$

The asymptotic regimes can be easily analysed. When $\lambda \to \infty$ the flux, j, is found to be:

$$j \simeq N\mu^* + \frac{\mu^*}{\lambda}((N-1)\mu - N^2\mu^*). \tag{4.53}$$

The leading term corresponds to an alternation of open (empty) and closed (blocked) states. The former is of an infinitesimally short duration where no particles exit and the latter is followed by the release of N blocked particles. This explains why the exiting flux j is independent of λ at large intensity. The second term of the asymptotic expansion, Eq.4.53, shows that the limit is approached from below when $\mu^* < \frac{N-1}{N^2}\mu$ and from above when $\mu^* > \frac{N-1}{N^2}\mu$. This implies that, in the latter case, the flux, j, displays a maximum at a finite value of λ, whereas j is a monotonically increasing function of λ in the former case. The same behaviour is observed in the non-FIFO single channel model studied in Section 4.3.1 [134]. It is, therefore, worth noting that the choice of discipline has no effect on a channel, or bundle of channels, when each has a threshold capacity of $N = 2$. At small λ, j is given by:

$$j \simeq \lambda - \frac{\lambda^{N+1}}{\mu^{N-1}\mu^*}. \tag{4.54}$$

The leading term of this expansion represents all particles leaving the channel without blockage and the sub-leading term corresponds to a decrement that becomes very small as the threshold N increases. The stationary probabilities allow the computation of many other quantities. For example, the variance of the stationary flux σ_j^2 is given by

$$\sigma_j^2 = \mu^2\sum_{k=1}^{N-1}\pi(k) + N^2\mu^{*2}\pi(N)) - \left(\mu\sum_{k=1}^{N-1}\pi(k) + N\mu^*\pi(N)\right)^2 \tag{4.55}$$

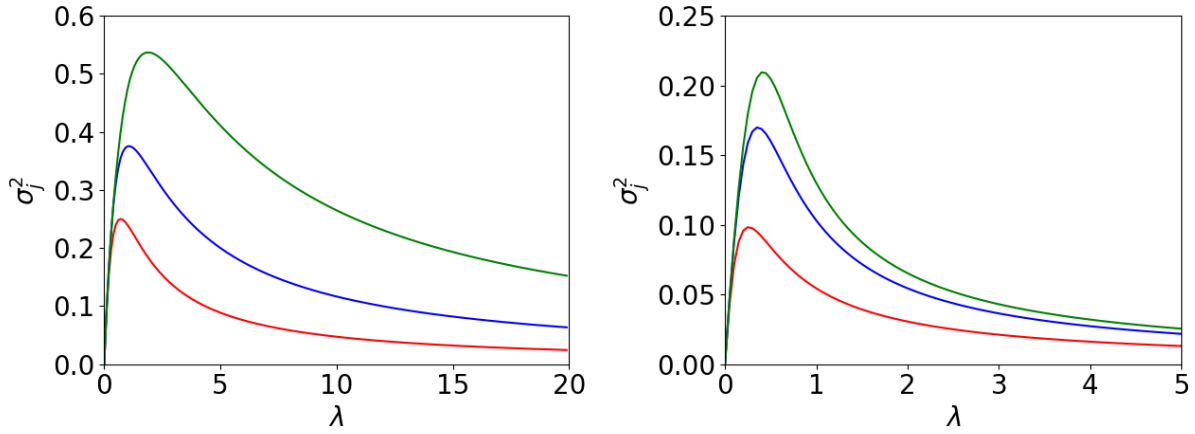

Figure 4.10: Variance of the stationary flux σ_j^2, from Eq. (4.55), as a function of λ for $N = 2,3,4$ (from bottom to top) with $\mu = 1$ and for two values of μ^*: (left) $\mu^* = 1/2$ and (right) $\mu^* = 0.1$.

For $N = 2$, one has

$$\sigma_j^2 = \mu^* \lambda \frac{[(\mu^2 - 4\mu\mu^* + 8\mu^{*2})\lambda^2 + \mu\mu^*(\mu + 4\mu^*)\lambda + \mu^3\mu^*]}{(\lambda^2 + 2\lambda\mu^* + \mu\mu^*)^2} \tag{4.56}$$

For $N > 2$, the expressions are lengthy and so are not displayed. For small λ, the variance vanishes as

$$\sigma_j^2 \simeq \mu\lambda \tag{4.57}$$

and is independent of μ^*. This can be interpreted by noting that blockages are rare in this regime and do not contribute to the leading term of variance. For large λ, the variance also vanishes as

$$\sigma_j^2 \simeq \frac{\mu^*}{\lambda}\left[(N-1)(\mu - N\mu^*)^2 + N^2\mu^{*2}\right]. \tag{4.58}$$

Figure 4.10 shows the variance of the stationary flux σ_j^2 as a function of λ for $\mu = 1$ and $\mu^* = 0.1, 0.5$. As shown above, the variance increases linearly at small values of λ, and decays to 0 at large λ. These results confirm that for low intensity the system is most likely to be in state 1, $\lambda \ll 1, \pi(N) \ll \pi(1)$, while for high intensity the system is most likely to be in the blocked state, $\lambda \gg 1, \pi(N) \gg \pi(1)$.

FIFO single channel time dependent flux

Fig 4.8 display simulation results of the transient, FIFO, mean flux, for a range of configurations well beyond those analytically considered. As for the NON-FIFO case, the time dependant average flux does, depending on the parameters chosen, may or may not present a maximum before settling to its equilibrium value. An observed difference is that the value of the equilibrium exiting flux for the channels following the FIFO queuing discipline is, in general, lower than for the NON-FIFO case, apart from the in the high capacity limit, which is expected.

4.4 Multi-channel FIFO model

We consider a bundle of N_c particle conveying channels [112]. As before, a single channel is open if the number of particles inside is less than N, and blocked at the threshold of N particles. When blocked, no more particles can enter until the channel is flushed. Particles randomly enter an open channel according to a Poisson process with intensity (rate) $\Lambda/(N_c - k)$ where k is the number of blocked channels at time t. The FIFO queuing discipline is

again used, in contrast with the discipline employed in Section 4.3.1 [134]. As in Section 4.3, a channel can be in one of $N+1$ states, corresponding to an index, i, ranging from 0 when the channel is empty to N, when it is blocked. The time evolution of N_c channels can be described by introducing N_c indices, which gives a number of states $(N+1)^{N_c}$. The flux of exiting particles depends on the number of channels in state i. The number of states can be labelled using indices i_j (whose values range from 0 to N_c) associated with the number of channels in a state j, with the global constraint $\sum_{j=0}^{N} i_j = N_c$.

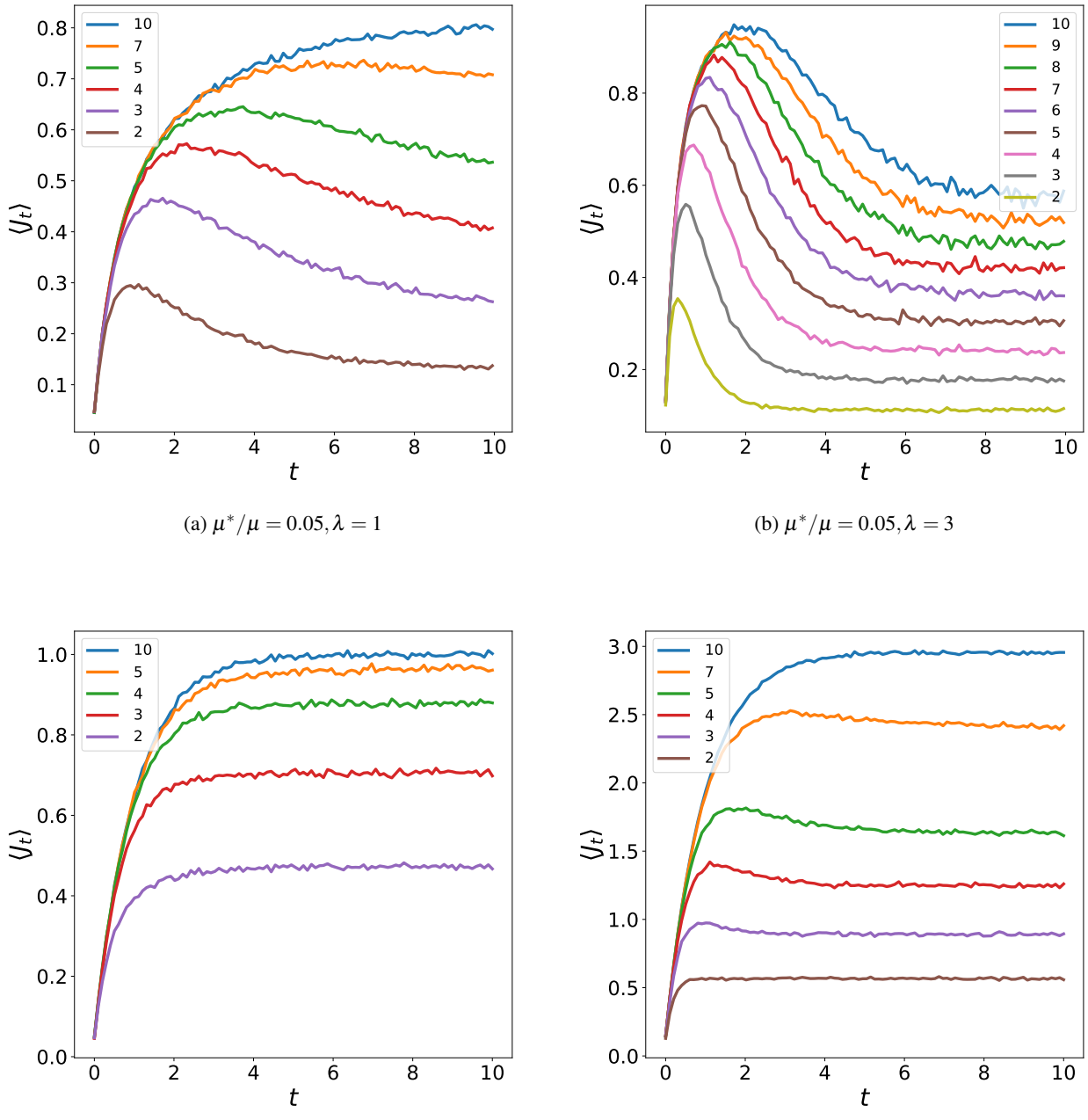

(a) $\mu^*/\mu = 0.05, \lambda = 1$

(b) $\mu^*/\mu = 0.05, \lambda = 3$

(c) $\mu^*/\mu = 0.3, \lambda = 1$

(d) $\mu^*/\mu = 0.3, \lambda = 3$

Figure 4.11: Numerically obtained transient average flux through a single FIFO Markovian channel for different N (shown in legend).

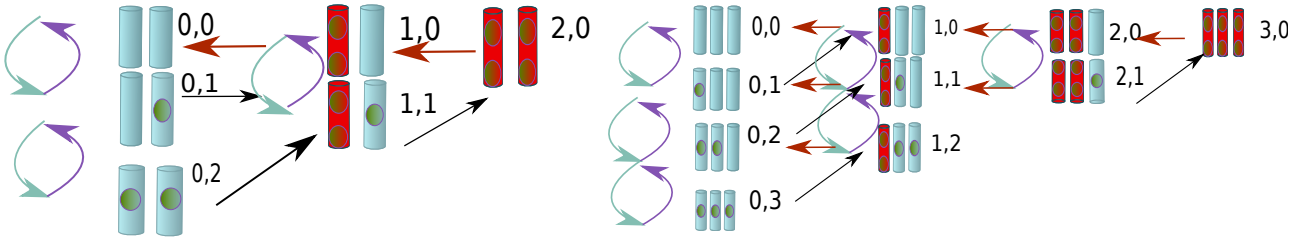

Figure 4.12: State diagrams for the multichannel models (for $N = 2$): The left and right indices correspond to the number of blocked channels and the number of particles present while open, respectively. The arrows represent all possible transitions between states: Curved purple and blue arrows correspond to a transition between open states by the gain/loss of a particle, respectively. The black arrows correspond to a channel blockage due to a particle entrance and the red arrows correspond to a deblockage. (left) $N_c = 2$ (right) $N_c = 3$ (Figure courtesy of Pascal Viot).

New notation is introduced such that, for $N = 2$, the state probabilities are given by $\pi(i, j, t)$ where i is an index counting the number of blocked channels and j is an index for the total number of open channels (i.e with one particle present). Because the total number of channels is given by $\sum_{j=0}^{2} i_j = N_c$, the index i_0 is not necessary to define the state probabilities. This labelling reduces the number of state probabilities to $(N_c+1)(N_c+2)/2$. Figure 4.12 displays state diagrams for $N_c = 2$ (left) and $N_c = 3$ (right). An example of the extension of the graphical method is as follows: For $N = 3$, the state probabilities are defined by three indices i, j, k, denoting the number of channels with $3, 2, 1$ particles, respectively. For example, for $N_c = 2$ when one-channel is blocked and the other has two particles present is denoted by $(1, 1, 0)$. The number of state probabilities is $(N_c+1)(N_c+2)(N_c+3)/6$. By using a three dimensional cubic lattice (whose nodes are labelled with the indices corresponding to the axes), one needs to add the the different arrows connecting the nearest neighbouring nodes with the rules described above. It is clear that when one increases both N_c and N, it is necessary to code these rules in order to build the transition matrix and finally to obtain the stationary probabilities by using a matrix inversion, which remains feasible.

4.4.1 $N_c = 2, N = 2$

The kinetic equations of the model are given by the matrix differential equation:

$$\frac{d\mathbf{P}(\mathbf{t})}{dt} = \mathbf{P}(\mathbf{t}) \cdot \mathbf{Q_6}, \tag{4.59}$$

where $\mathbf{P}(\mathbf{t})$ is the state vector with 6 components, $\mathbf{P}(\mathbf{t}) = (\pi(\mathbf{0},\mathbf{0},\mathbf{t}), \pi(\mathbf{0},\mathbf{1},\mathbf{t}), \pi(0,2,t), \pi(1,0,t), \pi(1,1,t), \pi(2,0,t))$ and the transition probability matrix $\mathbf{Q_6}$ is:

$$\mathbf{Q_6} = \begin{pmatrix} -\Lambda & \Lambda & 0 & 0 & 0 & 0 \\ \mu & -(\Lambda+\mu) & \frac{\Lambda}{2} & \frac{\Lambda}{2} & 0 & 0 \\ 0 & 2\mu & -(\Lambda+2\mu) & 0 & \Lambda & 0 \\ \mu^* & 0 & 0 & -(\Lambda+\mu^*) & \Lambda & 0 \\ 0 & \mu^* & 0 & \mu & -(\Lambda+\mu^*+\mu) & \Lambda \\ 0 & 0 & 0 & 2\mu^* & 0 & -2\mu^* \end{pmatrix}. \tag{4.60}$$

The non-zero coefficients of the matrix correspond to the different arrows shown in Fig.4.12. For clarity, we shall examine two example terms in detail. The time evolution of $\pi(0,1,t)$ has three gain terms and two loss terms: the gain terms correspond to the entry of one particle in an empty system, a particle exit from a state where each channel contains one particle (thus contributing a factor of 2), and the release of a blockage from a system with one blocked channel and a channel with one particle. The loss terms correspond to the entrance or exit of a particle

for a system in the state $(0,1)$. As a second example, the time evolution of $\pi(0,2,t)$ has one gain term and two loss terms. The gain term is associated with the entry of a particle in an empty channel, while the other channel already contains one particle (resulting in the factor of $1/2$). The two loss terms are associated with the entrance of a new particle and the exit of one particle. (The factor 2 comes from the fact that a particle can exit from either channel). The throughput of the two channel system is given by:

$$J = \mu[\pi(0,1,t) + 2\pi(0,2,t)] + 2\mu^*\pi(1,0,t) + (\mu + 2\mu^*)\pi(1,1,t) + 4\mu^*\pi(2,0,t), \tag{4.61}$$

where the first term corresponds to the exit of a particle from a system with no blocked channels. The second term corresponds to a blockage release. (The factor 2 is the number of particles in the blocked channel). The third term contains two contributions: a particle exit from the open channel and a blockage release. The last term corresponds to the release of two particles from one of the two blocked channels.
In the stationary state,

$$J = \Lambda(1 - \pi(2,0)), \tag{4.62}$$

which corresponds to the product of the entrance flux and the probability that at least one of the channels is open. We find

$$\pi(2,0) = \frac{2\Lambda^5 + (2\mu + \mu^*)\Lambda^4}{\Delta}, \tag{4.63}$$

with

$$\begin{aligned}\Delta \quad &= 2\Lambda^5 + (2\mu + 9\mu^*)\Lambda^4 + 4\mu^*(3\mu + 5\mu^*)\Lambda^3 + 2\mu^*(2\mu^2 + 21\mu\mu^* + 4\mu^{*2})\Lambda^2 \\ &\quad + 16\mu\mu^{*2}(2\mu + \mu^*)\Lambda + 8(\mu\mu^*)^2(\mu + \mu^*).\end{aligned} \tag{4.64}$$

By using Eq. (4.61), one obtains the stationary throughput J, which at small Λ, behaves as:

$$J \simeq \Lambda - \frac{2\mu + \mu^*}{8(\mu\mu^*)^2(\mu + \mu^*)}\Lambda^5. \tag{4.65}$$

Compared to the single channel model (with $N = 2$) (Eq.4.54), where the first term has a λ^3 dependence, the first term has now a Λ^5 dependence, which corresponds to a smaller probability of a full blockage of the system. At large Λ, one obtains

$$J \simeq 4\mu^* - \frac{2\mu^*(\mu - 4\mu^*)}{\Lambda}. \tag{4.66}$$

As expected, in this limit the only contribution to the throughput are deblocked particles. We note that the limit is approached from below for $\mu^* < \mu/4$ and from above for $\mu^* > \mu/4$. The latter case results in a maximum of the flux for a finite value of Λ. Both behaviours are shown in Fig. 4.13. The change of behaviour for the two-channel model at $\mu^* = \mu/4$ is also present in the previous one-channel model [134].

4.4.2 $N_c > 2, N = 2$

It is possible to derive the time evolution for a model with $N_c > 2$. The time evolution of the process with $N_c = 3$ is given by a system of differential equations similar to Eq.(4.59). The state vector $P(t)$ is now given as a 10-component vector, $\mathbf{P(t)} = (\pi(\mathbf{0},\mathbf{0},\mathbf{t}), \pi(\mathbf{0},\mathbf{1},\mathbf{t}), \pi(0,2,t), \pi(0,3,t), \pi(1,0,t), \pi(1,1,t), \pi(1,2,t), \pi(2,0,t), \pi(2,1,t)$ $, \pi(3,0,t))$. The matrix $\mathbf{Q_{10}}$ is given by:

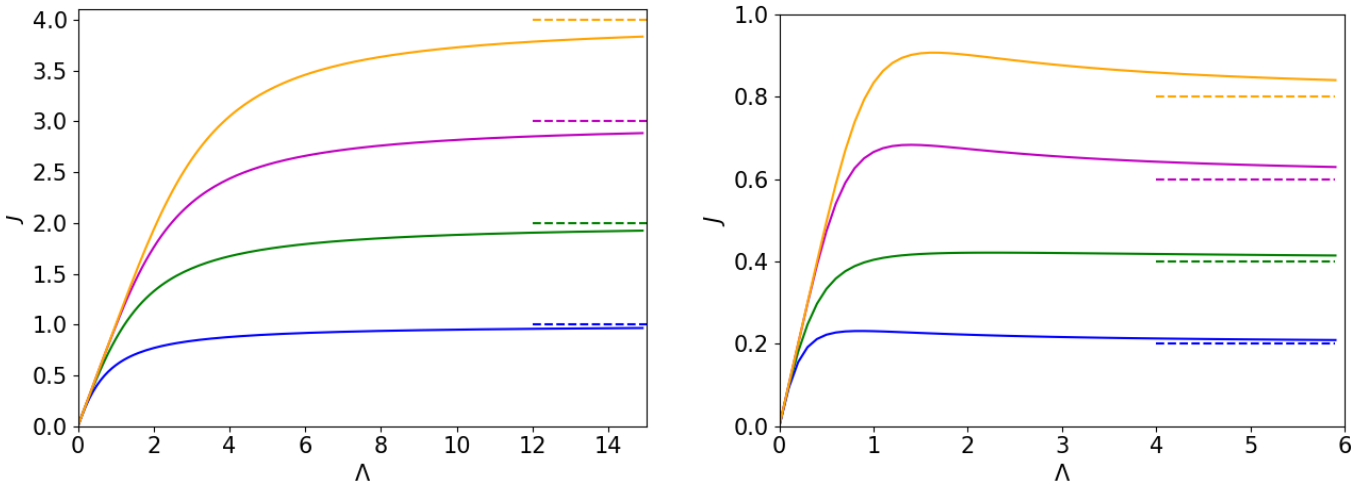

Figure 4.13: Stationary flux, J, from the theory as a function of Λ for $N_c = 1,2,3,4$ (from bottom to top) with $N = 2$, $\mu = 1$ and for two values of μ^*: (left) $\mu^* = 0.5$ and (right) $\mu^* = 0.1$.

$$\mathbf{Q_{10}} = \begin{pmatrix}
-\Lambda & \Lambda & 0 & 0 & 0 & 0 & 0 & 0 & 0 & 0 \\
\mu & -(\Lambda+\mu) & \frac{2\Lambda}{3} & 0 & \frac{\Lambda}{3} & 0 & 0 & 0 & 0 & 0 \\
0 & 2\mu & -(\Lambda+2\mu) & \frac{\Lambda}{3} & 0 & \frac{2\Lambda}{3} & 0 & 0 & 0 & 0 \\
0 & 0 & 3\mu & -(\Lambda+3\mu) & 0 & 0 & \Lambda & 0 & 0 & 0 \\
\mu^* & 0 & 0 & 0 & -(\Lambda+\mu^*) & \Lambda & 0 & 0 & 0 & 0 \\
0 & \mu^* & 0 & 0 & \mu & -(\Lambda+\mu^*+\mu) & \frac{\Lambda}{2} & \frac{\Lambda}{2} & 0 & 0 \\
0 & 0 & \mu^* & 0 & 0 & 2\mu & -(\Lambda+\mu^*+2\mu) & 0 & \Lambda & 0 \\
0 & 0 & 0 & 0 & 2\mu^* & 0 & 0 & -(\Lambda+2\mu^*) & \Lambda & 0 \\
0 & 0 & 0 & 0 & 0 & 2\mu^* & 0 & \mu & -(\Lambda+2\mu^*+\mu) & \Lambda \\
0 & 0 & 0 & 0 & 0 & 0 & 0 & 3\mu^* & 0 & -3\mu^*
\end{pmatrix}. \tag{4.67}$$

The exact solution is too lengthy to be displayed, but we focus on some partial results. The stationary throughput is given by

$$J = \Lambda(1 - \pi(3,0)). \tag{4.68}$$

At low Λ, one obtains

$$J \simeq \Lambda - \frac{18\mu^3 + 39\mu^2\mu^\mu + 22\mu\mu^{*2} + 4\mu^{*3}}{324(\mu\mu^*)^3(\mu+2\mu^*)(\mu+\mu^*)(2\mu+\mu^*)}\Lambda^7. \tag{4.69}$$

We have also solved the model for $N_c = 4$ with 15 probabilities. Since the expressions are very lengthy, we present the results graphically in Fig.4.13. For larger values of N, a complete solution can be obtained, by using symbolic software, once the transition matrix is obtained by using the graphical method depicted in the above section. However, because the linear size of the matrix increases as $(N_c+1)(N_c+2)/2$, the calculation rapidly becomes cumbersome. For general N_c we conjecture that the small λ expansion is

$$J \simeq \Lambda - \Lambda^{2N_c+1} f(\mu,\mu^*), \tag{4.70}$$

where $f(\mu,\mu^*)$ is a positive function of μ and μ^*, and the $\Lambda \to \infty$ limit is

$$J = 2N_c\mu^* + \frac{N_c\mu^*(\mu - 4\mu^*)}{\Lambda}. \tag{4.71}$$

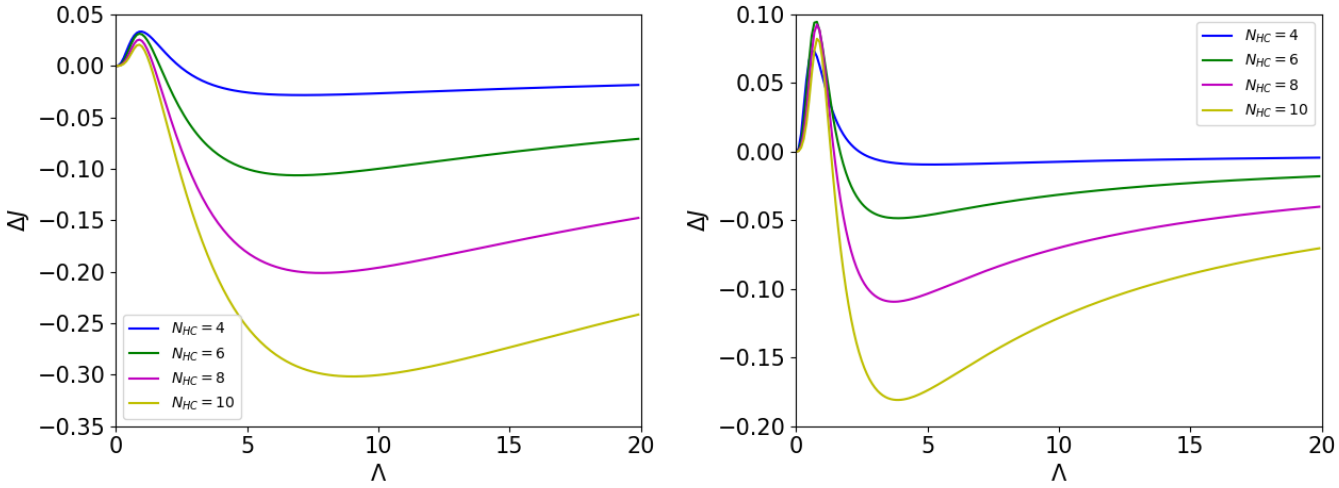

Figure 4.14: Flux difference, ΔJ, between one HC channel of different thresholds $N_{HC} = 4,6,8,10$ and $N_c = 2,3,4,5$ LC channels each of threshold $N = 2$ (from top to bottom, right hand side) as a function of Λ with $\mu = 1$ and $\mu^* = 0.5$ (left) and $\mu^* = 0.1$ (right). From Eq. (4.72)

Figure 4.13 shows the stationary flux J as a function of Λ for $N_c = 1,2,3,4$. As discussed above, J is a monotonically increasing function when $\mu^* = 0.5$, whereas J displays a maximum for $\mu^* = 0.1$. This result is independent of the number of channels N_c.

4.5 Optimized transport

Here we examine two different scenarios for conveying a particulate flux of given intensity Λ. The configurations studied are as already studied in the non-Markovian case, as shown in Section 3.6 Fig. 3.12, a. The first scenario compares a single, high capacity (HC), channel with a threshold equal to $N_{HC} = 2N_c$ with a bundle of N_c identical channels each with a low capacity (LC) of $N = 2$. For a bundle of identical channels, the intensity is equally distributed. The second scenario compares a system of N_c coupled channels, i.e. the total intensity is equally distributed over all open channels, each with threshold $N = 2$ with N_c independent channels each with threshold $N = 2$. In both cases we seek to determine which of the two configurations optimises the steady state throughput.

4.5.1 One HC channel versus several LC channels.

At low intensity, both configurations present few blockage events and so their fluxes are equal to Λ. At large intensity, the throughput of the HC channel is equal to $2N_c\mu^*$. Since each LC channel has a throughput equal to $2\mu^*$, the total outgoing flux is also equal to $2N_c\mu^*$. In order to determine the most efficient system for different values of the intensity Λ, one compares both systems by calculating the difference of their stationary fluxes.

$$\Delta J(\Lambda) = J_{N_{HC}}(\Lambda) - N_c J_2\left(\frac{\Lambda}{N_c}\right), \tag{4.72}$$

where $J_{N_{HC}}(\Lambda)$ denotes the stationary flux of the HC channel with entering intensity Λ and $J_2\left(\frac{\Lambda}{N_c}\right)$ the stationary flux of a LC channel of threshold $N = 2$ with a shared intensity Λ/N_c. This quantity clearly goes to zero for small and large Λ, illustrating the fact that the two systems have the same stationary flux in these limits.
Fig.4.14 displays the difference of stationary flux $\Delta J(\Lambda)$ between the HC channel $J_{N_{HC}}$ and the total flux of the LC channels, J_2, as a function of Λ for $\mu^* = 0.5, 0.1$, ($\mu = 1$) and for $N_{HC} = 4,6,8,10$. One observes that the HC channel is slightly more efficient at low intensity. At large intensity the HC channel is always less efficient than

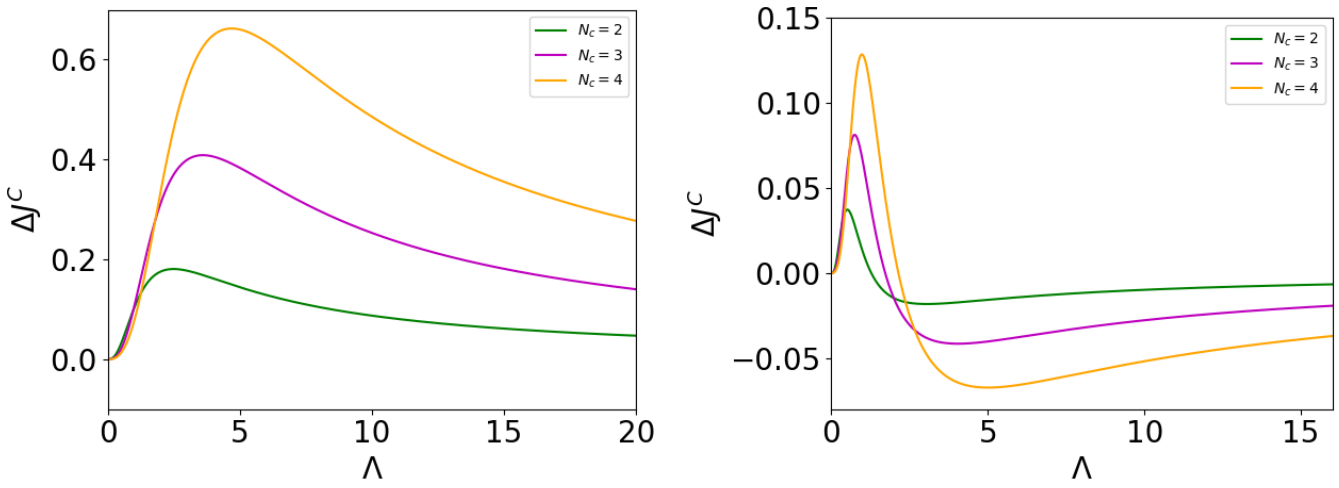

Figure 4.15: Flux difference ΔJ^C between $N_c = 2,3,4$ coupled channels with $N = 2$ and their uncoupled equivalents (lower and upper curves, respectively) as a function of Λ. $\mu = 1$ and $\mu^* = 1/2$ (left) and $\mu^* = 0.1$ (right). From Eq. (4.75).

the bundle of LC channels. This behaviour is more pronounced when N_c increases.

In summary, the throughput difference reaches a positive maximum for a finite value of Λ and then passes through zero before attaining a negative minimum, corresponding to the maximum efficiency of the bundle of LC channels. By expanding Eq. (4.72) to the first order it becomes clear that ΔJ is not a flat function of Λ:

$$\Delta J \simeq \frac{\Lambda^3}{\mu^* \mu^2} \left[N_c - \left(\frac{\Lambda}{\mu} \right)^{2(N_c-1)} \right], \tag{4.73}$$

which is positive for $N_c > 1$. Conversely at high intensity

$$\Delta J = -\frac{(N_c - 1)^2 \mu^* \mu}{\Lambda}, \tag{4.74}$$

which is always negative.

4.5.2 Comparison of N_c coupled with uncoupled channels of capacity $N = 2$.

We consider the flux difference between the two systems

$$\Delta J^C(\Lambda) = J_2^{N_c}(\Lambda) - N_c J_2 \left(\frac{\Lambda}{N_c} \right) \tag{4.75}$$

where $J_2^{N_c}$ denotes the total stationary flux of N_c coupled channels of threshold 2. At low intensity, there are few blockages in either system and the throughput is Λ in both. At large intensity, the throughput of the independent channels and the coupled correlated channels are both equal to $2N_c\mu^*$. By calculating the flux difference, one can determine the most efficient system for different values of intensity. Fig.4.15 shows the flux difference, $\Delta J^C(\Lambda)$, between the N_c coupled channels and the total flux of the independent channels as a function of Λ for two values of μ^*, ($\mu = 1$) and for $N_c = 2,3,4$. If the deblocking rate is sufficiently large, $\mu^* > 0.25$, the independent channels always convey the flux less effectively than the coupled channels. If $\mu^* < 0.25$ the behaviour is similar to the first scenario: ΔJ reaches a maximum for a finite value of Λ. At higher intensities, the coupled channels are less

efficient and ΔJ shows a minimum. At very large intensity, both models converge to the same limit as expected. This behaviour can be understood by examining the limiting behaviour of ΔJ. For small Λ one has (for $N_c > 1$)

$$\Delta J \simeq \frac{\Lambda^3}{N_c^2 \mu^* \mu^2}, \tag{4.76}$$

which is always positive, while at high intensity

$$\Delta J \simeq -\frac{N_c(N_c-1)\mu^*}{\Lambda}(\mu - 4\mu^*), \tag{4.77}$$

which is negative if $\mu^*/\mu < 0.25$ and positive otherwise. Coupled channels are always more efficient at low intensity and also at high intensity if the deblocking rate is sufficiently high. If, however, $\mu^* < \mu/4$ the coupled channels convey the flux less efficiently due to an accelerating cascade of blockages that is reminiscent of the irreversible model [135].

The next section will provide a discussion, and comparison of the two $1D$ models of blocking phenomena studied in Chapters 3 and 4.

CHAPTER
5

DISCUSSION

This Chapter compares the non-Markovian and Markovian models of $1D$ channel flow studied in Chapters 3 & 4 respectively. The physical assumption of constant transit and deblocking times, τ and τ_b respectively, of the former model is responsible for strong memory effects which prevented analytical solutions for general N from being obtained. Chapter 4 introduced Markovian models [117, 136], where the average transit and deblocking times are stochastic variables given by exponential distributions of intensity μ and μ^*, respectively.

The kinetic description of the Markovian model was given by a set of differential equations for the time evolution of the state probabilities $P(i,t)$ with $i \in [0 \cdots N]$ giving the number of particles in the channel. Unlike the non-Markovian model, analytic solutions for the steady state properties can be obtained for arbitrary N (some generalisations of the Markovian models for which time-dependent solutions can be obtained [137, 138] and could be investigated in the future).

5.1 Markovian versus non-Markovian models

A Markovian channel is open for a mean time, $\langle t \rangle$, and blocked for a mean time $1/\mu^*$. The stationary flux was obtained using recurrence arguments, giving

$$j(\lambda) = \frac{\lambda \langle t \rangle}{\langle t \rangle + 1/\mu^*}. \tag{5.1}$$

The average time for which the Markovian system is open in a recurrence cycle may be obtained from Eq.(4.23) [117] as:

$$\langle t \rangle = \frac{1}{\lambda} \sum_{j=0}^{N-1} \frac{N!}{(j+1)(N-j-1)!} \left(\frac{\mu}{\lambda}\right)^j. \tag{5.2}$$

To compare the two models, μ and μ^* must be related to τ, τ_b and λ. Eq. (5.1) with Eq. (3.35) shows that μ^* must equal $1/\tau_b$. To obtain an expression for μ, we consider the system's behavior at low and high intensities. When $\lambda\tau << 1$, the non-Markovian transit time is equal to τ. The mean transit time is $1/\mu$ in the Markovian model. A first approach was to therefore set $\mu = 1/\tau$. When $\lambda\tau >> 1$, we expect μ to decrease to zero. Figure 5.1(a) shows that the stationary flux of the Markovian model is always larger than that of the non-Markovian model. Even though the two models behave similarly at small and large input intensity, they increasingly deviate for intermediate intensities with increasing N.

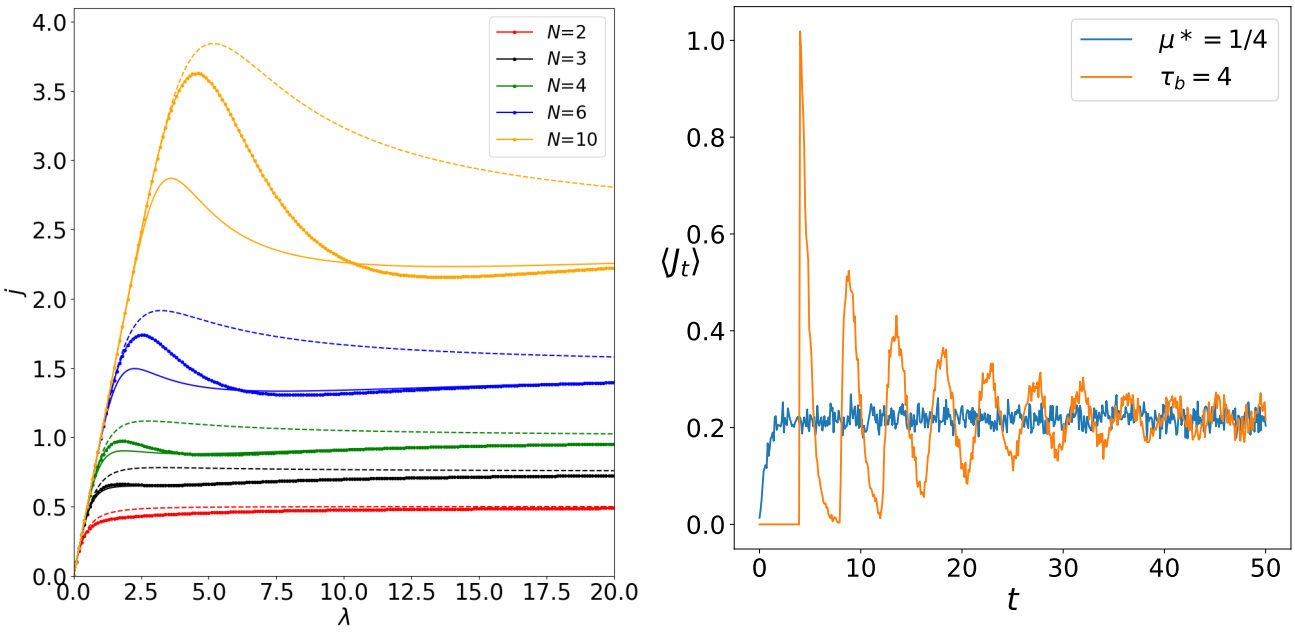

(a) (b)

Figure 5.1: (a) Comparison of stationary exiting flux, $j(\lambda)$, versus $\lambda\tau$ obtained for the non-Markovian model (dotted curves), the Markovian model by setting $\mu = 1/\tau$ (dashed curves) and the Markovian model by using the ansatz given by Eq.(5.6) (full curves), $\tau_b = 4$. (b) Time evolution of the average flux $< J >$ from a bundle of $N_c = 2, N = 1$ channels, $\Lambda = 1$. To relate the steady state of both systems, $\tau_b = 1/\mu*$. Where $\tau_b = 4$.

For $N_c = 1, N = 1$ (i.e., the channel is blocked by the entry of the first particle) it is easy to show that the steady state properties for the model with an exponentially distributed blocking time with rate μ^* are the same as for a model with a constant blocking time, τ_b, if the deblocking rate is equal to the inverse of the (constant) blocking time. The probabilities that the channel is open are $p_o = \mu^*/(\mu^* + \lambda)$ and $p_o = 1/(1 + \lambda\tau_b)$, respectively, and are therefore equal if $\tau_b = 1/\mu^*$. The kinetics of the two models are, however, different. When the blockage time is constant the exiting flux is strictly zero for $t < \tau_b$, while for an exponentially distributed blockage time the mean flux is finite for all $t > 0$. Figure 5.1 b shows the same behaviour for the time evolution of the average flux of a system of $N_c = 2$ channels, each with capacity $N = 1$, emphasising the fact that, even under this mapping, the transient regimes of the two models are appreciably different.

The corresponding $N_c = 1, N = 2$ model, with constant transit and blockage times, was originally examined in [44]. The steady state exiting flux is given by:

$$j_\infty = \frac{\lambda(2 - e^{-\lambda\tau})}{\lambda\tau_b(1 - e^{-\lambda\tau}) + 2 - e^{-\lambda\tau}}. \tag{5.3}$$

This equation may be compared to the steady state throughput of the $N = 2$ Markovian model, introduced in Chapter 4:

$$j_\infty = \lambda \frac{2\lambda + \mu}{\lambda^2/\mu^* + 2\lambda + \mu}. \tag{5.4}$$

There is no simple mapping that replaces τ with $1/\mu$ and τ_b with $1/\mu^*$. However, the two systems can be mapped by introducing the following effective exit (service) rate :

$$\begin{aligned} \mu^* &= \frac{1}{\tau_b}, \\ \mu &= \frac{\lambda e^{-\lambda\tau}}{1-e^{-\lambda\tau}}. \end{aligned} \tag{5.5}$$

i.e. substituting these effective rate equations into Eq. (5.4) returns Eq. (5.3). This is also obtained by equating the mean blocking time of the two models. For $N = 2$ we equate $\langle t \rangle$ given by Eq. (5.2) with the result for the non-Markovian model [107], $\langle t \rangle = (2-e^{-\lambda\tau})/(\lambda(1-e^{-\lambda\tau}))$. With this mapping, we recover the aforementioned expected limiting behaviour for both extremes of entering flux intensity. The exiting flux, Eq. (5.3) may be maximised for a finite value of intensity if $\tau/\tau_b < 0.16$.

The same procedure can be carried out for $N = 3$ using Eqs. (3.63) and (3.64), but the resulting expression for μ is considerably more complex. For general values of N we therefore propose the following ansatz, taking a similar form as the mapping for $N = 2$:

$$\mu = \frac{2\lambda/N}{e^{2\lambda\tau/N}-1}, \tag{5.6}$$

which behaves as $1/\tau$ at low intensity and approaches zero exponentially at large intensity. Substituting Eq.(5.6) into Eq.(5.1), produces a lower bound of the stationary flux (full curves). Furthermore, the maximum of the flux is underestimated and shifted to a lower intensity than in the non-Markovian model. For $N = 3$ and $N = 4$, the curves are very close to the results of the non-Markovian model. For $N > 4$, the ansatz leads to a significant underestimation of the exiting flux for small $\lambda\tau$.

5.2 Overview of results

A previously studied and published channel model, with a finite capacity of N that leads to blockage was studied in Chapter 3. The channel was exposed to an entering flux of fixed intensity, λ for a finite time, non blocking particles transit at a constant time, τ, and if N particles are simultaneously present, the channel blocks for time τ_b.

The irreversible case ($\tau_b \to \infty$) was first studied, where it was demonstrated that the first and second moments of the number of exiting particles are maximised for a finite intensity. For a single channel with capacity $N > 1$ the exiting flux displays a maximum value at finite intensity if τ_b is sufficiently large. If not, the exiting flux increases monotonically with the intensity.

The single channel model was then studied for the scenario of reversible blockage [114]. In this case, a particle transits through an open channel in time τ, but if N particles are simultaneously present in a channel, it is blocked for a time τ_b, before being emptied. Bundles consisting of N_c constituent channels, each with capacity N, were also considered. When a single channel is blocked, the entering flux is redistributed over the remaining open channels. A bundle of channels is open if, at least, one of its constituent channels is not blocked. If the entering stream is of constant intensity, the bundle evolves to a stationary state with a steady exiting flux, or throughput,

that depends on the intensity, τ_b and N. In the steady state the exiting flux is simply related to the probability that the bundle is open. For large N, the models display an abrupt change from a state with few blockages to one in which the bundle is permanently blocked and the output flux is entirely due to the release of blocked particles. This behaviour raises new questions about whether more general relationships describing the abrupt transitions in dynamics may be obtained for general N and N_c. The transport efficiency of a bundle, in which the entering flux is equally distributed over the open channels, was also compared with a bundle composed of independent channels. For $N = 1$, the coupled channels always have a higher throughput, but for larger values of N the behaviour becomes more complex.

Chapter 4 extends the model presented here so that both the transit time, and deblocking time (where applicable) follow a Poisson distribution, rendering the system 'memoryless'. This feature allows the time evolution of a stochastic circular Markov chain model of intermittent particle flow through a 1D channel to be described by a set of differential equations, for which exact solutions can, in principle, be obtained.

The optimisation of the throughput of a stream of particles subject to blocking was studied, by defining the entry and sojourn times of a particle transiting an open channel as exponentially distributed with rates λ & μ, respectively. If N particles are simultaneously present the channel is blocked and all newly arriving particles are rejected. After an exponentially distributed blockage time with rate $\mu^* < \mu$ all blocking particles are ejected.

General expressions were derived for the steady state probabilities and throughput. For $N = 2$ the steady state throughput was shown to assume a maximum value at finite intensity if $\mu^*/\mu < 1/4$. The time dependent throughput also displays a maximum if $\mu^*/\mu < 1/2$. This behaviour was shown to be qualitatively different from the well-known $M/M/N/N$ queuing model, whose steady state throughput always increases monotonically with the intensity of entering particles. The circular Markov chain model was then applied to multi-channel systems where the entering flux is evenly distributed over the open channels [135].

A bundle of N_c particle conveying channels was also considered. The total particulate flux enters the system according to a Poisson process of intensity Λ. If a single channel is blocked, the flux that would have otherwise entered is evenly distributed over the remaining open channels. If all channels are blocked, the input flux is rejected. A framework was provided to obtain both the time-dependent and steady state properties and have presented explicit results for the steady state throughput for $N_c = 2,3,4$. Analytical results were used to compare different configurations for transporting a particulate flux of given intensity.

A single 'high capacity' (HC) channel is shown to be more efficient than several coupled 'low capacity' (LC) channels at low intensity. but the reverse is true at higher values of Λ. We also compared N_c coupled channels with capacity, $N = 2$ with its uncoupled version. The coupled channels always have a higher throughput if $\mu^*/\mu > 0.25$. For $\mu^*/\mu < 0.25$ the coupled channels are more efficient at low intensity, but at higher intensities the order reverses.

5.3 Conclusion and outlook

The model introduced in Chapter 4 is fully stochastic in the sense that the interval between particle entries, transit and blockage times are all sampled from exponential distributions with given rates. While this choice can lead to a considerable simplification of the mathematics, it may be unrealistic in certain physical applications. A particle cannot traverse a channel instantaneously, while according to the exponential distribution this is the most likely outcome. For this reason, the model was compared with the constant transit and/or blockage times version [44], studied in Chapter 3.

Both the Markovian and non-Markovian channel models present a maximum in the stationary flow as a function of entering intensity. Furthermore, it was shown that Markovian model can be made to display the same steady state

behaviour with an appropriate mapping between the two models' parameters. Despite the transient behaviour being very different, the qualitative similarities in the steady state between the non-Markovian and Markovian models, as well as between the two queuing disciplines followed suggests that the details of the channel transport mechanisms and the blockage releases are irrelevant for determining whether or not a maximum in the steady state flux will be present for different variables. This behaviour can, therefore, be interpreted as universal of systems with carrying capacity, and may even be seen as related to the 'slower is faster' mechanism.

The next section will consider a microscopic approach to blockage induced intermittency in particle flow. The mechanism leading to blockage induced intermittency are explored by varying the system's parameters such as temperature, particle interaction force, constriction width and geometry. Just as in the simulations performed by Helbing [4, 139, 140], particles will acted on by many forces, such as the drift of the medium, inter-particle and particle-wall interaction forces, and Gaussian noise.

Part II

Metastable arches in constricted 2D channels

CHAPTER
6

INTRODUCTION

The second part of this thesis introduces a $2D$ microscopic approach to blocking phenomena. While the first part highlighted different behaviours directly related to the finite capacity of a $1D$ channel, the goal is now to identify different physical characteristics that may be tuned to induce intermittency. A single channel is studied, permitting $2D$ flow, with a well defined geometrical narrowing. The presence, size and shape of the narrowing will, among other factors such as the particle stiffness, determine whether stream of $2D$ Brownian particles will display intermittency. The new model parameters that will be introduced replace the previously used 'channel capacity' as the channel's control parameter.

6.1 Motivation

Early studies of the discharge of granular matter from silos showed that significant changes in the flow occur when the ratio of the orifice to particle diameter is in the range $3-5$ [15]. Later it was realised that the clogging phenomena is due to the formation of arches spanning the orifice [16–18]. The arch stability is normally strongly associated with interparticle frictional forces and is, for example, responsible for the well-known Janssen effect [141–143]. Recently a 'reverse Janssen effect' has been observed in narrow granular columns [144]. For granular materials, clogging is very often permanent and an additional shaking of the system is required to restart the flow. For many of these systems, when friction effects become negligible or entirely absent, the blockages become temporary, which leads to intermittent dynamics.

Recent studies have focused on the statistics of blocking processes [145–147]. The number of escaping particles in each successive burst, as well as the time intervals between bursts, are distributed exponentially, which implies a constant probability of blocking during the whole burst, however the time lapse distribution between successive particles has been shown to exhibit a power law tail, $p(\tau) \sim \tau^{-\alpha}$ [148]. The transition to clogging is characterised by the divergence of the average time lapse, i.e. $\alpha \leq 2$. Thomas and Durian [149] examined the fraction of grain configurations near the exit of granular hopper flow that cause clogging and concluded that there is no sharp transition. Colloidal systems, including bacteria [150], involve blocking mechanisms that are governed by, in addition to D/d, the driving force acting on the particles, long range hydrodynamic interactions and the nature of the particle-particle and particle-wall interactions. Ref [29] considers geometrical induced turbulence for bacterial mixing processes in micro-fluidic channels and Marin et al. [147] reported experimental results of clogging in charged-stabilized suspensions of particles flowing through a single constricted channel. The behaviour is remarkably similar to that observed in dry granular matter, even though the inter-particle interactions are considerably different. For $D/d < 3$ blockages form randomly while for $D/d > 3$ the flow is uninterrupted. They attributed this to the low friction of the particles. Recently, Souzy et al. [151], using a set up similar to that of Marin et al. [147] but with a larger constriction angle, observed an intermittent flow for $2.43 < D/d < 5.26$ with a power law

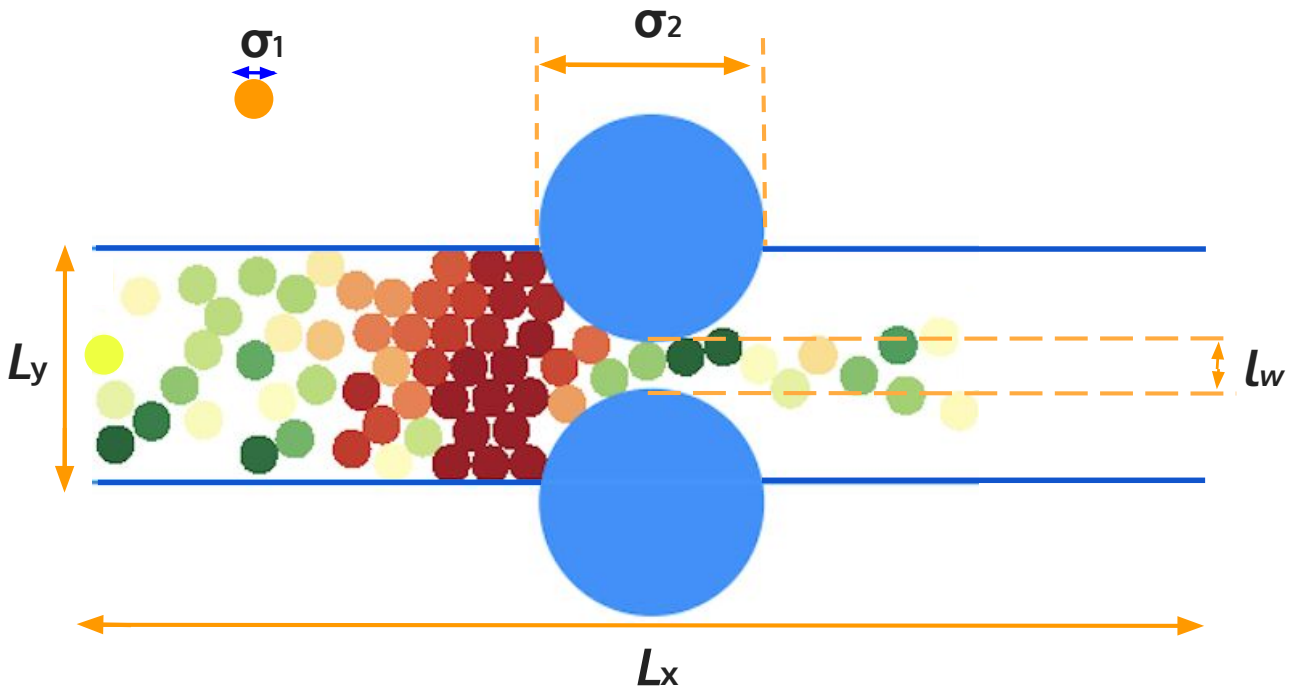

Figure 6.1: A channel of width L_y and length L_x with a constriction formed by two fixed disks each of diameter σ_2. l_w is the minimum distance between the obstacles and σ_1 is the particle diameter. A periodic boundary condition is imposed along the x-axis.

exponent $\alpha < 2$ in all cases. Hidalgo et al. [19] studied the flow of colloidal suspensions through small orifices using lattice Boltzmann methods with a focus on the effect of varying temperature. They observed that intermittent flow regimes precede clogging events. The mean number of colloids crossing the orifice between clogging events decreased with increasing temperature, i.e. thermal fluctuations can inhibit particle flow through the orifice, an example of 'freezing by heating'. Zimmermann et al. [152] studied a two-dimensional model of Brownian particles driven through a constriction by an external force using Brownian dynamics simulation and density functional theory. They observed four scenarios: complete blockage, monotonic decay to a constant flux, damped oscillatory behaviour or long-lived stop-and-go behaviour. State diagrams of the behaviour were constructed as a function of the coupling and the ratio of the constriction width to the channel width. Clogging phenomena can be strongly modified by placing an obstacle before the orifice: this can reduce or eliminate clogging in silos [43], sheep egress [153] and panic escape [154].

While these observations display some universal aspects, a simple model with a limited number of relevant parameters capable of capturing the essential dynamics of these systems is still missing. The new features in the work presented in this section are the consideration of the channel width L_y, the constriction width l_w, non-rigid frictionless particles and to highlight the essential role of the geometry of the constriction.

6.2 Model overview

We consider a minimal system, illustrated in Fig. 6.1, of identical soft discs of mass m of diameter σ_1 flowing through a channel of width L_y. The disks undergo Brownian motion and are driven, from left to right, by the drift force related to the flow of the immersing fluid. The particles we study can be deformed by the channel, i.e. the walls, or by neighbouring particles. In many biological situations, deformable molecules move through transport vesicles, which are spherical structures formed by a closed biological membrane, containing molecules and many

trans-membrane proteins [155, 156]. A constriction formed by two fixed disks of diameter σ_2 is symmetrically placed about the channel axis, at $x = 0$ so that the minimum distance between them is $l_w = L_y + \sigma_1 - \sigma_2$, i.e they are not centred on the channel walls, but displaced outward by $\sigma_1/2$. The curvature of the constriction is the inverse of radius of the disk obstacle radius, $2/\sigma_2$. In order to maintain a constant l_w, for varying channel width L_y the constriction's curvature needs to be changed. The total channel length, L_x is chosen to be significantly greater than L_y to minimise correlation effects.

The particle flow in the microchannel depends on several physical properties, including the ratio of the constriction width to the particle diameters, inter-particle, particle-wall interactions and drag forces.
The inter-particle force between the mobile particles i and j is

$$\mathbf{F}_{ij} = k\theta(\sigma_{12} - r_{ij})(r_{ij} - \sigma_{12})\hat{\mathbf{r}}_{ij}. \tag{6.1}$$

r_{ij} is the distance between two particles, and $\hat{\mathbf{r}}_{ij}$ is the unit vector along r_{ij}. $\theta(x)$ is the Heaviside function, k is the rigidity factor and $\sigma_{12} = \frac{\sigma_1+\sigma_2}{2}$. The same interaction force is used between a mobile particle i and the stationary particles that make up the constriction, i_0. The forces between particle i and the channel walls, denoted $w\pm$, is given by

$$\mathbf{F}_{w\pm,i} = k_w\theta(r_{iw\pm} - \sigma_i/2)(r_{i,w\pm} - \sigma_i/2)\hat{\mathbf{r}}_{iw\pm}, \tag{6.2}$$

where $r_{i,w\pm}$ is the distance between the particle i and the wall $w\pm$, $\hat{\mathbf{r}}_{iw\pm}$, the unit vector, and the rigidity factor k_w. The force between a moving particle and the two obstacles is given by Eq. 6.1. Finally, the moving particles are driven an external drag force

$$\mathbf{F}_{d,i} = -\alpha(\mathbf{v} - \mathbf{v}_0), \tag{6.3}$$

where $\mathbf{v}_0$ is a constant vector along the channel axis, $\mathbf{v}_0 = v_0\mathbf{e}_x$, and α is the drag coefficient of the driving medium. The mobile disks move under the the influence of both Brownian motion and the frictional force arising from the fluid in which the disks are immersed. The resulting equation of motion is given by:

$$m\frac{d\mathbf{v}_i(t)}{dt} = \sum_{j\neq i}\mathbf{F}_{ij} + \sum_w \mathbf{F}_{w,i} + \sum_{i_0}\mathbf{F}_{i,i_0} + \eta(t), \tag{6.4}$$

$\eta(t)$ is Gaussian noise, such that $< \eta(t) >= 0$ and $< \eta(t)\eta(t') >= \delta(t-t')$. To be sure that the noise used accurately represents the random shocks of the components of the immersing milieu the following must be true:

$$< \eta(t)\eta(t') >= 2mD\delta(t-t'), \tag{6.5}$$

where D is the velocity diffusion coefficient, which, by Einstein's relation is given by:

$$D = \frac{k_B T\alpha}{m}. \tag{6.6}$$

T is the temperature of the bath, and k_B is the Boltzmann constant. Substituting Eq. (6.6) into Eq. (6.5) returns:

$$< \eta(t)\eta(t') >= 2k_B T\alpha\delta(t-t'). \tag{6.7}$$

finally returning the Brownian equation of motion, with the rescaled noise, as:

$$m\frac{d\mathbf{v}_i(t)}{dt} = \sum_{j\neq i}\mathbf{F}_{ij} + \sum_w \mathbf{F}_{w,i} + \sum_{i_0}\mathbf{F}_{i,i_0} + \sqrt{2k_B T\alpha}\eta(t). \tag{6.8}$$

$\eta(t)$ is Gaussian noise, such that $< \eta(t) >= 0$ and $< \eta(t)\eta(t') >= \delta(t-t')$. In what follows, we only consider overdamped Brownian motion, i.e. the acceleration term is neglected. As a result, the system's dynamics is described by the following overdamped Langevin equation:

$$\mathbf{v}_i(t) = \mathbf{v}_0 + \frac{1}{\alpha}\left(\sum_{j\neq i}\mathbf{F}_{ij} + \sum_w \mathbf{F}_{w,i} + \sum_{i_0}\mathbf{F}_{i,i_0}\right) + \sqrt{\frac{2k_B T}{\alpha}}\eta(t).$$

Further physical parameters characterising the model are the intensities of the soft core repulsion k and k_w and the dimensions of the channel L_x and L_y. The particle density is $\rho = N/(L_x L_y)$, where the volume occupied by the constriction is neglected. This is reasonable if $L_x >> L_y$. It is convenient to switch to non-dimensional system parameters. Since in the case of overdamped motion studied here, the particle mass is irrelevant we select σ_1, σ_1/v_0 and $\sigma_1 v_0 \alpha$ as units of length, time and energy, respectively. The unit of time corresponds to ballistic displacement of a particle with the velocity v_0 and the unit of energy is the work done against the drag force in this time. With this choice of units, we switch to the following non-dimensional quantities:

$$k' = \frac{k\sigma_1}{\alpha v_0}, \qquad k'_w = \frac{k_w \sigma_1}{\alpha v_0}, \tag{6.9}$$

which are the reduced force strengths between particle-particle and particle-wall, respectively, and:

$$T' = \frac{k_B T}{\alpha v_0 \sigma_1}, \qquad \rho' = \rho \sigma_1^2 \tag{6.10}$$

are the the reduced temperature and particle density. The channel's geometric parameters are:

$$L'_x = \frac{L_x}{\sigma_1}, \quad L'_y = \frac{L_y}{\sigma_1}, \quad l'_w = \frac{l_w}{\sigma_1} \tag{6.11}$$

and,

$$\mathbf{v'_i}(\mathbf{t}) = \frac{\mathbf{v_i}(\mathbf{t})}{v_0}, \qquad r'_{ij} = \frac{r_{ij}}{\sigma_1} \tag{6.12}$$

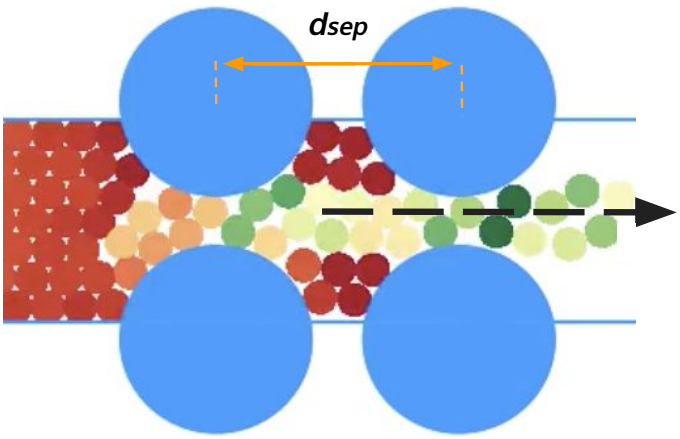

Figure 6.2: When d_{sep} is sufficiently large, the particles line the channel to form a passage between the two obstacles.

are the dimensionless velocity and interparticle distance. The Péclet number, giving the ratio of advective transport to diffusive transport is:

$$Pe = \frac{\sigma_1 v_0 \alpha}{k_B T} = \frac{1}{T'}. \tag{6.13}$$

In the following, we drop the primes of variables and of parameters. In order to decrease the dimensions of the parameter space, we furthermore assume that: $k = k_w$. In the limit of a long channel, which minimizes correlations between exiting and entering particles, L_x is an irrelevant parameter. Particles are initially randomly and uniformly placed within the channel without overlapping each other, the walls or the constriction. The collective particle trajectories were generated by using an Euler algorithm with a timestep $\Delta t = 10^{-2}$. Periodic boundary

conditions were imposed in the direction of the channel: as a particle exits the channel when the abscissa is equal to $L_x/2$, it is reinserted at $x = -L_x/2$. The channel domain is, thus, topologically an annulus. The dynamical motion in this model is purely rotational around the annulus due to the application of the unidirectional drift force. Whether the y-coordinate of the reinserted particle is conserved or chosen randomly within the interval of the channel has no noticeable influence on the dynamics of the system. The next chapter will investigate a simple convex constriction formed by two fixed large discs located in the middle of the channel (as in Fig. 6.1). Section 7.2 considers a double constriction formed by four fixed large discs, whose separation by a finite distance d_{sep}, creates a non-convex geometry see Fig. 6.2.

We focus on the low temperature regime, where the mobile particle display near-ballistic motion, as the the flux most prominently displays intermittent dynamics, due to blocking. Cascade statistics were monitored for various geometries, and the angular distribution of the blocking particles were collected.

CHAPTER
7

SIMULATION RESULTS

7.1 Single constriction

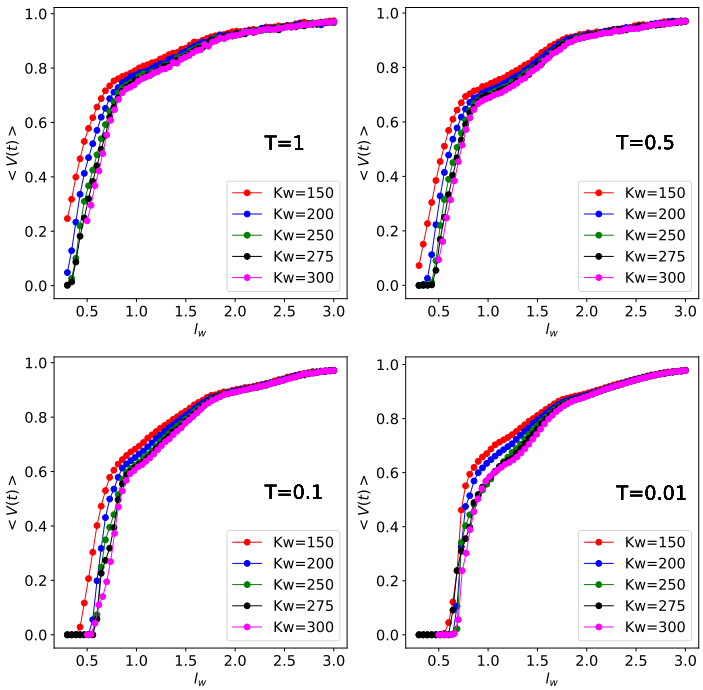

Figure 7.1: Mean velocity, $\langle V \rangle$, as a function of constriction l_w and for various rigidities $k_w = 150, 200, 250, 275, 300$ and with $L_Y = 5.5$, $\rho = 0.55$ at different temperatures.

Simulations were performed for reduced densities in the interval $0.5 \leq \rho \leq 0.6$ and Péclet numbers $1 < Pe < 100$. In this density range, high and low density regions coexist on each side of the obstacle when blocking occurs. After a transient time, which increases as the width of the constriction decreases, the system reaches a stationary state with a well-defined mean particle flux. The upper bound of the time required for the system to reach the

stationary state is L_x/v_0 which is equal to the time taken for the system's average velocity to equal zero when completely blocked.

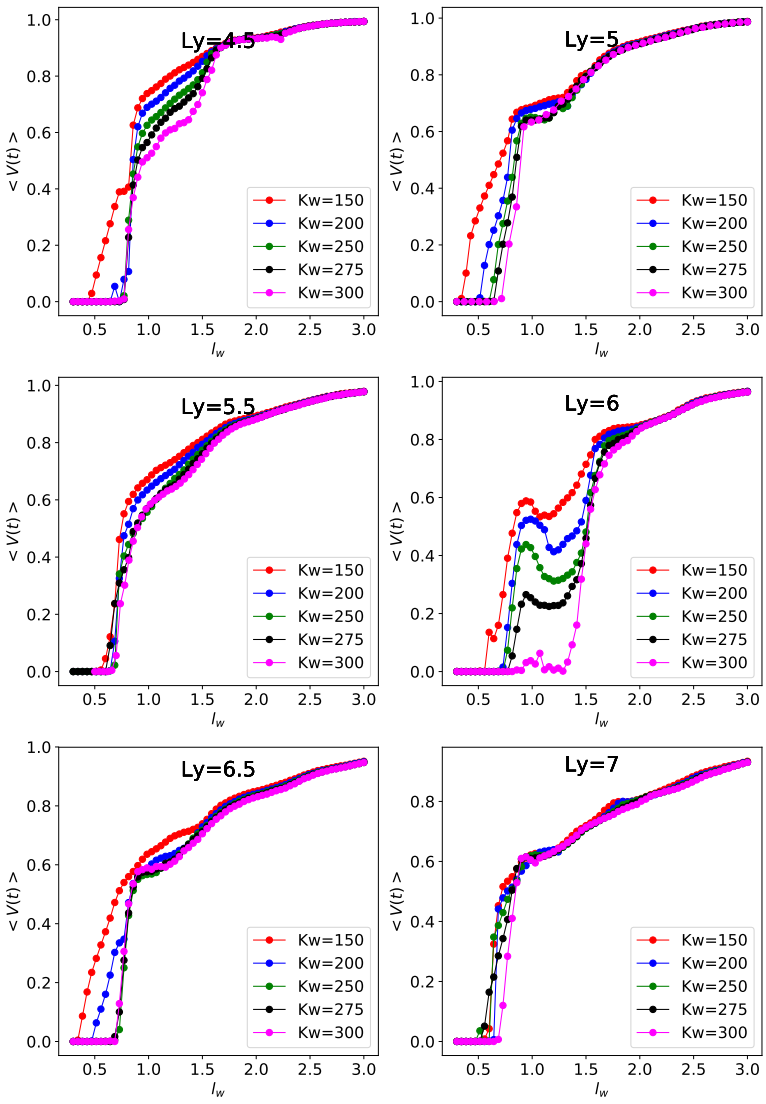

Figure 7.2: Mean velocity $\langle V \rangle$ as a function of l_W at low temperature $T = 0.01$ for different values of Ly

7.1.1 Velocity statistics

We first consider the mean velocity of the system of particles, $\langle V(t) \rangle$, as a function of the minimum distance l_w with $L_y = 5.5$ and for different values of k_w. Fig. 7.1 shows the following behaviour is repeatedly observed: When $l_w \geq 3$ the constriction has a small effect and the mean velocity remains close to v_0. For $l_{w_1} \leq l_w \leq 3$, the velocity decreases almost linearly with a slope which increases with decreasing temperature. The lower bound of the linear region, l_{w_1}, depends on the temperature: for $T = 1$ and $T = 0.5$, $l_{w_1} \simeq 2$ while for $T = 0.1$ and $T = 0.01$, $l_{w_1} \simeq 1.8$.

A second regime is observed in the range $l_{w_2} \leq l_w \leq l_{w_1}$ where l_{w_2} is slightly below 1. The mean velocity is a convex function of l_y and decreases more rapidly than before.

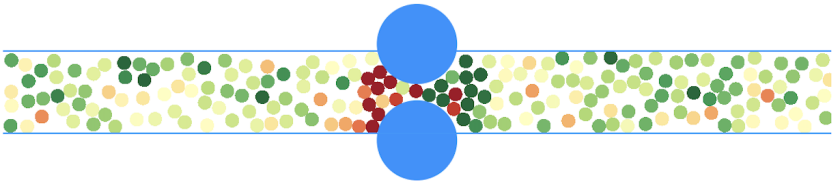

(a) $N = 0$, just after random initialisation.

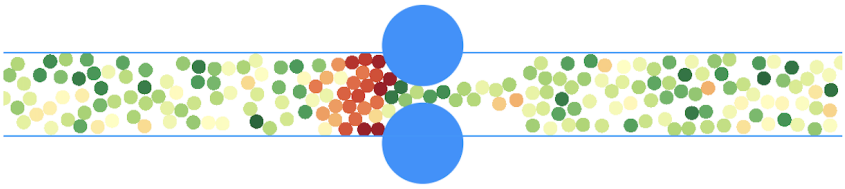

(b) $N = 10$, steady flow through the constriction.

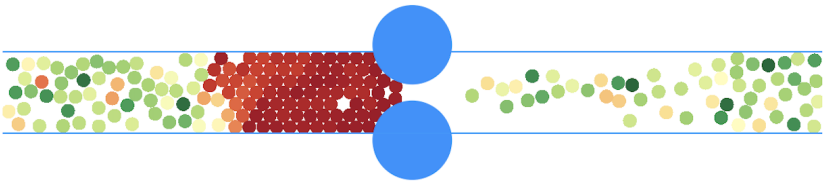

(c) $N = 40$, first blockage

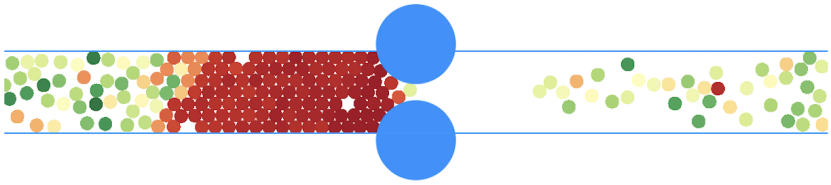

(d) $N = 49$, deblockage

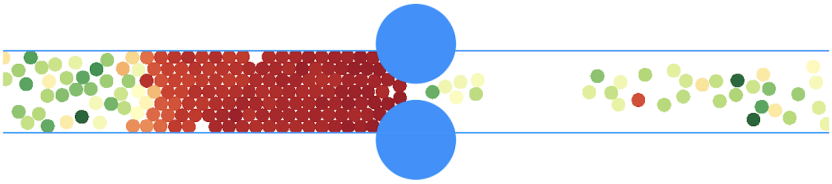

(e) $N = 56$ Cascade of size 6

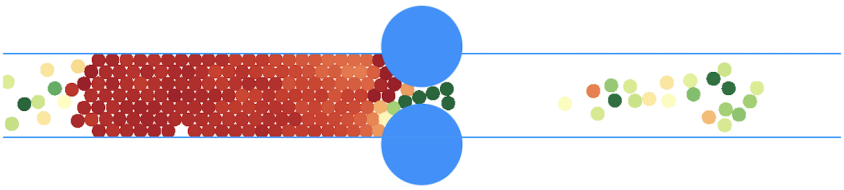

(f) $N = 192$ Continued cascading.

Figure 7.3: Time slices of the evolution of the driven particle flow. $L_y = 6$, $\sigma_2 = 5.75$.

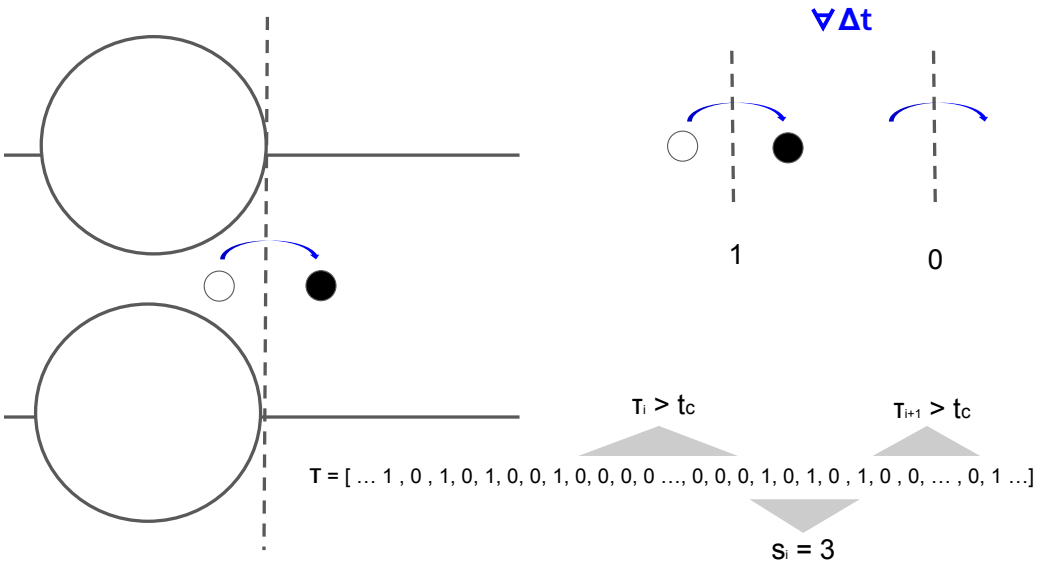

Figure 7.4: Illustration of the technique employed to characterise the system's cascade size and inter-time distribution. A slice is defined just beyond the geometrical constriction. If, in a time-step Δt, a particle passes over the slice, a 1 is recorded; otherwise, a 0. The time evolution of the system can then be represented as the binary stream **T**. If an unbroken string of zeros is longer than some predefined critical value, t_c, the system is said to be blocked for time τ_i, giving an intercascade time. The number of 1s counted between two consecutive blocking events is the cascade size, s. $N(\tau)$ and $N(s)$ are the cascades inter-time and size distribution, respectively, collected over a simulation.

There is little dependence on k_w, except at the lowest temperature $T = 0.01$. Finally, for $l_{w_3} < l_w < l_{w_2}$, which corresponds to a minimum distance less than a particle diameter, the velocity decreases rapidly to zero. The slope of the nearly linear curve increases as the temperature decreases. Moreover, whereas the behaviour in this regime depends on the strength of the forces for $T = 1, 0.5, 0.1$, it is almost independent of k_w at low temperature. l_{w_3} depends on both the temperature and k_w. This regime corresponds to single particle passing through the constriction. Finally, for $l_w < l_{w_3}$, the channel is unequivocally blocked, because the force required to sufficiently deform a particle exceeds the force exerted by the other particles behind the constriction.

At low temperatures one observes the formation of a dense region before the constriction in which the particles are almost at rest. When the size of this region exceeds a threshold length, the particles are able to pass through the constriction. The resulting burst is of short duration and is followed by a period of arrest before the next group of particles is released.

Figure 7.2 shows the mean velocity as a function of l_w for different channel widths L_y. The different regimes described for $L_y = 5.5$ are only slightly modified for $L_y = 4.5, 6.5, 7.0$. Substantial changes are, however, observed for $L_y = 5$ and $L_y = 6$: For $L_y = 5$, when $1 < l_w < 1.5$, the mean velocity is almost constant which is associated with the fact that only one particle at a time enters the constriction from the dense region before the bottleneck. Conversely, when $L_y = 6$, one observes a non-monotonic variation of the mean velocity with l_w.

The system now favours two vertically aligned particles at the entrance of the constriction. This configuration is metastable in the sense that when the fluctuation forces acting on the two particles are sufficiently large, one observes a small deviation of the vertical axis defined by the two particle centres that allows one of the two particles to enter the constriction, rapidly followed by the other. This effect only appears if the channel width, L_y, is able to 'select' this configuration at the entrance of the channel and if the core repulsion is not large (for

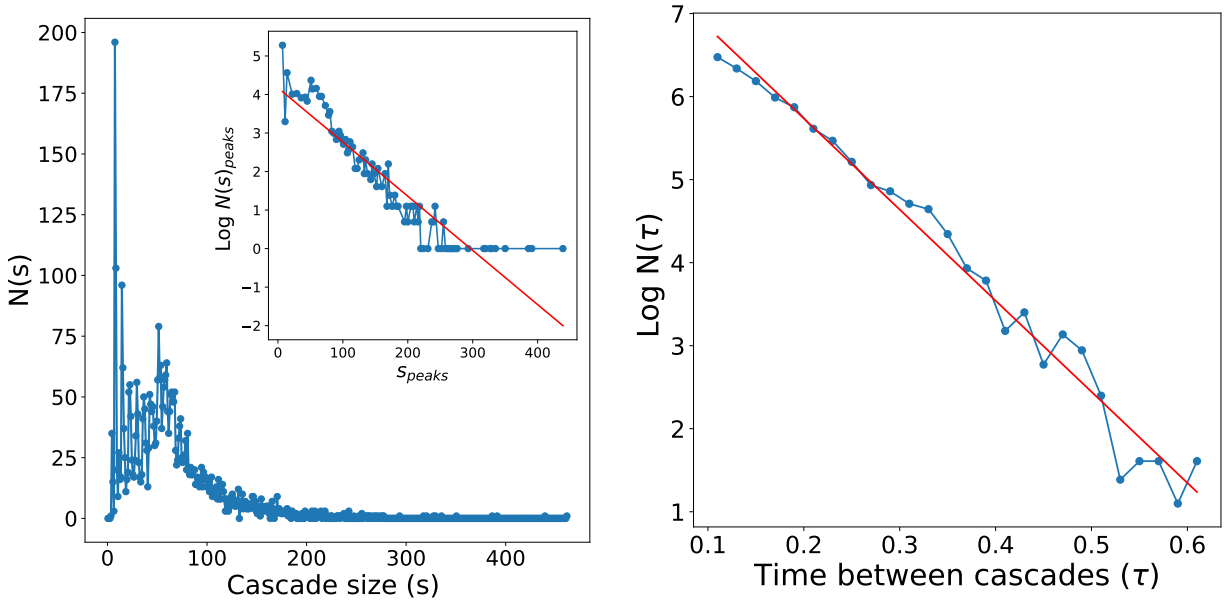

(a) (b)

Figure 7.5: $L_y = 6$, $\sigma_2 = 5.75$, $T = 0.01$ and $t_c = 0.1$ (a) Statistics for cascade size distribution. The inset displays a log-linear plot of the distribution envelop. $s_0 = 100$ (b) Log-linear plot of the inter cascade time distribution. $\tau_0 = 0.09$.

$k_w = 300$ this same configuration leads to a quasi-permanent blockage for $l_w < 1.5$, namely larger than a diameter of particle). Conversely, when $k_w = 100$ the particles are highly deformable and the minimum of the mean velocity versus l_w disappears. For a suitable choice of parameters, the model develops metastable minimal arches, resulting in blockages of finite duration, leading to cascading behaviour, as illustrated in Fig. 7.3. We also present the distribution of angles formed by the line passing through the centres of the two blocking particles, obtained over long simulation times. The next section examines this intermittent regime in more detail.

7.1.2 Cascade statistics

The dynamics is characterised by a sequence of cascades alternating with periods of arrest. Distributions of both the cascade size and the inter-cascade times (Fig. 7.5) were obtained for $L_y = 6, k_w = 200, \sigma_2 = 5.75$. This geometry was chosen as it corresponded to the local minimum in the mean velocity, as shown in Fig: 7.2 at $T = 0.01$. These were determined by recording the times at which a particle crosses a line perpendicular to the channel axis and just beyond the constriction, as illustrated by Figure 7.4. If, in a time-step Δt, a particle passes over the slice, a 1 is recorded. Else, a 0 is recorded. The time evolution of the system can then be represented as the binary stream $\mathbf{T}$. If the elapsed time between the passage of two particles is greater than a chosen characteristic time, t_c, the system is said to be blocked for time τ_i. The number of 1s counted between two consecutive blocking events is the cascade size, s. $N(\tau)$ and $N(s)$ are the cascades inter-time and size distribution, respectively, collected over a simulation. The cascade distributions are independent of t_c. Practically, we found that a good choice was $t_c = 10\Delta t$. As Fig. 7.5 b confirms, the histogram of inter-cascade times, τ follows exponential distributions:

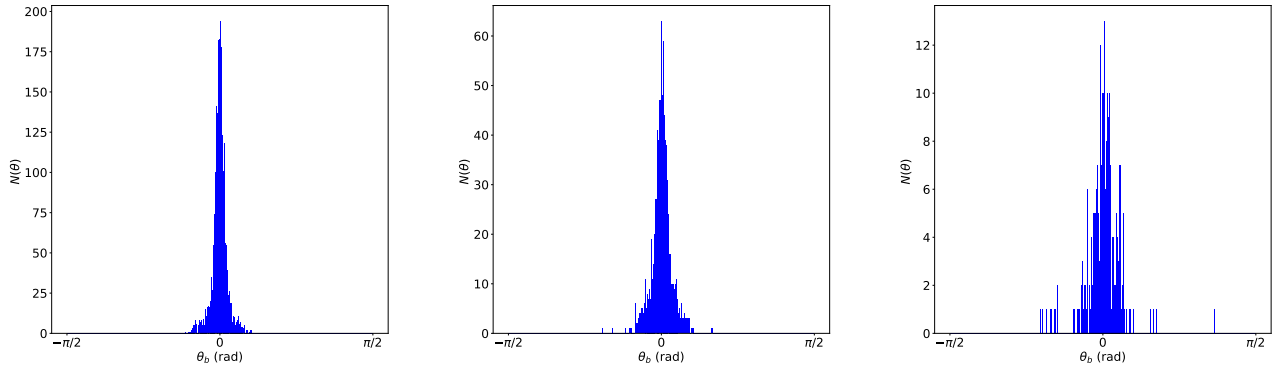

(a) $T = 0.01$ (b) $T = 0.02$ (c) $T = 0.05$

Figure 7.6: Angular distributions of axis running through blocking particle pairs

$$p(\tau) = \frac{1}{\tau_0} e^{-\tau/\tau_0}. \tag{7.1}$$

where τ_0 is the characteristic exponent. Similarly, as shown in the subfigure of Fig. 7.5a, the cascade size peaks also follow exponential distributions, as shown by Eq. 7.1, but with s_{peaks} replacing τ, and s_0 replacing τ_0. For the single constriction case, a single peak, with a maximum at $\theta_b = 0$ is observed, which is as expected.

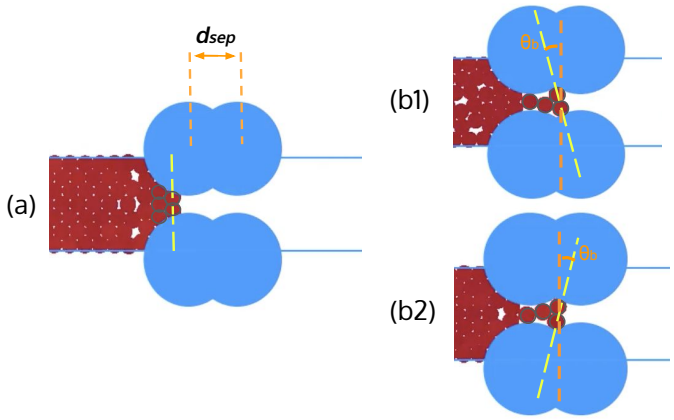

Figure 7.7: The two types of blocking mechanism that are possible with a double constriction $l_w = 1.5$, $d_{sep} = 3$. (a) Type I, which is the sole cause of the non-monotonic variation in the mean velocity as shown in Fig. 7.9; (b) Type II, arising from the non-convex geometry for $d_{sep} > 0$. The blocking angle, θ_b, is also illustrated.

7.1.3 Angular distribution

The angular distribution of the blocking particles, whose presence leads to the intermittent dynamics is studied. The blocking angle, θ_b is defined as the angle between the line passing through the axis of the two blocking particles, and the y-axis, as illustrated in Fig. 7.7. As the temperature is increase, the distribution broadens, and fewer blocking events are recorded, as expected.

7.2 Double constriction

We now consider a double constriction consisting of four disks, i.e. the original pair plus a replica displaced by d_{sep}. When $d_{sep} = 0$, the two pairs fully overlap and we recover the previous model. When $d_{sep} > 0$, the non-convex region between the two constrictions may trap the moving particles. Simulations were performed for different values of separation d_{sep} = {0,1,2,3,4,5,6} between the two pairs of obstacles. All the other parameters are chosen to correspond to those of the original model for which both monotonic and non-monotonic behaviour was observed, i.e., for $T = 0.01$, $k_w = 200$, $L_y = 5.5, 6, 6.5$.

Two distinct blocking mechanisms are now possible, as shown in Fig. 7.7: Type 1, involving the previously observed arch formation before the first pair of obstacles, and (depending on the geometries chosen) Type II, arising from the trapping of particles *between* the two pairs of obstacles. As illustrated in the figure, these mechanisms can be distinguished by the orientation of the blocking particles, θ_b. For the Type I mechanism, the points of contact between the two blocking particles and the obstacles lie almost parallel to the y-axis. Conversely, the non-convex geometry that gives rise to the Type II mechanism causes θ_b to be significantly misaligned with the y-axis in one of two different, yet symmetrically equivalent, orientations. The arches forming within the space encompassed by the non-convex geometry in Figs 7.7 b1 and b2 lead to regular triangular formations.

It is possible that different choices of l_w and d_{sep} will lead to the formation of different finite regular polygonal structures within the non-convex bound space, each of which may be associated to various degrees of intermittency, according to the structure's stability. The presence of the second blocking mechanism increases the likelihood of intermittent dynamics for values of L_y that would otherwise not display an overshoot in the mean velocity. It is often observed that the system passes a significant amount of time undergoing Type I followed by Type II blocking before releasing a cascade. It should also be noted that, once d_{sep} exceeds a certain length, particles between the two constrictions organise to form a passage from one obstacle pair to another, therefore reducing the possibility of the Type II blocking. See Fig. 6.2.

7.2.1 Velocity statistics

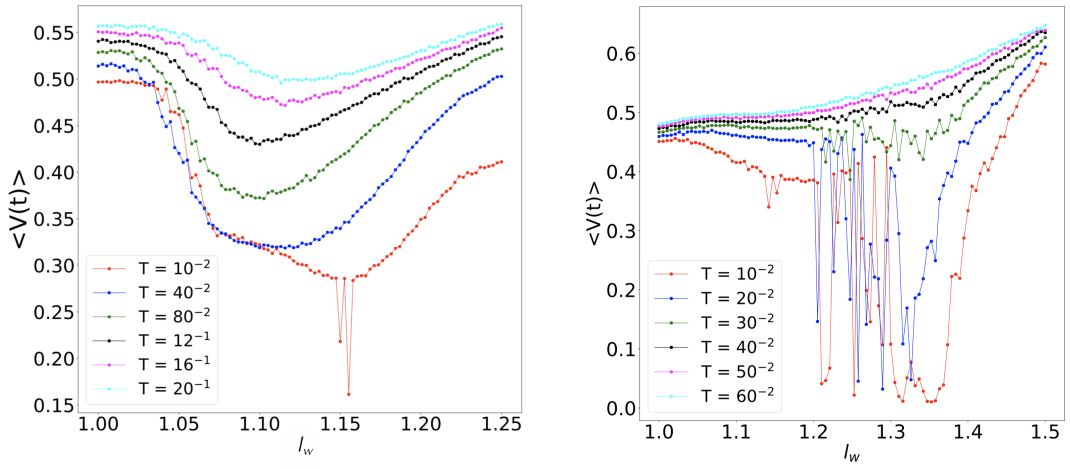

(a) $d_{sep} = 3$ (b) $d_{sep} = 4$

Figure 7.9: Mean velocity $\langle V \rangle$ as a function of l_w for increasing temperature T, and $L_y = 6$ for two values of d_{sep}. At low temperatures singular reductions in the velocity for certain geometries are present. Minor variations, of the order of 10^{-6}, corresponding to the numerical precision of the geometry explored, are sufficient to enter or leave the singular region.

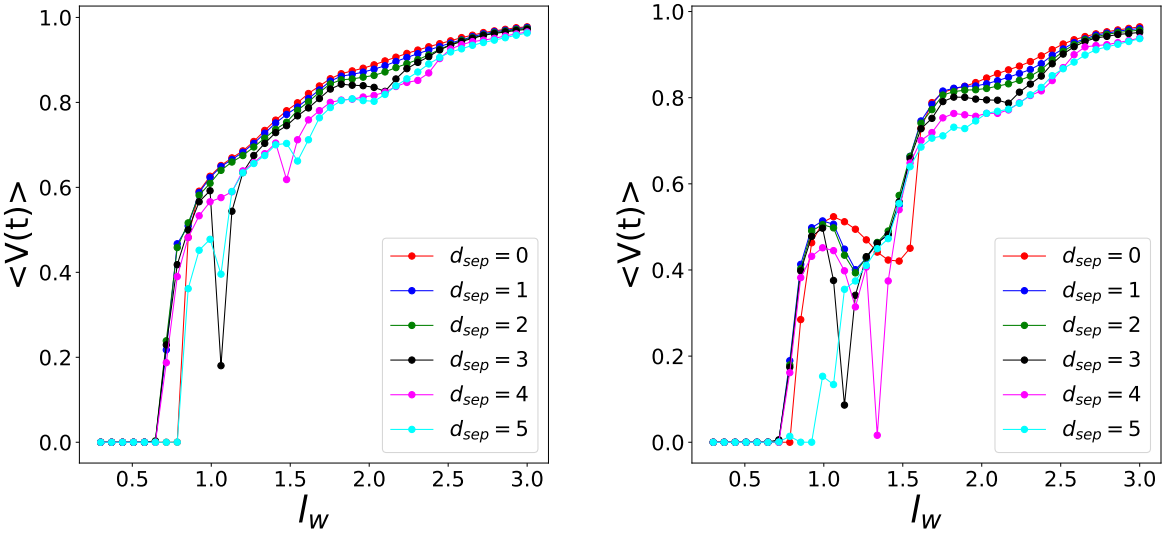

(a) $L_y = 5.5$ (b) $L_y = 6.0$

Figure 7.8: Mean velocity $\langle V \rangle$, as a function of l_w for two values of L_y, each for various values of d_{sep}. $\rho = 0.55$ and $T = 0.01$. Non-monotonic behaviour is observed for different non-zero values of d_{sep} for non-integer values of L_y.

Fig. 7.8 shows the mean velocity as a function of l_w for various values of d_{sep}. Let us first consider the system with channel width $L_y = 6$. For $l_w > 2$, the mean velocity decreases weakly with increasing d_{sep}, showing that the inter-constriction geometry has little influence. In the intermediate range, $0.7 < l_w < 2.0$, the situation is considerably different: for $d_{sep} = 1,2$, one observes an overshoot of the mean velocity for smaller values of l_w, followed by a minimum comparable to that displayed by the single constriction ($d_{sep} = 0$). For larger values, $d_{sep} = 3,4$, the minimum of the velocity is much smaller than the previous cases and occurs for $l_w = 1.1, 1.3$, respectively. For $d_{sep} = 5$, the velocity is almost monotonic (except for a tiny plateau in the interval $l_w = [1.0, 1.1]$), while for $d_{sep} = 6$, it increases monotonically with l_w.

The non-monotonic evolution of the mean velocity, for non-zero values of d_{sep}, persists for cases where the channel width is a non-integer ($L_y = 5.5, 6.5$). This indicates regions of geometry that display intermittent dynamics that are principally (but not solely) caused by the Type II blocking mechanism illustrated in Fig. 7.7. Figure 7.9 shows the effect of varying temperatures on the mean velocity as a function of l_w, around the geometries of interest for $L_y = 6, d_{sep} = 3,4$. At low temperatures, the mean velocity varies non-monotonically with l_w. The region in which the mean velocity displays a local minimum is associated with strongly intermittent behaviour, at low temperature. Increasing the temperature causes these regions to disappear, and the non-monotonic nature of the mean velocity decreases. For $T = 0.01$ the mean velocity undergoes many singular reductions. For $d_{sep} = 3$ the greatest observed singular reduction for $T = 0.01$ occurs at $\sigma_2 = 5.844737$ (i.e. $l_w = 1.155263$). It is interesting to note that the non-monotonicity exhibited for $d_{sep} = 3$, while showing fewer observed singular regions, is nonetheless more robust to increasing temperature than for $d_{sep} = 4$.

Particle-particle or particle-wall friction has been evoked to explain the formation of arches in silos and other situations, however, in the present model solid friction is absent, so it is reasonable to conclude that this effect is purely geometrical in origin. It must furthermore be noted that there exist some geometries that are critical in the sense that, at low temperatures, they cause the mean velocity to decrease to zero in a non-smooth fashion, for example, as seen in Fig. 7.9. Characterising the mean velocity with higher precision data points, at low

temperature, reveals the presence of multiple values at which the mean velocity approaches zero in a non-smooth manner. This effect is most prominent at low temperatures. Increasing the temperature, as shown in Fig. 7.9 causes these singular points to vanish, but the mean non-monotonic behaviour persists for a large range of increasing temperatures, as shown for the specific case of $d_{sep} = 3$.

7.2.2 Cascade statistics

This section characterises the intermittent behaviour observed for certain specific values of non-convex geometry that, at low temperature, result in the singular minima of the mean velocity, as seen in Figs. 7.8 and 7.9. The low temperature regime was chosen, as it is where the flux displays intermittent dynamics. Avalanche statistics were monitored for various geometries.

The intermittent dynamics can be best described as a sequence of particle cascades that are blocked during the inter-cascade times by one of the two blocking mechanisms shown in Fig. 7.7. The cascades are detected by counting the number of particles that pass a $1D$ section through the channel between pauses greater than a pre-defined critical time t_c.

Figures 7.10 a - c show cascade statistics for three increasing temperatures, at the geometry corresponding to the lowest valued minima for $L_y = 6$ $d_{sep} = 3$ as shown in Fig. 7.8. The appearance of peaks in the distribution of cascade sizes that were not present for $d_{sep} = 0$; shown in Fig 7.5, is a striking feature. The lower inset of each figure shows that the peaks follow exponential distributions, whose exponent increases with temperature. Furthermore, as for the $d_{sep} = 0$ case, the distribution of inter-cascade times also follows exponential distributions, whose exponent decreases with temperature.

T	s_0	τ_0
0.01	5.88	0.11
0.02	9.09	0.06
0.05	33.33	0.05

Table 7.1: Table showing the exponential fit parameters of both the distribution of intercascade times, τ_0 and peak distribution s_0, with increasing temperature, T, for $L_y = 6$, $\sigma_2 = 5.844737$

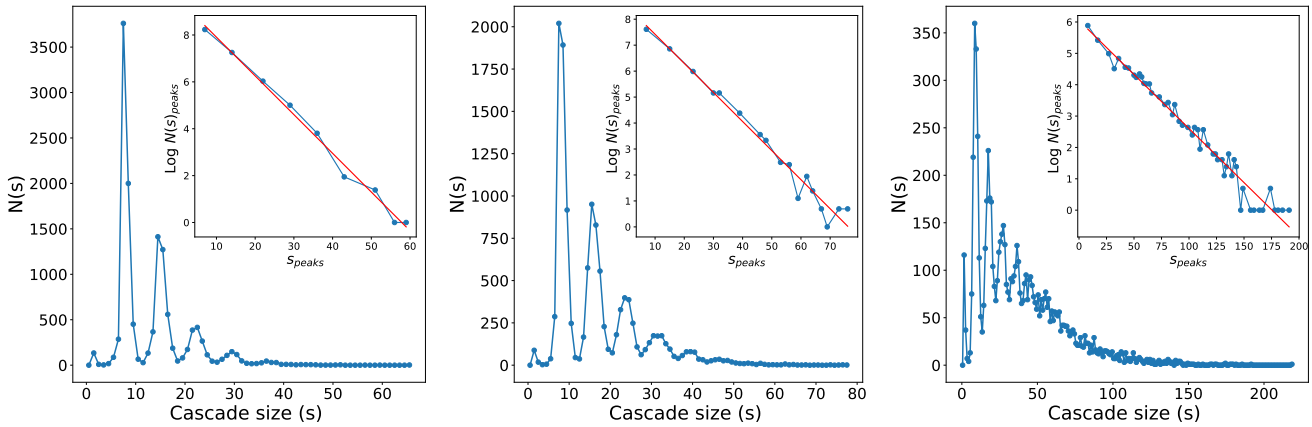

(a) $T = 0.01$ (b) $T = 0.02$ (c) $T = 0.05$

Figure 7.10: Cascade size distribution for $\sigma_2 = 5.844737$, $L_y = 6$, $d_{sep} = 3$, $T \in [0.01, 0.02, 0.05]$, $t_c = 0.1$; The main figures show the distribution of cascade sizes. The inset show the distribution of the cascade peaks, on a log-linear plot.

An initial study of the cascade statistics that manifest for $L_y = 6$, $d_{sep} = 3$, $\sigma_2 = 5.75$, show a distribution that is qualitatively very simlar to that presented in the $d_{sep} = 0$ case, as shown in Fig. 7.5.

7.2.3 Angular statistics

Distributions of θ_b are again taken, but for both Type I and II blocking mechanisms, for the specially chosen geometry studied in Sec 7.2.2, that induced a singular reduction in the system's global velocity, as well for the value of σ_2 already studied for the original constriction.

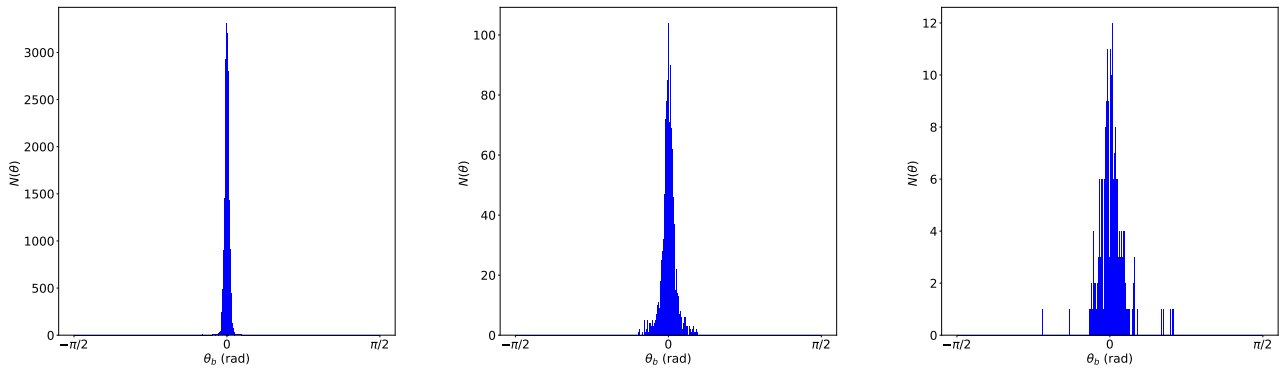

(a) $T = 0.01$ (b) $T = 0.02$ (c) $T = 0.05$

Figure 7.11: Type I distribution: $\sigma_2 = 5.844737$, $L_y = 6$, $d_{sep} = 3$

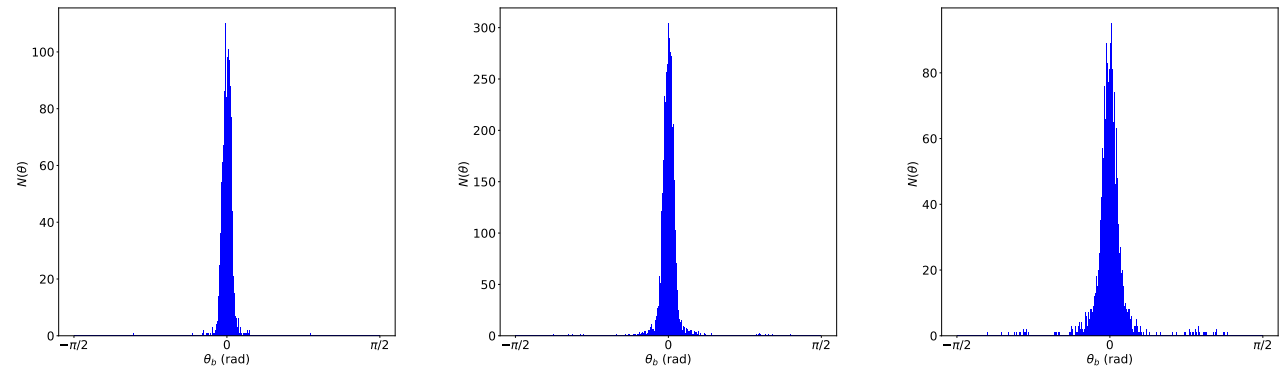

(a) $T = 0.01$ (b) $T = 0.02$ (c) $T = 0.05$

Figure 7.12: Type II distribution: $\sigma_2 = 5.844737$, $L_y = 6$, $d_{sep} = 3$

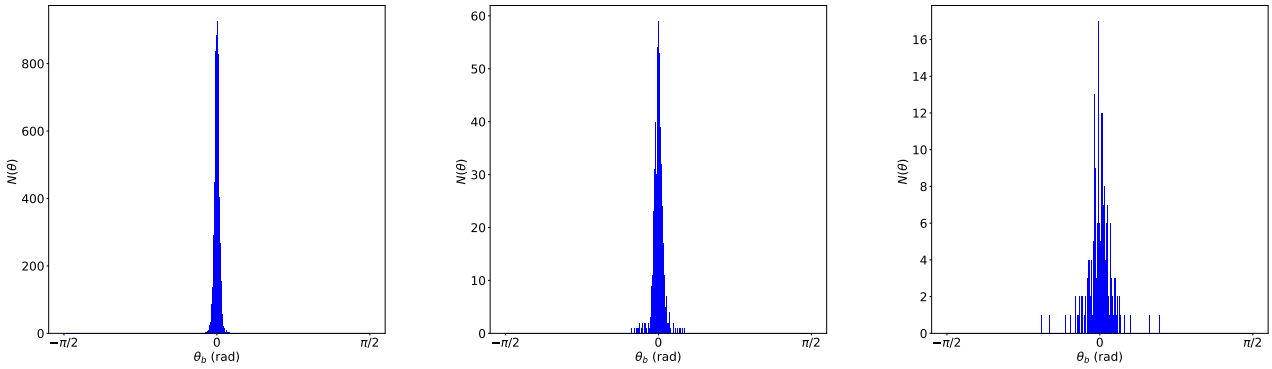

(a) $T = 0.01$ (b) $T = 0.02$ (c) $T = 0.05$

Figure 7.13: Type I distribution: $\sigma_2 = 5.75$, $L_y = 6$, $d_{sep} = 3$

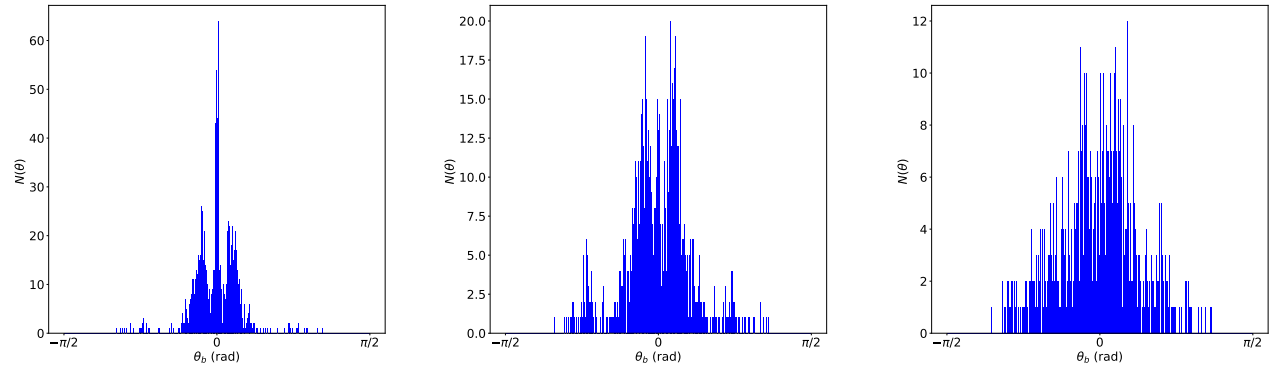

(a) $T = 0.01$ (b) $T = 0.02$ (c) $T = 0.05$

Figure 7.14: Type II distribution: $\sigma_2 = 5.75$, $L_y = 6$, $d_{sep} = 3$

The Type I angular distributions are of the same form as already seen for $d_{sep} = 0$ convex case, after accounting for possible correlations arising from any particle tailback caused by Type II blockages. In every geometry presented, increasing the temperature has the repeated effect of spreading the distribution of θ_b, and reducing its peak value, with the notable exception at Fig. 7.12 b, where increasing the temperature from $T = 0.01$ to 0.02, causes the peak of the distribution to increase three-fold, in an apparent 'freezing by heating' phenomenon, this may be a characteristic only found at the geometries that case the singular reduction in the system's average velocity.

Every θ_b distribution shown, displays a single peak with a maximum at $\theta_b = 0$, with the exception of the Type II blocking angle distributions at $\sigma_2 = 5.75$, $L_y = 6$, $d_{sep} = 3$. Here, three peaks are observed that clearly correspond to metastable arch formation induced by the dispersive and focussing elements of the modified constriction, that nonetheless disappears with increasing temperature.

CHAPTER
8

DISCUSSION

8.1 Importance of geometrical detail

The clogging phenomena that served as the mechanism leading to the intermittent flow observed in this system, are clearly of geometrical origin, as there are no inter-particle nor particle-wall frictional force. Decreasing the noise term caused the appearance of multiple parameter regimes, in which the mean velocity followed a non-monotonic evolution with constriction width, indicating when closing is more likely to happen. Increasing the contribution of the stochastic term reduces this likelihood, without eliminating it. The distribution of cascade times were measured, and shown to be exponential. Increasing the temperature reduced the cascade size, in agreement with [157] , while also increasing the number of cascade size peaks.

This chapter considered possible geometries in a somewhat course grained manner by, for example, only considering integer values of d_{sep}. We expect that the observed non-intuitive behaviour is also present for non-integer values of d_{sep}, though the complex behaviour makes it unlikely that a single universal relation between the constriction geometry and observable dynamical features could be easily observed. We have studied particle flow through single and double constrictions and have identified a novel blocking mechanism that leads to non-intuitive phenomena such as singular reductions of the mean particle velocity, indicating the presence of strongly intermittent dynamics. While increasing the temperature reduces this effect, some geometries are more 'robust' than others in retaining their intermittent character.

While most studies concerning the formation of arches and other blocking phenomena rely on the presence of frictional forces, this chapter demonstrates that, even in the absence of said forces, the geometrical detail of the constriction, especially in the double constriction case, plays a major role in the formation of arches that lead to intermittent dynamics. This poses the question relating to which geometrical conditions promote the the stability of the structures, which, as Fig. 7.9 demonstrates, is variable. i.e. Some structures are more likely to persist at higher temperatures than others.

These results suggest the presence of a geometrical phenomenon that is inverse to that shown by the presence of an obstacle upstream of the outlet of a flow. The upstream obstacle strongly reduced the occurrence of blockage, which may reduce or eliminate clogging in silos [43], panic escape [154], and even the flow of sheep [153]. However, in the work presented here, the introduction of the second pair of obstacles serves to increase the likelihood of blockage by the creation of spaces within which metastable arches may form.

8.2 Overview of results

The second part of this thesis studied a single channel permitting the flow of a set of soft $2D$ disks, of diameter $\sigma_1 = 1$, driven through a well defined geometrical narrowing, *via* Brownian dynamics simulation. The narrowing was initial defined by the placement of two stationary particles of diameter σ_2.

Regions of particle stiffness and channel geometry were identified where the average velocity of the system behaves non-monotonically, in the low temperature (near-ballistic) regime, signalling conditions for clogging-induced intermittency. Cascade size and inter-time distributions were collected, and were both shown to follow exponential distributions. The cascades were then further characterised by counting the number of particles that pass over a slice of the channel geometry, per unit time. To further understand the source of intermittency, a new observable was introduced, as the angular distribution of the axis passing through the pair of blocking particles.

The geometrical constriction was then modified to form four overlapping fixed particles, thus creating a boundary with both dispersive and focussing elements. The system's global velocity, cascade size and time statistics, and angular distribution of blocking were again taken, showing parameter values where the system's average velocity decreases in a singular fashion, which had not been seen before. The relationship between the non-monotonic evolution of the average global velocity and some specific channel geometries were also studied under increasing temperature. Some geometrical regions where consequently shown to have a more 'robust' non-monotonic effect on the system's average velocity than others. Finally, the distributions of blocking angle, θ_b, were taken for specially chosen geometries, that either do, or do not case a singular reduction in the system's global velocity.

8.3 Outlook

The current Brownian dynamics simulation does not account for the hydrodynamic effect in narrow channels. A direction for future research might, therefore be, to include the hydrodynamic interactions of a particle in the system with all the other particles. As our system is geometrically confined, the hydrodynamic interactions of a particle with its own image, and with the images of the other particles in the system, would have to be included. This is motivated by observed scattered and bound states of hydrodynamically coupled particles in narrow channels [158], whose effects have already been explored for *Volvox* algae colonies (Volvocine algae may be used to study collective dynamics of self-propelled objects [**dancing**]).

To include hydrodynamic interactions in a 2D domain, the 'Ermak McCammon' scheme [159] could be applied, where the displacement of the particle's centre of mass position is given by:

$$\Delta X_i(\Delta t) = \sum_j^N \frac{D_{ij}F_j}{k_bT}\Delta t + \sum_j^N \frac{\partial D_{ij}}{\partial r_j}\Delta t + R_i(\Delta t) \tag{8.1}$$

D_{ij} is a $dN \times dN$ diffusion tensor which couples the N particles and their d translational degrees of freedom, and is directly applied to external forces. The hydrodynamically correlated random displacements $R_i(\Delta t)$ are described by:

$$< R_i(\Delta t) >= 0 \qquad < R_i(\Delta t)R_j(\Delta t) >= 2D_{ij}\Delta t. \tag{8.2}$$

For N identical circular particles, of radius σ_1, choices for the diffusion tensor may either be the Onseen tensor or the Rotne-Prager-Yamakawa tensors [160]. Ref [161] provides steps towards generalising to both systems of

particles of differing radii as well as systems of non-circular particles. The work reviewed uses the latter, which consists of the following $d \times d$ submatrices D_{ij}:

$$D_{ii} = \frac{k_b T}{6\pi\eta\sigma_1} I, \tag{8.3}$$

$$D_{ij} = \frac{k_b T}{8\pi\eta r_i j}\left[(I + \vec{r}_{ij} \otimes \vec{r}_{ij}) + \frac{2\sigma_1^2}{3r_{ij}^2}(I - 3\vec{r}_{ij} \otimes \vec{r}_{ij})\right] \quad i \neq j \;\; \& \; r_{ij} \geq 2\sigma_1. \tag{8.4}$$

$$D_{ij} = \frac{k_b T}{6\pi\eta\sigma_1}\left[\left(1 - \frac{9r_{ij}}{32\sigma_1}\vec{r}_{ij}\right) I + \frac{3r_{ij}}{32\sigma_1}\vec{r}_{ij} \otimes \vec{r}_{ij}\right] \quad i \neq j \;\; \& \; r_{ij} < 2\sigma_1. \tag{8.5}$$

The entire tensor is positive definite for all particle configurations. To obtain the random motion, as presented in Eq. 8.2, $\mathbf{B}$ is defined such that $\mathbf{D} = \mathbf{B}\mathbf{B}^T$. The method employed by Ermack and McCammon applies Cholesky factorisation to return $\mathbf{B}$ as a triangular matrix. The random motion is then resolved as $\vec{R} = B\vec{X}$. Unfortunately, this results in a computational procedure whose complexity scales as $\mathcal{O}(N^3)$. Alternative methods proposed a Chebyshev approximation [162], whose runtime scales as $\mathcal{O}(N^{2.5})$, and a further approximation, that employs the so called 'truncated expansion ansatz', scales as $\mathcal{O}(N^2)$ [163].

Part III

The Iris Billiard

CHAPTER
9

INTRODUCTION

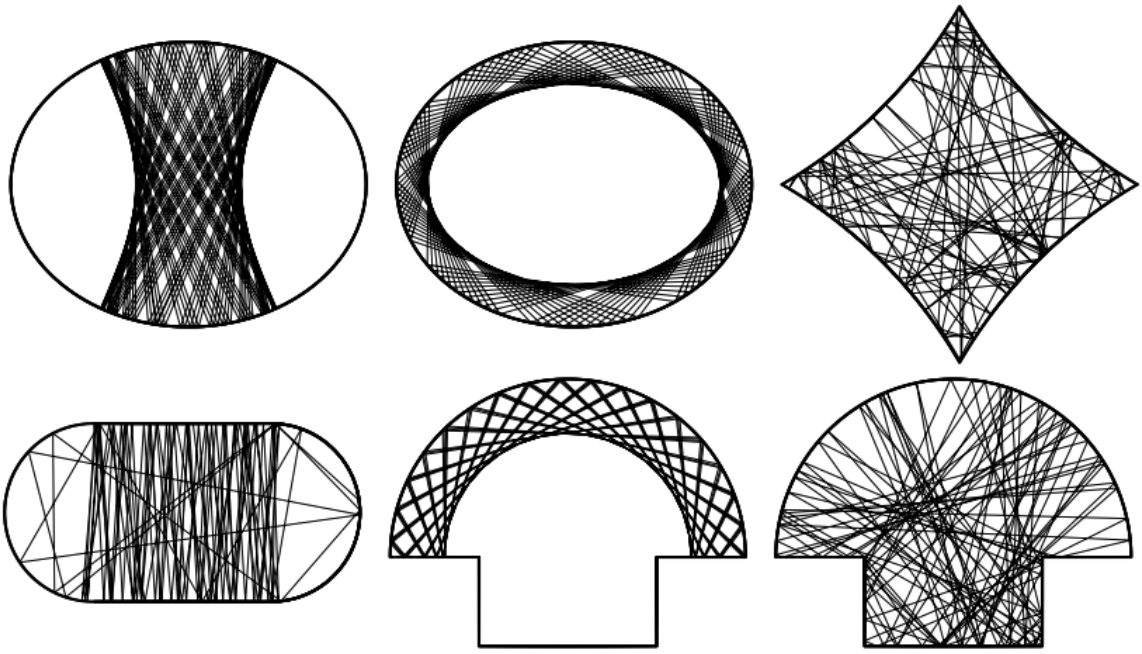

Figure 9.1: Geometry vs. dynamics [164]. An integrable elliptical billiard (top left and centre) has two types of regular motion depending on the initial condition, a dispersing diamond (top right) is chaotic, a defocusing stadium (bottom left) is intermittent, with orbits switching between regular and chaotic motion, and a mushroom (bottom centre and right) is mixed, with regular or chaotic motion depending on the initial condition. Apart from the ellipse, all these are constructed from circular arcs and straight lines; many other examples with more subtle dynamical distinctions exist. Figure courtesy of Carl Dettmann

The third and final part of this thesis will study dynamical chaos arising from a conservative Hamiltonian system, which, unlike the previous models studied, contains no statistical hypothesis [42]. Despite every aspect of these sorts of systems being deducible from their laws of evolution, deterministic randomness is nonetheless typical for a minimal number of degrees of freedom (> 1), and even familiar statistical properties may be recovered in special ergodic cases [165]. Throughout this thesis, fluctuation has been a key, repeatedly employed, statistical behaviour. However, it is well known that chaotic motion is a generator of noise that is purely intrinsic by definition

of the dynamical system. Examples where chaotic motion is retrieved include perturbed Kepler motion, which is a particular case of the famous three body problem. The motion of the comet Halley, perturbed by Jupiter, was found to be chaotic with an estimated lifetime in the solar system of the order of ten million years [166]. Another example of chaotic dynamics is found in the case of a charged particle confined in an adiabatic magnetic trap [167].

Our goal is to better understand the fundamental connection between geometry and chaotic dynamics, by studying a $2D$ billiard. These [168] are Hamiltonian systems in which a point particle freely moves within a compact, planar, Euclidean domain, whose motion is governed by the Hamiltonian:

$$H(q,p) = \begin{cases} p^2/2, & q \in B/\partial B. \\ \infty, & q \in \partial B. \end{cases} \tag{9.1}$$

The speed and mass of the particle can both be assumed to equal unity. The infinite boundary potential causes every collision to be elastic. Therefore, the component of the momentum projected onto the normal of each point of contact changes sign, while the tangential component stays constant. The momentum vector, $\boldsymbol{p}_{i+1}$, after the i^{th} collision at point q_i is:

$$\boldsymbol{p}_{i+1} = \boldsymbol{p}_i - 2[\boldsymbol{p}_i \cdot \hat{\boldsymbol{n}}(\boldsymbol{q}_i)]\hat{\boldsymbol{n}}(\boldsymbol{q}_i). \tag{9.2}$$

$\hat{\boldsymbol{n}}(\boldsymbol{q}_i)$ being the normal of the boundary at each collision. The particle exhibits dynamics that are purely determined by the interplay between its initial conditions and the boundary. These systems exhibit three behaviours: 1) Regular, i.e. periodic or quasiperiodic orbits, as found in circular [169, 170] elliptic [171] or confocal elliptic [172] billiards. 2) Ergodic, with orbits that fill the entire phase space, as found in the Sinai [35], Bunimovich stadium [173] and cardioid [174] billiards. 3) Mixed dynamics, i.e. with coexisting regular and irregular trajectories, as found in the family of limaçon, eccentric annular and mushroom billiards [175, 176].

A billiard phase space is mixed when it contains stable and unstable trajectories. Unstable (chaotic) trajectories have many interesting and unexpected characteristics, such as the existence of dynamical barriers to chaotic transport [177] and quasiregular chaotic motion near regions of stability, otherwise known as 'stickiness' [178–180]. Indeed, there are different varieties of stickiness in billiards that may be distinguished between, as discussed in [181]. 'Internal' stickiness presents in systems with no islands of stability, such as the Bunimovich stadium, or else are due to the presence of marginally unstable periodic orbits (MUPOs) that are completely contained withing the chaotic sea, such as in mushroom billiards [182]. 'External' stickiness, however, arises because of the existence of the boundaries between regular and chaotic regions. Stickiness results in non-exponential decays of both the time-correlation functions and Poincaré recurrence distributions [183–186].

The mathematics of billiard systems may be applied to experiments employing both two and three dimensional geometries that may be either open [169] or closed. Examples include situations where particles or waves are confined to cavities or other homogeneous regions [169] such as waveguides [187], electrons in semiconductors confined by electric potentials [188] and atoms interacting with laser beams [189, 190]. Dynamical tunnelling between classically isolated phase space regions has also been investigated and observed in both desymmetrized mushroom and eccentric annular superconducting microwave resonators [191, 192].

The behaviour of both closed and open systems is crucially determined by their geometry-dependent classical dynamics [169]. Escape rates of open billiards is a characteristic that is both experimentally accessible [190] and important for transport properties of many related systems, such as fractal conductance fluctuations [193, 194]. The billiard setup described may be subject to numerous variations [168], such as including a magnetic field [195], with strength, B, perpendicular to the plane.

9.1 Simple systems

Two related, simple, and well-studied systems are reviewed to provide greater detail and context of the concepts and results presented later.

9.1.1 Circle map

The circle map is the simplest possible $1D$ dynamical system, given by:

$$\mathbf{T} : \theta_{n+1} = \theta_n + \Omega, \quad mod\ 2\pi. \tag{9.3}$$

The time evolution of the circle map is characterised by a quotient of numbers such that: $\Omega_n = 2\pi\omega_1/\omega_2$, that defines the 'frequency' of the system. If rational, i.e. $\omega_1, \omega_2 \in \mathbb{Z}^+$, the orbit closes on itself after a finite number of iterations, i.e. it is periodic. If irrational, the set of points that defines it, $\theta \in [0, 2\pi]$, will fill ergodically as time tends to infinity.

It will be advantageous, at this stage, to distinguish between different categories of irrational number. It is well known that rational approximations of some irrational frequency are obtained through its continued fraction representation [196]:

$$\Omega = a_0 + \frac{1}{a_1 + \frac{1}{a_2 + ..}} = [a_0, a_1, a_2 ...], \tag{9.4}$$

$a_0, a_1, a_2 .. \in \mathbb{Z}^+$ are called partial quotients. Irrational numbers are represented by an infinite sequence of partial quotients, whereas it is finite for rationals. Numbers can be irrational to different degrees, the highest of which is the golden mean, represented by a continued fraction whose partial quotients are all equal to 1, which is an element of the set of noble frequencies, whose partial quotients always end in ones, although the first quotients may be different.

The simple, but little known, Slater's theorem [197] states that for any irrational value of $\Omega/2\pi$, the distribution of return times, τ_i, is at most three, and that the largest is the sum of the other two. This property of rotational quasiperiodic orbits allows for the fast and useful detection of quasiperiodicity from short trajectories. Furthermore, two of the three return times are always consecutive denominators in the continued fraction expression of the irrational Ω. Slater's theorem does not impose any requirement on the size of the recurrence interval, provided that it does not cover the whole trajectory in phase space [186].

9.1.2 Chirikov standard map

The Chirikov standard map is a simple system that presents universal characteristics of generic dynamics when integrable islands of stability are surrounded by a chaotic sea. Systems reducible to the standard map include charged particle confinement in mirror magnetic traps [198], particle dynamics in accelerators [199] and even comet dynamics in the solar system [166, 200]. Its significance is that it serves as a simple model for the Poincaré first return map of an area-preserving Hamiltonian system with two degrees of freedom. The standard map is given, with respect to its phase space coordinates (x, p), as:

$$\mathbf{T} : \begin{cases} x_{n+1} = x_n + p_{n+1} & [\text{ mod } 1], \quad (9.5a) \\ p_{n+1} = p_n - \dfrac{k}{2\pi}\sin(2\pi x_n) & [\text{ mod } 1], \quad (9.5b) \end{cases}$$

where p_{n+1} replaces the Ω used in the 1D circle map and the subindex, n, is the number of iterations. The nonlinear perturbation parameter, k, is a dimensionless constant that determines the extent to which the, otherwise

regular, unperturbed circle map displays chaotic dynamics. Due to the periodicity of sin, the dynamics may be considered as lying on a torus $\mathbb{T} = C \times C$, and may be interpreted as the Poincaré section of a periodically kicked rotor.

The onset of dynamical chaos is due to the destruction of tori (i.e. their cantor-set like transformation to cantori [201]), with increasing perturbation. As a result, chaotic and regular trajectories intermingle. Kolmogorov-Arnold-Moser (KAM) surfaces isolate stochastic layers from each other, forming transport barriers from one region to the other. (See Appendix B, for a discussion of the role of symmetry breaking in the creation of the system's mixed dynamics, and for some example phase portraits.) 'Converse KAM' theory states that no invariant rotational barriers will persist [202, 203] in a sufficiently perturbed area preserving twist map. Some transport barriers are more resistant than others to perturbation, as has been verified in work that numerically determined the frequency of the final destroyed invariant transport barrier for the standard map [204]. The obtained frequency of the final destroyed transport barrier is $\Omega = \gamma$, where γ is the golden mean $(1+\sqrt{5})/2 = [1;1,1,1...]$, which is destroyed at $k = 0.971635...$ [205]. The standard map may be given as a composition of two involutions, which was used to identify periodic orbits. Appendix B examines this decomposition and the repeated application of the involutions to identify fixed points within the standard map phase space for different values of k.

9.2 Iris Billiard geometry

The Iris Billiard is defined as a central scattering ellipse, with tunable axes, enclosed by a unit circle. When the ellipse degenerates to a circle, the system is integrable, and the system consequently displays dynamics that are equivalent to the circle map, introduced in Section 9.1.1.

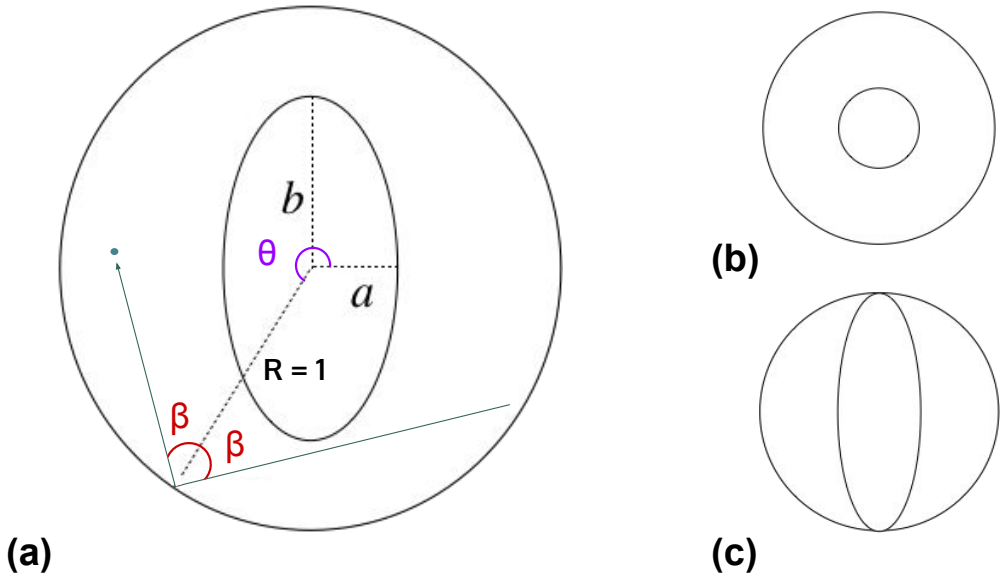

Figure 9.2: The Iris Billiard. (a) Generic configuration: $a \neq b$ (b) Limiting case $a = b$, which forms an annulus. (c) Case $b = 1$, which forms two separate crescents $a \in (0,1]$. Orientation, θ and reflection angle β are shown.

The billiard domain, $B \subset R^2$, has a two-part, continuous, boundary. The initial conditions of a given trajectory are defined by the arc length distance $s = \theta \in (-\pi, \pi]$ along the outer circular boundary, and the initial direction of motion, described by the angle between the initial velocity and the center-facing normal to the outer boundary, $\beta \in (-\pi/2, \pi/2]$. At any instant the point particle, mass $m = 1$, is described by its position, $q \in B$, and momentum, $|p| = 1$.

9.2.1 Ellipse geometry

An ellipse is the locus of points with cartesian coordinates (x,y) following the equation:

$$\frac{x^2}{a^2}+\frac{y^2}{b^2}=1. \tag{9.6}$$

$b,a\in\mathbb{R}$ are, respectively, the semi-major, and minor axes, ($b\in(0,1]$ and $a\in(0,b]$). If $a=b$, the ellipse reduces to a circle. If $a=0$, then the ellipse reduces to a line of length $2b$. The elongation, $e=b/a$, is used as a measure of the degree of the ellipse's eccentricity, and therefore the degree to which the system's symmetry is broken. Rewriting Eq.(9.6) in polar coordinates (ρ,θ) returns:

$$\rho(\theta,e,a)=\frac{a\,e}{\sqrt{e^2\cos^2\theta+\sin^2\theta}}, \tag{9.7}$$

The symmetry of the ellipse means that for a given geometry, $\rho(\theta)=\rho(-\theta)=\rho(\theta\pm\pi)$. When $e=1$, the system is totally symmetric, and integrable, by conservation of angular momentum, and so reduces to the 1D circle map. For $e>1$, the ellipse acts as a non-linear perturbation on the 1D circle map, but much more complex nature than that applied to the standard map.

9.3 Symbolic representation of Iris dynamics

We represent the dynamics by a course grained partition of the state space, namely collisions with the (inner) ellipse **E** and the (outer) circle **C**. Thereby creating a finite alphabet $A=\{\mathbf{E},\mathbf{C}\}$. The following diagram shows a state diagram of the flow of both systems:

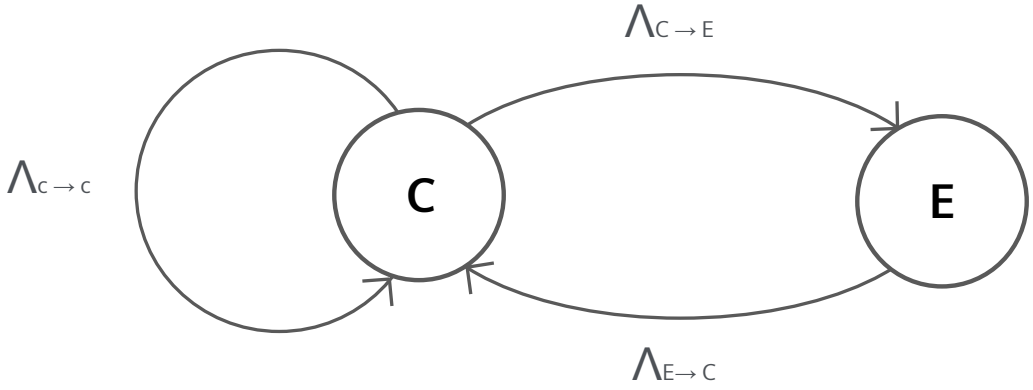

Figure 9.3: Symbolic flow diagram representation of billiard dynamics with finite state space partition.

The resulting symbolic trajectories are a projection (not a substitution) of the true trajectory onto a discrete partition of the phase space at discrete instants of time. Given the dispersive nature of the inner boundary, $\Lambda_{E\to C}=1$ for *all* geometries, i.e. there are no consecutive **E**s [1]. Two types of trajectory exist: those that never hit the central

[1] which corresponds to the definition of the *Golden Mean vertex shift*.

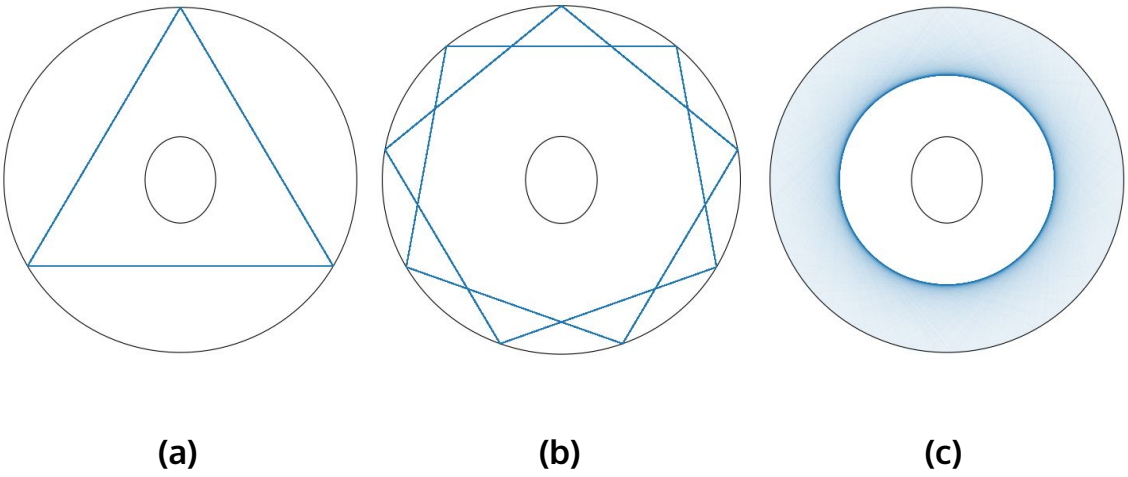

Figure 9.4: A selection of regular, circle map, trajectories. a) A periodic orbit with frequency $\omega_1/\omega_2 = 1/3$. b) A periodic orbit with frequency $\omega_1/\omega_2 = 2/9$. c) A rotational quasiperiodic orbit with frequency $\omega_1/\omega_2 = 1/\sqrt{2}$ that would densely fill the annulus if allowed to run for infinite time. All trajectories were generated with 10^4 collisions, and may be directly associated with the $1D$ circle map studied in Section 9.1.1.

ellipse and those that do. The first type, illustrated by Fig. 9.4, would be represented as a bi-infinite sequence of outer circle collisions:

$$\boldsymbol{T} = [..,c_i,c_{i+1},c_{i+2},c_{i+3},c_{i+4},c_{i+5},c_{i+6},....]. \tag{9.8}$$

These trajectories correspond to the dynamics already studied for the unperturbed circle map, and, in the quiasiperiodic case, are most simply characterised by a β that obeys the following tangency condition:

$$\beta \geq \beta_c = \arcsin b. \tag{9.9}$$

b is the radius of the inaccessible circular region, defined by a caustic edge, as seen in Fig 9.4c . The trajectories are regular, i.e. either periodic or quasiperiodic, with constant β, and reduce back to the 1D circle map, introduced in 9.1.1 such that:

$$\theta_{n+1} = \theta_n + \Omega \mod 2\pi, \text{ with } \Omega = \pi - 2\beta. \tag{9.10}$$

However, if the tangency condition is not satisfied, some rational ω_1/ω_2 circle map orbits may continue to exist over a finite range of geometries. A rational ω_1/ω_2 orbit, where $\omega_1 < \omega_2$, defines a ω_2 polygon, whose radius of intersection of the enclosed caustic formed by its rotation through $\theta \in [0,2\pi]$ follows:

$$r_{\omega_1,\omega_2} = \left|\cos\left(\frac{\omega_1\pi}{\omega_2}\right)\right|. \tag{9.11}$$

Considering the parametric form of the ellipse, and applying simple geometric arguments returns the following condition for intersection,

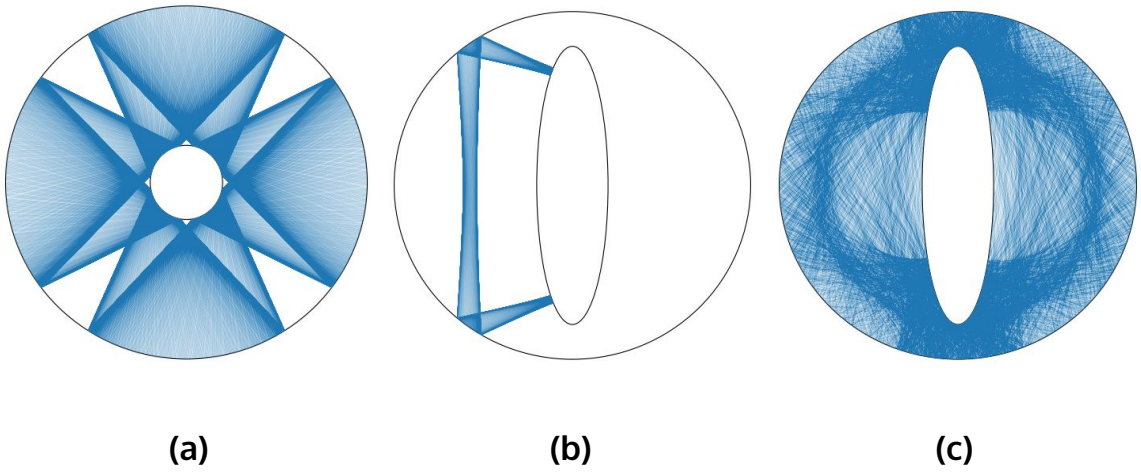

Figure 9.5: A selection of orbits that collide with the ellipse. a) $a = 0.2, e = 1.05$. Perturbed rotational $\Omega = 1/\sqrt{(5)}$ Quasiperiodic orbit b) $a = 0.2, e = 4$. Perturbed librational quasiperiodic orbit: launched from initial conditions: $\theta = 2.48, \beta = 0.577$. Librational orbits reverse direction, rotational orbits don't. c) $a = 0.2, e = 4$. Chaotic orbit. All trajectories were generated with 10^4 collisions.

$$b^2 \sin^2\theta + a^2 \cos^2\theta - r^2_{\omega_1,\omega_2} \geq 0, \tag{9.12}$$

which is true for all values of θ *iff* $r^2_{\omega_1,\omega_2} \leq a^2$. Conversely, there are no intersections for any value of θ when $r^2_{\omega_1,\omega_2} \geq b^2$. In the regime $a^2 \leq r^2_{\omega_1,\omega_2} \leq b^2$, the following must be solved to determine if there's an intersection:

$$b^2 \sin^2\theta + a^2 \cos^2\theta - r^2_{\omega_1,\omega_2} = 0, \tag{9.13}$$

returning:

$$\sin^2\theta = \frac{r^2_{\omega_1,\omega_2} - a^2}{b^2 - a^2}. \tag{9.14}$$

Therefore the conditions for intersection with the inner ellipse are therefore met by:

$$|\theta - \pi/2| \leq \arccos\sqrt{\frac{r^2_{\omega_1,\omega_2} - a^2}{b^2 - a^2}}, \tag{9.15}$$

or, by the symmetry of the system,

$$|\theta - 3\pi/2| \leq \arccos\sqrt{\frac{r^2_{\omega_1,\omega_2} - a^2}{b^2 - a^2}}, \tag{9.16}$$

In order for a rational ω_1/ω_2 orbit to exist, one must avoid intersections for all $\theta + 2\pi n/\omega_2 \ \ \forall n \in [0,..,\omega_2 - 1]$. Therefore, the following condition must be met:

$$\arccos\sqrt{\frac{r_{\omega_1,\omega_2}^2-a^2}{b^2-a^2}} < \frac{\pi}{\kappa(\omega_2)\,\omega_2}\,,\quad \omega_2 \in \{3,4,5...\} \tag{9.17}$$

where:

$$\kappa(\omega_2) = 1+\omega_2 \bmod 2. \tag{9.18}$$

Equation (9.17) may be finally rearranged to give:

$$\frac{b}{a} \geq e_{min} = \left[\frac{1}{\cos^2(\pi/\kappa(\omega_2)\,\omega_2)}\left(\frac{r_{\omega_1,\omega_2}^2}{a^2}-1\right)+1\right]^{1/2}. \tag{9.19}$$

fixing ω_1 at some value and taking the limit $\omega_2 \to \infty$ returns, for both cases, the limit:

$$\lim_{\omega_2\to\infty} e_{min} = 1/a. \tag{9.20}$$

On the contrary, the maximum value of e, at which a collision *must* happen follows:

$$e_{max} = r_{\omega_1,\omega_2}/a. \tag{9.21}$$

and so approaches the same limit as e_{min}.

The second type of trajectory that involves collisions with the ellipse which, as illustrated by Fig. 9.5, results in rotational and librational periodic and quasiperiodic orbits (i.e. $\beta \neq constant$) as well as chaotic orbits. Figure 9.5 (b) is an example of a librational orbit. These differ from rotational orbits, shown in Fig. 9.4, and Fig. 9.5 (a) in that they change direction, which may be interpreted as time reversal. Both rotational and librational orbits are possible for trajectories that interact with the ellipse. The trajectories shown in Figures 9.5 (a) and (b) may also be represented by the following different ordered bi-infinite symbolic codes :

$$\boldsymbol{T} = [..,c_i,e_{i+1},c_{i+2},e_{i+3},c_{i+4},e_{i+5},c_{i+6},e_{i+7},c_{i+8},e_{i+9}...], \tag{9.22}$$

and

$$\boldsymbol{T} = [..,c_i,c_{i+1},e_{i+2},c_{i+3},c_{i+4},e_{i+5},c_{i+6},c_{i+7},e_{i+8},c_{i+9}...], \tag{9.23}$$

respectively. *A priori* it is reasonable to expect that a chaotic orbit, launched at random within the chaotic phase space, as shown in Fig. 9.5c, will follow a disordered symbolic codification. The following sections show that there is an uncountable number of ordered sequences that both stable and unstable, periodic or quasiperiodic trajectories could follow. To better understand how the interaction with the central ellipse may give rise to chaotic motion, we must first perform a linear stability analysis for the simplest period-two orbits along the axes of symmetry of the ellipse.

9.4 Linear stability analysis: Geometrical derivation

The main condition for dynamical chaos is a strong local instability of motion, i.e. whether or not the long time motion is sensitive to minute changes in the initial condition [36]. The initial conditions may be changed in four ways:

1) A displacement along the initial direction of the particle's trajectory, $r_{||}$.

2) A displacement perpendicular to the initial direction of the particle's trajectory, $r_{\perp_0}$.

3) An increase in magnitude of the particle's initial momentum.

4) A change in direction in the initial momentum, $\delta\beta_0$.

Changes 1 and 3 have no effect on the system as they only serve to displace the particle along its preset trajectory, or to run through said trajectory at a different velocity, respectively. However, changes 2 and 4 have non-trivial effects on the overall trajectory. Let $\binom{r_\perp}{\delta\beta}$ denote the change to a trajectory subject to a change in initial condition which combines small shifts perpendicular to the trajectory $r\perp_0$, and shifts in the initial angle β_0.

9.4.1 Straight lines

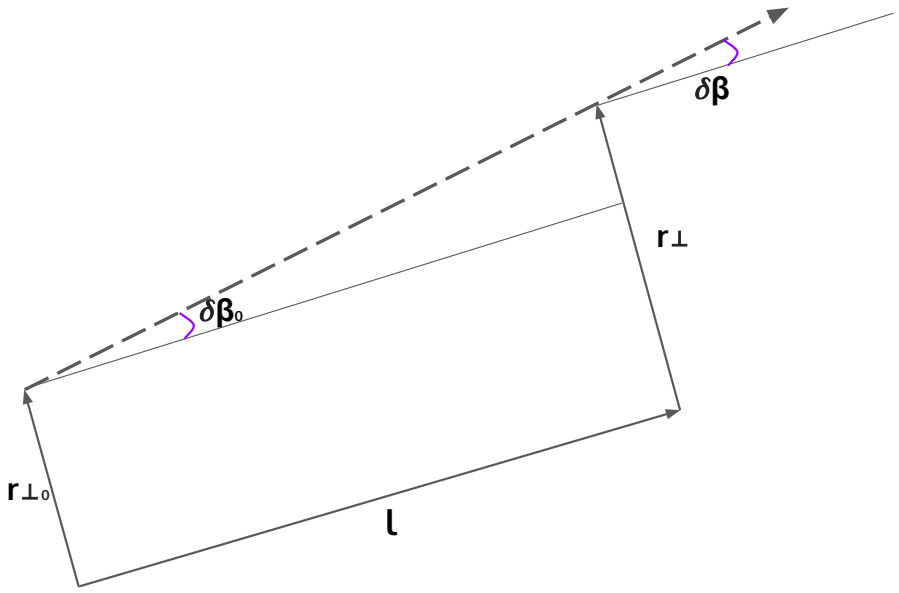

Figure 9.6: Initial deviations $r_{\perp_0}$ and $\delta\beta_0$, and final deviations $r_\perp$ and β for a straight line of length l.

Considering a straight line segment of length, l, along this path the perpendicular deviation increases by $\lim_{\delta\beta_0\to 0}\tan\delta\beta_0 l \to l\delta\beta_0$. $r_\perp$ can be approximated by $r_{\perp_0} + l\delta\beta_0$.

Since in a straight line, the direction never changes, $\delta\beta = \delta\beta_0$. The resulting change to a straight line trajectory may be finally described in matrix form by:

$$\begin{pmatrix} r_\perp \\ \delta\beta \end{pmatrix} = \mathbf{L}\begin{pmatrix} r_{\perp_0} \\ \beta_0 \end{pmatrix} \quad , \quad \mathbf{L} \approx \begin{pmatrix} 1 & l \\ 0 & 1 \end{pmatrix} \tag{9.24}$$

This equation is an approximation to the leading order in $r_{\perp_0}$ and $\delta\beta_0$.

9.4.2 Reflections

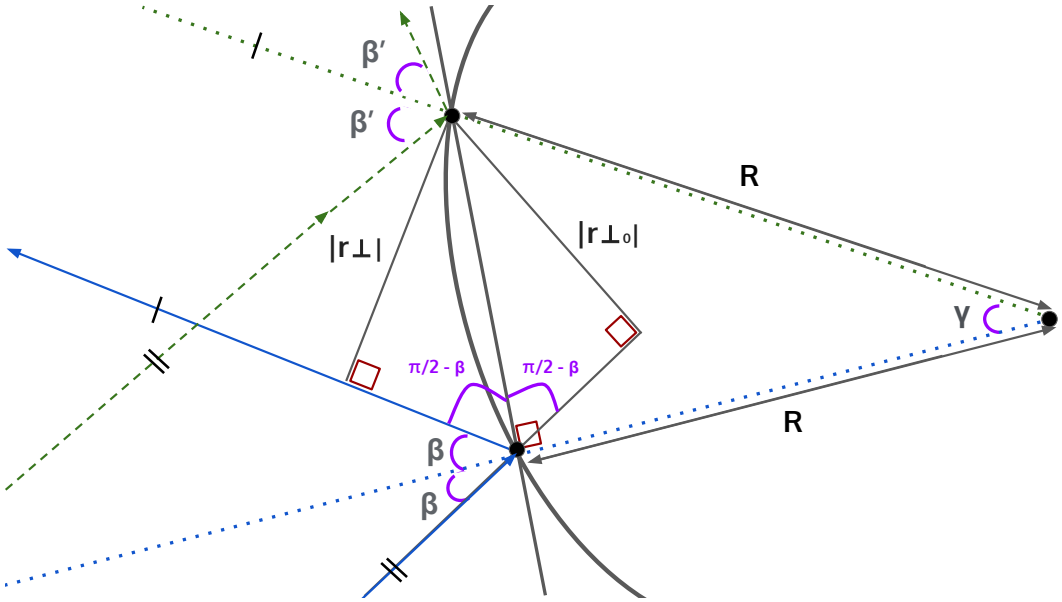

Figure 9.7: Initial deviations and final deviations for a reflection on a curve, approximated as a circle of radius R.

We study reflections at a boundary that may be locally approximated by a circle. (The radius of that circle, R, is the radius of curvature of the boundary at that point). The centre of the circle is assumed to lie outside the billiard, i.e. it is dispersive. The trajectory is reflected from the circle with an angle of incidence and reflection of β, as shown in Fig. 9.7. To understand the effect of applying deviations $r_{\perp_0}$ and $\delta\beta_0$ to the trajectory after a reflection, we compare the original trajectory to a slightly changed path, with angles of incidence and reflection, β'. The angle difference between the two trajectories is denoted $\delta\beta_0$ before the reflection, and $\delta\beta$ after. Similarly, the perpendicular separation before the reflection is denoted $r_{\perp_0}$,and $r_\perp$ for after.

As we are only interested in an approximation for small deviations $r_{\perp_0}$, we are not concerned if this is taken perpendicular to the original or changed trajectory.

We treat the two reflection points as being close enough to approximate the part of the circle between them by a straight line.

The two constructed triangles in Fig. 9.7 are, therefore, similar, as they share one side, both contain one right angle and angle, β. Hence $|r_{\perp_0}| = |r_\perp|$. The directions of the perpendicular deviations are, however, opposite, i.e

$$r_{\perp_0} = -r_\perp. \tag{9.25}$$

To determine $\delta\beta$ with respect to $r_{\perp_0}$ and $\delta\beta_0$, we must first observe that the line, approximating the distance between the two reflection points has length $r_{\perp_0}/\cos\beta$. Therefore, the angle γ in the figure can be approximated by by

$$\gamma \approx \frac{r_{\perp_0}}{R\cos\beta}. \tag{9.26}$$

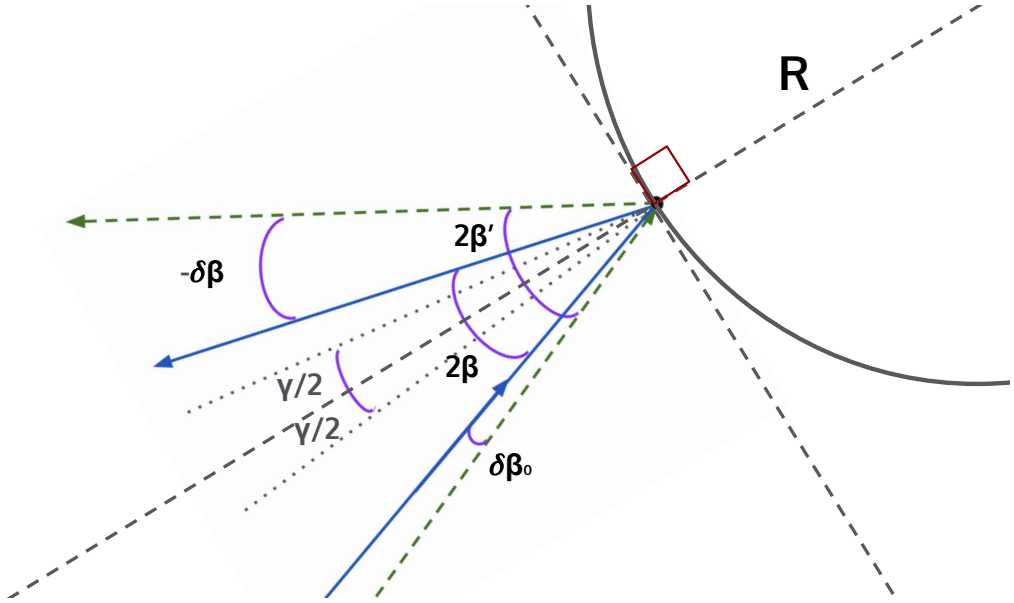

Figure 9.8: Angles involved in a reflection.

In order to relate $\delta\beta_0$, $\delta\beta$, β, β', and γ, we consider Fig. 9.8, where the three points, as marked in Fig. 9.7, are overlayed. The angle between the two incoming trajectories must be $\delta\beta_0$ by definition. The sign is made positive as the incoming line of the changed trajectory is further to the left than the original. The angle between the outgoing trajectories is, therefore related to $\delta\beta$, however a minus sign must be included as the changed trajectory is now deviated to the right of the original. From Fig. 9.7, we may now write the following relation:

$$-\delta\beta = \beta' - (\beta - \gamma), \tag{9.27}$$

Using that the lower angle β' is a sum of $\delta\beta_0$, β and γ

$$= \overbrace{(\delta\beta_0 + \beta + \gamma)}^{\beta'} - (\beta - \gamma), \tag{9.28}$$

$$= \delta\beta_0 + 2\gamma, \tag{9.29}$$

which upon substituting Eq. 9.26 returns:

$$\approx \beta_0 + \frac{2}{R\cos\beta} r_{\perp_0}. \tag{9.30}$$

Finally, writing both Eqs. 9.30 & 9.25 in matrix form allows the description of a resulting change to a reflection, after an initial deviation, as:

$$\begin{pmatrix} r_\perp \\ \delta\beta \end{pmatrix} = \mathbf{C}\begin{pmatrix} r_{\perp_0} \\ \delta\beta_0 \end{pmatrix} \quad , \quad \mathbf{C} \approx \begin{pmatrix} -1 & 0 \\ \frac{-2}{Rcos\beta} & -1 \end{pmatrix}\begin{pmatrix} r_{\perp_0} \\ \delta\beta_0 \end{pmatrix} \tag{9.31}$$

R is the radius of curvature of the circle that locally approximates the curvature of the boundary (positive if dispersive, negative if focusing, ∞ if straight). β is the angle between the incoming trajectory and the normal of the boundary.

9.4.3 Trajectories with several reflections and straight lines

A trajectory consists of an ensemble of alternating straight lines and reflections. To describe the effect of changing the initial conditions on the trajectory as a whole, we construct a stability matrix, which is the product of all the straight line and reflection matrices derived in Sections 9.4.1 & 9.4.2, that make up the entire trajectory of n straight lines and n reflections:

$$\begin{pmatrix} r_\perp \\ \delta\beta \end{pmatrix} = \mathbf{M}_n\begin{pmatrix} r_{\perp_0} \\ \delta\beta_0 \end{pmatrix}, \quad \mathbf{M}_n = \prod^{n}\begin{pmatrix} 1 & l_n \\ 0 & 1 \end{pmatrix} \cdot \begin{pmatrix} -1 & 0 \\ \frac{-2}{R_n cos\beta_n} & -1 \end{pmatrix}. \tag{9.32}$$

From now on, β_n describes the angle from the normal of the n^{th} collision with the boundary. As $det|\mathbf{L}| = det|\mathbf{C}| = 1$, the determinant of the stability matrix is also equal to 1. Therefore, the eigenvalues of the stability matrix are related by $m_1 m_2 = 1$. As $Tr(\mathbf{M}) = m_1 + m_2$, the following is true:

$$m_{1,2} = \frac{1}{2}\left(Tr(\mathbf{M}_n) \pm \sqrt{Tr(\mathbf{M}_n)^2 - 4}\right) \tag{9.33}$$

$|Tr(\mathbf{M}_n)| < 2$: Stable case

The eigenvalues of the stability matrix are complex and conjugate (as are the associated eigenvectors), i.e.

$$\mathbf{M}_n u_1 = e^{i\phi} u_1 \tag{9.34}$$

$$\mathbf{M}_n u_1^* = e^{-i\phi} u_1^* \tag{9.35}$$

To understand the effect on the total deviation of the trajectory, the initial deviation, $\binom{r_{\perp_0}}{\delta\beta_0}$, is split into components along the real and imaginary basis of the eigenvector u_1 which are $Re(u_1)$, $-Im(u_1) \in R^2$ respectively, with components a_0 and b_0. The initial deviation may now be written as:

$$a_0 Re(u_1) - b_0 Im(u_1), \tag{9.36}$$

Rewriting the initial deviation as $z_0 = a_0 + ib_0$,

$$= Re(z_0)Re(u_1) - Im(z_0)Im(u_1) = Re(z_0 u_1). \tag{9.37}$$

The deviation at the end of the trajectory may be similarly written as:

$$aRe(u_1) - bIm(u_1) = Re(zu_1) = \mathbf{M}_n Re(z_0 u_1) = Re(z_0 \mathbf{M}_n u_1). \tag{9.38}$$

Applying the eigenvalue equation above therefore shows:

$$z = e^{i\phi} z_0, \tag{9.39}$$

i.e. any initial deviation is rotated in the complex plane, spanned by $Re(u_1), Im(u_1)$, but neither increases nor decreases.

$|Tr(\mathbf{M}_n)| = 2$: Marginally stable case

$$m_{1,2} = \frac{1}{2} Tr(\mathbf{M}_n) = \pm 1 \tag{9.40}$$

The deviation between two slightly displaced trajectories remains the same, or flips signs. This can be found in many integrable systems, such as the rectangular or circular billiard.

$|Tr(\mathbf{M}_n)| > 2$: Unstable case

Both m_1 and m_2 take real values, and may be expressed as:

$$m_1 = \pm e^{\lambda_L L} \quad m_2 = \pm e^{-\lambda_L L}. \tag{9.41}$$

L is the length of the trajectory. λ_L is 'Lyapunov's exponent', which characterises the rate of separation of two infinitesimally close trajectories. Note, as one of the eigenvalues is the inverse of the other, one will continue to expand while the other diminishes to zero.

The eigenvalues of the stability matrix $\mathbf{M_n}$, and therefore the properties of the trajectory, depend only upon the trace of $\mathbf{M_n}$. To obtain the analytical properties of the trajectory, its residue, R, as defined by Greene [205], is typically used, where:

$$R = \frac{1}{4}(2 - tr\mathbf{M}_n). \tag{9.42}$$

The values of R, determined by the value of $tr\mathbf{M}_n$, characterise the analytic properties of a trajectory as follows:

$$\begin{cases} R < 0 & \text{Hyperbolic} \\ R = 0, & \text{Marginally stable} \\ 0 < R < 1 & \text{Stable.} \\ R > 1 & \text{Reflection hyperbolic} \end{cases} \tag{9.43}$$

Hyperbolic trajectories correspond to $\mathbf{M}_n$ having real eigenvalues that are positive (or negative in the reflection case). They always undergo significant deviation due to the finite limits of numerical precision. Marginally stable trajectories correspond to eigenvalues of ± 1. The stable case yields complex eigenvalues with magnitude unity. Two stable trajectories, with slightly different initial conditions, undergo a linear deviation over time.

9.5 Stability analysis of period-two orbits

This section will carry out a linear stability analysis on the simplest period-two orbits that make contact with the ellipse. The stability matrix of a period-two orbit, reflecting off the vertex of the semi-minor axis, a, is:

$$\mathbf{M}_2^a = \mathbf{L}_a \cdot \mathbf{C}_\perp \cdot \mathbf{L}_a \cdot \mathbf{E}_a \tag{9.44}$$

where $\mathbf{L}_a$ is the contribution to the stability matrix arising from a straight line, of length $l = 1 - a$, between the inner and outer boundary as derived in Section 9.4.1,

$$\mathbf{L}_a = \begin{pmatrix} 1 & 1-a \\ 0 & 1 \end{pmatrix}, \tag{9.45}$$

The outer circular boundary is defined as having a negative radius of curvature, as it is focusing (the typical convention here is opposite to that normally encountered elsewhere). The resulting contribution to the stability matrix, from Eq. (9.31), is therefore:

$$\mathbf{C}_{\perp} = \begin{pmatrix} -1 & 0 \\ 2 & -1 \end{pmatrix}, \tag{9.46}$$

The radius of curvature at the vertice of the minor axis has the largest dispersive radius of value curvature of b^2/a.

$$\mathbf{E}_a = \begin{pmatrix} -1 & 0 \\ \frac{-2a}{b^2} & -1 \end{pmatrix}. \tag{9.47}$$

Note, that the matrix components reflect that the angle of incidence of the particle on each boundary is zero.

After some calculation, one obtains :

$$\mathbf{M}_2^a = \begin{pmatrix} -\frac{2(a-1)(2a-1)a}{b^2} + 4a - 3 & 2(a-1)\left(\frac{(a-1)a}{b^2} - 1\right) \\ -\frac{2\left(-2a^2+a+b^2\right)}{b^2} & 1 - \frac{2(a-1)a}{b^2} \end{pmatrix} \tag{9.48}$$

with trace:

$$Tr(\mathbf{M}_2^a) = \frac{4b\left(e^2-1\right)}{e^3} + \frac{4}{e^2} - 2. \tag{9.49}$$

where $e = b/a$. $|Tr(\mathbf{M}_2^a)| \leq 2 \quad \forall a, e$. Therefore the residue of the orbit always indicates stability ($0 < R < 1$).

period-two orbit along semi-major axis.

We repeat the above calculation, for a period-two orbit along the semi-major axis (i.e. $l = 1 - b$). The radius of curvature of the ellipse at the point of contact is a^2/b. Upon substitution of the new values, the resulting trace of the stability matrix is:

$$Tr(\mathbf{M}_2^b) = -4b\left(e^2-1\right) + 4e^2 - 2. \tag{9.50}$$

In this case the orbit is always hyperbolic ($R < 0$), except for when the orbit yields marginal stability ($R = 0$) in the limiting cases, $a = b$ and $b = 1$. (If $a = b$, i.e. for a circular inner scatterer, all trajectories from every initial condition are either periodic or quasiperiodic, with conserved angular momentum. If $b = 1$, the system becomes two separate crescents). As time tends to infinity, the stable orbit will continue unchanged; while the unstable orbit will always be knocked off course by inherent numerical imprecision. This important property will be repeatedly exploited in the following sections.

9.6 Phase space

The phase space is a set of points, each of which fully describes the system. For planar billiard systems it is four dimensional, (x, y, v_x, v_y). However, the conservation of energy reduces the dimension by one. It will furthermore be shown that the complete description of an orbit can be shown using a two-dimensional Poincaré phase section. The next section will introduce the Birkhoff coordinates [206], $(\theta, \sin(\beta))$ used to define the section.

9.6.1 Birkhoff coordinates

A Poincaré section requires a surface that is everywhere transversal to the dynamical flow. The outer circle is chosen as the surface, so that θ describes where on the circle the collision occurs. Due to the system's axial symmetry, it can be restricted to the range $\theta \in (-\pi/2, \pi/2]$. $\sin\beta \in (-1,1)$ is the momentum component, at the point of collision, tangential to the boundary. The phase section is created by the repeated application of the Poincaré first return map, which may be written as $f(\theta_n, \sin\beta_n) \to (\theta_{n+1}, \sin\beta_{n+1})$. For the Iris Billiard, the 'twist condition' [203], $\partial\theta_{n+1}/\partial\sin\beta_n \neq 0$, is always satisfied.

9.6.2 Phase section selection

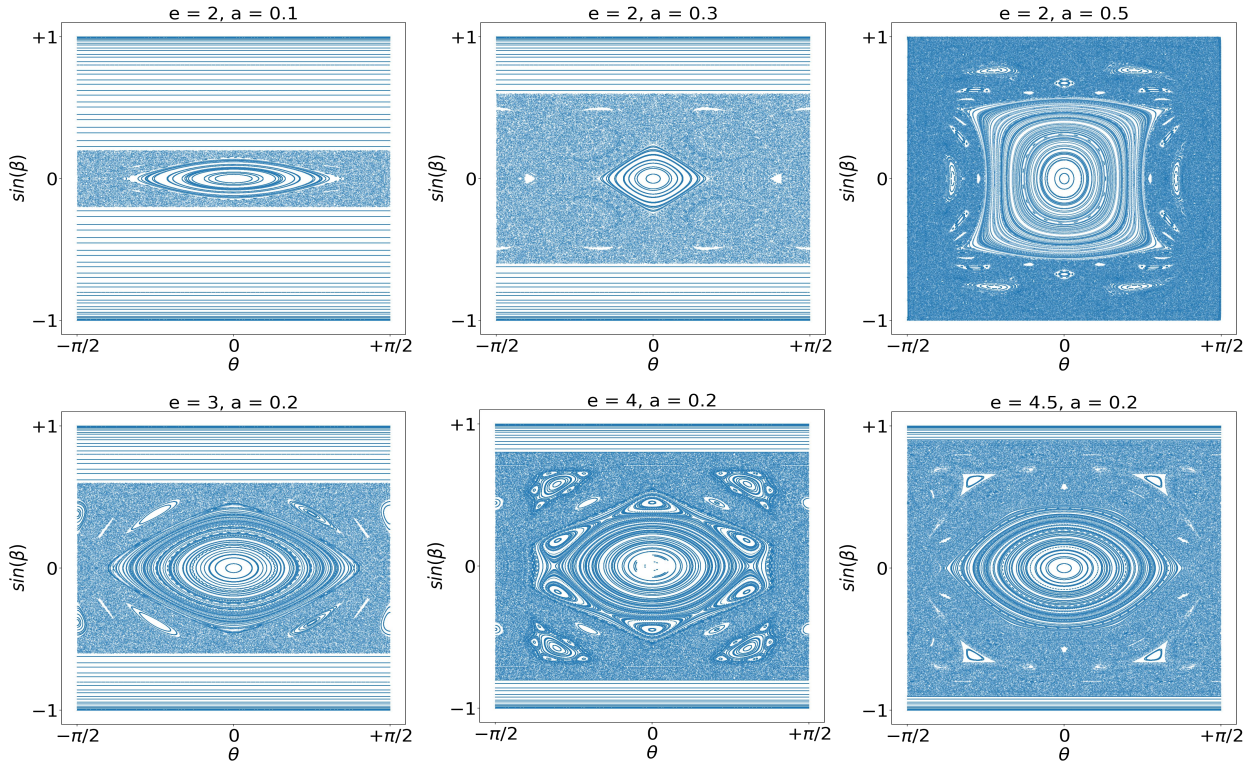

Figure 9.9: A set of complete Poincaré phase sections. Top row: Constant elongation: $e = 2$, for increasing semi-minor axis from left to right. Bottom row: Constant semi-minor axis: $a = 0.2$, for increasing elongation from left to right.

Fig. 9.9 shows a series of sections constructed by trajectories launched from initial conditions spanning $\theta, \beta \in (-\pi/2, \pi/2)$. If the tangency condition, Eq.(9.9), is obeyed, all quasiperiodic trajectories follow the rotational curves above and below the central mixed region, defined by $\beta = constant$. The periodicity in θ makes the phase section topologically an annulus, $\mathbb{S} \times [-1,1]$, unlike the torus for the, previously seen, standard map. Lines corresponding to periodic, but from a disjoint set of initial conditions, and rotational quasiperiodic motion shown in Fig. 9.4, smoothly wind around the annulus. These circles are homotopically non-trivial and are known as 'rotational circles'. Increasing the elongation of the ellipse, e, until the tangency condition, Eq.(9.9), is just violated, causes the trajectory to make contact with the ellipse, therefore deforming the orbit's associated invariant rotational circle in the phase section. The curves often persist with increasing elongation, as predicted by KAM theory, and there is, consequently, no flux of trajectories between the regions partitioned by the deformed circle. As the elongation is further increased the invariant curves are increasingly deformed until a critical value is reached, corresponding to the quasiperiodic frequency of the deformed curve in question. At this point the curve is destroyed. When $\beta < \beta_c$, the phase section displays mixed dynamics. i.e. it is divided into several invariant components.

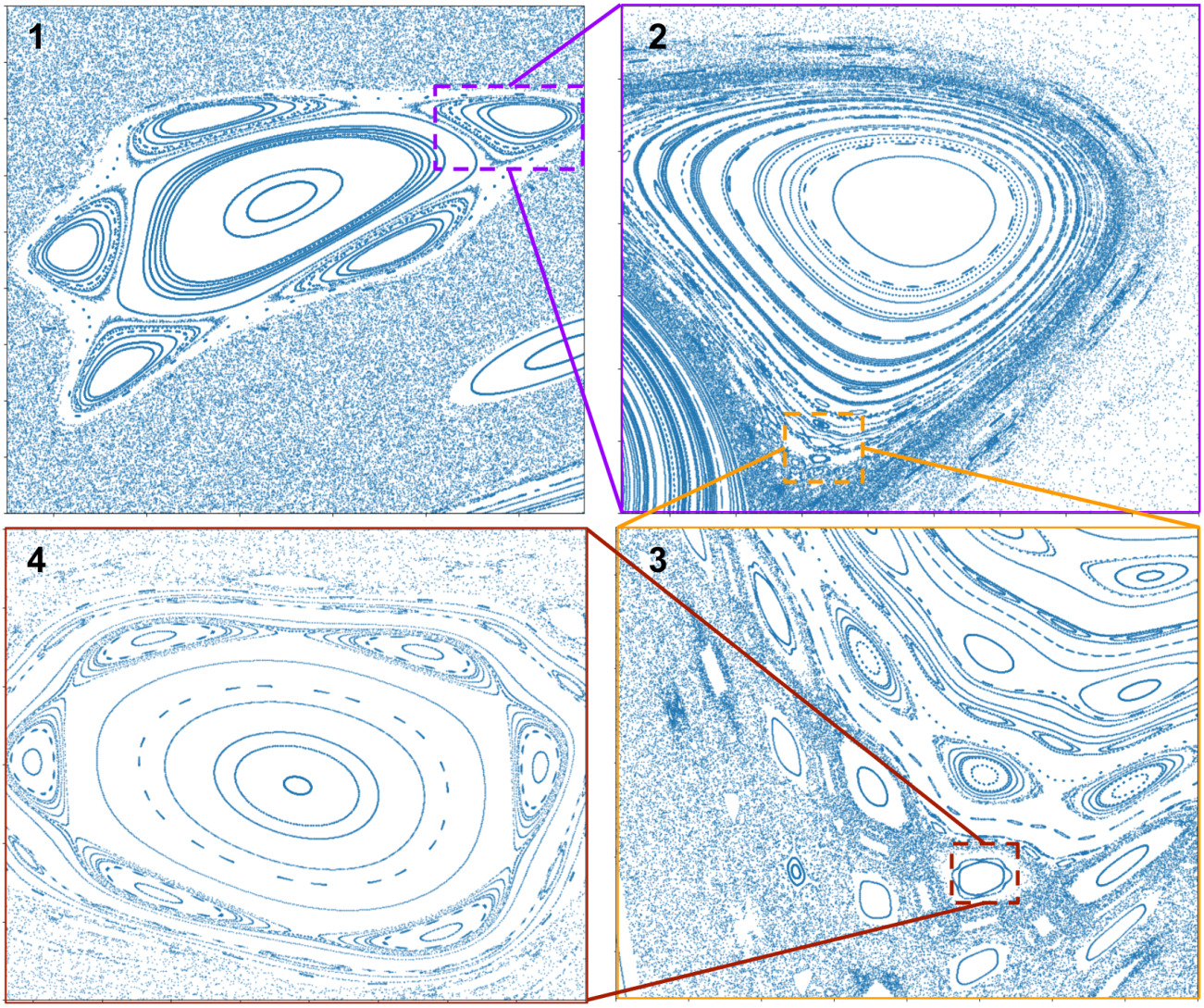

Figure 9.10: 1-4, Successive magnifications of the archipelago seen in the top left of the phase section obtained for $e = 4, a = 0.2$. (Figure 9.9, bottom, centre).

The centre of the billiard phase section, i.e. $\theta = 0, \beta = 0$, or equivalently $\pm\pi$, is an elliptical fixed point for all geometries, corresponding to the stable period-two orbit along the semi-minor axis. Sets of concentric, circles, known as 'liberational circles', representing quasiperiodic motion (as seen, for example, in Fig. 9.5b) bifurcate out of the elliptical period-two orbit, for all geometries, as well as from other geometry-dependent elliptical periodic orbits. It is thought that these curves only cause a limited impediment to the diffusion of chaotic orbits since they do not encircle the entire annulus [205]. Librational circles occur in concentric sets. The outermost circle forms the critical boundary of the 'island of stability', which can be destroyed by an arbitrarily small perturbation. The boundaries between the regular and chaotic components of the phase space exhibit scale invariant structures, as illustrated by Fig. 9.10, in which an island archipelago is magnified indicating where a critical curve used to lie.

The whole phase space can be decomposed into a complicated mixture of domains, with chaotic trajectories coexisting with regular, or periodic ones. These sub-regions are associated with qualitatively distinct dynamical properties. In what follows, we will focus on the properties of the chaotic portion of the phase space.

The hyperbolic period-two orbit along the ellipse semi-major axis is always within the chaotic sea, as Eq 9.5 suggests. (The exception to this is when $e = 1$, i.e. when the system is integrable). Fig. 9.10, provides a deeper view of the scale invariant structures found between the regular and chaotic components of the phase space. in which an island archipelago is magnified indicating where a critical curve used to lie. Insets 2-4 clearly show scale invariant structures that reveal the different dynamics present inside the islands, i.e. quasiperiodic trajectories enclosing narrow stochastic layers. These island chains create partial barriers to chaotic transport, and are the source of external stickiness.

As there is no known way to exactly determine the boundaries of the KAM islands, a frequently used method is the estimation of the, previously introduced, Lyapunov exponents. However, when applied to numerical calculations, finite time (or 'local') Lyapunov exponents can only be applied. However stickiness causes substantial difficulties [186] in the characterisation of a chaotic orbit, which therefore demands much more computational effort. Chapter 10 therefore introduces different tools that enable the deeper characterisation of stickiness and its relationship with the system's geometry.

9.6.3 Fractal dimension of the chaos/order boundary.

The fractal nature of the chaos/order boundary in the billiard system's phase space is demonstrated. The boundary is the feature of greatest interest in the system due to the great variety of behaviours associated with the extreme complexity of this frontier with the regular components of the phase space, as illustrated in Fig. 9.10. To gain deeper information of its structure within the phase space, the special unstable period-two orbit studied in Section 9.5 is chosen as the initial condition. This initial condition is special as it is always within the largest chaotic component of phase space for all values of e except $e = 1$. The total phase space is partitioned into a grid of $L \times L$ cells, where each cell has a side of length $\varepsilon \propto 1/L$ in the y-axis, and rescaled length $\varepsilon \propto \pi/L$ in the x-direction. This is equivalent to covering the phase space by $L \times L$ (square) L_∞ neighbourhoods.

We characterise the chaos/order boundary by considering its box-counting dimension. This is done by defining $N_B(\varepsilon)$ as the number of cells needed to cover the chaos border at given value of ε. We understand dimension to mean how much space a set occupies *near* each of its points.
The idea of a 'measurement' of a set at scale, ε, defined by L_∞., is fundamental. For each ε, one measures the set in a way that detects irregularities of size $\Delta\varepsilon$. Ultimately we want to know how these measurements behave as $\varepsilon \to 0$ [207].

Defining the chaos border as the subset, B, for $\varepsilon > 0$, define the smallest number of sets of maximum diameter ε as $N_B(\varepsilon)$. The dimension of B reflects the way in which $N_B(\varepsilon)$ grows as $\varepsilon \to 0$. If $N_B(\varepsilon)$ even approximately behaves as a power law, i.e.

$$N_B(\varepsilon) \simeq c\, \varepsilon^{-D},\ \forall c, D \geq 0 \tag{9.51}$$

where c is some constant, B is then said to have a 'box-counting dimension' D. This is solved via:

$$log N_B(\varepsilon) \simeq log(c) - D log(\varepsilon) \tag{9.52}$$

$$\therefore\ D \simeq \frac{-log N_B(\varepsilon)}{log(\varepsilon)} + \frac{log(c)}{log(\varepsilon)} \tag{9.53}$$

alowing us to obtain D, in the limit, as:

$$D = lim_{\varepsilon \to 0} \frac{log N_B(\varepsilon)}{log(1/\varepsilon)}. \tag{9.54}$$

The second term disappears in the limit. The chaos border subset, B, is defined as the set of 'border cells', i.e. that have been visited but have at least one 'empty' neighbouring cell alongside. The chaotic orbit must have visited

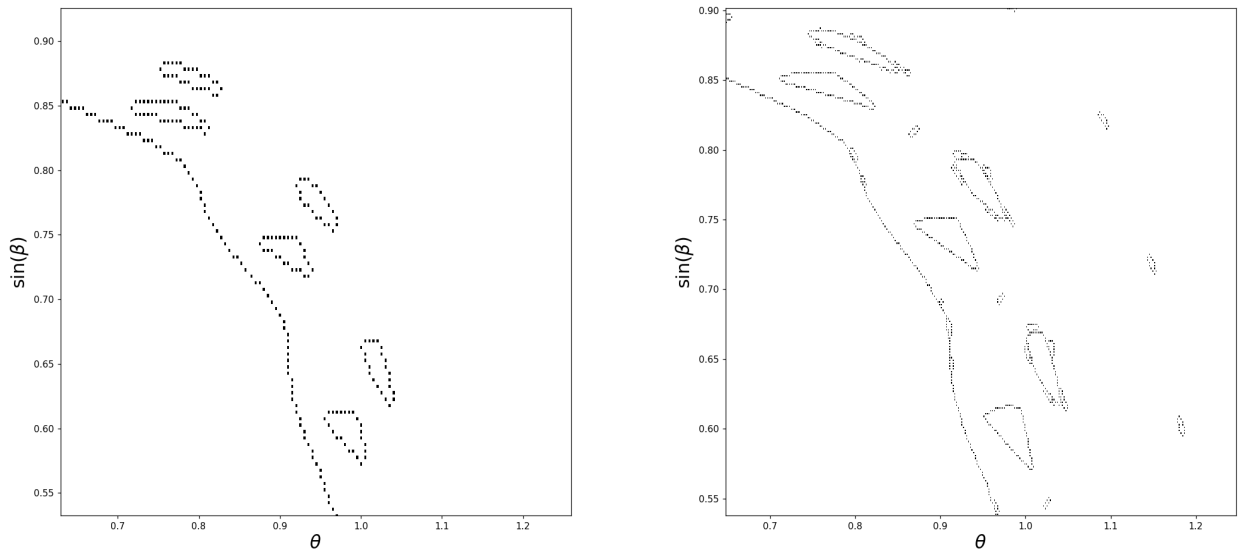

(a) $L = 200$ (b) $L = 500$

Figure 9.11: Plots showing the border cells, outlining the largest chaotic component in the vicinity of the central stable island for $a = 0.9, e = 1.11$, for different numbers of grid cells L.

a border cell at least once, meaning that some part of the phase space contained within is the chaotic component. However, it must be recognised that, in all probability, the whole cell is not filled by the chaotic phase component.

To determine the fractal dimension, grid cells between $L = 500$ and $L = 1500$ were used. The length of each chaotic orbit was 2×10^9, to ensure a large number of counts per cell, even for larger values of L. Using short trajectories to fill the chaotic set results in an anomalous deviation of the border cell count with number of cells L from the expected power law. This is because the sparsity of points recorded within the chaotic phase portion leads to the misidentification of border cells where, in fact, there are none. The following set of tables show the power law evolution of the chaos boundary with L, and hence its fractal nature, for a set of different geometries.

e	D	e	D
1.1	$1.21 \pm 4 \times 10^{-3}$	6	$1.02 \pm 5 \times 10^{-4}$
2	$1.02 \pm 8 \times 10^{-4}$	7	$1.03 \pm 9 \times 10^{-4}$
3	$1.11 \pm 7 \times 10^{-4}$	8	$1.05 \pm 1 \times 10^{-3}$
4	$1.03 \pm 5 \times 10^{-4}$	9	$1.15 \pm 4 \times 10^{-3}$
5	$1.32 \pm 8 \times 10^{-3}$	–	–

Table 9.1: Table of the evolution of the fractal dimensions for the border of the chaotic component, for $a = 0.1$. The error is estimated from the linear regression slope.

e	D	e	D
1.1	$1.13 \pm 3 \times 10^{-3}$	1.6	$1.01 \pm 5 \times 10^{-4}$
1.2	$1.41 \pm 5 \times 10^{-3}$	1.7	$1.23 \pm 9 \times 10^{-3}$
1.3	$1.62 \pm 1 \times 10^{-2}$	1.8	$1.07 \pm 7 \times 10^{-3}$
1.4	$1.30 \pm 9 \times 10^{-3}$	1.9	$1.02 \pm 2 \times 10^{-3}$
1.5	$1.27 \pm 1 \times 10^{-2}$	–	–

Table 9.2: Same as for Table 10.2, but for $a = 0.5$.

e	D	e	D
1.01	$1.003 \pm 2 \times 10^{-4}$	1.06	$1.13 \pm 4 \times 10^{-3}$
1.02	$1.002 \pm 2 \times 10^{-4}$	1.07	$1.92 \pm 8 \times 10^{-3}$
1.03	$1.002 \pm 1 \times 10^{-4}$	1.08	$1.71 \pm 1 \times 10^{-2}$
1.04	$1.002 \pm 2 \times 10^{-4}$	1.09	$1.51 \pm 8 \times 10^{-3}$
1.05	$1.01 \pm 1 \times 10^{-3}$	1.10	$1.47 \pm 1 \times 10^{-2}$

Table 9.3: Same as for Table 10.2, but for $a = 0.9$.

The fractal dimension of the chaos/order boundary is always between one and two, which is expected as this set outlines the fractal codimensional transport barriers confining the explored chaotic portion of the phase space, and gives a measure for how much the $1D$ outline 'fills' the enclosing $2D$ space. However, the measured fractal dimension of the boundary does not follow a simple evolution with increasing elongation e. One striking feature can be observed for $a = 0.9$, where the fractal dimension undergoes a pronounced increase between $e = 1.06$ and 1.07. These power laws allow us to understand that a major cause of fluctuations in the billiard's chaotic dynamics is the presence of an infinite structure between the chaotic and regular phase space components.

CHAPTER
10

DYNAMICAL RECURRENCES IN THE IRIS BILLIARD

We make predictions and have developed memory. The sun rises every morning, and sets every evening. Birds seasonally migrate. We roughly guess where a thrown rock might land. Often, these predictions come, not from the development and evaluation of long, complicated mathematical expressions, but rather, from two crucial facts [208]:

- similar situations often evolve in similar ways;
- some situations are repeated.

These facts are linked to a certain determinism in real world systems. However, we understand that some deterministic systems, such as the Iris Billiard, may be sensitive to fluctuations at any scale. The smallest perturbation to an initial condition in the chaotic set can render long term prediction impossible, as examined in the case of the unstable period-two orbit in the previous chapter. Typical chaotic motion can be regarded as a superposition of an infinite number of different frequencies with respect to the unstable periodic orbits within the phase space of the system. Homoclinic orbits were discovered by Henri Poincaré in 1890, in his work addressing the stability of the solar system. Recurrences were formally introduced as a by-product, and shown to always apply to chaotic motion

However, we now account for recurrence properties, in the sense that the dynamics returns to a state similar to one already visited. The time between subsequent recurrences to a measurable set, $A \in X$ of a measurable dynamical system is:

$$\tau(A) = min\{n > 0 : \mathbf{T}^n A \cap A \neq \varnothing\}. \tag{10.1}$$

In the following, the previously visited idea of an L_∞ 'ε measure', is and always will be, used to demark the measurable set A, within X, the chaotic portion of the billiard phase space explored in the previous section. Recurrences, and recurrence quantification analysis (RQA), will be applied to better understand the chaotic motion of the Iris Billiard. The following examines the proof demonstrating this behaviour.

10.1 Poincaré recurrence theorem

Poincaré demonstrated, in 1890 [209], that a conservative dynamical system returns arbitrarily close to its initial condition an infinite number of times as time tends to infinity [210].

Consider the dynamical system (X,T), where X is the compact metric space and T is a homeomorphism of X, generating a group $\{T^n, n \in Z\}$ of transformations. $x \in X$ is recurrent if $T^n x \in A$ for some $n > 0$, where A is the finite measurable neighbourhood of x. Recurrence is treated as a topological property of the individual points that compose the space. For the system to be measure-preserving, we require a quadruple $(X, \mathscr{B}, \mu, T)$. $\mathscr{B}$ is a σ-algebra of subsets of X, μ is a probability measure in $\mathscr{B}$ and T is now a measure-preserving transformation of $(X, \mathscr{B}, \mu)$ [1]. For $\mu(A) \geq 0$ $A \in \mathscr{B}$, and $T^{-1}A \in \mathscr{B}$ with $\mu(T^{-1}A) = \mu(A)$.

Poincarés recurrence theorem. *Let $(X, \mathscr{B}, \mu, T)$ be a measure-preserving set, with $\mu(X) = 1$, and $V \in \mathscr{B}$ with $\mu(A) > 0$. There exists some point $x \in A$ with $T^n x \in A$ for some $n > 0$.*

Proof. Assume that no point $x \in A$ ever returned to A. Then $T^{-n}A \cap A = \varnothing$ $\forall n > 0$. $\therefore$ $T^{-n}A \cap T^{-m}A = \varnothing$ whenever $n \neq m$. However, this is impossible as by definition the sets $T^{-m}V$ are measure-preserving with $\mu(A) > 0$, and are not disjoint since $\mu\left(\bigcup_{n=1}^{\infty} T^{-n}A\right) \leq \mu(X) = 1$. □

It follows, from Poincaré's theorem, that every point, $x \in A$, with non-zero measure must return to A an arbitrary number of times as time tends to infinity, i.e, even though nearby trajectories in the chaotic set will deviate exponentially in a finite time, they must nonetheless return arbitrarily close and evolve in ways similar to before, an arbitrary number of times, as time approaches infinity [211]. Poincaré's theorem, however, neither gives an indication of the frequency with which the orbit of a point visits a given set, nor does it give the rate at which the point particle will return to an arbitrarily small neighbourhood around its initial condition. A complete answer to the former is given by Birkhoff's ergodic theorem. Recurrence Plots allow the quantitative and qualitative study of the latter recurrence behaviour of dynamical systems [212] by visualising their recurrences in phase space.

10.2 Recurrence plots

Recurrence plots (RPs), introduced in 1980 [208, 212], permit the quantitative and qualitative study of phase space recurrences. This tool has already been applied in the fields of economy [213], physiology [214], ecology [215], neuroscience [216] and astrophysics [217]. Although recurrence statistics have been extensively studied in billiards [177, 180, 185], RPs appear to have only been applied to position recurrences in a two particle billiard system of an eccentric annular billiard [218]. We will consider time recurrences in the billiard's phase section. Poincare's theorem states that every point with non-zero measure will return to its neighbourhood, after a finite number of measure preserving transformations, an arbitrary number of times, as time approaches infinity. Therefore even exponentially deviant chaotic billiard trajectories [219] must, given enough time, return arbitrarily close to their initial conditions and evolve in ways similar to before, an arbitrary number of times, as time approaches infinity [211]. Although this theorem gives no indication of the frequency at which recurrences occur, RPs allow the quantitative and qualitative study of this property [212]. Throughout an orbit of length N_{col}, the particle collides with the enclosing circular boundary $N_\circ$ times. The time evolution of the points corresponding to a trajectory in the phase section can be symbolised as: $\{\boldsymbol{v}_i\}$ $i = 1...N_\circ$. A state, $\boldsymbol{v}_j$, is defined as recurrent to a former state, $\boldsymbol{v}_i$, if both are within each others neighbourhood, i.e. a region around each state defined by ε.

The neighbourhood, A, may be defined in different ways. The L_∞ norm, originally introduced in Section 9.6.3, is always applied, which defines a square of length ε with $\boldsymbol{v}_i$ at its centre, such that $\boldsymbol{v}_j$ is a recurrent state of v_i if and only if the two states lie within the same square region. The value of ε is important. If too small, no recurrences would be recorded in a finite time. If too big, every point would be recorded as a recurrence of every other point, leading to artefacts unrelated to the dynamics. Although these artefacts may be analytically determined for simple periodic and quasiperiodic motions [220], in general they cannot be completely removed by any known means.

[1] Borel sets are the sets that can be constructed from open or closed sets by repeatedly taking countable unions and intersections. Let X be a set. Then a σ-algebra, F is a nonempty collection of subsets of X such that the following hold: 1. X is in F. 2. If A is in F, then so is the complement of A. (i.e. we partition the collection of sets) 3. If A_n is a sequence of elements of F, then the union of the A_ns is in F.

We have followed the convention of consistently defining ε as 10% of the width of its corresponding phase component [208].

The binary, $N_\circ \times N_\circ$, recurrence matrix is defined as:

$$\mathbf{R}_{i,j} = \Theta(\varepsilon - ||\boldsymbol{v}_i - \boldsymbol{v}_j||), \quad i,j = 1...N_\circ, \tag{10.2}$$

where $\Theta(\cdot)$ is the Heaviside function. RPs are the graphical representation of $\mathbf{R}_{i,j}$. The value '1', encoded by a black point, indicates that $|\boldsymbol{v}_i - \boldsymbol{v}_j| < \varepsilon$. Otherwise, points are blank, representing the value '0'. All RPs will show a diagonal line, i.e. $\mathbf{R}_{i,j} = 1 \; \forall i = j$, known as the Line of Identity (LOI). RPs display many patterns associated with different behaviours. At the small scale, they exhibit single points, diagonal lines and vertical lines, (the combination of the latter two results in rectangular clusters of recurrence points) [208]. Single, isolated recurrence points indicate that a state is rare, or only briefly persists. Diagonal lines, running parallel to the LOI, of length l occur when part of a trajectory runs almost in same phase neighbourhood as a previous portion, for l segments. Finally, vertical lines indicate time intervals in which a state is either stationary or changes very slowly.

10.2.1 Recurrence plot selection

Recurrence plots of the various dynamics of the Iris Billiard are shown. Applying the L_∞ neighbourhood, the trajectory's return times τ, as defined by Eq. 10.1, are also shown such that $N(\tau)$ is the total distribution of return times measured over the total trajectory. Figures 10.2 and 10.3 show rotational unperturbed periodic and quasiperiodic orbits. These orbits can be directly mapped to the $1D$ circle map. Figs. 10.3 & 10.4 show unperturbed and perturbed quasiperiodic orbits respectively. These demonstrate that Slater's theorem, examined in Section 9.1.1, applies. Furthermore this provides an effective way to distinguish between rotational quasiperiodic and chaotic orbits using short trajectories, as has been verified in the case of the standard map [186]. Figure 10.5 shows one RP of an arbitrarily chosen chaotic orbit, where many recurrence times are now present. Variations in the density and the presence of many white spaces indicate the presence of dynamical transitions. We focus on the recurrence properties of the chaotic orbits of the Iris Billiard, for different geometries. The next section will introduce two typically used measures that quantify some of the features observed in the RPs so far presented. These features will then be applied to the chaotic orbits of the Iris billiard, as sensitive indicators of stickiness.

10.3 Recurrence quantification analysis of chaotic Iris orbits

To study the structures presented by RPs, several measures [221], known as Recurrence Quantification Analysis (RQA), are already in use. We will focus specifically on two in the context of the chaotic dynamics of the Iris Billiard. The first measure is the recurrence rate (RR), defined as the percentage of black points in an RP:

$$RR(\varepsilon) = \frac{1}{N^2} \sum_{i,j=1}^{N} \mathbf{R}_{i,j}(\varepsilon). \tag{10.3}$$

This may be better understood as the 'sparsity' of the $N \times N$ binary matrix under consideration. In the limit $N \to \infty$, RR is the probability that a state recurs to its phase neighbourhood, as demarked by ε.

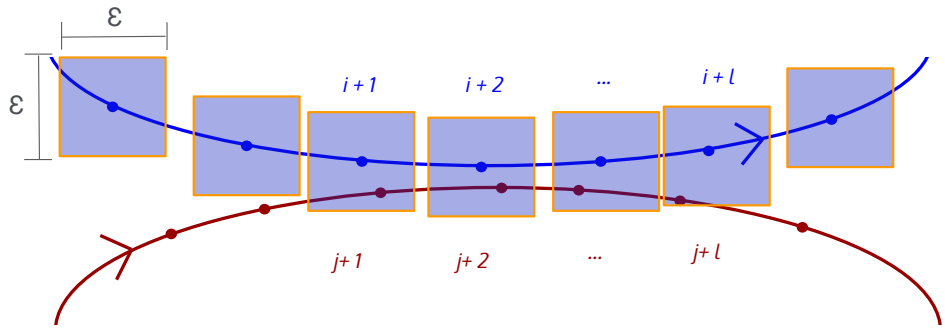

Figure 10.1: A diagonal line in an RP corresponds with a part of a trajectory (blue) that stays within the ε defined $Ł_\infty$ neighbourhood of another section (red) , for l iterations. The proportions of these present above a minimal length l_{min}

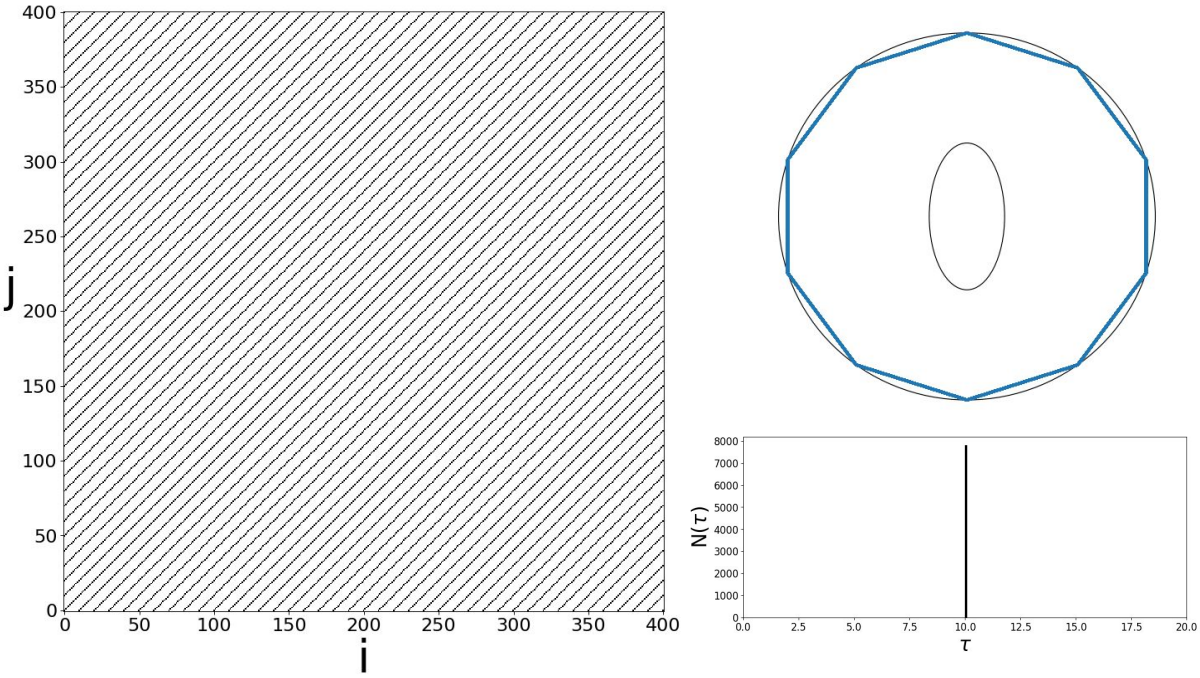

Figure 10.2: *RP* of an unperturbed periodic $\Omega = 1/10$ orbit

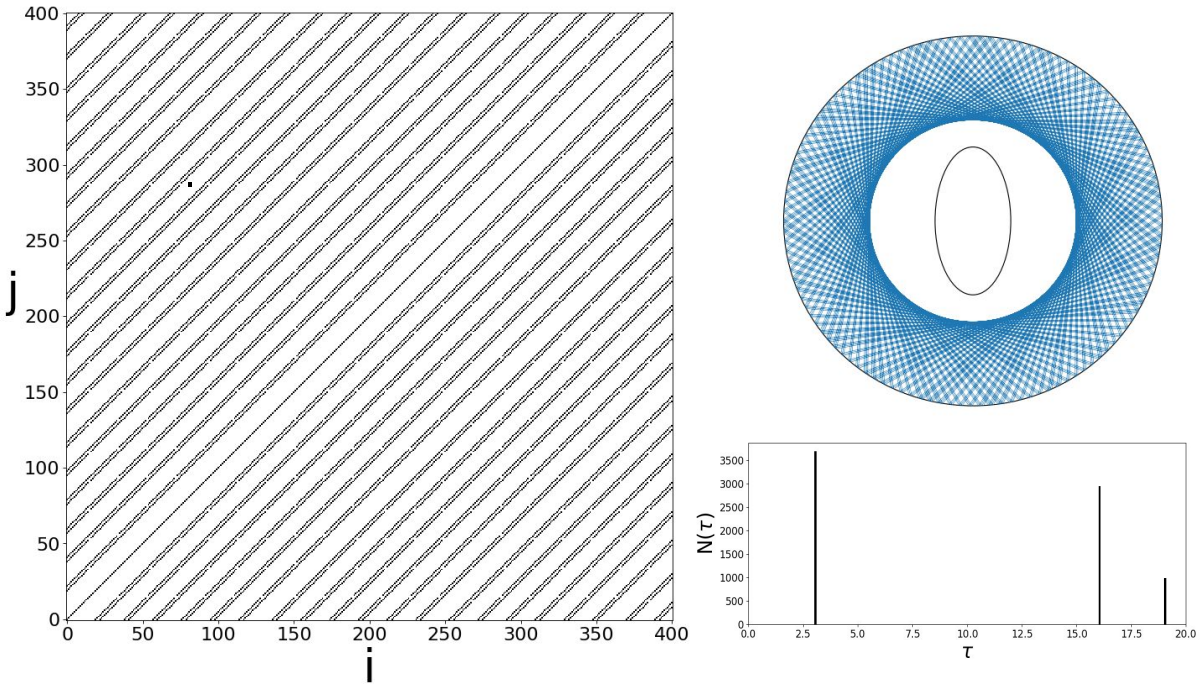

Figure 10.3: *RP* of an unperturbed quasiperiodic $\Omega = 1/\sqrt{10}$ orbit. The distribution of return times shows $\tau \in [3, 16, 19]$. The return time distribution demonstrates that Slater's three-gap theorem, introduced with the 1D circle map, in Sec, 9.1.1 is satisfied.

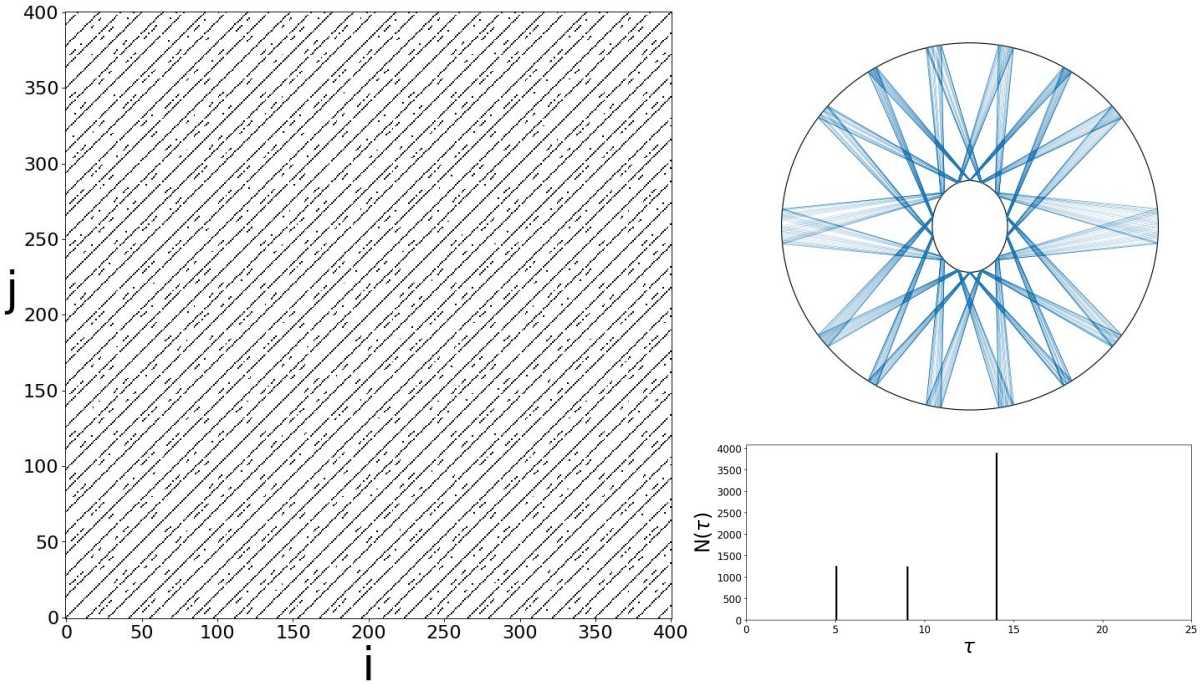

Figure 10.4: *RP* of a perturbed rotational quasiperiodic orbit. $a = 0.2$, $e = 1.25$. Launched from $\theta = 0$, $\beta = 0.2$. The distribution of return times shows $\tau \in [5, 9, 14]$, in accordance with the three-gap theorem.

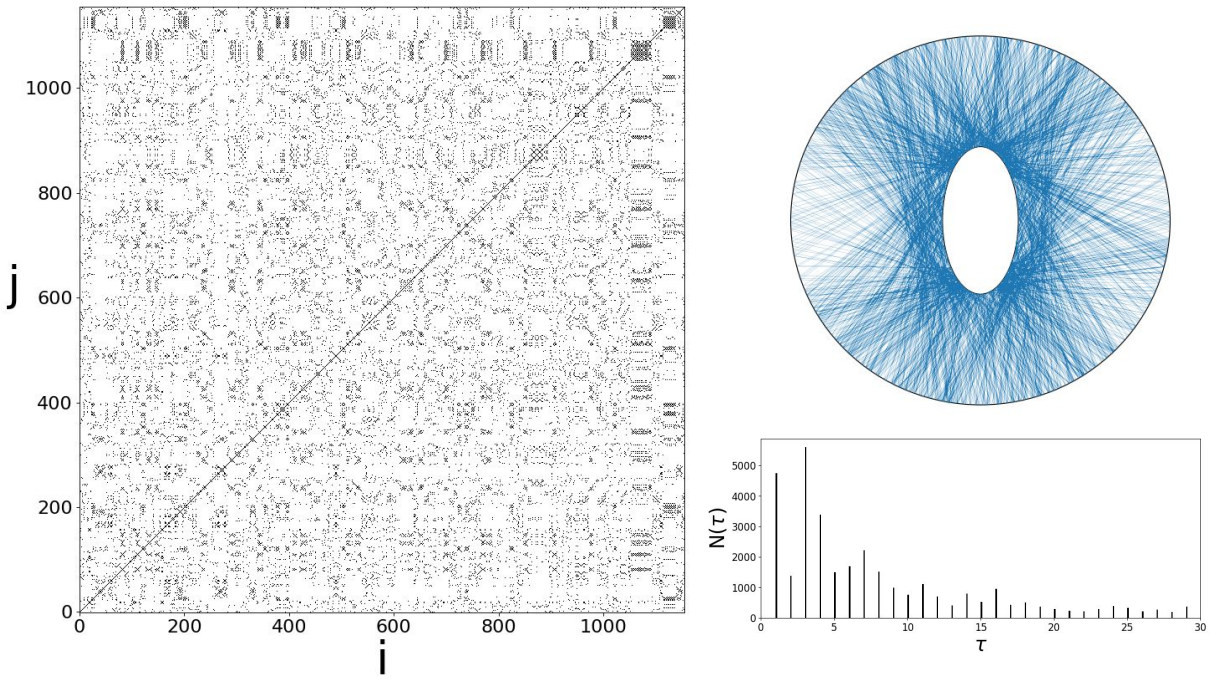

Figure 10.5: RP or an arbitarily chosen chaotic orbit. $a = 0.2$, $e = 2$. Many recurrence times are now present.

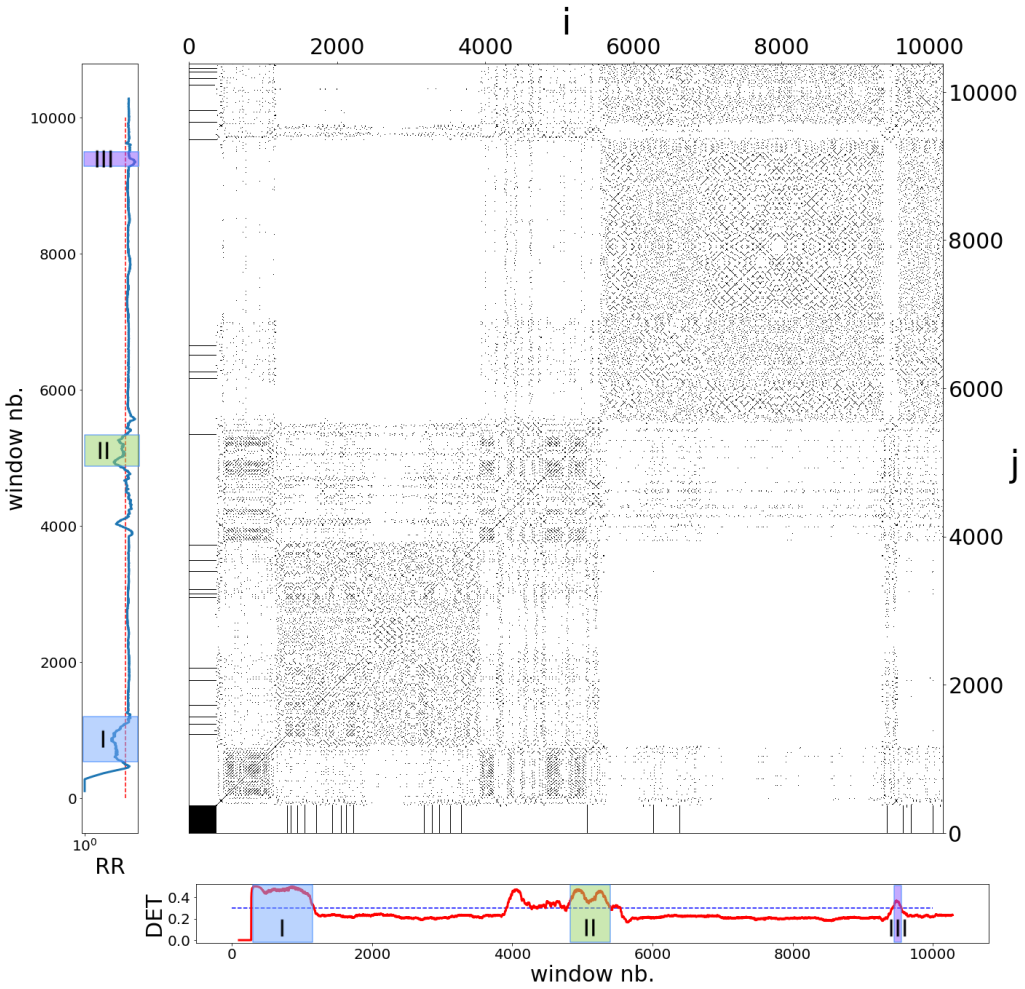

Figure 10.6: RP of a 2×10^4 long chaotic trajectory, launched from the unstable period-two orbit, for $a = 0.9, e = 1.1$. $RR_{crit} = 0.1$. $DE_{crit} = 0.3$. Three separate regions of interest are selected and marked as I, II and III.

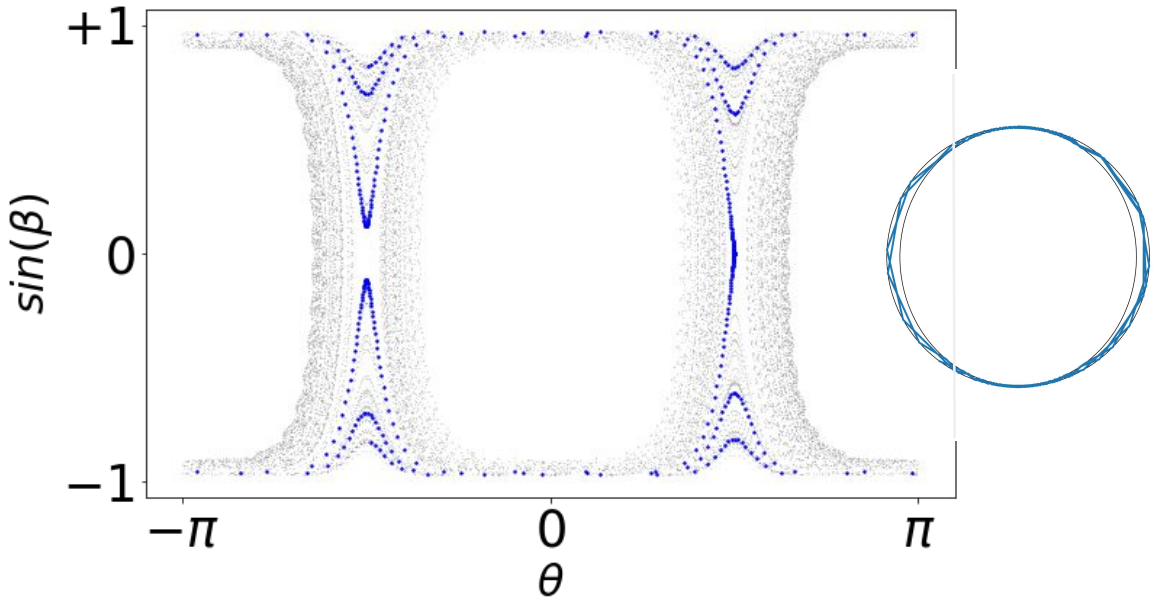

Figure 10.7: Domain I, $i \in 352, 1100$: Rotational motion, of different frequencies,

The second measure is based on the distribution of diagonal lines present within the *RP*:

$$P(\varepsilon, l) = \sum_{i,j=1}^{N} (1 - \mathbf{R}_{i-1,j-1})(1 - \mathbf{R}_{i+l,j+l}) \prod_{k=0}^{l-1} \mathbf{R}_{i+k,j+k} \tag{10.4}$$

Recurrence plots principally show diagonal lines for periodic and quasiperiodic orbits, as shown by Figs 10.2 10.3 ,10.4. A diagonal line of length l shows that a segment of a trajectory is close to another segment from a different time, for l iterations, as illustrated in Fig. 10.1. The trajectory's determinism (DET), is defined as the percentage of black points belonging to a diagonal line of at least l_{min}. The ratio of recurrence points that form a diagonal line, of at least length l_{min}, to all the recurrence points, therefore, provides a measure of how deterministic (predictable) the trajectory is,

$$DET = \frac{\sum_{l=l_{min}}^{N} lP(\varepsilon, l)}{\sum_{l=1}^{N} lP(\varepsilon, l)}. \tag{10.5}$$

In what follows, $l_{min} = 3$. For all periodic orbits $DET = 1$. To apply these measures as indicators of stickiness within the billiard dynamics, windows of size $l_w = 200$ will be overlayed the original recurrence plot. *RQA* will be applied to each window, and the evolution of the above introduced variables will serve as indicators of dynamical transitions.

10.3.1 Indicators of stickiness

An example RP applied to a chaotic orbit of length 2×10^4 is shown. The measures introduced above are applied as a particularly sensitive measurement of intra-chaotic dynamical transitions. Fig 10.6 shows the RP of a long, chaotic orbit for $a = 0.9, e = 1.1$. The trajectory is then analysed by applying the previously introduced RQA measures to moving windows of length $w = 200$. The selected RQA measures (*RR* & *DET*) are monitored with respect to time. When the chaotic trajectory encounters a sticky region, the *RR* significantly changes as its evolution becomes much more regular. Three examples are highlighted in Fig 10.6 as Domains I, II and III.

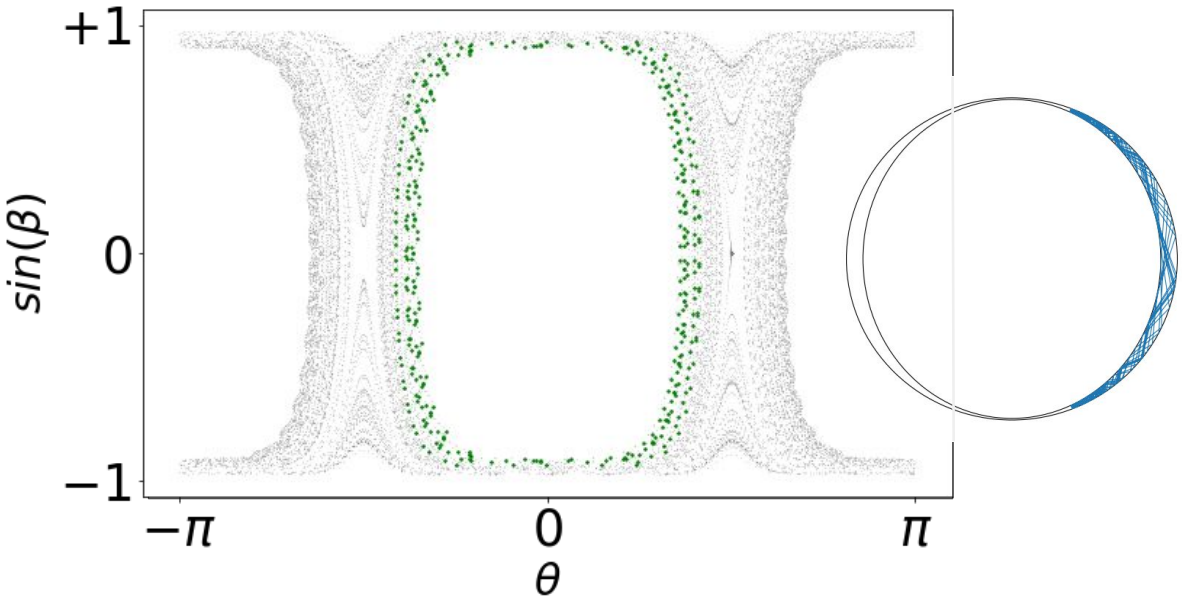

Figure 10.8: Domain II, $i \in 9420, 5200$: Librational diffusion.

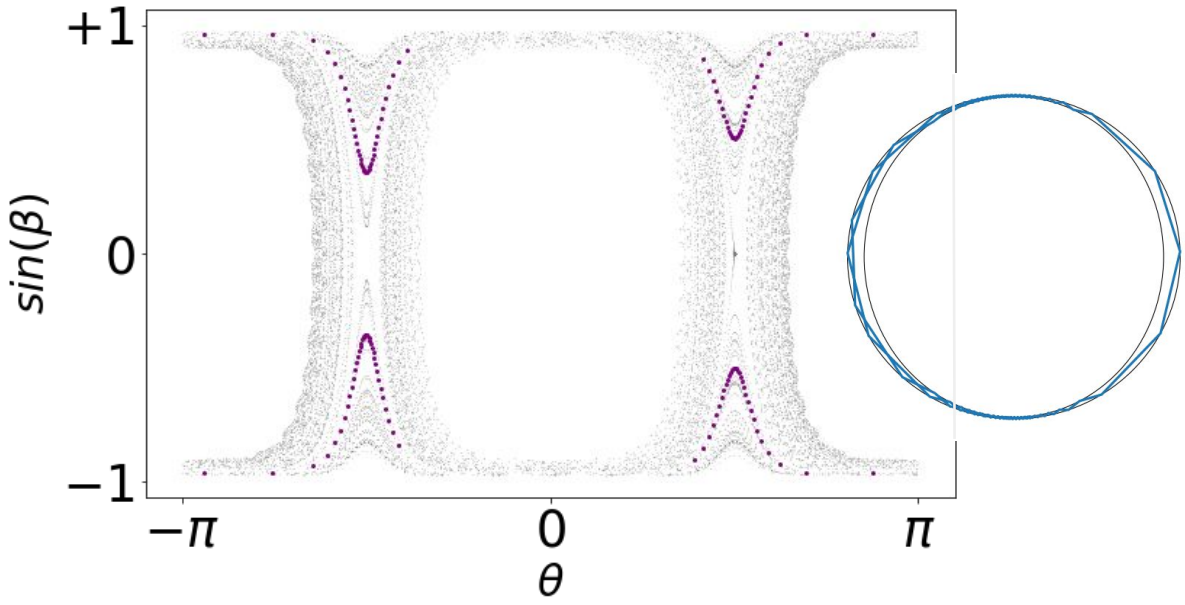

Figure 10.9: Domain III, $i \in 9400, 9540$ Short rotational motion.

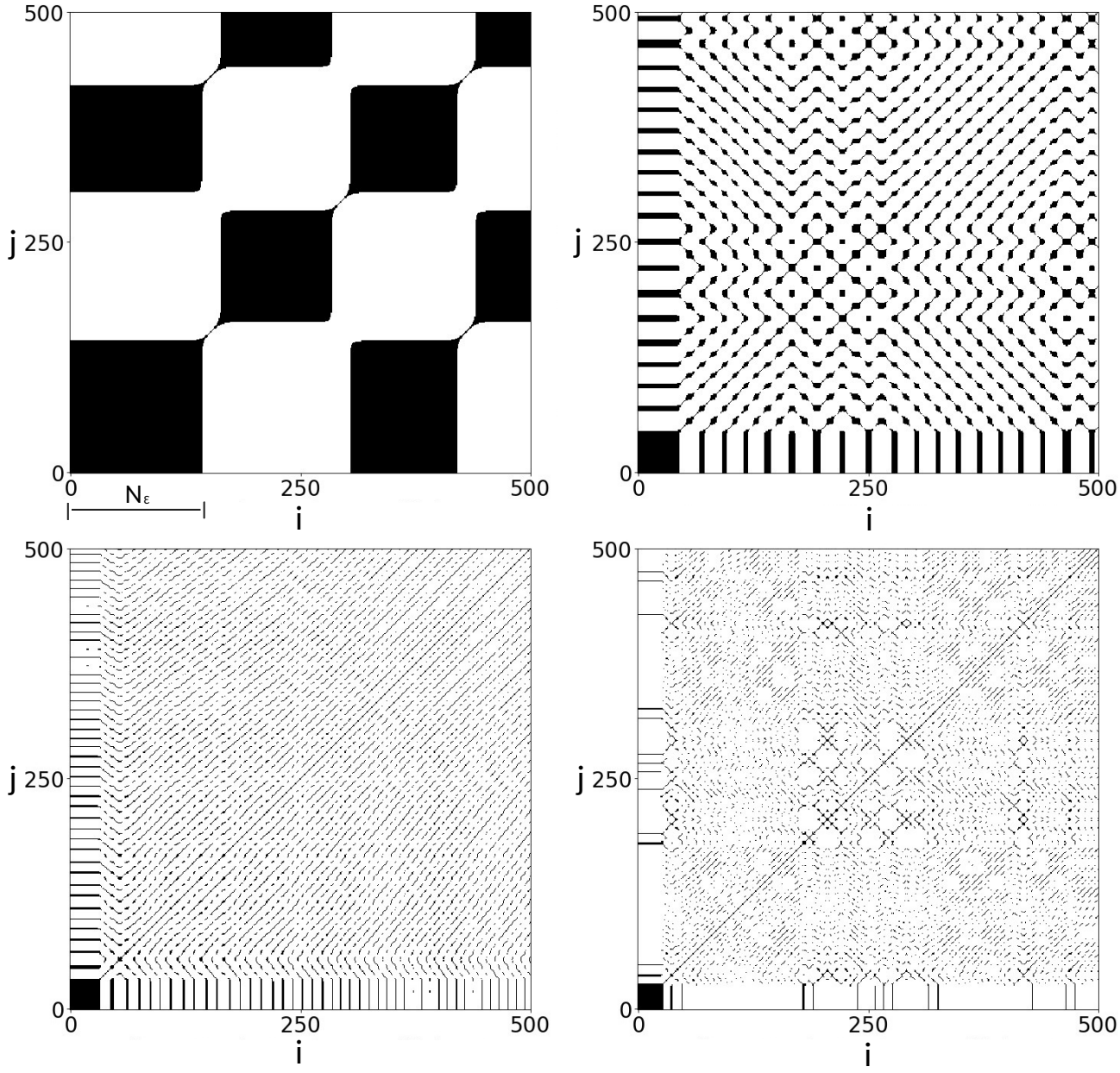

Figure 10.10: Recurrence Plots (RPs), visualizing the dynamics resulting from the unstable period-two orbit for different geometries. $a = 0.2$ Top left: $e = 1.01$, where the measure of interest; N_ε is indicated, Top right: $e = 1.1$, Bottom left: $e = 1.2$, Bottom right: $e = 1.3$, for which dynamical transitions, as indicated by the variation of density of recurrence points, are clearly present.

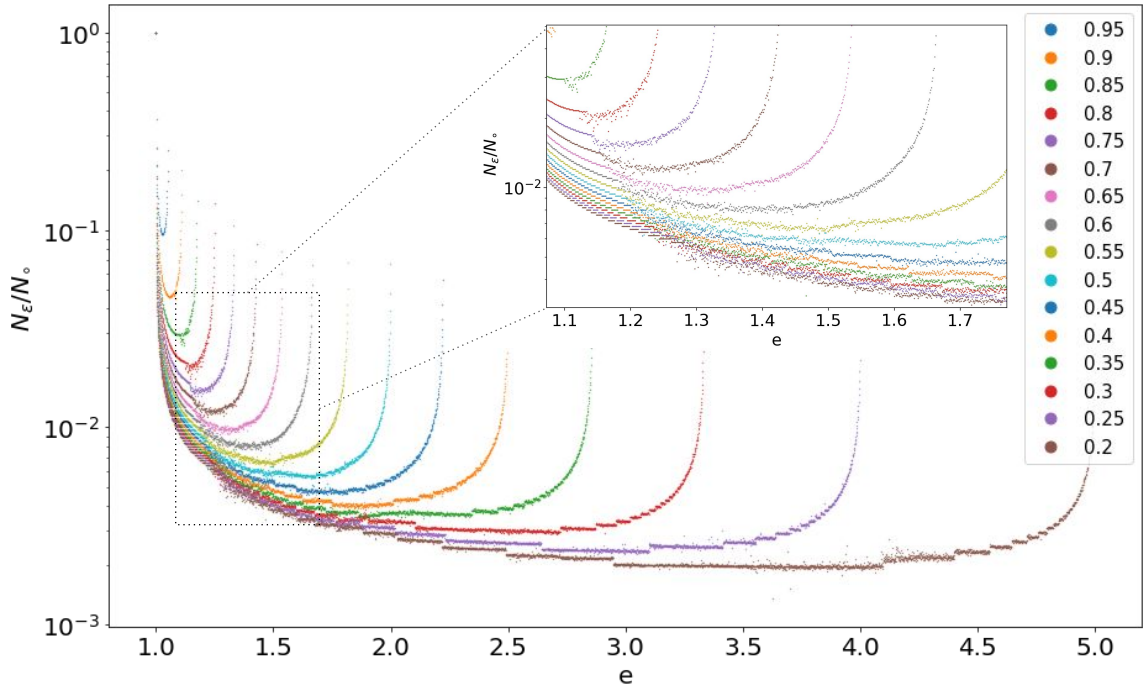

Figure 10.11: The ratio of the number of collisions within the initial recurrence phase section region of the unstable period -two orbit, N_ε, to the total number of collisions with the outer circular boundary, $N_\circ$, as a function of the elongation, e. A logarithmic scale is used to show the transition point clearly on each curve. X-axis: The elongation of the inner scatterer for different values of a, each identified by a color in the legend. In each case, total trajectory length, $N_{col} = 10^4$.

These correspond to regions where both RR and DET surpass RR_{crit} and DET_{crit}, defined as 0.1 and 0.3 respectively. These values were chosen for the purpose of demonstrating the presence and detection of stickiness for one specific geometry, and would have to be reevaluated for each different geometry considered. Domain III is of particular interest as it corresponds a high deviation for only the DET measure, but not for RR. Figs. 10.7 10.8 & 10.9 show the phase occupation of the sticky orbits observed by the RR and DET measures.

While it is clear that further study of recurrence plot features, their associated quantitative measures and their relation to the billiard geometry would very likely be fruitful, the next section will focus instead on a new measure, defined by a, until now unconsidered, feature of recurrence plots of chaotic trajectories.

10.3.2 Study of new time measure

We carry out a simple analysis by introducing a new time measure, N_ε: The number of collisions with the outer boundary before the particle, launched from the unstable period two orbit, studied in Section 9.5, exits its initial L_∞, ε-neighbourhood for the first time. RPs of a 10^3 iteration trajectory, with geometries $a = 0.2$, $e = 1.01, 1.1, 1.2, 1.3$ are illustrated in Fig.10.10. The new time measure of interest manifests as the black box in the bottom left-hand corner of all four plots in Fig.10.10.

Fig.10.11 shows the evolution of $N_\varepsilon/N_\circ$, for a fixed value of $N_{col} = 10^4$, for different geometries. For all values of a considered, as $e \to 1$, so does $N_\varepsilon/N_\circ$. This is because the initial period -two orbit approaches stability, as demonstrated in Sec. 9.5, so it always remains in its initial neighbourhood. Similarly, as $e \to 1/a$, $N_\varepsilon/N_\circ$ again approaches unity as the period -two orbits approaches stability. This can be expected as, intuitively, as the region becomes more confined, the distance the particle traverses between each collision approaches zero, meaning that

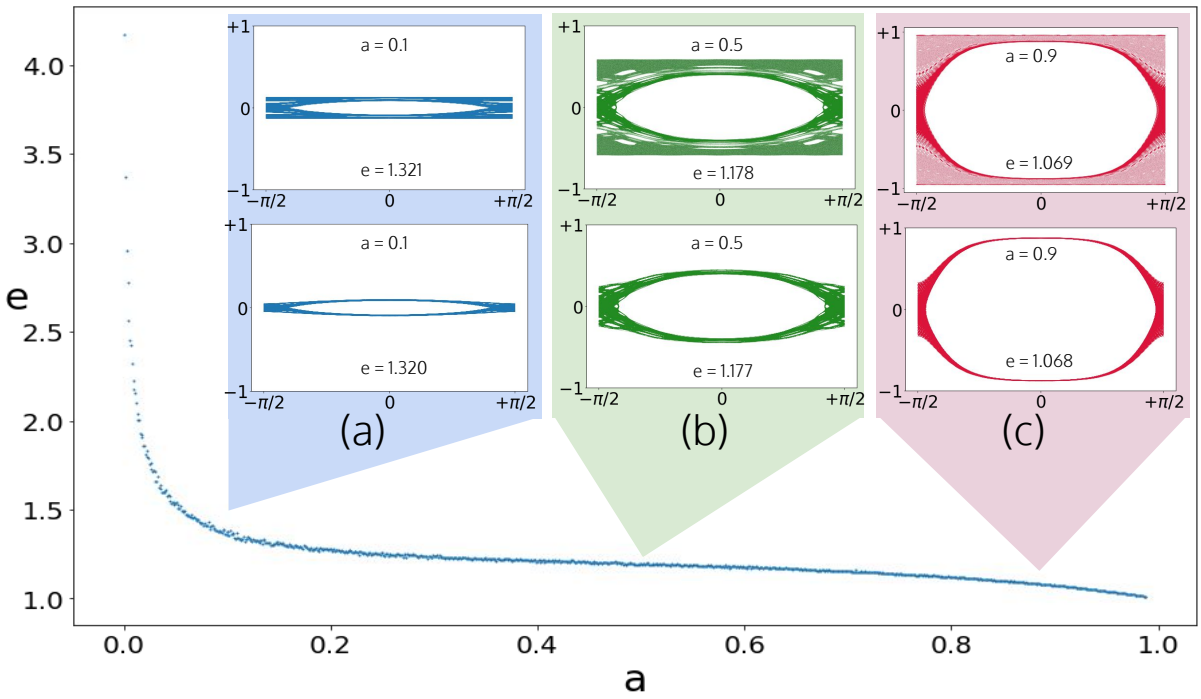

Figure 10.12: Evolution of $e_{crit}(a)$ for $a \in (0,1)$. Trajectories of length $N_{col} = 2^6$ were used to obtain each point. The curve indicates the geometry at which the final rotational curve is destroyed. The subfigures show the phase section occupation of the long time chaotic trajectory ($N_{col} = 10^7$) for values of geometry just above and below e_{crit} (a) $a = 0.1$, below: $e = 1.320$ above: $e = 1.321$. (b) $a = 0.5$, below: $e = 1.178$ above: $e = 1.179$. (c) $a = 0.9$, below: $e = 1.068$ above: $e = 1.069$.

small deviations from the initial conditions will have an increasingly negligible effect on the orbits stability matrix.

The most important feature of the main plot in Fig. 10.11 is the transition of $N_\varepsilon/N_\circ$ from smooth to rough. This happens at different values of elongation for each value of semi-minor axis, a. To understand this phenomenon, recall that the trajectory begins as the unstable period -two orbit, i.e. The particle collides with the boundary at every other iteration. When $e = 1$, $N_\varepsilon = N_\circ = N_{col}/2$. As e increases, $N_\varepsilon/N_\circ$ smoothly evolves until a critical value of the elongation, $e = e_{crit}(a)$. This critical geometry causes a non-zero probability that the particle, having just collided with the circular outer boundary, will miss the ellipse, and collide again with the outer circle, therefore breaking the parity condition. The first time this event occurs in a trajectory will be referred to as the 'endogenous escape event', or $\mathscr{E}$ for brevity. This must not be confused with the escape events normally studied in open billiard systems, as the hole through which the particle is escaping in this case is intrinsic to the system's phase space. The true value of e_{crit} depends neither on ε, nor the numerical precision chosen. $e_{crit}(a)$ is defined as the set of geometries for which the following is true:

$$\lim_{N_{col}\to\infty} \left(N_\circ - \frac{N_{col}}{2} \right) = 1. \tag{10.6}$$

Due to finite simulation times, any obtained value of e_{crit} will inevitably be an overestimation. Figure 10.12 shows that $e_{crit}(a)$ demarks the geometries that permit two classes of behaviour by reconstructing, and including as insets, the long-term trajectories of the unstable period -two orbit for values below and above $e_{crit}(a)$. When $e < e_{crit}(a)$, the trajectory explores an extended stochastic region that is bounded by a dense rotational KAM curve/surface. This rotational curve is destroyed at $e = e_{crit}(a)$, i.e. holes are created which allow the trajectory to escape its reduced chaotic portion of the phase space after a finite number of iterations. By simple inspection of Fig. 10.12, the absence of any further similar transitions suggests that for elongations beyond the critical value,

the chaotic region of the phase space is never again so divided nor reconnected.

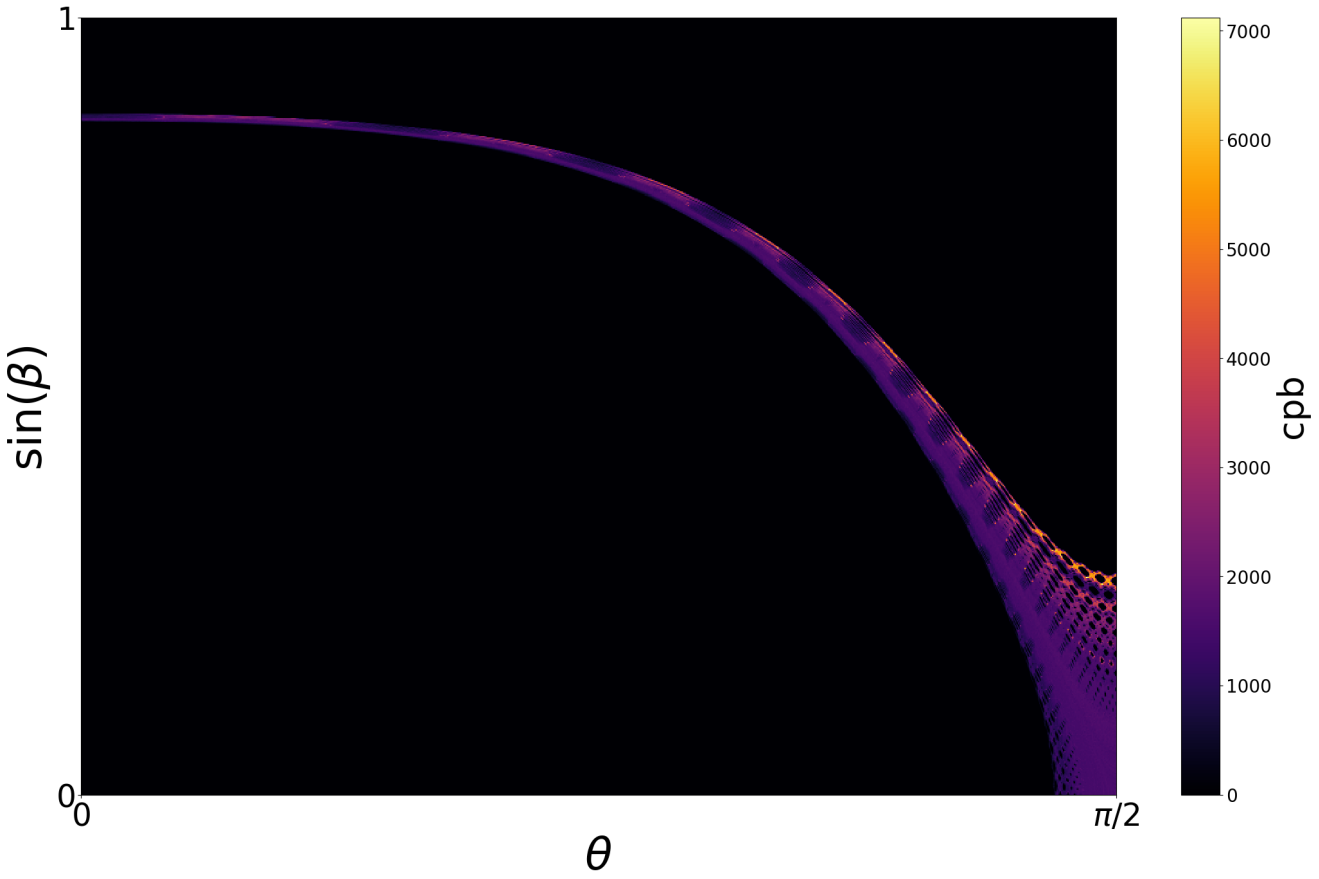

Figure 10.13: Heatmap of the reduced chaotic portion of the phase space, prior to global connection, filled by a 2×10^9 long trajectory launched from the unstable period-two orbit. $L = 300$, $a = 0.9, e = 1.067$. All trajectories launched from any initial condition, within this chaotic set, will obey the symbolic parity condition for all time.

For values of elongation below the critical value, $e_{crit}(a)$, the trajectories exploring the bounded chaotic region are clearly still subject to both position and momentum diffusion, yet under the constraint that the point particle will *always* alternately collide with the circle (c) and the ellipse (e). In this case, one may symbolize the trajectory, **T** as:

$$\boldsymbol{T} = [.., e_i, c_{i+1}, e_{i+2}, c_{i+3}, e_{i+4}, c_{i+5}, e_{i+6}, c_{i+7}....]. \tag{10.7}$$

For $e > e_{crit}$, this constraint no longer applies. The moment this parity condition is broken implies the dynamical transition has occurred, and is characterized by $\mathscr{E}$, i.e. the first passage of the particle's trajectory from one major fractal subset to the rest of the chaotic phase space. In this case, the trajectory may now be symbolized as:

$$\boldsymbol{T} = [.., c_{n_{esc}-4}, e_{n_{esc}-3}, c_{n_{esc}-2}, e_{n_{esc}-1}, \overbrace{c_{n_{esc}}, \mathbf{c}}^{\mathscr{E}}, \ ?? \ ]. \tag{10.8}$$

The first, bold, consecutive **c** represents $\mathscr{E}$ by hitting the outer circular boundary twice in a row, which, as before specified, never occurs when $e < e_{crit}(a)$. We note that $\lim_{e \to e_{crit}} n_{esc} = \infty$. It is not currently possible to predict

the order of the following c and es following $\mathscr{E}$, though any future work on characterising the average separation between consecutive endogenous escape events would likely bring some interesting results. The set $[\mathscr{E}_1, \mathscr{E}_2, \mathscr{E}_3 ...]$, is defined as the first, second, third, etc. times the trajectory consecutively hits the outer boundary after $\mathscr{E}$.

10.4 Discussion

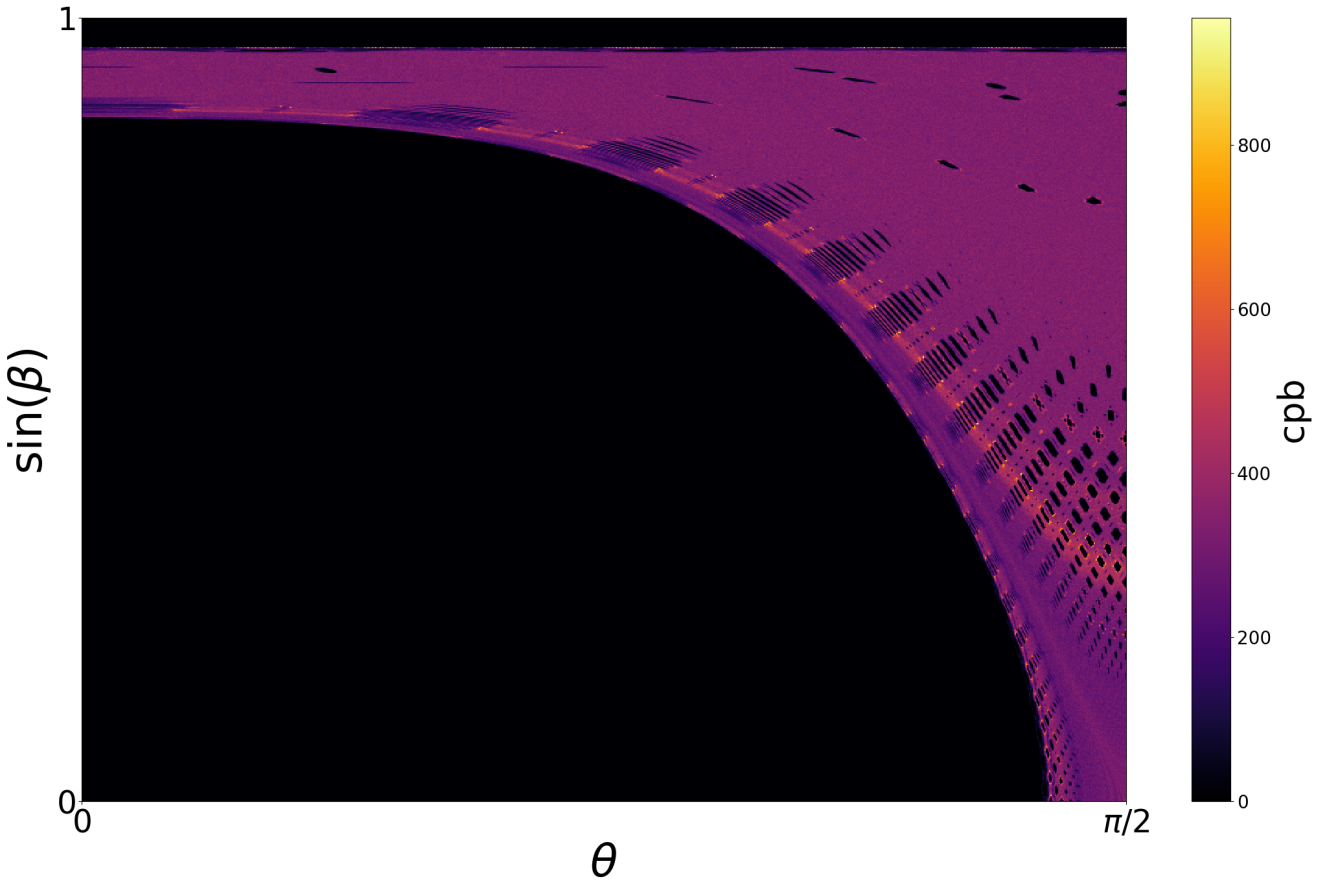

Figure 10.14: Heatmap of chaotic potion of the phase space post global connection. $L = 300$, $a = 0.9, e = 1.069$, filled by a 2×10^9 long trajectory launched from the unstable period-two orbit. In this case, all chaotic trajectories, may diffuse in and out of the region that obeys the parity condition. The closer to the critical geometry one approaches, from above, the more time passes between the passages between the two dynamical regime. For values of geometry that approach the critical limit from above, the rate of diffusion lessens.

10.4.1 Chaos-order fractal dimension around critical geometries

The fractal dimension of the chaos/order boundary at values of geometry above and below the critical geometry values measured by trajectories of length $N = 2 \times 10^9$ are presented. The methods introduced in Sec. 9.6.3 are employed. We observe a much higher than the average of what was previously measured.

a	e	D
0.1	1.317	$1.70 \pm 1 \times 10^{-2}$
0.5	1.175	$1.62 \pm 2 \times 10^{-3}$
0.9	1.067	$1.80 \pm 7 \times 10^{-3}$

Table 10.1: Table the fractal dimensions of the border of the chaotic component, for chosen values under the critical geometry set.

a	e	D
0.1	1.321	$1.63 \pm 1 \times 10^{-2}$
0.5	1.178	$1.53 \pm 3 \times 10^{-3}$
0.9	1.069	$1.95 \pm 1 \times 10^{-2}$

Table 10.2: Table of the evolution of the fractal dimensions for the border of the chaotic component, for chosen values above the critical geometry set.

Both Figs. 10.13 and 10.14 show very clearly the presence of cantori (destroyed remnants of perturbed robust transport barriers) above and below the critical destroyed barrier, that must correspond to the the remains of previously destroyed (but nonetheless robust) rotational transport barriers. The marked presence of these structures is what causes the fractal dimension of the chaos order border for $a = 0.9$ to be very high, higher than any other measured, and close to the upper dimensional limit, 2. The effect they have on the dynamics at, and shortly after, the endogenous escape event will be characterised in the next chapter.

10.4.2 Conclusion

The result presented in Fig. 10.12 is consistent with predictions given by the "Converse KAM" theorem, which states that no invariant rotational barriers will persist [202, 203] in a sufficiently perturbed area preserving twist map. In the cases of both the standard map, introduced in Section 9.1.2, and the double pendulum, the obtained frequency of the ultimately destroyed transport barrier is $\Omega = \gamma$, where γ is the golden ratio $(1+\sqrt{5})/2$. The subfigures within Fig. 10.12 clearly show that the frequencies of the ultimately destroyed rotational transport barriers correspond to different values of β. Contrary to the result obtained for the transition to global chaos in the standard map, we therefore expect that each critical value of elongation is directly associated to a different noble fraction, each defining the frequency of the final destroyed rotational transport barrier. As $\Omega = \gamma$ corresponds to only one value of β from Eq. 9.10. The evidence suggests a connection between the set of noble numbers and the critical ellipse geometries, with deep consequences for the global structure of the chaotic phase space. To further explore this phenomenon, in the context of the system's symmetries, one would need a Poincaré first return map which, until now, is unobtainable by any known means. Furthermore, is is well known that analytically tractable Poincaré first return maps are more the exception than the rule [222, 223].

CHAPTER
11

DISCUSSION

> "I wish it need not have happened in my time," said Frodo.
> "So do I," said Gandalf, "and so do all who live to see such times. But that is not for them to decide.
> All we have to decide is what to do with the time that is given us."
> Tolkien.

The values of θ at which the escaping trajectory segment comes closest to the ellipse, denoted θ_{esc}, and the distance of closest approach, d_{min} are presented. These quantities were obtained by following the argument that, at the point of $\mathscr{E}$'s closest approach, it will lie parallel to the ellipse at the closest point on the ellipse circumference. These quantities therefore define the space at which the trajectory tangentially intersects some constructed ellipse that is confocal to the scatterer. It will be demonstrated that values presented below can sometimes be 'virtual', in the sense that the θ_{esc} and d_{min} calculated don't belong to a part of the trajectory within the billiard domain.

11.1 Study of escape event

11.1.1 Geometric derivation of measured quantities

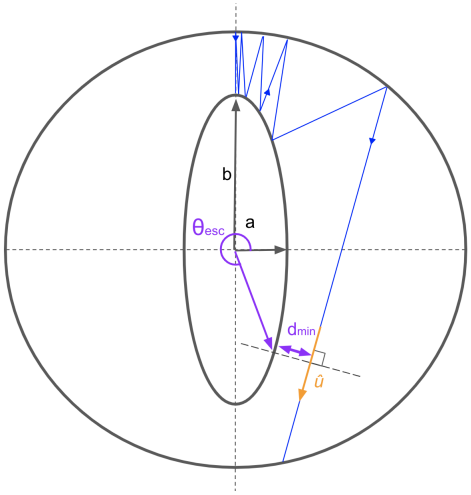

Figure 11.1: An illustration of the endogenous dynamical escape event, $\mathscr{E}$, of a trajectory launched from the unstable period-two orbit, that signals the transition to global chaos. The relevant observable variables, θ_{esc} and d_{min} are indicated. The unit vector of the escape segment, $\hat{u}$ is also shown.

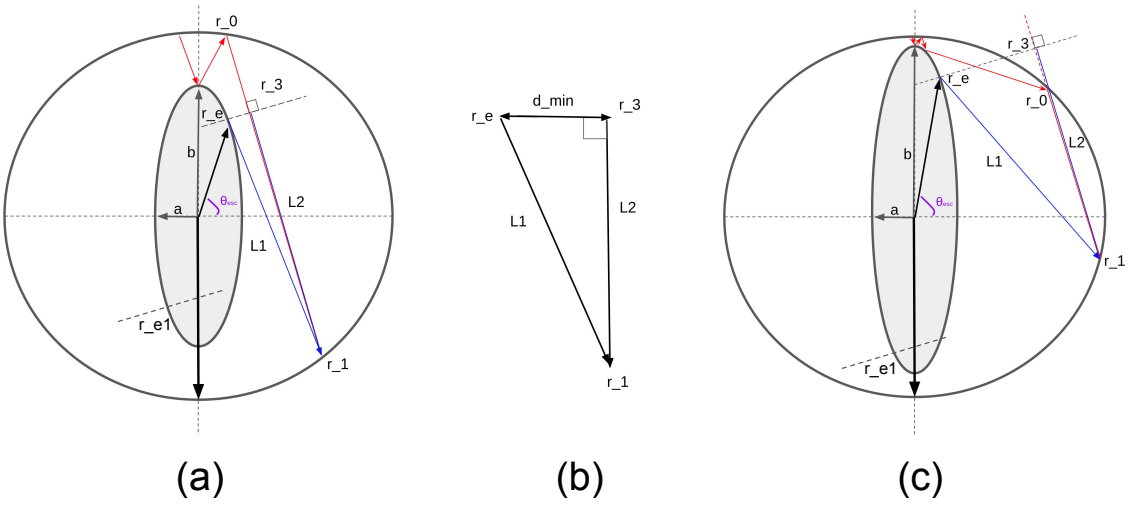

Figure 11.2: Geometrical construction used to obtain θ_{esc} and d_{min}. (a) A 'real' case. Where d_{min} is obtained via reasoning shown in (b): $L2 = \hat{\mathbf{u}} \cdot (\mathbf{r_1} - \mathbf{r_e})$. (c) A 'virtual' case, where the escaping trajectory is only parallel to the ellipse at a constructed point extended beyond the Iris boundary. This situation is most likely for geometries close to the crescent configuration.

Let $\hat{u}$ be the unit vector specifying the trajectory. For a non-intersecting trajectory, there is a point of closest approach on the ellipse, $r_e = (x_e, y_e)$, whose tangent is parallel to $\hat{u}$. Thus

$$\frac{dy}{dx} = -\frac{xb^2}{ya^2} = \frac{u_y}{u_x}. \tag{11.1}$$

Substituting for x in the ellipse equation, returns:

$$y^2 = \frac{b^4}{(au_y/u_x)^2 + b^2}. \tag{11.2}$$

Since there are two points on the ellipse whose tangents are parallel to $\hat{u}$, we obtain two solutions: (x_e, y_e) and (x_{e1}, y_{e1}). Applying simple geometric reasoning, as shown in Fig. 11.2, gives the minimum distance of approach as:

$$d_{min}^2 = |\boldsymbol{r}_\mathbf{1} - \mathbf{r_{e/e1}}|^2 - \left[\hat{\mathbf{u}} \cdot (\mathbf{r_1} - \mathbf{r_{e/e1}})\right]^2. \tag{11.3}$$

The sought after solution is the one that returns the smallest value of d_{min}, from which one may directly obtain the associated value of θ_{esc}.

11.1.2 Numerical procedure

To ensure that the results presented reflect the global properties of the chaotic region of the phase space, the N_{sample} trajectories studied were launched from slightly different initial conditions, within the neighborhood of the unstable period-two orbit. The starting position on the outer boundary is defined by:

$$\theta_k = (-)^k \, \pi/2 + \varepsilon_\theta \, \eta_\theta \tag{11.4}$$

Where $1 \leq k \leq N_{sample}$. The starting orientation is defined by:

$$\beta_k = \varepsilon_\beta \ \eta_\beta \tag{11.5}$$

Where $\varepsilon_\beta = \varepsilon_\theta = 10^{-10}$ and η_θ, η_β are random numbers chosen from independent uniform random distributions between $[1-1]$. i.e. the starting position for the two unstable orbits with very slight, unbiased variations, which will cause the trajectories to exponentially deviate over a finite time, and therefore follow very different trajectories within the reduced chaotic phase space before escaping. All following results displayed only minor variations upon setting ε_θ or ε_β to zero. $N_{sample} = 10^6$ for each result presented.

11.1.3 Results

The set $[\mathscr{E}_1, \mathscr{E}_2, \mathscr{E}_3 ...]$, is defined as the first, second, third, etc. times the trajectory consecutively hits the outer boundary after $\mathscr{E}$. A principal function $f(\theta_{esc})$ is defined that describes the distribution of θ_{esc} in $\theta \in [-\pi/2, \pi/2]$, so that we can write the escape angle distribution over the total domain, $\Psi(\theta_{esc})$, for all geometries as:

$$\Psi(\theta_{esc}) = \begin{cases} f(|\theta_{esc}|) & : |\theta_{esc}| \leq \pi/2 \\ f(\pi - |\theta_{esc}|) & : \pi > |\theta_{esc}| \geq \pi/2 \end{cases} \tag{11.6}$$

Figures 11.1.3 and Figure 11.1.3 show the escape angle and the minimum escape distance distributions respectively for $\mathscr{E}, \mathscr{E}_{10}$ and $\mathscr{E}_{50}$, for $a = 0.1, e = 1.4$. The joint probability distribution of θ_{esc} and d_{min} are thereafter displayed as heatmaps for $\mathscr{E}, \mathscr{E}_{10}$ and $\mathscr{E}_{50}$ for elongations approaching the e_{crit} . This may be written as:

$$\Psi(\theta_{esc}) = \int_0^{b-a} f^{(2)}(\theta_{esc}, d_{min}) d(d_{min}) \tag{11.7}$$

where $f^{(2)}(\theta_{esc}, d_{min})$ is the joint probability of observing the d_{min}, θ_{esc} (within some neighbourhood). The following heatmaps were constructed by discretizing the θ_{esc} and d_{min} values for each geometry studied, and plotting the correspondences between the two values on a 2D histogram. The global heatmaps were made with a resolution of $L \times L$ cells where $L = 500$. A colorbar is used to count the number of events recorded per 'cell', whose units are given as 'counts per bin': cpb. Results for $a = 0.1, 0.5, 0.9$ are collected for two values of e above and approaching e_{crit} .

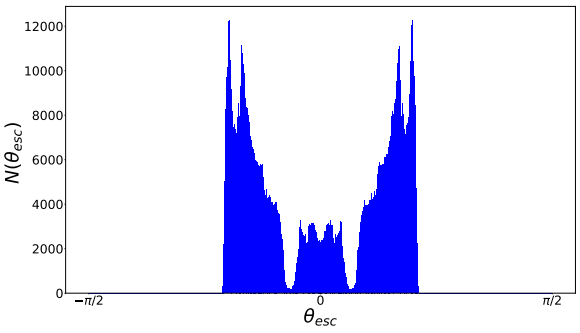

(a) $\mathscr{E}$

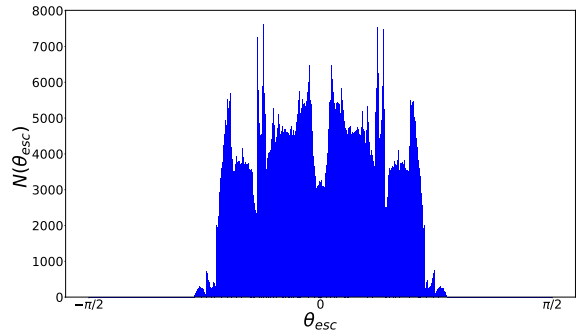

(b) $\mathscr{E}_{10}$

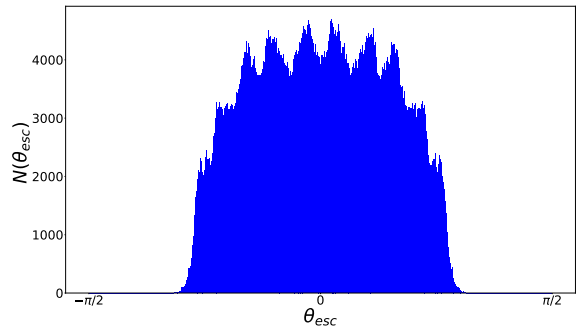

(c) $\mathscr{E}_{50}$

Figure 11.3: $f(\theta_{esc})$ for different escape segments.

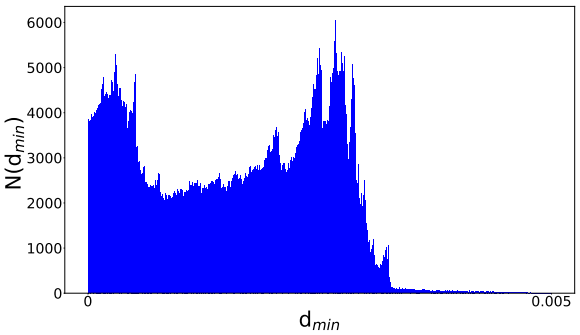

(a) $\mathscr{E}$

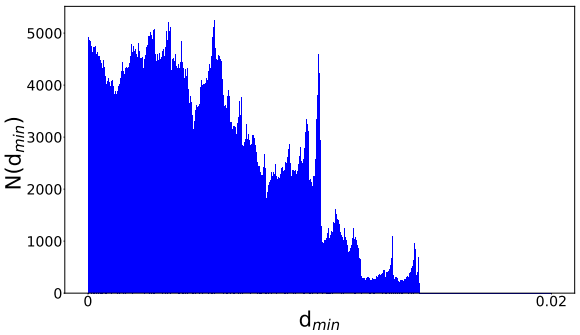

(b) $\mathscr{E}_{10}$

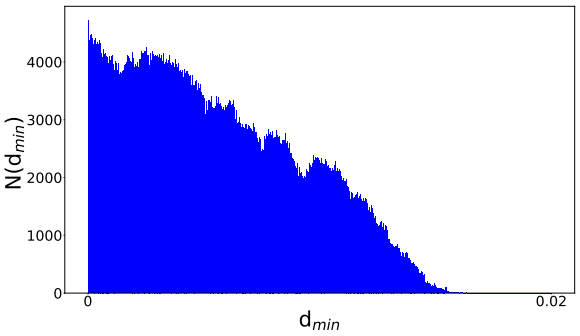

(c) $\mathscr{E}_{50}$

Figure 11.4: Distribution of minimum escape for different escape segments.

Survival probabilities before $\mathscr{E}$ are presented of which a semi-log linear fit is performed $log(P_{survival}) = An + B$, over the domain demarked by the two vertical red dashed lines, using the method of least squares. Both A and B are given within the figures. n_{min} is the minimum recorded value before any escape, and so may be thought of as a deterministic dead time. Each value is given in the figures. No power-law behaviours were observed.

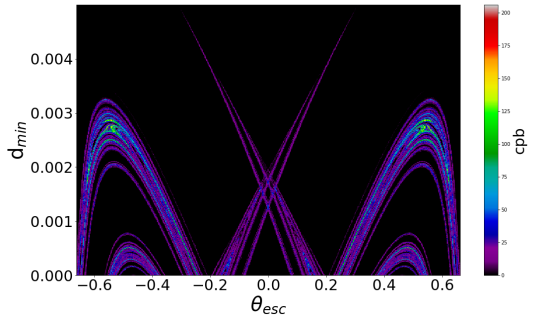

(a) $\mathscr{E}$

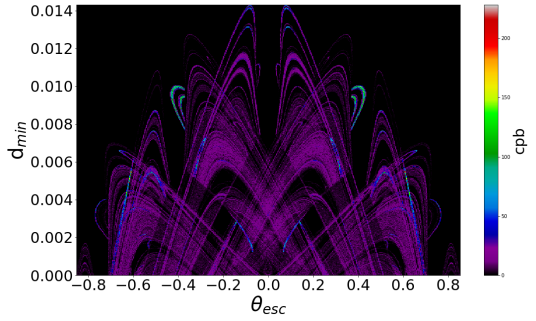

(b) $\mathscr{E}_{10}$

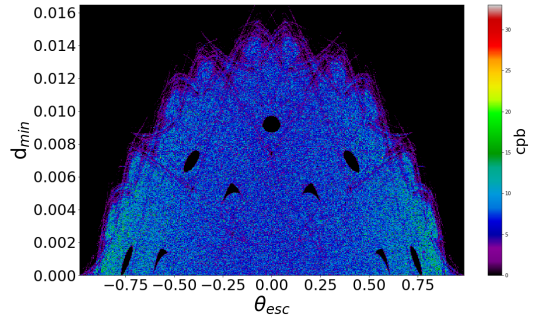

(c) $\mathscr{E}_{50}$

Figure 11.5: Heatmaps of θ_{esc} against d_{min}. $a = 0.1, e = 1.4$.

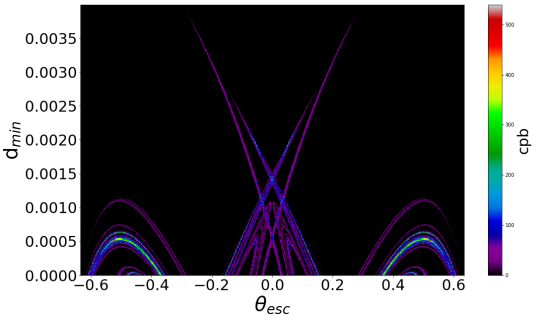

(a) $\mathscr{E}$

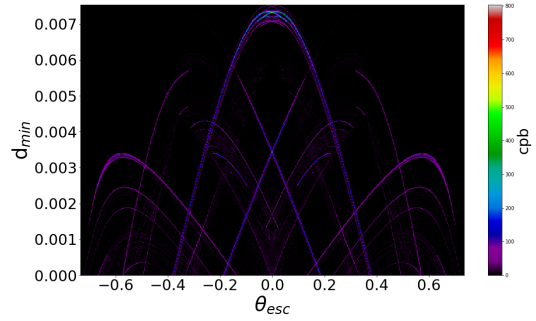

(b) $\mathscr{E}_{10}$

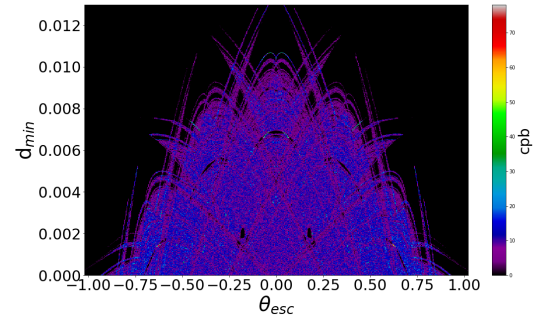

(c) $\mathscr{E}_{50}$

Figure 11.7: Heatmaps of θ_{esc} against d_{min}. $a = 0.1, e = 1.321$

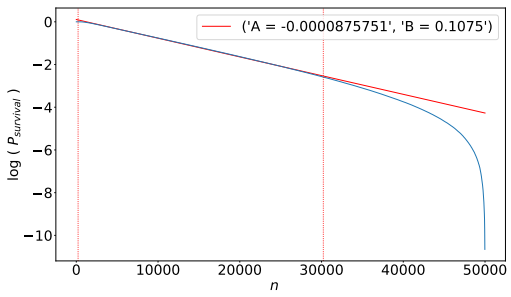

Figure 11.6: Survival probability on semi-log scale. $n_{min} = 239$. $a = 0.1, e = 1.4$.

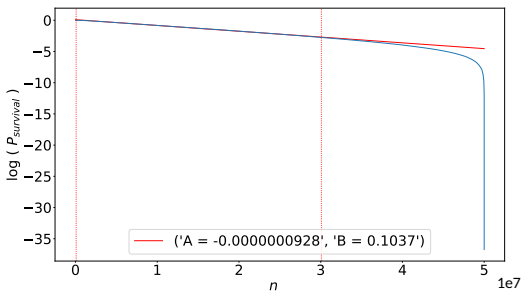

Figure 11.8: Survival probability on semi log scale. $n_{min} = 83759$. $a = 0.1, e = 1.321$.

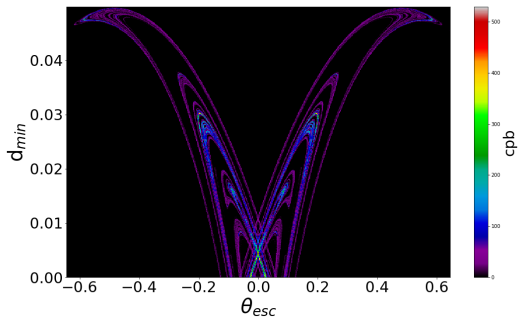

(a) $\mathscr{E}$

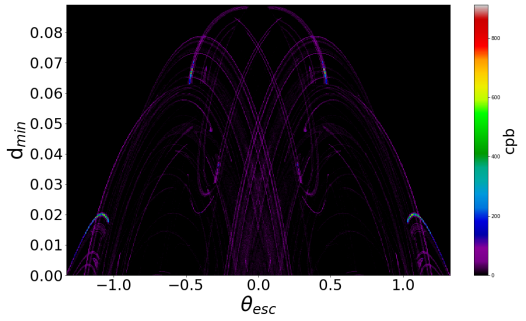

(b) $\mathscr{E}_{10}$

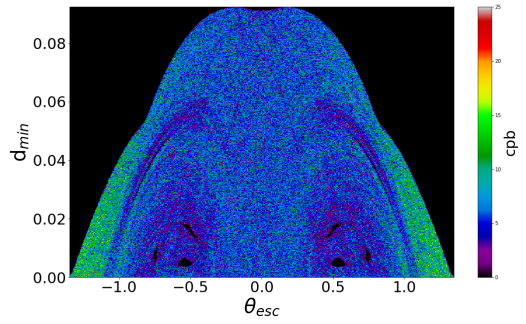

(c) $\mathscr{E}_{50}$

Figure 11.9: Heatmaps of θ_{esc} against d_{min}. $a = 0.5, e = 1.2$.

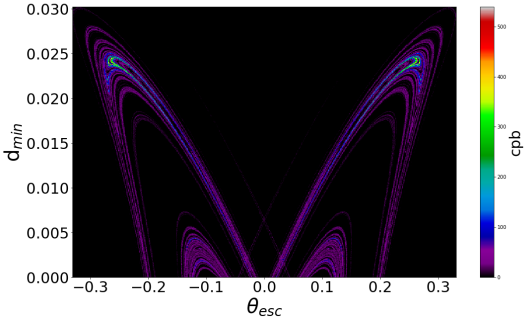

(a) $\mathscr{E}$

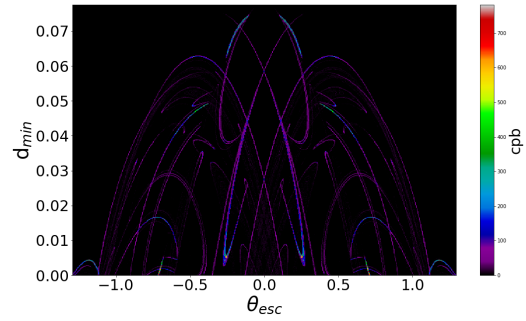

(b) $\mathscr{E}_{10}$

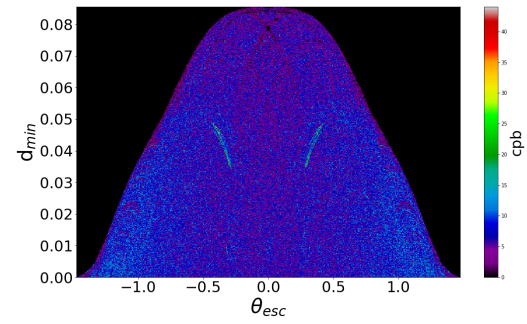

(c) $\mathscr{E}_{50}$

Figure 11.11: Heatmaps of θ_{esc} against d_{min}. $a = 0.5, e = 1.178$.

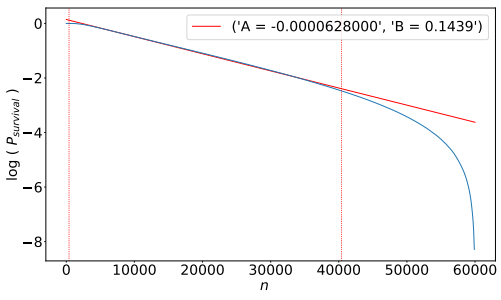

Figure 11.10: Survival probability on semi log scale. $n_{min} = 469$. $a = 0.5, e = 1.2$.

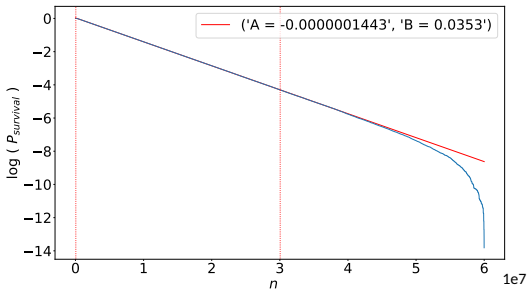

Figure 11.12: Survival probability on semi log scale. $n_{min} = 52137$. $a = 0.5, e = 1.178$.

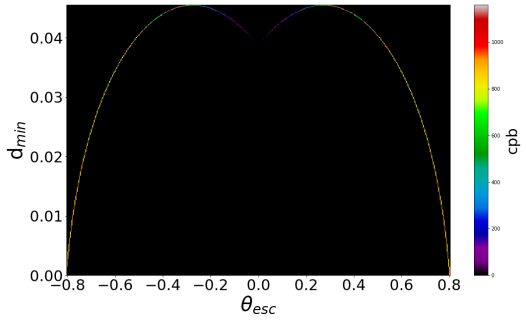

(a) $\mathscr{E}$

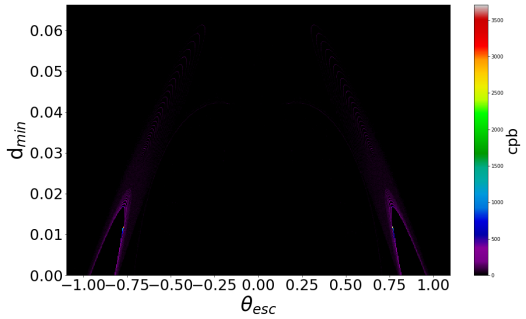

(b) $\mathscr{E}_{10}$

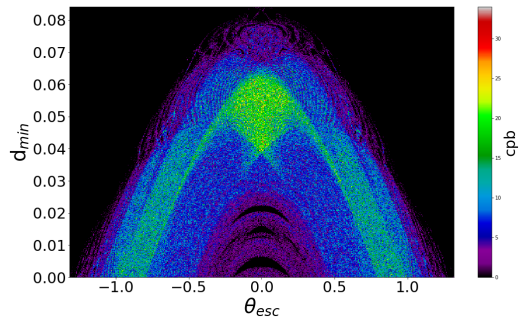

(c) $\mathscr{E}_{50}$

Figure 11.13: Heatmaps of θ_{esc} against d_{min}. $a = 0.9, e = 1.1$.

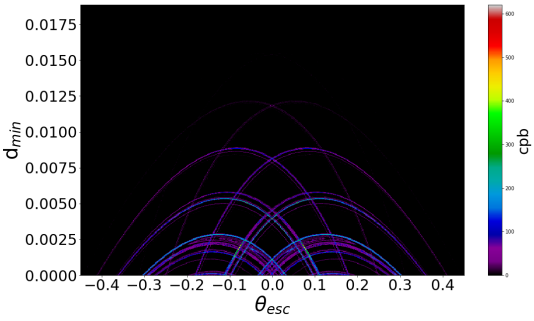

(a) $\mathscr{E}$

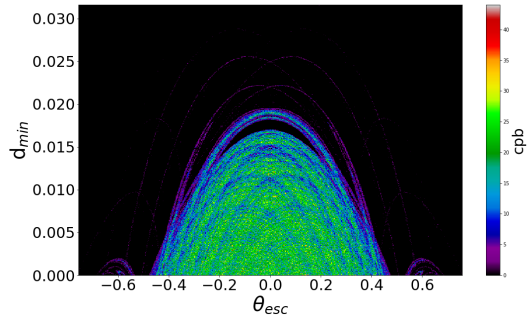

(b) $\mathscr{E}_{10}$

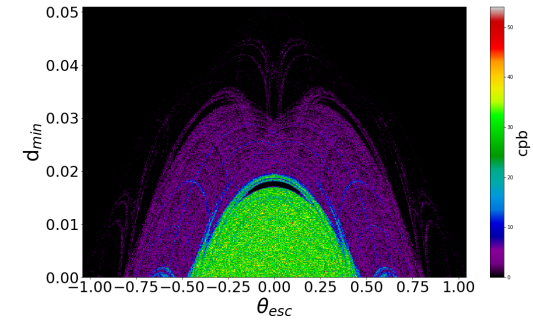

(c) $\mathscr{E}_{50}$

Figure 11.15: Heatmaps of θ_{esc} against d_{min}. $a = 0.9, e = 1.069$.

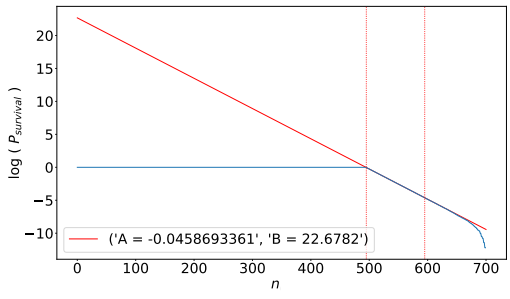

Figure 11.14: Survival probability on semi log scale. $n_{min} = 495$. $a = 0.9, e = 1.1$.

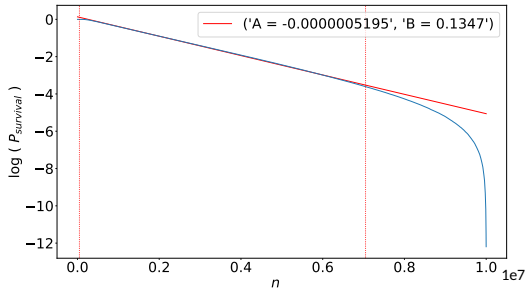

Figure 11.16: Survival probability on semi log scale. $n_{min} = 48891$. $a = 0.9, e = 1.069$.

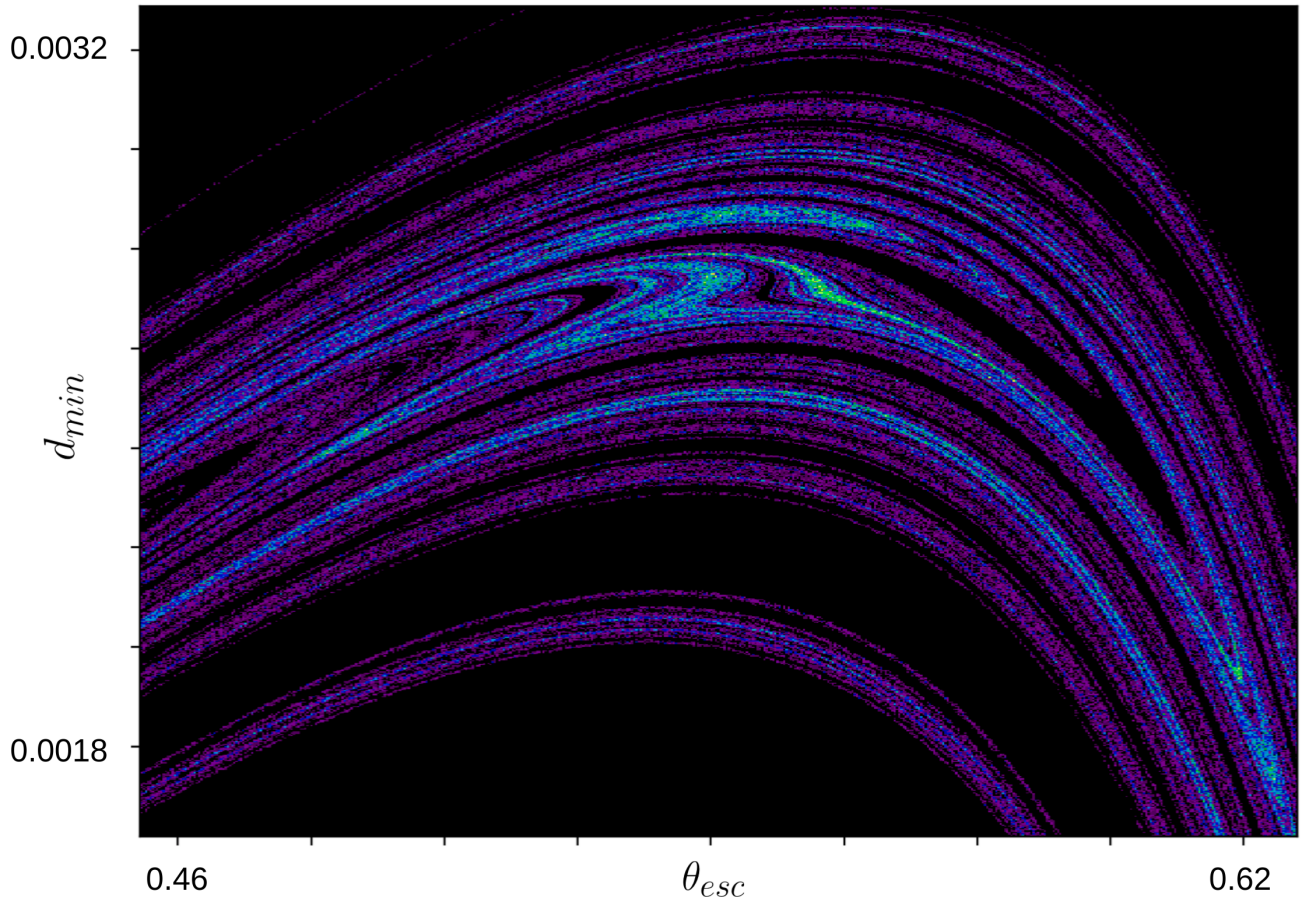

Figure 11.17: Closeup of Fig. 11.5a highlighting the consistent 'merging' feature, present in most of the above heatmaps at $\mathscr{E}$.

As it is challenging to fully characterise the forms displayed by the results, we focus on their common properties. In every case, the distribution of the joint probability distribution, shown by the heatmap of θ_{esc}, d_{min}, at $\mathscr{E}$, is unintuitive and even, as for Fig. 11.11a, counter-intuitive. One might expect $\mathscr{E}$ to occur when the distance between the inner and outer boundaries is maximum, i.e. at $\theta_{esc} = 0$, yet here it is clearly a minimum. However, for every geometry, the distributions of θ_{esc} and d_{min} approach those that might be expected intuitively by $\mathscr{E}_{50}$, i.e. $\theta_{esc} = 0$ approaches a maximum. The holes that persist must relate to the structure of the global chaotic phase space, i.e. any trajectories within them belong to a disjoint set of trajectories within some KAM island. However, the same cannot be said for the dark bands within the heatmaps at $\mathscr{E}$. A common feature of most of the heatmaps at $\mathscr{E}$ is shown in greater detail within Fig. 11.17, where two distinctive band formations seem to merge into one. The difference in colour is due to the variation of occupancy within different regions of the escape variable space, indicating that even within the set of coordinates at which the trajectory may escape, some are, nonetheless, more likely to be occupied than others. This may be analogous to the stickiness observed within the usual Poincaré phase sections. For values of e close to the critical value, the survival probability distribution is exponential. However, for values well above the critical value, the behaviours observed can be broken into two classes, those that clearly exponentially decrease immediately after n_{min}, and those that decrease exponentially after a transitory regime following n_{min}. For all geometries studied, the prefactor A of the linear semi-log fit of the survival probability distribution decreases by several orders of magnitude as e approaches e_{crit}. This is expected as, during this approach, the probability of escape in a finite time decreases to zero. Section 11.1.4 displays the joint probability distributions of $f(\theta_{esc})$ and n_{esc}.

11.1.4 Heat maps of θ_{esc} vs n_{esc}

The following heatmaps show the distributions of the number of iterations before escape, n, against the distribution of angles of escape, $f(\theta_{esc})$, for the same values of escaping trajectory as before. These results stress the high sensitivity of the escape event's dynamics to the billiard geometry. An example is given in Figs. 11.20 (a) and 11.21 (b), where there is only a 2% difference in the elongation. Furthermore, for every case studied, there is a clear averaging effect on the distribution of the observable as the number of ellipse misses increases, whereas the statistics of the first escape show bands of non-occupation, that can be related to the structures observed in Sec. 11.1.3.

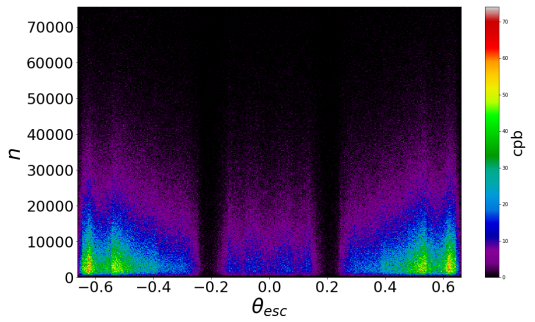

(a) $\mathscr{E}$

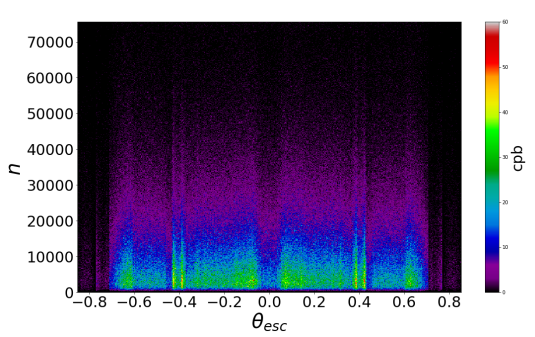

(b) $\mathscr{E}_{10}$

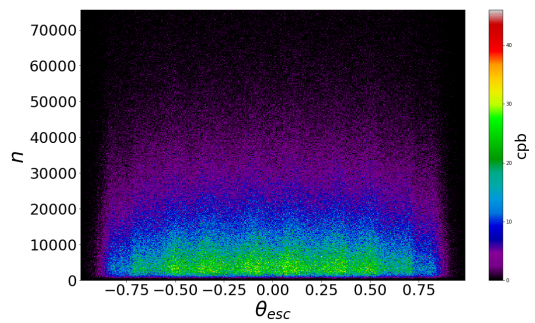

(c) $\mathscr{E}_{50}$

Figure 11.18: Heat maps relating the escape angle θ_{esc} to the number of trajectory iterations at (a) the first escape event (i.e. the first miss), (b) the tenth miss, (c) the fiftieth miss. The sample was collected from a set of trajectories launches from the unstable period-two orbit with slight deviations as given in Eqs. 11.1.2 11.1.2. Geometry of the system is: $a = 0.1, e = 1.4$

.

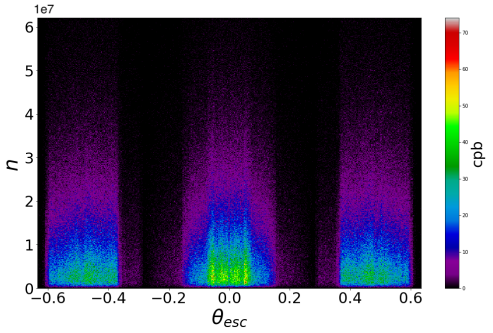

(a) $\mathscr{E}$

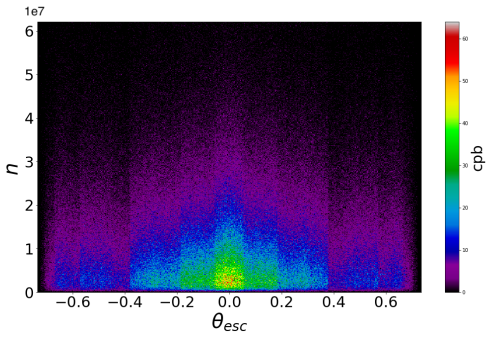

(b) $\mathscr{E}_{10}$

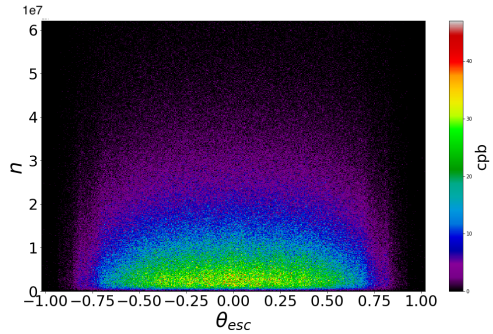

(c) $\mathscr{E}_{50}$

Figure 11.19: Same as for Fig. 11.18, but $a = 0.1, e = 1.321$

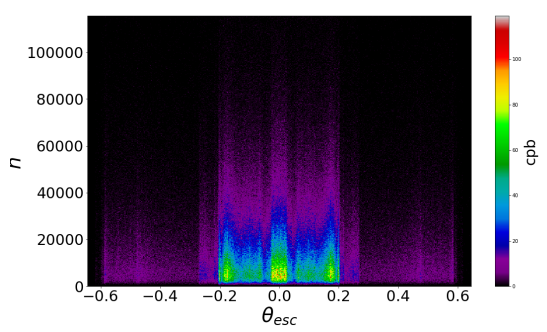

(a) $\mathscr{E}$

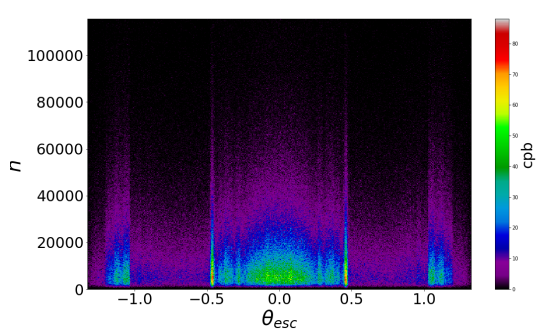

(b) $\mathscr{E}_{10}$

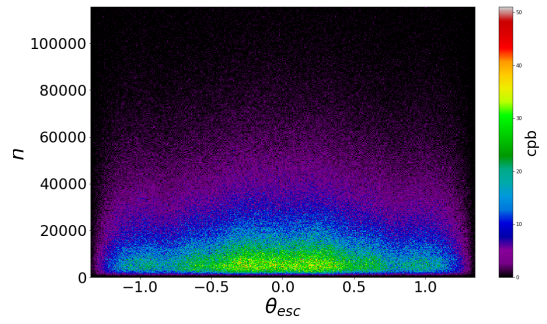

(c) $\mathscr{E}_{50}$

Figure 11.20: Same as for Fig. 11.18, but $a = 0.5, e = 1.2$

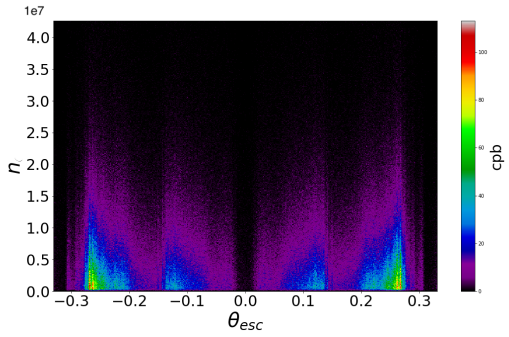

(a) $\mathscr{E}$

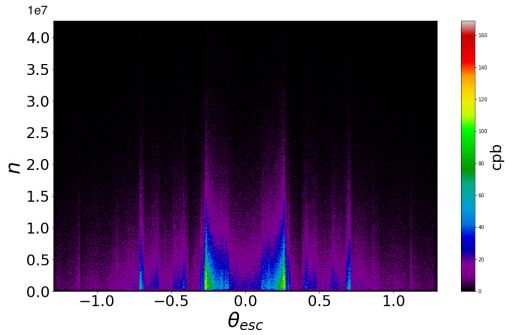

(b) $\mathscr{E}_{10}$

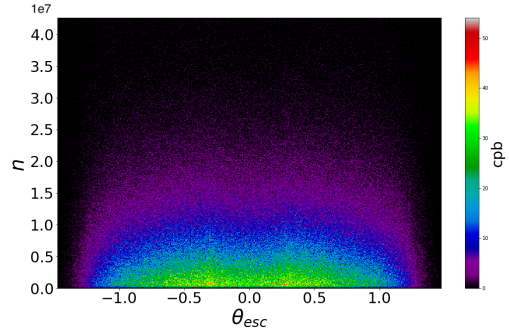

(c) $\mathscr{E}_{50}$

Figure 11.21: Same as for Fig. 11.18, but $a = 0.5, e = 1.178$

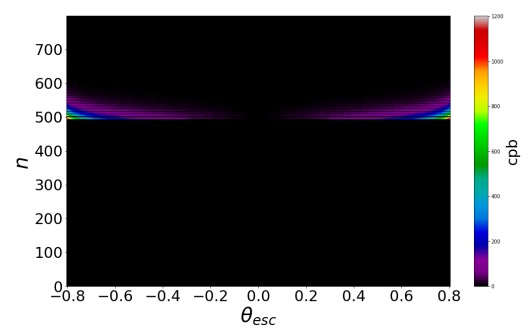

(a) $\mathscr{E}$

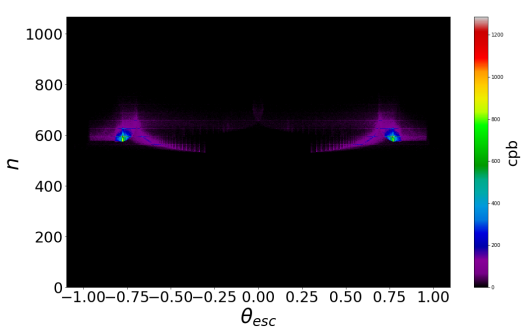

(b) $\mathscr{E}_{10}$

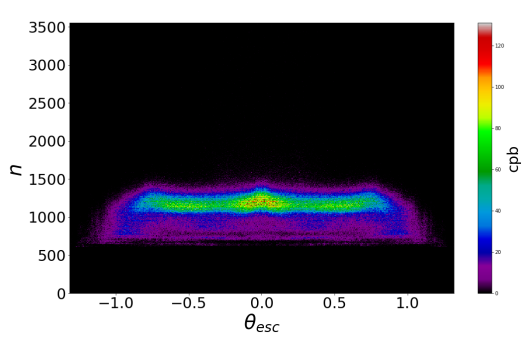

(c) $\mathscr{E}_{50}$

Figure 11.22: Same as for Fig. 11.18, but $a = 0.9, e = 1.1$

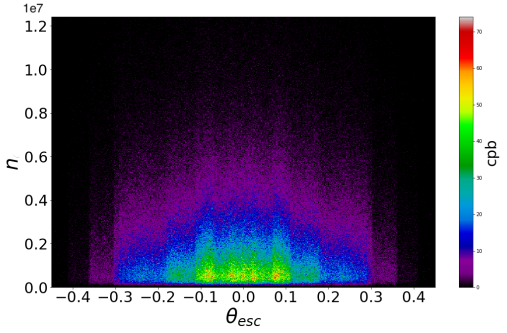

(a) $\mathscr{E}$

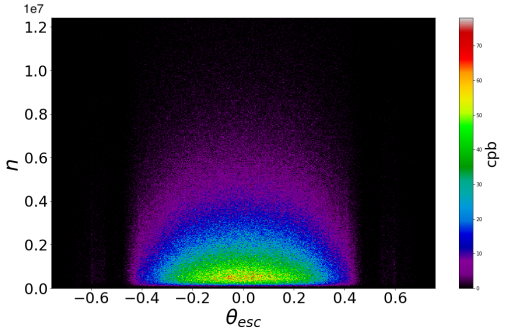

(b) $\mathscr{E}_{10}$

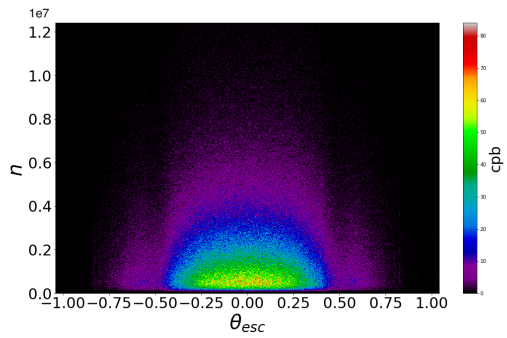

(c) $\mathscr{E}_{50}$

Figure 11.23: Same as for Fig. 11.18, but $a = 0.9, e = 1.069$

11.2 Overview of results

The third and final part of this thesis introduced a new 2D billiard system, whose geometry is defined by a unit circle enclosing a centred ellipse of variable geometry. The trajectory described by a freely moving point particle, that undergoes elastic collisions at the boundary are distinguished as periodic, quasiperiodic, and chaotic.

In chapter Chapter 9, the geometric conditions for the existence of periodic orbits that are equivalent to the circle map were identified. It was then demonstrated, by a linear stability analysis that the period-two orbit lying along the ellipse's semi-major axis is unstable for all but the totally symmetry geometrical configurations.

The billiards Poincaré phase section was obtained for a range of geometries, and it was demonstrated that the fractal dimension of the chaos-order boundary is always between one and two. No simple relationship was observed, however, between the evolution of the dimension with elongation.

Chapter 10 explored in greater depth the recurrence properties of the billiard's chaotic motion, which is a direct consequence of the universal nature of the chaos/order boundary via recurrence plots. Two associated recurrence quantification analysis tools, the recurrence rate (RR) and determinism (DET). The two measures were applied top a long orbit to demonstrate their use as sensitive indicators of stickiness in the Iris Billiard's chaotic motion.

The study of recurrence plots of the billiard's chaotic motion, when launched from the unstable periodic orbit revealed a new time measure, the study of which showed the existence of a set of critical ellipse geometries, which, in relation to the unit circle surrounding it, indicates whether or not the phase space of the billiard system undergoes a transition to global chaos, signalled by an 'escape event' symbolised by Eq. (10.3.2). This result may prove to be a generalisation of the global chaotic transition observed for the Chirikov standard map, examined in Section 9.1.2. This conclusion was further reinforced by measuring the fractal dimension of the chaos order, for very close values of elongation, above and below the critical value.

Finally, joint distributions of the escape angle, and minimum distance to the inner scatterer, as well as for the escape angle and the number of iterations until the first, tenth and fiftieth escape event were presented. The resulting forms obtained are very rich, and provide a new insight into the dynamical behaviour of the system at the moments of escape studied.

11.3 Outlook

The Iris billiard's Hamiltonian is always non-degenerate, i.e. there are no two different values of β that would map to the same θ, which would manifest as 'meandering' transport barriers in the phase space. This situation would however change, if one were to use the 'n symmetrical general' ellipse:

$$\rho_n(\theta, a, e) = \frac{a\, e}{\sqrt{e^2 \cos^2 \frac{n\theta}{2} + \sin^2 \frac{n\theta}{2}}}. \tag{11.8}$$

Various examples are shown in Fig. 11.24, whose symbolic dynamical flow, for all $n > 2$, in all but the degenerate cases is shown in Fig: 11.25. These new symmetry configurations may permit a deeper exploration of the relationship between geometry and symbolic intermittency, which, following the new symbolic flow diagram in Fig. 11.24, that will display a richer variety of symbolic trajectories than those already studied.

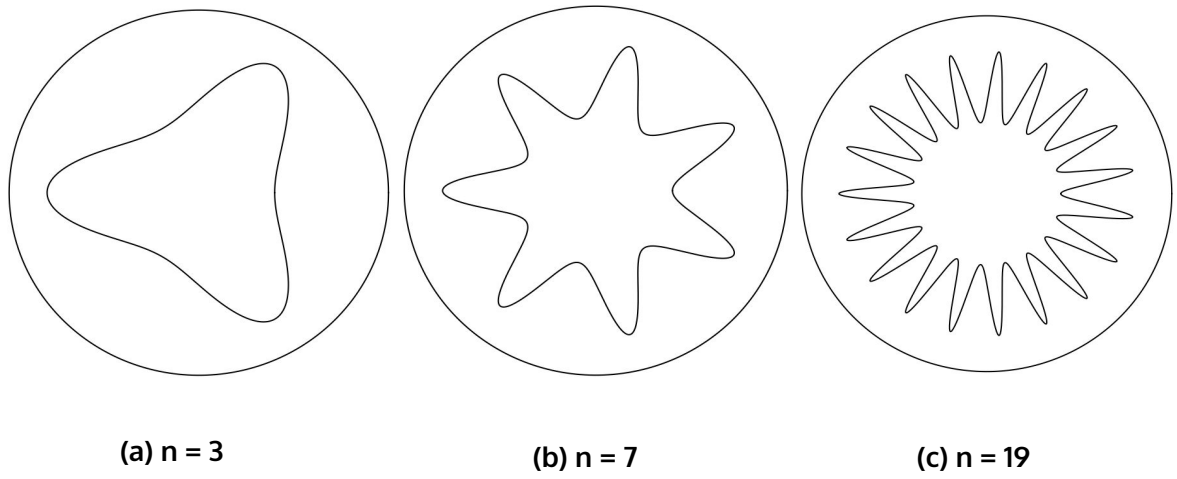

Figure 11.24: Generalised n symmetrical Iris Billiard. $a = 0.2, e = 4$.

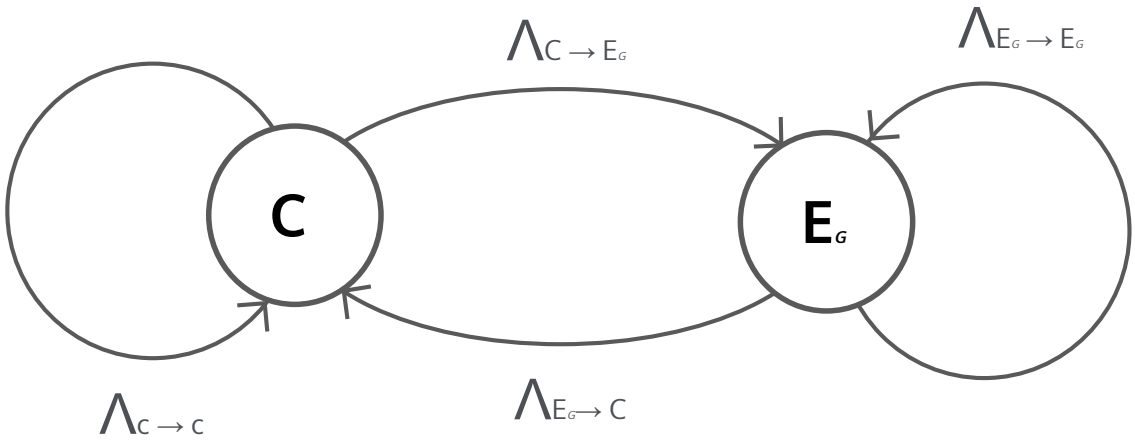

Figure 11.25: Symbolic flow diagram representation of the Iris Billiard's dynamics with a generalised $n > 3$ symmetrical ellipse. The state space is partitioned as before.

For values of $n > 2$, the central ellipse has both focusing and defocusing parts of the boundary.

Initial investigations of the 3D version of the Iris Billiard, suggest that an analogous critical geometric property discussed in this paper persists. It would therefore be natural to carry out a similar characterisation of the 3D escape event $\mathscr{E}$. It is not clear how to obtain the observable escape features in 3 dimensions by the similar geometrical arguments as employed here.

It would be interesting, and straightforward, to carry out a comparative study on the same phenomena, in the context of the eccentric annular billiard [218]. If the transition to global chaos is again observed, it would then be possible to study the Poincaré map, which has already been obtained [218], in order to identify the periodic orbits that become unstable at the critical perturbation value, via Greene's residue criterion [205, 224]. Appendix C studies how the, already obtained, Poincaré map of the annular billiard may be decomposed into two involutions, as has been done for the standard map in Appendix B. Finally, it would be of great interest to perform superconducting microwave resonator experiments, such as those previously used to explore chaos-assisted dynamical tunnelling [191, 192], with an Iris domain, or its desymmetrized version [191]. These could be carried out, for precisely machined geometries close to the critical values presented here. Such experiments could facilitate a detailed study of transport between the wave analogues of the parts of phase space that always, sometimes or never impinge upon the central ellipse.

CHAPTER
12

GENERAL CONCLUSION

This thesis presented three distinct dynamical models of particle flow, each characterised by different parameters such as temperature, constituent particle size, softness, confining geometry and its carrying capacity, to examine different conditions for intermittent flow. The first two models exchange matter or energy with their environment, while the final model is completely isolated.

Part I studied blocking phenomena in $1D$ channels. Chapter 3, considers a previously introduced model, with a finite capacity N that, when reached, causes a blockage that lasts for a constant time τ_b. When not blocked, a particle transits in a time $\tau < \tau_b$. The irreversible ($\tau_b \to \infty$) and reversible[114] cases were studied. Channel bundles, each subjected to reversible blocking, with different capacities, were also considered. Chapter 4 extended the first model by taking the transit and deblocking times, τ and τ_b, as exponentially distributed random variables with mean μ and μ^* respectively. This mathematically simpler circular Markov model, generalizable to arbitrary N, was applied to both a single channel and bundles of coupled channels. Both models present a maximum in the stationary flow as a function of entering intensity. Furthermore, it was shown in Chapter 5 that the Markovian model can be made to display the same steady state behaviour as the non-Markovian model, with an appropriate mapping between the two models' parameters. The transient behaviours of the two systems are, however, quite different. The qualitative similarities in the steady state between the non-Markovian and Markovian models suggest that the details of the channel transport mechanisms and the blockage releases are irrelevant for determining whether a maximum in the steady state flux will be present. This behaviour can therefore be interpreted as a universal property of systems with a restricted carrying capacity.

Part II studied a single channel permitting the flow of a set of soft $2D$ disks driven through a well defined geometrical narrowing. The particles within the channel were subject to repulsive 'soft-core' interparticle and particle-wall forces, as well as a driving force and a stochastic (thermal) contribution. The motivation was to introduce a statistical physics model of blockage induced intermittency with a small number of parameters. In Chapter 7, regions of particle stiffness and channel geometry were identified where the average velocity of the system behaves non-monotonically, in the low temperature regime, signalling conditions for intermittency caused by clogging. Cascade size and inter-time distributions were collected, and were both shown to follow an exponential distribution. The cascades were measured by counting the number of particles that pass over a slice of the channel geometry, per unit time. The angular distribution of the axis passing through the clogging particles were also collected. The geometrical constriction was then modified to form four overlapping fixed particles, to explore the role that the resulting competing dispersive and focussing elements play in causing intermittency. The system's global velocity, cascade size and time statistics, and angular distribution of blocking were again taken. The relationship between the non-monotonic evolution of the average global velocity and some specific channel geometries are shown to be more 'robust' to increasing stochastic perturbations (i.e. increasing temperature) than others. This

robustness determines how likely the dynamics shows intermittency for a given geometry and temperature. The importance of the system's geometrical detail, permitting the formation of meta-stable arches in the absence of friction, was highlighted.

Part III, introduced a new 2D billiard, consisting of a unit circle enclosing a centred ellipse. The trajectories described by a freely moving point particle undergoing elastic collisions with the boundaries are distinguished as periodic, quasiperiodic, and chaotic. Chapter 9 identifies the conditions for the existence of orbits equivalent to the circle map. A linear stability analysis carried out on the period-two orbit lying along the ellipse's semi-major axis showed it to be unstable for all but the totally symmetric geometrical configurations. The billiards phase space was studied, and the fractal dimension of the chaos-order boundary was characterised for a range of geometries. In Chapter 10, recurrence plots were applied to the billiard's chaotic motion, and quantifiable variables were demonstrated to be sensitive indicators of chaotic stickiness. A new time measure was introduced and used to investigate whether the system can undergo a major global chaos transition. This behaviour was then represented using a symbolic code, derived from a simple partitioning of the system's state space. The geometrically tunable symbolic intermittency signals an endogenous escape event, marked by the first time a chaotic trajectory, launched from the unstable period-two orbit, hits the outer boundary two consecutive times. Chapter 11 presented joint distributions of the escape angle, and minimum distance to the inner scatterer, as well as for the escape angle and the number of iterations until the first, tenth and fiftieth escape event, that display both unintuitive and counter-intuitive behaviours. Finally, a superconducting microwave resonator experiment, with an Iris domain for precisely machined geometries for values close above and below the critical values was proposed, for the critical geometries observed and presented, that would facilitate a detailed study of intermittent chaos-assisted tunnelling between the wave analogues of the parts of the phase space connected by the transition to global chaos.

This thesis presented different models of particulate flow, exhibiting complex behaviours delicately poised between order and disorder, as often encountered in real-life situations. Such systems often have critical states, which in the context of phase transitions, describe sharp changes in its properties upon changing an accessible control parameter. Many different control parameters were varied. These include, but are not limited to: a rule of blocking due to a finite capacity, the rigidity of a two-dimensional flow's components, and finally the symmetry breaking of the flow's enclosing geometry. The theme connecting the results produced in pursuit of this thesis is the suggestion that, for confined particulate flow, the richest dynamical behaviour requires controlling the motile components and its surrounding space in a way that can be interpreted as the optimal trade-off between robustness and flexibility.

APPENDIX
A

DERIVATION OF THE MEAN FIRST PASSAGE TIME TO THE BLOCKED STATE

In Cohen [131] the following formulas can be found for the average first hitting times $\nu_{i,j}$ of hitting level j, starting from level i, in a birth-death process with birth rates λ_n and death rates μ_n in state n:
For $i < j$,

$$\nu_{i,j} = \sum_{n=i}^{j-1} \frac{1}{\lambda_n \pi_n} \sum_{k=0}^{n} \pi_k. \tag{A.1}$$

For $i = j$ (= average first return time of state j),

$$\nu_{i,j} = \frac{\sum_{k=0}^{\infty} \pi_k}{(\lambda_j + \mu_j)\pi_j}. \tag{A.2}$$

For $i > j$,

$$\nu_{i,j} = \sum_{n=j}^{i-1} \frac{1}{\lambda_n \pi_n} \sum_{k=n+1}^{\infty} \pi_k. \tag{A.3}$$

Here,

$$\pi_0 = 1, \quad \pi_n = \frac{\lambda_0 \lambda_1 \cdots \lambda_{n-1}}{\mu_1 \mu_2 \cdots \mu_n}. \tag{A.4}$$

In the special case of an $M/M/\infty$ queue we have $\lambda_n = \lambda$ and $\mu_n = n\mu$, leading to $\pi_n = \frac{\lambda^n}{n!\mu^n} = \frac{\rho^n}{n!}$, where $\rho = \lambda/\mu$. In this case, we obtain

$$\nu_{0,j} = \sum_{n=0}^{j-1} \frac{1}{\lambda \frac{\rho^n}{n!}} \sum_{k=0}^{n} \frac{\rho^k}{k!} = \frac{1}{\lambda} \sum_{n=0}^{j-1} n! \sum_{k=0}^{n} \frac{\rho^{k-n}}{k!}. \tag{A.5}$$

that is Eq. (4.20).

A.0.1 Joint probabilities for irreversible blockage at finite time

In [109] we considered the joint probability that m particles have exited at time t *and* the system is blocked, which we denoted as $h(m,t)$. Let us consider the joint probability $g(m,t)$ that m particles have exited the channel at time t *and* that the channel is still open. Clearly

$$m(t) = \sum_{k=1}^{\infty} k(g(k,t) + h(k,t)) \tag{A.6}$$

and $f(k,t)$ introduced in Sec. 3.3 is simply $f(k,t) = g(k,t) + h(k,t)$.

The time evolution of $g(n,t)$ is given by

$$\begin{aligned}
\frac{dg(0,t)}{dt} &= -\lambda \int_0^{\min(t,1)} dt_1 \lambda e^{-\lambda t_1} q_s(0,t-t_1) - \lambda e^{-\lambda} q_s(0,t-1) \\
\frac{dg(1,t)}{dt} &= \lambda e^{-\lambda} q_s(0,t-1) - \lambda \int_0^{\min(t-1,1)} dt_1 \lambda e^{-\lambda(t_1+1)} q_s(1,t-1-t_1) - \lambda e^{-2\lambda} q_s(1,t-2) \\
\frac{dg(n,t)}{dt} &= \lambda e^{-2\lambda} q_s(n-1,t-2) - \lambda \int_0^{\min(t-1,1)} dt_1 \lambda e^{-\lambda(t_1+1)} q_s(n,t-1-t_1) - \lambda e^{-2\lambda} q_s(n,t-2).
\end{aligned} \tag{A.7}$$

The time derivative of $g(n,t)$ is given as the sum of a gain term and two loss terms. The gain term is the probability density that the *nth* particle exits at time t and that the channel is still open. This corresponds to the event where the *nth* particle enters at $t-1$ and that $n-1$ particles have already exited the channel. The first loss term corresponds to a particle which blocks the channel at time t knowing that n particles already exited. This means that a particle is still in the channel at t and a new one entering at time t blocks the channel. The last term corresponds to the exit of the *nth* particle at time t with a channel still open. The boundary term for $n=0$ does not require a time lag in the two loss terms because for $t>1$ a particle can enter without clogging the channel. A similar argument applies for $n=1$ to the gain term. Defining the Laplace transform as

$$\tilde{g}(u) = \int_0^{\infty} dt e^{-ut} g(t), \tag{A.8}$$

the differential equations become

$$u\tilde{g}(0,u) - 1 = -\lambda \frac{\lambda + ue^{-(\lambda+u)}}{\lambda+u} \tilde{q}_s(0,u). \tag{A.9}$$

Knowing that $\tilde{q}_s(0,u) = \frac{1}{\lambda+u}$, the inverse Laplace transform of $\tilde{g}(0,u)$ is

$$\tilde{g}(0,u) = \frac{1}{u} - \frac{\lambda}{u}\left(\frac{\lambda + ue^{-(\lambda+u)}}{(\lambda+u)^2}\right), \tag{A.10}$$

which gives

$$g(0,t) = (1+\lambda t - \theta(t-1)\lambda(t-1))e^{-\lambda t}. \tag{A.11}$$

To go further, let us recall that the generating function for $h(k,t)$, $G_h(z,t) = \sum_k z^k h(k,t)$, is given in Laplace space by (see [109])

$$\tilde{G}_h(z,u) = \frac{\lambda^2(1-e^{-(\lambda+u)})}{u(\lambda+u)(u+\lambda(1-ze^{-(\lambda+u)})}. \tag{A.12}$$

Introducing a generating function for $g(k,t), G_g(z,t) = \sum_k z^k g(k,t)$, one can express the number of exiting particles as

$$m(t) = \frac{\partial G_g}{\partial z}(1,t) + \frac{\partial G_h}{\partial z}(1,t). \tag{A.13}$$

By combining the differential equations of $g(k,t)$ and $h(k,t)$, one obtains

$$\frac{\partial(G_g(z,t)+G_h(z,t))}{\partial t} = (z-1)\lambda e^{-\lambda} q_s(0,t-1) + (z-1)\lambda e^{-2\lambda}(G(z,t-2) - q_s(0,t-2)), \tag{A.14}$$

where $G(z,t)$ is the generating function of $q_s(k,t)$. By taking the Laplace transform of Eq.(A.14), one has

$$u(\tilde{G}_g(z,u)+\tilde{G}_h(z,u)) - 1 = (z-1)\frac{\lambda e^{-(\lambda+u)}}{\lambda+u} + (z-1)\lambda e^{-2(\lambda+u)}(\tilde{G}(z,u) - \frac{1}{\lambda+u}). \tag{A.15}$$

Taking the partial derivative of Eq.(A.15) with respect to z and using Eq.(A.13), one obtains

$$\tilde{m}(u) = \frac{1}{u}\left(\frac{\lambda}{\lambda+u}e^{-(\lambda+u)}(1-e^{-(\lambda+u)}) + \lambda e^{-2(\lambda+u)}\tilde{G}(1,u)\right). \tag{A.16}$$

Let us recall that (see Ref.[109])

$$\tilde{G}(1,u) = \frac{1}{\lambda+u}\left[1+\frac{\lambda}{\lambda+u-\lambda e^{-(\lambda+u)}}\right]. \tag{A.17}$$

Finally, inserting Eq. (A.17) in Eq. (A.16), the Laplace transform of $m(t)$ is given by

$$\tilde{m}(u) = \frac{\lambda}{u}\frac{e^{-(\lambda+u)}}{\lambda+u-\lambda e^{-(\lambda+u)}}. \tag{A.18}$$

Note that Eq. (A.18) can be written as

$$\tilde{m}(u) = \frac{\tilde{j}(u)}{u} \tag{A.19}$$

and one now recovers that $m(t) = \int_1^t dt' j(t')$. One also checks that $m(\infty) = \lim_{u\to 0} u\tilde{m}(u) = \frac{e^{-\lambda}}{1-e^{-\lambda}}$ as expected.

APPENDIX
B

SYMMETRY LINES OF THE STANDARD MAP

Many thanks to Charles Antoine for this calculation, permitting an insight of the role of the involution structure of a $2D$ area preserving map for identifying its periodic orbits.

B.1 Involutions of standard map, and fixed points

$\mathbf{T}$ may be written as the composition of two different involutions: $\mathbf{T} = \mathbf{I_1} \circ \mathbf{I_0}$. $\mathbf{I_0^2} = \mathbf{I_1^2} = \mathbb{I}$. As a result of the composition:

$$\mathbf{T^{-1}} = (\mathbf{I_1} \circ \mathbf{I_0})^{-1} = \mathbf{I_0} \circ \mathbf{I_1} = \mathbf{I_0} \circ \mathbf{T} \circ \mathbf{I_0}. \tag{B.1}$$

New involutions may be generated by following the rule:

$$\mathbf{I_j} = \mathbf{T^j} \circ \mathbf{I_0}, \qquad \mathbf{I_j} \circ \mathbf{I_j} = \mathbb{I}. \tag{B.2}$$

We may therefore consider the set of all transformations, $\mathbf{T^k}$, $\mathbf{I_j}$, $\{k, j\} \in \mathbb{Z}$ which constitutes the following discrete infinite group [225] :

$$\mathbf{T^k} \circ \mathbf{I_j} = \mathbf{I_{j+k}}, \tag{B.3}$$

$$\mathbf{I_j} \circ \mathbf{I_k} = \mathbf{T^{j-k}}, \tag{B.4}$$

$$\mathbf{I_j} \circ \mathbf{T^k} = \mathbf{I_{j-k}}. \tag{B.5}$$

In the linear regime ($k = 0$), the *position inversion operator*, $\mathbf{I_0}$ is given by:

$$\mathbf{I_0} \begin{pmatrix} x \\ p \end{pmatrix} = \begin{pmatrix} -1 & 0 \\ 0 & 1 \end{pmatrix} \begin{pmatrix} x \\ p \end{pmatrix} = \begin{pmatrix} -x \\ p \end{pmatrix} \tag{B.6}$$

However, as we move beyond the linear regime ($k \neq 0$), we must instead apply operator notation such that:

$$\mathbf{I_0} : \begin{cases} x = -x & [\text{ mod } 1], \quad \text{(B.7a)} \\ p = p - \dfrac{k}{2\pi} \sin(2\pi x) & [\text{ mod } 1]. \quad \text{(B.7b)} \end{cases}$$

Note: once may equally well define a momentum inversion operator, that result from **T**'s *time reversal symmetry*, which would in turn lead to the generation of a different set of involution operators, that will not be considered here.

A point, $\mathbf{r} = (x, p)$ is N periodic of **T** when N is the smallest integer that satisfies $\mathbf{T}^N\mathbf{r} = \mathbf{r}$. We define a symmetry line, Γ_j , $j \in \mathbb{Z}$, as the set of fixed points of the involution $\mathbf{I_j}$, i.e.

$$\Gamma_j \ : \ \{\, \mathbf{r} \mid \mathbf{I_j r} = \mathbf{r} \,\}. \tag{B.8}$$

A point, lying on the symmetry is only a **fixed point** (**FP**) if *both* the x and p components of the involution under study satisfy (B.8), i.e. one condition is contained within the other. Upon re-examining Eq.(B.4), we can therefore expect that any point of intersection of the symmetry lines Γ_i, Γ_j, resulting from the set of fixed points of $\mathbf{I_i}$, $\mathbf{I_j}$ will be a periodic point. Eqs: (B.3) & (B.5) show that a symmetry line is transformed by $\mathbf{T}^N$ or $\mathbf{I}_N$ onto other symmetry lines [223].

The symmetry lines are fundamental to the structure of the mixed dynamics of the standard map, as they can be used to determine the system's periodic orbits that form the 'skeleton' of the phase space. These periodic orbits are determined by the set of fixed points of the set of involution operators that are generated by the above rules.

B.1.1 FP of $\mathbf{I_0}$

We introduce a new variable, $g \in \mathbb{Z}$, to help us account for fixed points within the toroidal structure of the phase space. It is important to note at this point that every value of g considered for each condition must be seen as a seperate variable. Applying Eq:(B.8) to Eq (B.7a) returns:

$$2x = g \in \mathbb{Z}. \tag{B.9}$$

As $x \in [0,1]$, therefore $g = \{0,1,2\}$. The values of x that correspond to the fixed points are therefore $x = \{0, 1/2, 1\}$. Considering the fixed point behavior derived from Eq (B.7b) gives:

$$-\frac{k}{2\pi}\sin(2\pi x) = g \in \mathbb{Z}, \tag{B.10}$$

Setting $g = 0$ returns the previously obtained $x = \{0, 1/2, 1\}$. Otherwise setting $|g| > 0$ gives:

$$\sin(2\pi x) = \pm\frac{2\pi g}{k} \tag{B.11}$$

which only returns solutions $\forall k > 2\pi|g|$, otherwise, condition (B.7b) returns no solutions. Therefore, the fixed points of $\mathbf{I_0}$, for $k \leq 1$ are :

$$\begin{pmatrix} 0 \\ p \end{pmatrix}, \quad \begin{pmatrix} 1/2 \\ p \end{pmatrix}, \quad \begin{pmatrix} 1 \\ p \end{pmatrix}, \ \forall p. \tag{B.12}$$

B.2 Definition & FP of $\mathbf{I_1}$.

Applying the rule given by Eq:(B.2) to $\mathbf{I_0}$, and some simplification returns :

$$\mathbf{I_1} : \begin{cases} x = -x + p & [\text{ mod } 1], \quad \text{(B.13a)} \\ p = p & [\text{ mod } 1]. \quad \text{(B.13b)} \end{cases}$$

We immediately see that Eq (B.13b) gives no conditions. Considering Eq (B.13a) and following the same procedure as in Sec B.1.1, returns:

$$p_g - 2x = g \in \mathbb{Z} \mid 0 \leq x \leq 1,\ 0 \leq p_g \leq 1 \quad \therefore\ -2 \leq p_g - 2x \leq 1. \tag{B.14}$$

Therefore, the permitted values of g within the above bounds are $\{1, 0, -1, -2\}$. Setting p as subject returns the following four lines of fixed points of $\mathbf{I_1}$, $\forall k \neq 0$:

$$\begin{pmatrix} x \\ 2x+1 \end{pmatrix},\ \begin{pmatrix} x \\ 2x \end{pmatrix},\ \begin{pmatrix} x \\ 2x-1 \end{pmatrix},\ \begin{pmatrix} x \\ 2x-2 \end{pmatrix}. \tag{B.15}$$

B.3 Definition & FP of $\mathbf{I_{-1}}$

To understand how to obtain inverse involutions, we again consider the decomposition of the standard map:

$$\mathbf{T} = \mathbf{I_1} \circ \mathbf{I_0}, \tag{B.16}$$

whose inverse may be obtained, as shown in (B.1) by:

$$\mathbf{T^{-1}} = (\mathbf{I_1} \circ \mathbf{I_0})^{-1} = \mathbf{I_0}^{-1} \circ \mathbf{I_1}^{-1} = \mathbf{I_0} \circ \mathbf{I_1}. \tag{B.17}$$

The final term follows from the intrinsic characteristics of involutes. We can therefore define the inverse of the first involute by:

$$\mathbf{I_{-1}} = \mathbf{T^{-1}} \circ \mathbf{I_0} = \mathbf{I_0} \circ \overbrace{\mathbf{I_1} \circ \mathbf{I_0}}^{\mathbf{T}} = \mathbf{I_0} \circ \mathbf{T}. \tag{B.18}$$

Applying the inverse of the first involute to some pair of co-ordinates (x, p) returns:

$$\mathbf{I_{-1}} \circ \begin{pmatrix} x \\ p \end{pmatrix} = \mathbf{I_0} \circ \left(\mathbf{T} \circ \begin{pmatrix} x \\ p \end{pmatrix} \right) = \mathbf{I_0} \circ \begin{pmatrix} x + p - \frac{k}{2\pi}\sin(2\pi x) \to x' \\ p - \sin(2\pi x) \to p' \end{pmatrix} = \begin{pmatrix} -x' \\ p' - \frac{k}{2\pi}\sin(2\pi x'). \end{pmatrix} \tag{B.19}$$

therefore:

$$\mathbf{I_{-1}} \circ \begin{pmatrix} x \\ p \end{pmatrix} = \begin{pmatrix} -(x+p) + \frac{k}{2\pi}\sin(2\pi x) \\ p - \frac{k}{2\pi}\sin(2\pi x) - \frac{k}{2\pi}\sin A_{x,p} \end{pmatrix}. \tag{B.20}$$

where:

$$A_{x,p} = 2\pi \left(x + p - \frac{k}{2\pi}\sin(2\pi x) \right). \tag{B.21}$$

Considering Eq B.20 returns:

$$\mathbf{I_{-1}}: \begin{cases} x = -(x+p) + \dfrac{k}{2\pi}\sin(2\pi x) & [\text{ mod } 1], \quad \text{(B.22a)} \\ p = p - \dfrac{k}{2\pi}\sin(2\pi x) - \dfrac{k}{2\pi}\sin A_{x,p} & [\text{ mod } 1]. \quad \text{(B.22b)} \end{cases}$$

Condition (B.22a) may be rewritten as:

$$2x + p_g - \frac{k}{2\pi}\sin(2\pi x) = g \in \mathbb{Z}. \tag{B.23}$$

Reconsidering the limits imposed on $x, p \in [0,1]$ returns the possible values of $g = \{0,1,2,3\}$ $\forall k \leq 2$. Further increasing k widens in both directions the set of possible values of g. Within the range $0 \leq k \leq 2$, we obtain four lines of fixed points by setting p_g as the subject:

$$\left(\begin{matrix} x \\ -2x + \frac{k}{2\pi}\sin(2\pi x), \end{matrix}\right), \quad \left(\begin{matrix} x \\ 1 - 2x + \frac{k}{2\pi}\sin(2\pi x), \end{matrix}\right), \quad \left(\begin{matrix} x \\ 2 - 2x + \frac{k}{2\pi}\sin(2\pi x), \end{matrix}\right), \quad \left(\begin{matrix} x \\ 3 - 2x + \frac{k}{2\pi}\sin(2\pi x). \end{matrix}\right). \tag{B.24}$$

We now consider condition (B.22b) which returns:

$$\sin(2\pi x) + \sin\left(2\pi(x+p) - k\sin(2\pi x)\right) = \frac{2\pi}{k} g \;\; g \in \mathbb{Z}. \tag{B.25}$$

in the limit $k < 1$, the only possible solution corresponds to $g = 0$, which, by considering the arguments of both left hand sin terms, returns the following possible solutions:

$$x + p_g - \frac{k}{2\pi}\sin(2\pi x) = -x \qquad [mod 1], \tag{B.26}$$

$$= x + 1/2 \; [mod 1]. \tag{B.27}$$

Eq (B.26) returns the same condition as (B.22a), whose four fixed points were obtained. Simplifying condition (B.27) returns:

$$p_g - \left(\frac{1}{2} + \frac{k}{2\pi}\sin(2\pi x)\right) = g \in \mathbb{Z}. \tag{B.28}$$

therefore, $g \in [-1/2 - k/(2\pi), 1/2 + k/(2\pi)]$. Therefore, for $k < \pi$, $g = 0$, giving:

$$p_0 = \frac{1}{2} + \frac{k}{2\pi}\sin(2\pi x) \tag{B.29}$$

which gives the points satisfied by *both* (B.22b) & (B.22a).

B.4 Definition & FP of $\mathbf{I_2}$

Following the rule given by Eq. (B.2) , the re-application of the standard map operator,$\mathbf{I_2} = \mathbf{T} \circ \mathbf{I_1}$, returns :

$$\mathbf{I_2} : \begin{cases} x = -x + 2p - \frac{k}{2\pi}\sin X_{x,p} & [\text{ mod } 1], \quad \text{(B.30a)} \\ p = p - \frac{k}{2\pi}\sin X_{x,p} & [\text{ mod } 1]. \quad \text{(B.30b)} \end{cases}$$

where

$$X_{x,p} = 2\pi(p - x), \tag{B.31}$$

Considering the fixed point of Eq. B.30a returns:

$$2(p-x) - \frac{k}{2\pi}\sin X_{x,p} = 2(p-x) - \frac{k}{2\pi}\sin(2\pi(p-x)) = g \in \mathbb{Z}. \tag{B.32}$$

for $k < 2\pi$, $g \in \{-2,-1,0,1,2\}$, therefore returning a set of five implicit equations given by.

$$p_g = x + \frac{g}{2} + \frac{1}{4\pi}\sin\left(2\pi(p_g - x)\right), \;\; g \in \{-2,-1,0,1,2\}. \tag{B.33}$$

However, we now take advantage of the fact that any equation of the form :

$$\alpha = \beta \sin\alpha, \tag{B.34}$$

presents only one root, $\alpha = 0$, given $|\beta| \leq 1$. More than one roots are present for greater values of β. We accordingly re-arrange the system of equations given by B.33 as:

$$2\pi(p_g - x - g/2) = (-)^g \frac{k}{2} \sin(2\pi(p_g - x - g/2)),\ \ g \in \{-2,-1,0,1,2\}. \tag{B.35}$$

Where both the $(-)^g$ term and the $-g/2$ in the argument of the right hand sine term are introduced, which the periodic *and* anti-symmetric nature of the sine function permits. We therefore retrieve the form of Eq. B.34, which, given $k < 2$, returns roots satisfying:

$$\alpha/(2\pi) = p_g - x - g/2 = 0. \tag{B.36}$$

i.e.

$$p_g = x + g/2,\ \ g \in \{-2,-1,0,1,2\}. \tag{B.37}$$

therefore returning the following five lines of fixed points of $\mathbf{I_2}$.

$$\begin{pmatrix} x \\ x-1 \end{pmatrix},\ \begin{pmatrix} x \\ x-1/2 \end{pmatrix},\ \begin{pmatrix} x \\ x \end{pmatrix},\ \begin{pmatrix} x \\ x+1/2 \end{pmatrix},\ \begin{pmatrix} x \\ x+1 \end{pmatrix}. \tag{B.38}$$

We now consider the fixed points obtained from condition (B.30b) which returns:

$$\sin(2\pi(p-x)) = \frac{2\pi g}{k},\ \ g \in \mathbb{Z}. \tag{B.39}$$

which as similarly seen in section B.1.1, will only return solutions for $g = 0$ for sufficiently small k. Under this condition, reconsidering the term within the left hand sin argument gives:

$$2\underbrace{(p-x)}_{\in[-1,1]} = 0\ \ [mod 1]. \tag{B.40}$$

therefore returning the same condition as in B.37.

B.4.1 Definition & FP of $\mathbf{I_{-2}}$

We construct $\mathbf{I_{-2}}$ by reapplying the rule given by (B.2) on to $\mathbf{I_{-1}}$:

$$\mathbf{I_{-2}} = \mathbf{T^{-1}} \circ \mathbf{I_{-1}} = \mathbf{T^{-2}} \circ \mathbf{I_0}. \tag{B.41}$$

Therefore:

$$\mathbf{I_{-2}} \circ \begin{pmatrix} x \\ p \end{pmatrix} = \mathbf{I_0} \circ \mathbf{I_1} \circ \mathbf{I_{-1}} \circ \begin{pmatrix} x \\ p \end{pmatrix} \tag{B.42}$$

We have already studied the application of $\mathbf{I_{-1}}$ to $\mathbf{r} = (x, p)$, and so we reuse the result here to give:

$$\mathbf{I_{-2}} \circ \begin{pmatrix} x \\ p \end{pmatrix} = \mathbf{I_0} \circ \mathbf{I_1} \circ \begin{pmatrix} -(x+p) + \frac{k}{2\pi}\sin(2\pi x) \to x' \\ p - \frac{k}{2\pi}\sin(2\pi x) - \frac{k}{2\pi}\sin A_{x,p} \to p' \end{pmatrix}, \tag{B.43}$$

We can finally write the application of the second inverse involution as:

$$\mathbf{I_{-2}} \circ \begin{pmatrix} x \\ p \end{pmatrix} = \mathbf{I_0} \circ \mathbf{I_1} \circ \begin{pmatrix} x' \\ p' \end{pmatrix} = \mathbf{I_0} \circ \begin{pmatrix} p'-x' \\ p' \end{pmatrix} = \begin{pmatrix} x'-p' \\ p' - \frac{k}{2\pi}\sin(2\pi(p'-x')) \end{pmatrix}. \tag{B.44}$$

Which, upon re-substitution of x' and p' returns:

$$\mathbf{I_{-2}} \circ \begin{pmatrix} x \\ p \end{pmatrix} = \begin{pmatrix} -(x+2p) + \frac{k}{\pi}\sin(2\pi x) + \frac{k}{2\pi}\sin A_{x,p} \\ p - \frac{k}{2\pi}\sin(2\pi x) - \frac{k}{2\pi}\sin A_{x,p} + \frac{k}{2\pi}\sin B_{x,p} \end{pmatrix}. \tag{B.45}$$

Where

$$B_{x,p} = 2\pi\left(x + 2p - \frac{k}{2\pi}\sin(2\pi x) - \frac{k}{2\pi}\sin A_{x,p}\right). \tag{B.46}$$

To find the FP, the following is considered:

$$\mathbf{I_{-2}}: \begin{cases} x = -(x+2p) + \dfrac{k}{\pi}\sin(2\pi x) + \dfrac{k}{2\pi}\sin A_{x,p} & [\text{ mod } 1], \quad \text{(B.47a)} \\ p = p - \dfrac{k}{2\pi}\sin(2\pi x) - \dfrac{k}{2\pi}\sin A_{x,p} + \dfrac{k}{2\pi}\sin B_{x,p} & [\text{ mod } 1]\,. \quad \text{(B.47b)} \end{cases}$$

Considering the fixed points of Eq B.47a returns:

$$2x + 2p - \frac{k}{\pi}\sin(2\pi x) - \frac{k}{2\pi}\sin A_{x,p} = g \in \mathbb{Z}. \tag{B.48}$$

which for small enough $k < 2\pi/3$, gives $g \in [0,1,2,3,4]$. We now search for the fixed points in a similar way as for $\mathbf{I_2}$ by retrieving an equation of form (B.34) by the following re-arrangement:

$$2\pi\left(x + p - \frac{k}{2\pi}\sin(2\pi x) - \frac{g}{2}\right) = \frac{k}{2}\sin A_{x,p} = \frac{k}{2}\sin\left(2\pi\left(x + p - \frac{k}{2\pi}\sin(2\pi x)\right)\right). \tag{B.49}$$

As before, we introduce a new variable, α_g such that:

$$\alpha_g = 2\pi\left(x + p - \frac{k}{2\pi}\sin(2\pi x) - \frac{g}{2}\right). \tag{B.50}$$

which substituting into Eq. B.49 gives:

$$\alpha_g = \frac{k}{2}\sin(\alpha_g \pm \pi g) = (-)^g\frac{k}{2}sin(\alpha_g). \tag{B.51}$$

which $\forall g$, $|k| < 2$ only permits one solution, $\alpha_g = 0$. We can therefore determine the five solutions to condition (B.47a) :

$$p_g = \frac{k}{2\pi}\sin(2\pi x) + \frac{g}{2} - x, \;\; g \in \{0,1,2,3,4\}. \tag{B.52}$$

Considering the fixed points of Eq. (B.47b) returns:

$$\sin(2\pi x) + \sin A_{x,p} + \sin B_{x,p} = \frac{2\pi g}{k}, \;\; g \in \mathbb{Z}. \tag{B.53}$$

Therefore $g \in [-3k/2\pi, 3k/2\pi]$. Meaning, that $\forall k < 2\pi/3$, $g = 0$.

The true fixed points of $\mathbf{I_{-2}}$ are those that satisfy *both* (B.54) & (B.52). As (B.54) with (B.49) shows that $\sin A_{x,p} = 0$, which upon substitution to (B.52) which in turn is resubstituted into (B.52) returns:

$$\sin(2\pi x) + 0 + \sin\left(2\pi\overbrace{\left(x + 2p - \frac{k}{2\pi}\sin(2\pi x)\right)}^{g-x}\right) = \sin(2\pi x) - \sin(2\pi x) = 0. \tag{B.54}$$

Therefore (B.54) provides the fixed points of $\mathbf{I_{-2}}$.

B.5 Definition & FP of $\mathbf{I_3}$

We will once more apply the standard map operator to return $\mathbf{I_3} = \mathbf{T} \circ \mathbf{I_2}$, giving:

$$\mathbf{I_3}: \begin{cases} x = -x + 3p - \frac{k}{\pi}\sin X_{x,p} - \frac{k}{2\pi}\sin Y_{x,p} & [\text{ mod } 1], \quad \text{(B.55a)} \\ p = p - \frac{k}{2\pi}\sin X_{x,p} - \frac{k}{2\pi}\sin Y_{x,p} & [\text{ mod } 1], \quad \text{(B.55b)} \end{cases}$$

where

$$Y_{x,p} = 2\pi\left(-x + 2p - \frac{k}{2\pi}\sin X_{x,p}\right). \tag{B.56}$$

Re-arranging Eg (B.55a) gives:

$$2x - 3p + \frac{k}{\pi}\sin X_{x,p} + \frac{k}{2\pi}\sin Y_{x,p} = g \in \mathbb{Z}. \tag{B.57}$$

returns the limits of g as $g \in [-2 - \frac{3k}{2\pi}, 3 + \frac{3k}{2\pi}]$, therefore giving five values of $g \in [-2,-1,0,1,2,3]$ in turn defining five lines of fixed points that must be implicitly solved.

Note: In the limit $k = 0$, these **FP** lines follow:

$$p_g = \frac{2}{3}x + \frac{g}{3}, \quad g \in \{-2,-1,0,1,2,3\}. \tag{B.58}$$

We now consider (B.55b) , which re-arranging returns:

$$\frac{k}{\pi}(\sin X_{x,p} + \sin Y_{x,p}) = g \in \mathbb{Z} \tag{B.59}$$

Therefore, the range of values within which g may lie is $\in [-k/\pi, k/\pi]$. i.e. for small values of k, $g = 0$. Re-arranging returns:

$$-X_{x,p} = Y_{x,p} \quad [mod\ 2\pi], \tag{B.60}$$
$$= \pi - Y_{x,p}\ [mod\ 2\pi]. \tag{B.61}$$

Unpacking $X_{x,p}$ & $Y_{x,p}$ in (B.60) and re-arranging returns:

$$3p - 2x + \frac{k}{2\pi}\sin(2\pi(p-x)) = g \in \mathbb{Z}. \tag{B.62}$$

returning the limits of g as $g \in [-2 - k/2\pi, 3 + k/2\pi]$, which therefore $\forall k < 2\pi$ returns $g \in \{-2,-1,0,1,2,3\}$ and so rearranging we obtain the following six **FP** lines:

$$p_g(x) = \frac{2x+g}{3} - \frac{k}{6\pi}\sin(2\pi(p_g(x) - x)) = \frac{2x+g}{3} - \frac{k}{6\pi}\sin X_{x,p_g} \quad g \in \{-2,-1,0,1,2,3\}. \tag{B.63}$$

Returning condition(B.62) into (B.55a) (as well as considering (B.60)) returns $g = g$, showing that the results are satisfied by both conditions.
We may also Unpack $X_{x,p}$ & $Y_{x,p}$ in (B.61) which returns:

$$p - \frac{1}{2} - \frac{k}{2\pi}\sin(2\pi(p-x)) = g \in \mathbb{Z} \tag{B.64}$$

returning the limits of g as $g \in [-\frac{1}{2} - \frac{k}{2\pi}, \frac{1}{2} + \frac{k}{2\pi}]$ which when considering again small values of $k < 2\pi$ gives $g = 0$ as the only possible solution. We therefore obtain one more **FP** line:

$$p_0(x) = \frac{1}{2} + \frac{k}{2\pi}\sin(2\pi(p_0(x) - x)) = \frac{1}{2} + \frac{k}{2\pi}\sin(X_{x,p_0}). \tag{B.65}$$

We can finally give all **FP** of $\mathbf{I_3}$ as the implicit equation given by (B.63), which will be numerically plotted. The condition given by Eq. (B.65) is not included as it is *not* included in (B.60).

B.6 Graphics of analytical symmetry lines

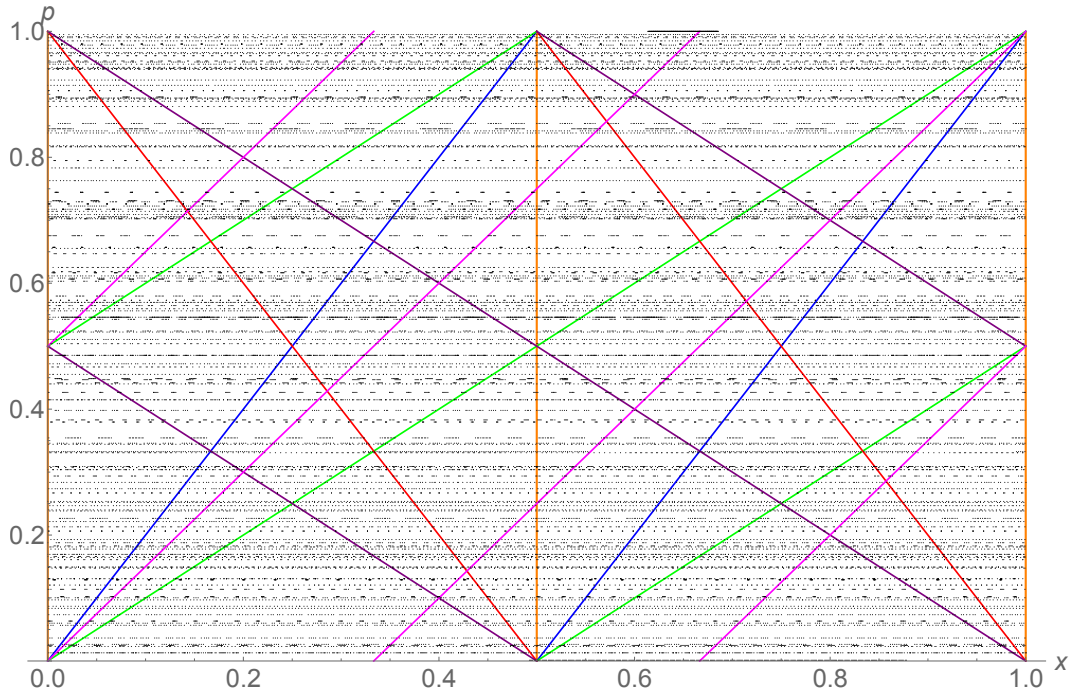

Figure B.1: $k = 0.0$, Symmetry lines : $\rightarrow \mathbf{I_0}$ $\rightarrow \mathbf{I_1}$ $\rightarrow \mathbf{I_{-1}}$ $\rightarrow \mathbf{I_2}$ $\rightarrow \mathbf{I_{-2}}$ $\rightarrow \mathbf{I_3}$

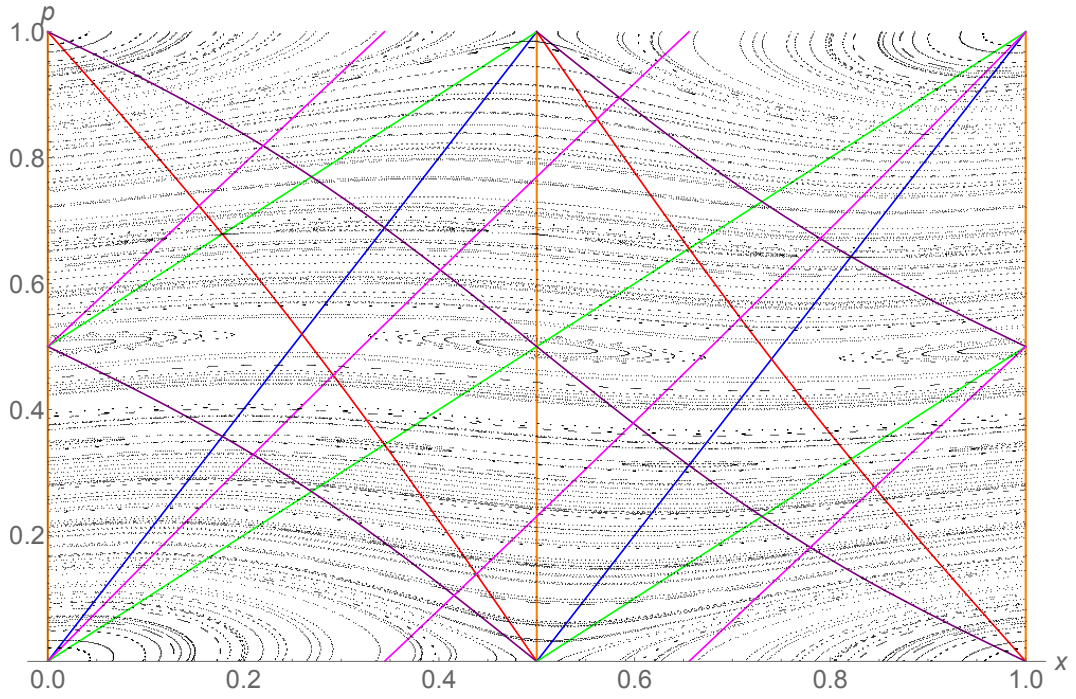

Figure B.2: $k = 0.25$, Symmetry lines : $\rightarrow \mathbf{I_0}$ $\rightarrow \mathbf{I_1}$ $\rightarrow \mathbf{I_{-1}}$ $\rightarrow \mathbf{I_2}$ $\rightarrow \mathbf{I_{-2}}$ $\rightarrow \mathbf{I_3}$

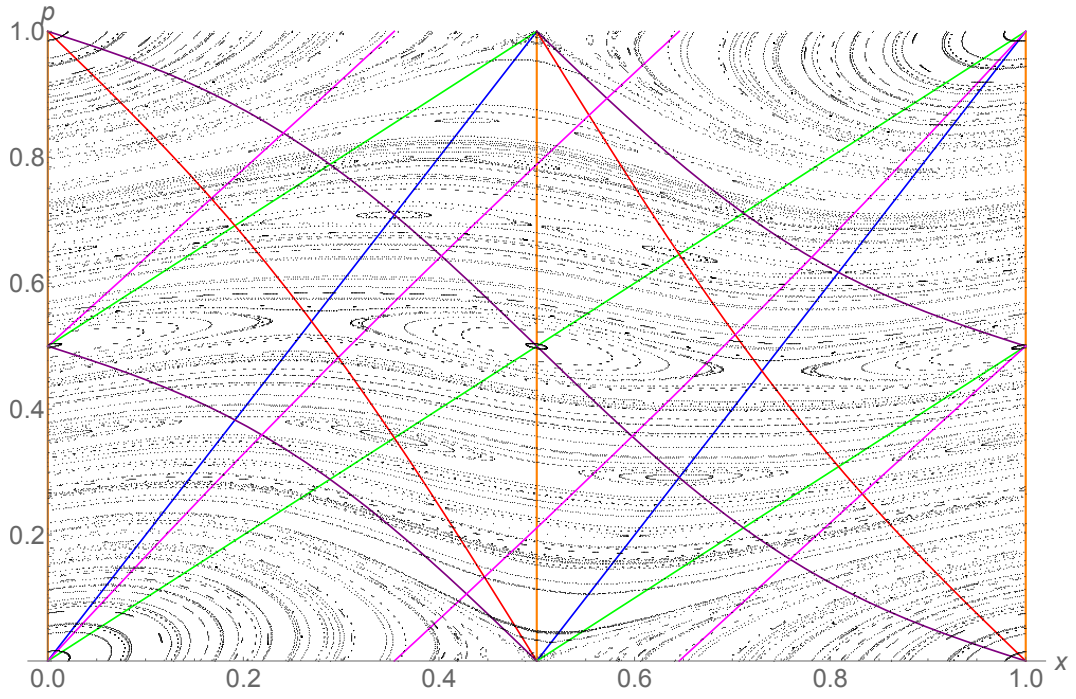

Figure B.3: $k = 0.5$, Symmetry lines : $\rightarrow \mathbf{I_0}$ $\rightarrow \mathbf{I_1}$ $\rightarrow \mathbf{I_{-1}}$ $\rightarrow \mathbf{I_2}$ $\rightarrow \mathbf{I_{-2}}$ $\rightarrow \mathbf{I_3}$

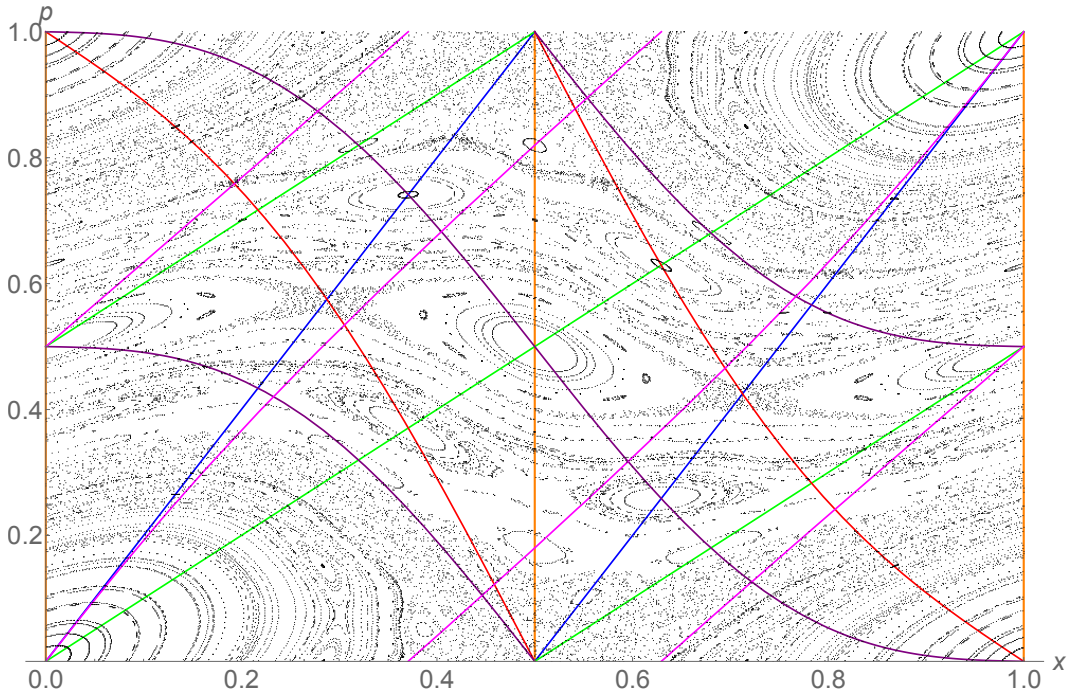

Figure B.4: $k = 0.97$, Symmetry lines : $\rightarrow \mathbf{I_0}$ $\rightarrow \mathbf{I_1}$ $\rightarrow \mathbf{I_{-1}}$ $\rightarrow \mathbf{I_2}$ $\rightarrow \mathbf{I_{-2}}$ $\rightarrow \mathbf{I_3}$

APPENDIX
C

ECCENTRIC ANNULAR BILLIARD POINCARÉ MAP

Many thanks to Charles Antoine for this calculation, permitting a first step for applying the involution structure of a first return map of the $2D$ eccentric annular billiard, for identifying its periodic orbits.

The Eccentric Annular billiard, like the Iris billiard, is composed of a two part boundary. An outer circle, and an inner curve that in both cases, reduces to a centred annulus at the symmetric integrable limit. Chaotic dynamics is introduced in both systems but making the system pass from having only one centred geometric focus, to many. In the case of of the iris billiard, for $e > 1$, the number of foci is three. One central focus for the outer circle, and two foci corresponding to the ellipse. In the case of the eccentric annular billiard however, there are two. One, again for the outer circle, and the other corresponding to the displaced inner circle, at distance d from the origin along the axis of displacement. In both cases, the use of $d > 0$ or $e > 1$ serve a role analogous to that of $k > 0$ in the standard map, in that it causes the onset of chaotic dynamics.

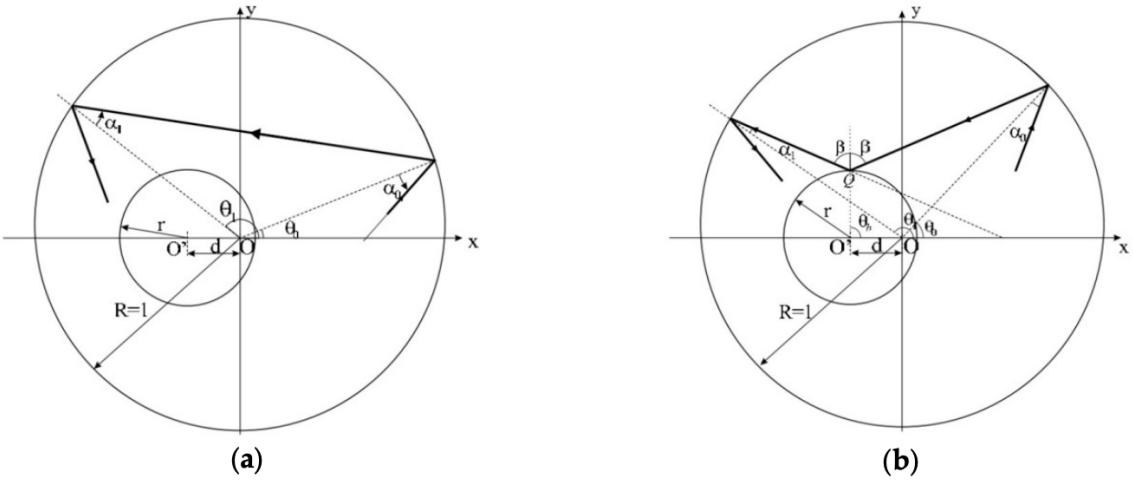

Figure C.1: Schema of eccentric annular billiard system. (a) showing $\{..\mathbf{O},\mathbf{O}..\}$ dynamic. (b) showing $\{..\mathbf{O},\mathbf{I},\mathbf{O}..\}$ dynamic. Source: Ref. [218].

The annular billiard, like the Iris billiard, displays two types of dynamics when undergoing a first return to the outer boundary, O. Either a direct transition $O \to O$, or with an intermediate collision with the inner scatter:

$O \to I \to O$. The latter is considered, whose Poincaré map is given by:

$$\mathbf{P_n}: \begin{cases} \alpha_{n+1} = \sin^{-1}(r\sin\beta - d\sin(2\beta + \theta_n - \alpha_n)), & \text{(C.1a)} \\ \theta_{n+1} = 2\beta + \theta_n - \alpha_n - \alpha_{n+1}. & \text{(C.1b)} \end{cases}$$

where

$$\beta = \sin^{-1}\left[\frac{1}{r}\{\sin\alpha_n - d\sin(\theta_n - \alpha_n)\}\right]. \tag{C.2}$$

Here we use the notation as in Ref [218].

C.1 Theory for obtaining billiard periodic orbits

Given a billiard map $\mathbf{P}$, & a time reversal symmetry $\mathbf{T}$ involution such that:

$$\mathbf{T}^{-1} \circ \mathbf{P} \circ \mathbf{T} = \mathbf{P}^{-1} \tag{C.3}$$

under the condition that $\mathbf{T}^2 = \mathbb{I}$. The curves of fixed points **(FP)** of $\mathbf{P^n} \circ \mathbf{T}$ return the periodic orbits of $\mathbf{P}$. If $\mathbf{r} = (\alpha, \theta)$ is a **FP** of *both* $\mathbf{P^n} \circ \mathbf{T}$ & $\mathbf{P^m} \circ \mathbf{T}$, $m \neq n$, $\mathbf{r}$ is therefore a **FP** of $\mathbf{P^{n-m}}$

Proof.

$$\mathbf{P^{n-m}} \circ \mathbf{r} = \mathbf{P^n} \circ \mathbf{P^{-m}} \circ \mathbf{r} = \mathbf{P^n} \circ \underbrace{\mathbf{T}^{-1}}_{=\mathbf{T}} \circ \mathbf{P^m} \circ \mathbf{T} \circ \mathbf{r} = (\mathbf{P^n} \circ \mathbf{T}) \circ (\mathbf{P^m} \circ \mathbf{T}) \circ \mathbf{r} \tag{C.4}$$

therefore $\mathbf{P^{n-m}} \circ \mathbf{r} = \mathbf{r}$ since $\mathbf{P^n} \circ \mathbf{r} = \mathbf{r}$ and $\mathbf{P^m} \circ \mathbf{r} = \mathbf{r}$.

□

We now consider the case of *two* different time reversal symmetries, under the involution condition $\mathbf{T_1}$ & $\mathbf{T_2}$ *s.t.* $\mathbf{T_1}^2 = \mathbf{T_2}^2 = \mathbb{I}$. Recall, we now can write:

$$\mathbf{P}^{-1} = \mathbf{T_1}^{-1} \circ \mathbf{P} \circ \mathbf{T_1} = \mathbf{T_2}^{-1} \circ \mathbf{P} \circ \mathbf{T_2}. \tag{C.5}$$

The intersection of **FP** lines of $\mathbf{P^n} \circ \mathbf{T_1}$ & $\mathbf{P^m} \circ \mathbf{T_2}$ give the $2(n-m)$ period orbits of $\mathbf{P}$.

Proof. Given that $\mathbf{P^n} \circ \mathbf{T_1} \circ \mathbf{r} = \mathbf{r}$ & $\mathbf{P^m} \circ \mathbf{T_2} \circ \mathbf{r} = \mathbf{r}$:

$$\mathbf{P^n} \circ \underbrace{\mathbf{T_1} \circ \mathbf{P^m}}_{\mathbf{P^{-m}} \circ \mathbf{T_1}} \circ \mathbf{T_2} \circ \mathbf{r} = \mathbf{r}. \tag{C.6}$$

therefore:

$$\mathbf{P^{n-m}} \circ \mathbf{T_1} \circ \mathbf{T_2} \circ \mathbf{r} = \mathbf{r}. \tag{C.7}$$

Which means that the double application of (C.8) therefore returns:

$$\left(\mathbf{P^{n-m}} \circ \mathbf{T_1} \circ \mathbf{T_2}\right) \circ \left(\mathbf{P^{n-m}} \circ \mathbf{T_1} \circ \mathbf{T_2}\right) \circ \mathbf{r} = \mathbf{r}. \tag{C.8}$$

We then respectively apply $\mathbf{T_2} \circ \mathbf{P^{n-m}} = \mathbf{P^{m-n}} \circ \mathbf{T_2}$ followed by $\mathbf{T_1} \circ \mathbf{P^{m-n}} = \mathbf{P^{m-n}} \circ \mathbf{T_1}$ to return:

$$\mathbf{P^{2(n-m)}} \circ (\mathbf{T_1} \circ \mathbf{T_2})^{\mathbf{2}} \circ \mathbf{r} = \mathbf{P^{2(n-m)}} \circ \mathbf{r} = \mathbf{r}. \tag{C.9}$$

Where the final manipulation was made possible by the fact that $\mathbf{T'} = \mathbf{T_1} \circ \mathbf{T_2}$ may be squared to return $\mathbf{T'}^2 = \mathbb{I}$.

□

C.2 Symmetry considerations

We follow the reasoning employed in (CITE: Symbolic Dynamics and Periodic Orbits for the Cardioid Billiard). The time symmetry properties of the billiard dynamics along with its spatial symmetry leads to symmetry classes of orbits.

The time reversal symmetry $\mathbf{T}$ is given by:

$$\mathbf{T}(\alpha,\theta): \begin{cases} \alpha_{n+1} = -\alpha_n & \text{(C.10a)} \\ \theta_{n+1} = \theta_n. & \text{(C.10b)} \end{cases}$$

The eccentric annular billiard also has a reflection symmetry with respect to the x axis, $\mathbf{X}$.

$$\mathbf{X}(\alpha,\theta): \begin{cases} \alpha_{n+1} = \alpha_n, & \text{(C.11a)} \\ \theta_{n+1} = -\theta_n. & \text{(C.11b)} \end{cases}$$

NOTE: Extra symmetry of Iris billiard.

The Iris billiard contains yet an extra symmetry with respect to the y axis, that may be expressed as

$$\mathbf{Y}(\alpha,\theta): \begin{cases} \alpha_{n+1} = -\alpha_n, & \text{(C.12a)} \\ \theta_{n+1} = \theta_n - \pi. & \text{(C.12b)} \end{cases}$$

To identify the periodic orbits of interest, $\mathbf{X}$, $\mathbf{Y}$ and $\mathbf{T}$ must be *involutions*, i.e. $\mathbf{X}^2 = \mathbf{Y}^2 = \mathbf{T}^2 = \mathbb{I}$.

C.3 Verification of involution properties

The double application of the time inversion operator $\mathbf{T}$ returns us to the original vector, i.e:

$$\mathbf{T}^2 \circ \begin{pmatrix} \alpha \\ \theta \end{pmatrix} = \mathbf{T} \circ \begin{pmatrix} -\alpha \\ \theta \end{pmatrix} = \begin{pmatrix} \alpha \\ \theta \end{pmatrix} \implies \mathbf{T}^2 = \mathbb{I}. \tag{C.13}$$

similarly for $\mathbf{X}$:

$$\mathbf{X}^2 \circ \begin{pmatrix} \alpha \\ \theta \end{pmatrix} = \mathbf{X} \circ \begin{pmatrix} \alpha \\ -\theta \end{pmatrix} = \begin{pmatrix} \alpha \\ \theta \end{pmatrix} \implies \mathbf{X}^2 = \mathbb{I}. \tag{C.14}$$

We now pose the question if $\mathbf{X^{-1}} \circ \mathbf{P_n} \circ \mathbf{X} \stackrel{?}{=} \mathbf{P_n^{-1}}$ s.t. $\mathbf{P_n^{-1}} \circ \mathbf{P_n} = \mathbb{I}$. We first consider:

$$\mathbf{P_n} \circ \mathbf{X} \begin{pmatrix} \alpha_n \\ \theta_n \end{pmatrix} = \mathbf{P_n} \circ \begin{pmatrix} \alpha_n \\ -\theta_n \end{pmatrix} = \begin{pmatrix} \sin^{-1}\left(r\sin\beta' - d\sin(2\beta' - \theta_n - \alpha_n)\right) \to \alpha' \\ 2\beta' - \theta_n - \alpha_n - \alpha' \to \theta' \end{pmatrix}, \tag{C.15}$$

where β' is defined as:

$$\beta' = \sin^{-1}\left[\frac{1}{r}\{\sin\alpha_n + d\sin(\theta_n + \alpha_n)\}\right]. \tag{C.16}$$

We may now write:

$$\mathbf{P_n^{-1}} \circ \begin{pmatrix} \alpha_n \\ \theta_n \end{pmatrix} \stackrel{?}{=} \underbrace{\mathbf{X}^{-1}}_{\mathbf{X}} \circ \mathbf{P_n} \circ \mathbf{X} \circ \begin{pmatrix} \alpha_n \\ \theta_n \end{pmatrix} = \mathbf{X} \circ \begin{pmatrix} \alpha' \\ \theta' \end{pmatrix} = \begin{pmatrix} \alpha' \\ -\theta' \end{pmatrix} \tag{C.17}$$

which we now verify is indeed the inverse Poincaré map by calculating:

$$\mathbf{P_n}\circ\mathbf{P_n^{-1}}\circ\begin{pmatrix}\alpha_n\\ \theta_n\end{pmatrix}=\mathbf{P_n}\circ\begin{pmatrix}\alpha'\\ -\theta'\end{pmatrix}=\begin{pmatrix}\sin^{-1}\left(r\sin\beta_X-d\sin(2\beta_X-\theta'-\alpha')\right)\to\alpha_X\\ 2\beta_X-\theta'-\alpha'-\alpha_X\to\theta_X\end{pmatrix} \tag{C.18}$$

where β_X is defined as for β' (C.16) but with $\theta_n\to\theta'$ and $\alpha_n\to\alpha'$. We may say that $\beta_X=\beta'\ [\pi]$.

We now focus on the α_X term which returns:

$$\alpha_X=\sin^{-1}\left(\overbrace{\sin\alpha_n+d\sin(\alpha_n+\theta_n)}^{\sin\beta_X=\sin\beta'}+d\sin\underbrace{(\alpha'+\theta'-2\overbrace{\beta_X}^{\beta'})}_{\alpha'+\theta'-2\beta'=-\theta_n-\alpha_n}\right) \tag{C.19}$$

$$=\sin^{-1}\left(\sin\alpha_n+d\sin(\alpha_n+\theta_n)-d\sin(\alpha_n+\theta_n)\right)=\alpha_n. \tag{C.20}$$

Focusing on the θ_X term returns:

$$\theta_X=\overbrace{2\underbrace{\beta_X}_{\beta'}-\theta'-\alpha'}^{\theta_n+\alpha_n}-\alpha_n=\theta_n. \tag{C.21}$$

Therefore demonstrating that $\mathbf{P_n}\circ\mathbf{P_n^{-1}}=\mathbb{I}$.

We may also similarly pose the question if $\mathbf{T^{-1}}\circ\mathbf{P_n}\circ\mathbf{T}\overset{?}{=}\overline{\mathbf{P_n^{-1}}}$ such that $\mathbf{P_n}\circ\overline{\mathbf{P_n^{-1}}}=\mathbb{I}$. We consider:

$$\mathbf{P_n}\circ\mathbf{T}\begin{pmatrix}\alpha_n\\ \theta_n\end{pmatrix}=\mathbf{P_n}\circ\begin{pmatrix}-\alpha_n\\ \theta_n\end{pmatrix}=\begin{pmatrix}\sin^{-1}\left(r\sin\beta''-d\sin(2\beta''+\theta_n+\alpha_n)\right)\to\alpha''\\ 2\beta''+\theta_n+\alpha_n-\alpha''\to\theta''\end{pmatrix}, \tag{C.22}$$

where β'' is defined as:

$$\beta''=-\sin^{-1}\left[\frac{1}{r}\{\sin\alpha_n+d\sin(\theta_n+\alpha_n)\}\right]. \tag{C.23}$$

We may now write:

$$\overline{\mathbf{P_n^{-1}}}\circ\begin{pmatrix}\alpha_n\\ \theta_n\end{pmatrix}\overset{?}{=}\underbrace{\mathbf{T}^{-1}}_{\mathbf{T}}\circ\mathbf{P_n}\circ\mathbf{T}\circ\begin{pmatrix}\alpha_n\\ \theta_n\end{pmatrix}=\mathbf{T}\circ\begin{pmatrix}\alpha''\\ \theta''\end{pmatrix}=\begin{pmatrix}-\alpha''\\ \theta''\end{pmatrix} \tag{C.24}$$

which we also verify is indeed the inverse Poincaré map by calculating:

$$\mathbf{P_n}\circ\overline{\mathbf{P_n^{-1}}}\circ\begin{pmatrix}\alpha_n\\ \theta_n\end{pmatrix}=\mathbf{P_n}\circ\begin{pmatrix}-\alpha''\\ \theta''\end{pmatrix}=\begin{pmatrix}\sin^{-1}\left(r\sin\beta_T-d\sin(2\beta_T+\theta''+\alpha'')\right)\to\alpha_T\\ 2\beta_T+\theta''+\alpha''-\alpha_T\to\theta_T\end{pmatrix} \tag{C.25}$$

where β_T is defined as for β'' (C.23) but with $\theta_n\to\theta''$ and $\alpha_n\to\alpha''$. Expanding and simplifying β_T returns:

$$\beta_T=\sin^{-1}\left(\frac{1}{r}\left(d\sin(\beta''-\theta_n-\alpha_n)-r\sin\beta'')-d\sin(\overbrace{2\beta''+\theta_n+\alpha_n-\alpha''}^{\theta''}-\overbrace{\sin^{-1}(d\sin(\beta''+\theta_n+\alpha_n)-r\sin\beta'')}^{-\alpha''})\right)\right) \tag{C.26}$$

$$=\sin^{-1}\left(\frac{1}{r}\left(d\sin(\beta''-\theta_n-\alpha_n)-r\sin\beta'')-d\sin(2\beta''+\theta_n+\alpha_n)\right)\right)=-\beta'' \tag{C.27}$$

We may say that $\beta_T = -\beta''\ [\pi]$. We now focus on α_T to obtain:

$$\alpha_T = sin^{-1}\left(-r\sin\beta'' - d\sin(-2\beta'' + 2\beta'' + \theta_n + \alpha_n - \alpha'' + \alpha'')\right) = sin^{-1}\left(\overbrace{-r\sin\beta'' - d\sin(\theta_n + \alpha_n)}^{\sin\alpha_n}\right) = \alpha_n. \tag{C.28}$$

where the last manipulation comes from Eq. (C.23). We now consider θ_T

$$\theta_T = -2\beta'' + \overbrace{2\beta'' + \theta_n + \alpha_n - \alpha''}^{\theta''} + \alpha'' - \underbrace{\alpha_T}_{\alpha_n} = \theta_n. \tag{C.29}$$

Therefore demonstrating that $\mathbf{P_n} \circ \overline{\mathbf{P_n^{-1}}} = \mathbb{I}$.

BIBLIOGRAPHY

[1] D. Helbing et al., "Modelling the evolution of human trail systems", Nature **388**, 47–50 (1997) (cit. on p. 1).

[2] T. Nagatani, "Dynamical transition and scaling in a mean-field model of pedestrian flow at a bottleneck", Physica A: Statistical Mechanics and Its Applications **300**, 558–566 (2001) (cit. on p. 1).

[3] T. Ezaki et al., "Pedestrian flow through multiple bottlenecks", Phys. Rev. E **86**, 026118 (2012) (cit. on p. 1).

[4] D. Helbing and P. Molnar, "Social force model for pedestrian dynamics", Physical review E **51**, 4282 (1995) (cit. on pp. 1, 61).

[5] D. Helbing et al., "Simulating dynamical features of escape panic", Nature **407**, 487–490 (2000) (cit. on p. 1).

[6] A. Garcimartín et al., "Flow of pedestrians through narrow doors with different competitiveness", Journal of Statistical Mechanics: Theory and Experiment **2016**, 043402 (2016) (cit. on p. 1).

[7] J. M. Pastor et al., "Experimental proof of faster-is-slower in systems of frictional particles flowing through constrictions", Physical Review E **92**, 062817 (2015) (cit. on p. 1).

[8] K. Suzuno et al., "Analytical investigation of the faster-is-slower effect with a simplified phenomenological model", Physical Review E **88**, 052813 (2013) (cit. on p. 1).

[9] D. Helbing et al., "Self-organized pedestrian crowd dynamics: experiments, simulations, and design solutions", Transportation science **39**, 1–24 (2005) (cit. on p. 1).

[10] H. E. Stanley, "Non-equilibrium physics: freezing by heating", Nature **404**, 718–719 (2000) (cit. on p. 1).

[11] P.-G. de Gennes, "Granular matter: a tentative view", Reviews of modern physics **71**, S374 (1999) (cit. on pp. 1, 2).

[12] T. Shinbrot and F. Muzzio, "Nonequilibrium patterns in granular mixing and segregation", Physics Today **53**, 25–30 (2000) (cit. on p. 2).

[13] W. Zablotny, "Movement of charge in rotary kilns", International Chemical Engineering **5**, 360 (1965) (cit. on p. 2).

[14] K. M. Hill et al., "Mixing of granular materials: a test-bed dynamical system for pattern formation", International Journal of Bifurcation and Chaos **9**, 1467–1484 (1999) (cit. on p. 2).

[15] W. A. Beverloo et al., "The flow of granular solids through orifices", Chemical engineering science **15**, 260–269 (1961) (cit. on pp. 2, 65).

[16] D. Hong and J. McLennan, "Molecular dynamics simulations of hard sphere granular particles", Physica A: Statistical Mechanics and its Applications **187**, 159–171 (1992) (cit. on pp. 2, 65).

[17] K. To et al., "Jamming of granular flow in a two-dimensional hopper", Phys. Rev. Lett. **86**, 71–74 (2001) (cit. on pp. 2, 65).

[18] A. Janda et al., "Clogging of granular materials in narrow vertical pipes discharged at constant velocity", Granular Matter **17**, 545–551 (2015) (cit. on pp. 2, 65).

[19] R. C. Hidalgo et al., "Flow of colloidal suspensions through small orifices", Phys. Rev. E **97**, 012611 (2018) (cit. on pp. 2, 66).

[20] B. J. Ennis et al., "The legacy of neglect in the us", Chemical engineering progress **90**, 32–43 (1994) (cit. on p. 2).

[21] T. M. Knowlton et al., "The importance of storage, transfer, and collection", Chemical Engineering Progress;(United States) **90** (1994) (cit. on p. 2).

[22] F. Franklin and L. Johanson, "Flow of granular material through a circular orifice", Chemical Engineering Science **4**, 119–129 (1955) (cit. on p. 2).

[23] L. M. Schwartz et al., "Particle filtration in consolidated granular systems", Phys. Rev. B **47**, 4953–4958 (1993) (cit. on p. 2).

[24] K. Sharp and R. Adrian, "On flow-blocking particle structures in microtubes", Microfluidics and Nanofluidics **1**, 376–380 (2005) (cit. on p. 2).

[25]A. Berezhkovskii and G. Hummer, "Single-file transport of water molecules through a carbon nanotube", Physical review letters **89**, 064503 (2002) (cit. on p. 2).

[26]J. C. Eijkel and A. Van Den Berg, "Nanofluidics: what is it and what can we expect from it?", Microfluidics and Nanofluidics **1**, 249–267 (2005) (cit. on p. 2).

[27]L. Bocquet and E. Charlaix, "Nanofluidics, from bulk to interfaces", Chemical Society Reviews **39**, 1073–1095 (2010) (cit. on p. 2).

[28]K. Drescher et al., "Direct measurement of the flow field around swimming microorganisms", Physical Review Letters **105**, 168101 (2010) (cit. on p. 2).

[29]H. Wioland et al., "Directed collective motion of bacteria under channel confinement", New Journal of Physics **18** (2016) (cit. on pp. 2, 65).

[30]X. Yang et al., "Hydrodynamic and entropic effects on colloidal diffusion in corrugated channels", Proceedings of the National Academy of Sciences, 201707815 (2017) (cit. on p. 2).

[31]D. Bernoulli, "Hydrodynamica", Dulsecker. Consultable en ligne (1738) (cit. on p. 2).

[32]L. Boltzmann, "Weitere studien über das wärmegleichgewicht unter gasmolekülen", in *Kinetische theorie ii* (Springer, 1970), pp. 115–225 (cit. on p. 2).

[33]H. A. Lorentz, "Le mouvement des électrons dans les métaux", (1905) (cit. on p. 2).

[34]C. P. Dettmann, "Diffusion in the lorentz gas", Communications in Theoretical Physics **62**, 521–540 (2014) (cit. on p. 2).

[35]Y. Sinai, "Doklady akademii nauk", in, 6 (1963), pp. 1261–1264 (cit. on pp. 2, 90).

[36]M. V. Berry, "Regular and irregular motion", in AIP conference proceedings (1978) (cit. on pp. 2, 96).

[37]G. D. Birkhoff, "On the periodic motions of dynamical systems", Acta Mathematica **50**, 359–379 (1927) (cit. on p. 2).

[38]J. S. Portela et al., "Tokamak magnetic field lines described by simple maps", The European Physical Journal Special Topics **165**, 195–210 (2008) (cit. on p. 2).

[39]D. F. Oliveira and E. D. Leonel, "On the dynamical properties of an elliptical–oval billiard with static boundary", Communications in Nonlinear Science and Numerical Simulation **15**, 1092–1102 (2010) (cit. on p. 2).

[40]F. Haake, "Quantum signatures of chaos", (2010) (cit. on p. 2).

[41]I. C. Percival, "Regular and irregular spectra", Journal of Physics B: Atomic and Molecular Physics **6**, L229–L232 (1973) (cit. on p. 2).

[42]B. Chirikov, "Natural laws and human prediction", 10–33 (1996) (cit. on pp. 3, 89).

[43]I. Zuriguel et al., "Silo clogging reduction by the presence of an obstacle", Phys. Rev. Lett. **107**, 278001 (2011) (cit. on pp. 7, 66, 83).

[44]C. Barré et al., "Stochastic model of single-file flow with reversible blockage", EPL **104**, 60005 (2013) (cit. on pp. 7, 19, 42, 58, 60).

[45]G. C. Hunt, "Sequential arrays of waiting lines", Operations Research **4**, 674–683 (1956) (cit. on p. 7).

[46]J. Medhi, "Stochastic models in queueing theory (second edition)", xv–xviii (2003) (cit. on pp. 7, 39, 41).

[47]N. A. Cookson et al., "Queueing up for enzymatic processing: correlated signaling through coupled degradation", Molecular Systems Biology **7** (2011) (cit. on p. 7).

[48]D. J. Watts, "A simple model of global cascades on random networks", Proceedings of the National Academy of Sciences **99**, 5766–5771 (2002) (cit. on p. 7).

[49]P. Crucitti et al., "Model for cascading failures in complex networks", Phys. Rev. E **69**, 045104 (2004) (cit. on p. 7).

[50]Z. Zhao et al., "Cascading failures in interconnected networks with dynamical redistribution of loads", Physica A: Statistical Mechanics and its Applications **433**, 204–210 (2015) (cit. on p. 7).

[51]D.-H. Kim et al., "Universality class of the fiber bundle model on complex networks", Phys. Rev. Lett. **94**, 025501 (2005) (cit. on p. 7).

[52]F. Peirce, "32—x.—tensile tests for cotton yarns v.—"the weakest link" theorems on the strength of long and of composite specimens", Journal of the Textile Institute Transactions **17**, T355–T368 (1926) (cit. on p. 7).

[53]H. E. Daniels, "The statistical theory of the strength of bundles of threads. i", Proceedings of the Royal Society of London A: Mathematical, Physical and Engineering Sciences **183**, 405–435 (1945) (cit. on p. 7).

[54]B. Coleman, "On the strength of classical fibres and fibre bundles", Journal of the Mechanics and Physics of Solids **7**, 60–70 (1958) (cit. on p. 7).

[55]S. Pradhan et al., "Failure processes in elastic fiber bundles", Reviews of modern physics **82**, 499 (2010) (cit. on p. 7).

[56]M. D. Hager et al., "Self-healing materials", Adv. Mater. **22**, 5424–5430 (2015) (cit. on p. 7).

[57]S. Manfredi et al., "Mobility and congestion in dynamical multilayer networks with finite storage capacity", Phys. Rev. Lett. **120**, 068301 (2018) (cit. on p. 7).

[58]C. Gershenson and D. Helbing, "When slower is faster", Complexity **21**, 9–15 (2015) (cit. on p. 8).

[59]A. Garcimartín et al., "Flow of pedestrians through narrow doors with different competitiveness", J. Stat. Mech. **2016**, 043402 (2016) (cit. on p. 8).

[60]A. Nicolas et al., "Pedestrian flows through a narrow doorway: effect of individual behaviours on the global flow and microscopic dynamics", Transportation Research Part B: Methodological **99**, 30–43 (2017) (cit. on p. 8).

[61]I. Dobson et al., "A loading-dependent model of probabilistic cascading failure", Probab. Eng. Inf. Sci. **19**, 15–32 (2005) (cit. on p. 8).

[62]Didier Sornette, "Mean-field solution of a block-spring model of earthquakes", J. Phys. I France **2**, 2089–2096 (1992) (cit. on p. 8).

[63]W. I. Newman et al., "An exact renormalization model for earthquakes and material failure statics and dynamics", Physica D: Nonlinear Phenomena **77**, Special Issue Originating from the 13th Annual International Conference of the Center for Nonlinear Studies Los Alamos, NM, USA, 17–21 May 1993, 200–216 (1994) (cit. on p. 8).

[64]B. K. Chakrabarti, "A fiber bundle model of traffic jams", Physica A: Statistical Mechanics and its Applications **372**, Common Trends in Traffic Systems, 162–166 (2006) (cit. on p. 8).

[65]T. Ezaki et al., "Taming macroscopic jamming in transportation networks", Journal of Statistical Mechanics: Theory and Experiment **2015**, P06013 (2015) (cit. on p. 8).

[66]C. F. Daganzo et al., "Macroscopic relations of urban traffic variables: bifurcations, multivaluedness and instability", Transportation Research Part B: Methodological **45**, 278–288 (2011) (cit. on p. 8).

[67]V. V. Gayah and C. F. Daganzo, "Clockwise hysteresis loops in the macroscopic fundamental diagram: an effect of network instability", Transportation Research Part B: Methodological **45**, 643–655 (2011) (cit. on p. 8).

[68]Y. Ji and N. Geroliminis, "On the spatial partitioning of urban transportation networks", Transportation Research Part B: Methodological **46**, 1639–1656 (2012) (cit. on p. 8).

[69]L. Mishnaevsky and P. Brondsted, "Micromechanical modeling of damage and fracture of unidirectional fiber reinforced composites: a review", Computational Materials Science **44**, 1351–1359 (2009) (cit. on p. 8).

[70]F. Raischel et al., "Failure process of a bundle of plastic fibers", Phys. Rev. E **73**, 066101 (2006) (cit. on p. 8).

[71]S. Bhunia et al., "Stochastic model for cognitive radio networks under jamming attacks and honeypot-based prevention", in *Distributed computing and networking*, Vol. 8314, edited by M. Chatterjee et al., Lecture Notes in Computer Science (Springer Berlin Heidelberg, 2014), pp. 438–452 (cit. on pp. 8, 10).

[72]N. Roussel et al., "General probabilistic approach to the filtration process", Physical review letters **98**, 114502 (2007) (cit. on p. 9).

[73]M. Edwards and M. M. Benjamin, "Adsorptive filtration using coated sand: a new approach for treatment of metal-bearing wastes", Research Journal of the Water Pollution Control Federation, 1523–1533 (1989) (cit. on p. 9).

[74]A. Jones et al., "Integrated treatment of shrimp effluent by sedimentation, oyster filtration and macroalgal absorption: a laboratory scale study", Aquaculture **193**, 155–178 (2001) (cit. on p. 9).

[75]G. H. Goldsztein and J. C. Santamarina, "Suspension extraction through an opening before clogging", Applied physics letters **85**, 4535–4537 (2004) (cit. on p. 9).

[76]N. Roussel and A. Gram, "Physical phenomena involved in flows of fresh cementitious materials", in *Simulation of fresh concrete flow* (Springer, 2014), pp. 1–24 (cit. on p. 9).

[77]G. Veylon et al., "Performance of geotextile filters after 18 years' service in drainage trenches", Geotextiles and Geomembranes **44**, 515–533 (2016) (cit. on p. 9).

[78]K. To et al., "Jamming of granular flow in a two-dimensional hopper", Physical review letters **86**, 71 (2001) (cit. on p. 9).

[79]I. Zuriguel et al., "Silo clogging reduction by the presence of an obstacle", Physical review letters **107**, 278001 (2011) (cit. on p. 9).

[80]Y. Morita and J. L. Tilly, "Oocyte apoptosis: like sand through an hourglass", Developmental biology **213**, 1–17 (1999) (cit. on p. 9).

[81]R. Kapon et al., "A possible mechanism for self-coordination of bidirectional traffic across nuclear pores", Physical Biology **5**, 036001 (2008) (cit. on p. 10).

[82]Y. J. Kim et al., "Papaverine, a vasodilator, blocks the pore of the herg channel at submicromolar concentration", Journal of cardiovascular pharmacology **52**, 485–493 (2008) (cit. on p. 10).

[83]M. J. Twiner et al., "Marine algal toxin azaspiracid is an open-state blocker of herg potassium channels", Chemical research in toxicology **25**, 1975–1984 (2012) (cit. on p. 10).

[84]A. Finkelstein and O. S. Andersen, "The gramicidin a channel: a review of its permeability characteristics with special reference to the single-file aspect of transport", The Journal of membrane biology **59**, 155–171 (1981) (cit. on p. 10).

[85]F. Gao et al., "Research of sip dos defense mechanism based on queue theory", in International conference on computer science, environment, ecoinformatics, and education (Springer, 2011), pp. 99–104 (cit. on p. 10).

[86]S. Jin and D. S. Yeung, "A covariance analysis model for ddos attack detection", in 2004 ieee international conference on communications (ieee cat. no. 04ch37577), Vol. 4 (IEEE, 2004), pp. 1882–1886 (cit. on p. 10).

[87]S. Limkar and R. K. Jha, "An effective defence mechanism for detection of ddos attack on application layer based on hidden markov model", in Proceedings of the international conference on information systems design and intelligent applications 2012 (india 2012) held in visakhapatnam, india, january 2012 (Springer, 2012), pp. 943–950 (cit. on p. 10).

[88]C. T. MacDonald et al., "Kinetics of biopolymerization on nucleic acid templates", Biopolymers: Original Research on Biomolecules **6**, 1–25 (1968) (cit. on p. 11).

[89]B. Derrida, "An exactly soluble non-equilibrium system: the asymmetric simple exclusion process", Physics Reports **301**, 65–83 (1998) (cit. on p. 11).

[90]F. Spitzer, "Interaction of markov processes", Adv. Math **5**, 246 (1970) (cit. on p. 11).

[91]J. Cividini, "Multilane transport systems: application to pedestrian traffic" () (cit. on p. 11).

[92]M. Wölki et al., "Asymmetric exclusion processes with shuffled dynamics", Journal of Physics A: Mathematical and General **39**, 33 (2005) (cit. on p. 11).

[93]A. Keßel et al., "Microscopic simulation of pedestrian crowd motion", Pedestrian and evacuation dynamics, 193–200 (2002) (cit. on p. 11).

[94]C. Appert-Rolland et al., "Frozen shuffle update for an asymmetric exclusion process on a ring", Journal of Statistical Mechanics: Theory and Experiment **2011**, P07009 (2011) (cit. on p. 11).

[95]B. Derrida et al., "An exact solution of a one-dimensional asymmetric exclusion model with open boundaries", Journal of Statistical Physics **69**, 667–687 (1992) (cit. on p. 11).

[96]J. Krug, "Boundary-induced phase transitions in driven diffusive systems", Physical review letters **67**, 1882 (1991) (cit. on p. 11).

[97]M. Moussaid et al., "Traffic instabilities in self-organized pedestrian crowds", PLoS Comput Biol **8**, e1002442 (2012) (cit. on p. 11).

[98]C. Appert-Rolland et al., "Intersection of two tasep traffic lanes with frozen shuffle update", Journal of Statistical Mechanics: Theory and Experiment **2011**, P10014 (2011) (cit. on p. 11).

[99]D. Chowdhury and A. Schadschneider, "Self-organization of traffic jams in cities: effects of stochastic dynamics and signal periods", Physical Review E **59**, R1311 (1999) (cit. on p. 11).

[100]M. E. Fouladvand et al., "Optimized traffic flow at a single intersection: traffic responsive signalization", Journal of Physics A: Mathematical and General **37**, 561 (2004) (cit. on p. 11).

[101]A. Jelić et al., "A bottleneck model for bidirectional transport controlled by fluctuations", EPL (Europhysics Letters) **98**, 40009 (2012) (cit. on p. 11).

[102]S. Großkinsky et al., "Rigorous results on spontaneous symmetry breaking in a one-dimensional driven particle system", Journal of Statistical Physics **128**, 587–606 (2007) (cit. on p. 11).

[103]C. Godreche et al., "Spontaneous symmetry breaking: exact results for a biased random walk model of an exclusion process", Journal of Physics A: Mathematical and General **28**, 6039 (1995) (cit. on p. 11).

[104]M. R. Evans et al., "Spontaneous symmetry breaking in a one dimensional driven diffusive system", Physical review letters **74**, 208 (1995) (cit. on p. 11).

[105]R. Zia et al., "Modeling translation in protein synthesis with tasep: a tutorial and recent developments", Journal of Statistical Physics **144**, 405 (2011) (cit. on p. 11).

[106]N. Champagne et al., "Traffic jams and intermittent flows in microfluidic networks", Physical review letters **105**, 044502 (2010) (cit. on p. 11).

[107]A. Gabrielli et al., "Non-Markovian Models of Blocking in Concurrent and Countercurrent Flows", Phys. Rev. Lett. **110**, 170601 (2013) (cit. on pp. 11, 59).

[108]E. Elsayed, "Multichannel queueing systems with ordered entry and finite source", Comput. & Ops Res. **10**, 213–222 (1983) (cit. on p. 11).

[109]J. Talbot et al., "Irreversible blocking in single-file concurrent and countercurrent particulate flows", J. Stat. Mech. **2015**, P01027 (2015) (cit. on pp. 11, 12, 16, 17, 139–141).

[110]C. Barré et al., "Generalized model of blockage in particulate flow limited by channel carrying capacity", Phys. Rev. E **92**, 032141 (2015) (cit. on pp. 12, 21, 25).

[111]C. Barré and J. Talbot, "Stochastic model of channel blocking with an inhomogeneous flux of entering particles", EPL **110**, 20005 (2015) (cit. on p. 12).

[112]C. Barré and J. Talbot, "Cascading blockages in channel bundles", Phys. Rev. E **92**, 052141 (2015) (cit. on pp. 12, 49).

[113]C. Barré and J. Talbot, "Diminishing blocking interval in particle-conveying channel bundles", Eur. Phys. J. B **89**, 208 (2016) (cit. on p. 12).

[114]C. Barré et al., "Stochastic model of single-file flow with reversible blockage", EPL **104**, 60005 (2013) (cit. on pp. 12, 19, 21, 22, 24, 59, 137).

[115]N. Roussel et al., "General Probabilistic Approach to the Filtration Process", Phys. Rev. Lett. **98**, 114502 (2007) (cit. on p. 12).

[116]S. Redner and S. Datta, "Clogging time of a filter", Phys. Rev. Lett. **84**, 6018–6021 (2000) (cit. on p. 12).

[117]G. Page et al., "Optimizing the throughput of particulate streams subject to blocking", J. Stat. Mech. **2018**, 063213 (2018) (cit. on pp. 24, 57).

[118]L. Takacs, "On Erlang's formula", Ann. Math. Statist. **40**, 71–78 (1969) (cit. on p. 29).

[119]J. Medhi, "Stochastic models in queueing theory", (1991) (cit. on p. 29).

[120]D. G. Kendall, "Stochastic processes occurring in the theory of queues and their analysis by the method of the imbedded markov chain", The Annals of Mathematical Statistics, 338–354 (1953) (cit. on p. 37).

[121]A. K. Erlang, "Solution of some problems in the theory of probabilities of significance in automatic telephone exchanges", Post Office Electrical Engineer's Journal **10**, 189–197 (1917) (cit. on p. 38).

[122]N. T. Bailey, "On queueing processes with bulk service", Journal of the Royal Statistical Society: Series B (Methodological) **16**, 80–87 (1954) (cit. on p. 38).

[123]M. F. Neuts, "A general class of bulk queues with poisson input", The Annals of Mathematical Statistics **38**, 759–770 (1967) (cit. on p. 38).

[124]S. Sim and J. Templeton, "Steady state results for the m/m (a, b)/c batch-service system", European journal of operational research **21**, 260–267 (1985) (cit. on p. 38).

[125]M. Berg et al., "Optimal batch provisioning to customers subject to a delay-limit", Management science **44**, 684–697 (1998) (cit. on p. 38).

[126]S. K. Bar-Lev et al., "Applications of bulk queues to group testing models with incomplete identification", European Journal of Operational Research **183**, 226–237 (2007) (cit. on p. 38).

[127]A. Glazer and R. Hassin, "Equilibrium arrivals in queues with bulk service at scheduled times", Transportation Science **21**, 273–278 (1987) (cit. on p. 38).

[128]M. Matsui and J. Fukuta, "On a multichannel queueing system with ordered entry and heterogeneous servers", AIIE Transactions **9**, 209–214 (1977) (cit. on p. 38).

[129]H. Gumbel, "Waiting lines with heterogeneous servers", Operations Research **8**, 504–511 (1960) (cit. on p. 38).

[130]I. Adan and J. Resing, "Queuing theory", (2002) (cit. on pp. 39, 41, 47).

[131]J. W. Cohen, "The single server queue", (1982) (cit. on pp. 40, 139).

[132]C. Barré et al., "Generalized model of blockage in particulate flow limited by channel carrying capacity", Phys. Rev. E **92**, 032141 (2015) (cit. on p. 41).

[133]I. Adan and J. Resing, "Steady state probabilities for circular markov chains", Math. Scientist **22**, 27 (1997) (cit. on p. 47).

[134]G. Page et al., "Optimizing the Throughput of Particulate Streams Subject to Blocking", ArXiv e-prints **1803.04406** (2018) (cit. on pp. 48, 50, 52).

[135]C. Barré and J. Talbot, "Cascading blockages in channel bundles", Phys. Rev. E **92**, 052141 (2015) (cit. on pp. 56, 60).

[136]C. Barré et al., "Stochastic models of multi-channel particulate transport with blockage", J. Phys.: Condens. Matter **30**, 304004 (2018) (cit. on p. 57).

[137]G. Leonenko, "A new formula for the transient solution of the erlang queueing model", Statistics & Probability Letters **79**, 400–406 (2009) (cit. on p. 57).

[138]M. Escobar et al., "Approximate solution for multiserver queueing systems with erlangian service times", Computers & Operations Research **29**, 1353–1374 (2002) (cit. on p. 57).

[139]D. Helbing et al., "Simulating dynamical features of escape panic", Nature **407**, 487– (2000) (cit. on p. 61).

[140]D. Helbing, "Traffic and related self-driven many-particle systems", Rev. Mod. Phys. **73**, 1067–1141 (2001) (cit. on p. 61).

[141]H. A. Janssen, Z. Ver. Dtsch. Ing **39**, 1045 (1895) (cit. on p. 65).

[142]L. Vanel and E. Clément, "Pressure screening and fluctuations at the bottom of a granular column", The European Physical Journal B - Condensed Matter and Complex Systems **11**, 525–533 (1999) (cit. on p. 65).

[143]M. Sperl, "Experiments on corn pressure in silo cells - translation and comment of janssen's paper from 1895", Granular Matter **8**, 59–65 (2006) (cit. on p. 65).

[144]S. Mahajan et al., "Reverse janssen effect in narrow granular columns", Phys. Rev. Lett. **124**, 128002 (2020) (cit. on p. 65).

[145]K. To, "Jamming transition in two-dimensional hoppers and silos", Physical Review E **71**, 060301 (2005) (cit. on p. 65).

[146]I. Zuriguel et al., "Jamming during the discharge of granular matter from a silo", Physical Review E **71**, 051303 (2005) (cit. on p. 65).

[147]A. Marin et al., "Clogging in constricted suspension flows", Phys. Rev. E **97**, 021102 (2018) (cit. on p. 65).

[148]I. Zuriguel et al., "Clogging transition of many-particle systems flowing through bottlenecks", Sci Rep **4**, 7324– (2014) (cit. on p. 65).

[149]C. C. Thomas and D. J. Durian, "Fraction of clogging configurations sampled by granular hopper flow", Phys. Rev. Lett. **114**, 178001 (2015) (cit. on p. 65).

[150]E. Altshuler et al., "Flow-controlled densification and anomalous dispersion of E. coli through a constriction", Soft Matter **9**, 1864 (2013) (cit. on p. 65).

[151]M. Souzy et al., "Clogging transitions in constricted particle suspension flows", (2020) (cit. on p. 65).

[152]U. Zimmermann et al., "Flow of colloidal solids and fluids through constrictions: dynamical density functional theory versus simulation", Journal of Physics: Condensed Matter **28**, 244019 (2016) (cit. on p. 66).

[153]I. Zuriguel et al., "Effect of obstacle position in the flow of sheep through a narrow door", Phys. Rev. E **94**, 032302 (2016) (cit. on pp. 66, 83).

[154]Helbing Dirk et al., "Simulating dynamical features of escape panic", Nature **407**, 10.1038/35035023, 487–490 (2000) (cit. on pp. 66, 83).

[155]H. Noguchi et al., "Dynamics of fluid vesicles in flow through structured microchannels", EPL (Europhysics Letters) **89**, 28002 (2010) (cit. on p. 67).

[156]K. Stamer et al., "Tau blocks traffic of organelles, neurofilaments, and app vesicles in neurons and enhances oxidative stress", The Journal of cell biology **156**, 1051–1063 (2002) (cit. on p. 67).

[157]R. C. Hidalgo et al., "Simulating competitive egress of noncircular pedestrians", Phys. Rev. E **95**, 042319 (2017) (cit. on p. 83).

[158]W. E. Uspal and P. S. Doyle, "Scattering and nonlinear bound states of hydrodynamically coupled particles in a narrow channel", Physical Review E **85**, 016325 (2012) (cit. on p. 84).

[159]D. L. Ermak and J. McCammon, "Brownian dynamics with hydrodynamic interactions", The Journal of chemical physics **69**, 1352–1360 (1978) (cit. on p. 84).

[160]J. Rotne and S. Prager, "Variational treatment of hydrodynamic interaction in polymers", The Journal of Chemical Physics **50**, 4831–4837 (1969) (cit. on p. 84).

[161]J. G. de la Torre and V. A. Bloomfield, "Hydrodynamic properties of complex, rigid, biological macromolecules: theory and applications", Quarterly reviews of biophysics **14**, 81–139 (1981) (cit. on p. 84).

[162]M. Fixman, "Construction of langevin forces in the simulation of hydrodynamic interaction", Macromolecules **19**, 1204–1207 (1986) (cit. on p. 85).

[163]T. Geyer and U. Winter, "An o (n 2) approximation for hydrodynamic interactions in brownian dynamics simulations", The Journal of chemical physics **130**, 114905 (2009) (cit. on p. 85).

[164]C. P. Dettmann, "Recent advances in open billiards with some open problems", in *World scientific series on nonlinear science series b* (World Scientific, Mar. 2011), pp. 195–218 (cit. on p. 89).

[165]S. Koga, "On ergodicity in 3d closed billiards", Progress of Theoretical Physics **93**, 19–46 (1995) (cit. on p. 89).

[166]R. Chirikov and V. Vecheslavov, "Chaotic dynamics of comet halley", Astronomy and Astrophysics **221**, 146–154 (1989) (cit. on pp. 90, 91).

[167]B. Chirikov, "Stability of the motion of a charged particle in a magnetic confinement system", FizPl **4**, 521–541 (1978) (cit. on p. 90).

[168]S. Tabachnikov, "Geometry and billiards", (2005) (cit. on p. 90).

[169]L. A. Bunimovich and C. P. Dettmann, "Open circular billiards and the riemann hypothesis", Physical Review Letters **94** (2005) (cit. on p. 90).

[170]M. V. Berry, "Regularity and chaos in classical mechanics, illustrated by three deformations of a circular billiard", European Journal of Physics **2**, 91–102 (1981) (cit. on p. 90).

[171]R. Garcia, "Elliptic billiards and ellipses associated to the 3-periodic orbits", The American Mathematical Monthly **126**, 491–504 (2019) (cit. on p. 90).

[172]M. A. Bandres and J. C. Gutiérrez-Vega, "Classical solutions for a free particle in a confocal elliptic billiard", American Journal of Physics **72**, 810–817 (2004) (cit. on p. 90).

[173]L. A. Bunimovich, "Conditions of stochasticity of two-dimensional billiards", Chaos: An Interdisciplinary Journal of Nonlinear Science **1**, 187–193 (1991) (cit. on p. 90).

[174]A. Bäcker and H. R. Dullin, "Symbolic dynamics and periodic orbits for the cardioid billiard", Journal of Physics A: Mathematical and General **30**, 1991–2020 (1997) (cit. on p. 90).

[175]L. A. Bunimovich, "Mushrooms and other billiards with divided phase space", Chaos: An Interdisciplinary Journal of Nonlinear Science **11**, 802–808 (2001) (cit. on p. 90).

[176]A. Bäcker et al., "Dynamical tunneling in mushroom billiards", Physical Review Letters **100** (2008) (cit. on p. 90).

[177]Č. Lozej and M. Robnik, "Structure, size, and statistical properties of chaotic components in a mixed-type hamiltonian system", Physical Review E **98** (2018) (cit. on pp. 90, 110).

[178]C. F. Karney, "Long-time correlations in the stochastic regime", Physica D: Nonlinear Phenomena **8**, 360–380 (1983) (cit. on p. 90).

[179]G. Cristadoro and R. Ketzmerick, "Universality of algebraic decays in hamiltonian systems", Physical Review Letters **100** (2008) (cit. on p. 90).

[180]E. G. Altmann et al., "Stickiness in mushroom billiards", Chaos: An Interdisciplinary Journal of Nonlinear Science **15**, 033105 (2005) (cit. on pp. 90, 110).

[181]L. A. Bunimovich and L. V. Vela-Arevalo, "Many faces of stickiness in hamiltonian systems", Chaos: An Interdisciplinary Journal of Nonlinear Science **22**, 026103 (2012) (cit. on p. 90).

[182]C. Dettmann, "How sticky is the chaos/order boundary?", arXiv preprint arXiv:1603.00667 (2016) (cit. on p. 90).

[183]F. Vivaldi et al., "Origin of long-time tails in strongly chaotic systems", Physical Review Letters **51**, 727–730 (1983) (cit. on p. 90).

[184]G. Zaslavsky, "Chaos, fractional kinetics, and anomalous transport", Physics Reports **371**, 461–580 (2002) (cit. on p. 90).

[185]C. V. Abud and R. E. de Carvalho, "Multifractality, stickiness, and recurrence-time statistics", Physical Review E **88** (2013) (cit. on pp. 90, 110).

[186]Y. Zou et al., "Characterization of stickiness by means of recurrence", Chaos: An Interdisciplinary Journal of Nonlinear Science **17**, 043101 (2007) (cit. on pp. 90, 91, 105, 111).

[187]E. Persson et al., "Observation of resonance trapping in an open microwave cavity", Physical Review Letters **85**, 2478–2481 (2000) (cit. on p. 90).

[188]J. P. Bird, "Recent experimental studies of electron transport in open quantum dots", Journal of Physics: Condensed Matter **11**, R413–R437 (1999) (cit. on p. 90).

[189]V. Milner et al., "Optical billiards for atoms", Physical Review Letters **86**, 1514–1517 (2001) (cit. on p. 90).

[190]N. Friedman et al., "Observation of chaotic and regular dynamics in atom-optics billiards", Physical Review Letters **86**, 1518–1521 (2001) (cit. on p. 90).

[191]B. Dietz et al., "Spectral properties of bunimovich mushroom billiards", Physical Review E **75** (2007) (cit. on pp. 90, 136).

[192]C. Dembowski et al., "First experimental evidence for chaos-assisted tunneling in a microwave annular billiard", Physical Review Letters **84**, 867–870 (2000) (cit. on pp. 90, 136).

[193]R. P. Taylor et al., "Self-similar magnetoresistance of a semiconductor sinai billiard", Physical Review Letters **78**, 1952–1955 (1997) (cit. on p. 90).

[194]R. Crook et al., "Imaging fractal conductance fluctuations and scarred wave functions in a quantum billiard", Physical Review Letters **91** (2003) (cit. on p. 90).

[195]M. Robnik and M. V. Berry, "Classical billiards in magnetic fields", Journal of Physics A: Mathematical and General **18**, 1361 (1985) (cit. on p. 90).

[196]A. Rockett and P. Szüsz, "Continued fractions", (1992) (cit. on p. 91).

[197]N. B. Slater, "Gaps and steps for the sequence n theta mod 1", in Mathematical proceedings of the cambridge philosophical society, Vol. 63, 4 (Cambridge University Press, 1967), pp. 1115–1123 (cit. on p. 91).

[198]B. V. Chirikov, "Resonance processes in magnetic traps", The Soviet Journal of Atomic Energy **6**, 464–470 (1960) (cit. on p. 91).

[199]F. Izraelev, "Nearly linear mappings and their applications", Physica D: Nonlinear Phenomena **1**, 243–266 (1980) (cit. on p. 91).

[200]T. Petrosky, "Chaos and cometary clouds in the solar system", Physics Letters A **117**, 328–332 (1986) (cit. on p. 91).

[201]R. MacKay and J. Meiss, "Cantori for symplectic maps near the anti-integrable limit", Nonlinearity **5**, 149 (1992) (cit. on p. 92).

[202]J. Meiss, "Symplectic maps, variational principles, and transport", Reviews of Modern Physics **64**, 795 (1992) (cit. on pp. 92, 122).

[203]R. MacKay and I. I.C. Percival, "Converse kam: theory and practice", Communications in mathematical physics **98**, 469–512 (1985) (cit. on pp. 92, 103, 122).

[204]A. Paul and P. H. Richter, "Application of greenes method and the MacKay residue criterion to the double pendulum", Zeitschrift fur Physik B Condensed Matter **93**, 515–520 (1994) (cit. on p. 92).

[205]J. M. Greene, "A method for determining a stochastic transition", Journal of Mathematical Physics **20**, 1183–1201 (1979) (cit. on pp. 92, 101, 104, 136).

[206]M. Robnik, "Classical dynamics of a family of billiards with analytic boundaries", Journal of Physics A: Mathematical and General **16**, 3971–3986 (1983) (cit. on p. 102).

[207]K. Falconer, "Fractal geometry: mathematical foundations and applications", (2004) (cit. on p. 105).

[208]N. Marwan et al., "Recurrence plots for the analysis of complex systems", Physics Reports **438**, 237–329 (2007) (cit. on pp. 109–111).

[209]H. Poincaré, "Sur le problème des trois corps et les équations de la dynamique", Acta mathematica **13**, 1–270 (1890) (cit. on p. 109).

[210]H. Furstenberg, "Poincaré recurrence and number theory", Bulletin of the American Mathematical Society **5**, 211–235 (1981) (cit. on p. 109).

[211]N. Marwan, "Encounters with neighbours: current developments of concepts based on recurrence plots and their applications", (2003) (cit. on p. 110).

[212]J. Eckmann et al., "Recurrence plots of dynamical systems", Europhysics Letters (EPL) **4**, 973–977 (1987) (cit. on p. 110).

[213]P. M. Addo et al., "Nonlinear dynamics and recurrence plots for detecting financial crisis", The North American Journal of Economics and Finance **26**, 416–435 (2013) (cit. on p. 110).

[214]J. P. Zbilut et al., "Recurrence quantification analysis as a tool for nonlinear exploration of nonstationary cardiac signals", Medical Engineering & Physics **24**, 53–60 (2002) (cit. on p. 110).

[215]L. Parrott, "Analysis of simulated long-term ecosystem dynamics using visual recurrence analysis", Ecological Complexity **1**, 111–125 (2004) (cit. on p. 110).

[216]N. Marwan and A. Meinke, "Extended recurrence plot analysis and its application to erp data", International Journal of Bifurcation and Chaos **14**, 761–771 (2004) (cit. on p. 110).

[217]N. Asghari et al., "Stability of terrestrial planets in the habitable zone of gl 777 a, HD 72659, gl 614, 47 uma and HD 4208", Astronomy & Astrophysics **426**, 353–365 (2004) (cit. on p. 110).

[218]R. S. Baroni et al., "Time recurrence analysis of a near singular billiard", Mathematical and Computational Applications **24**, 50 (2019) (cit. on pp. 110, 136, 153, 154).

[219]J. Szezech et al., "Finite-time lyapunov spectrum for chaotic orbits of non-integrable hamiltonian systems", Physics Letters A **335**, 394–401 (2005) (cit. on p. 110).

[220]Y. Zou et al., "Analytical description of recurrence plots of dynamical systems with nontrivial recurrences", International Journal of Bifurcation and Chaos **17**, 4273–4283 (2007) (cit. on p. 110).

[221]J. Zbilut and C. W. Jr, "Embeddings and delays as derived from quantification of recurrence plots", Physics letters A **171**, 199–203 (1992) (cit. on p. 111).

[222]D. L. Gonzalez and O. Piro, "Chaos in a nonlinear driven oscillator with exact solution", Physical Review Letters **50**, 870 (1983) (cit. on p. 122).

[223]E. Piña and L. J. Lara, "On the symmetry lines of the standard mapping", Physica D: Nonlinear Phenomena **26**, 369–378 (1987) (cit. on pp. 122, 144).

[224]A. M. Fox and J. D. Meiss, "Greene's residue criterion for the breakup of invariant tori of volume-preserving maps", Physica D: Nonlinear Phenomena **243**, 45–63 (2013) (cit. on p. 136).

[225]R. C. Lyndon et al., "Groups and geometry", **101** (1985) (cit. on p. 143).

Gregory PAGE **3 septembre 2020**

Sujet : Modélisations d'écoulement intermittent

Résumé :
Les écoulements de particules sont au cœur d'un grand nombre de phénomènes physiques régulables et ce sur plusieurs échelles de taille : le déplacements des piétons, le flux des ions dans des canaux et le transfert d'informations pour n'en citer que quelques uns. Ces phénomènes sont d'autant plus intéréssants que la variation de certains paramètres peuvent entrainer une myriade de comportements intéréssants et imprévus, et notamment exhiber des phénomènes de flux intermitents.

Cette thèse présente et analyse trois modèles distincts qui peuvent être utilisés pour décrire ces phénomènes :

1) Nous présentons d'abord une modélisation des flux de particules dans d'abord dans un canal unidimensionnel, puis dans des groupes de canaux couplés ou non, en considérant dans tout ces cas que chaque canal à une occupation maximale. La dynamique aléatoire de ces modèles est étudiée en utilisant des outils de la théorie des queues et une technique de régénération.

2) Nous étudions ensuite le flux de particules de taille finies et molles qui se déplacent dans un canal bidimensionnel avec une simple ou double contrainte et qui se déplacent par dynamique browinienne. Nous observions dans ce cas là que des conditions spécifiques mènent à des phénomènes d'intermittence du flux de particules, liée à l'apparition de structures metastables. L'origine géométrique de ces effets est particulierement étudiée et caractérisée dans le régime ballistique.

3) Nous finissons par une analyse du Billard Iris, un système qui consiste en une particule point qui bouge librement, confinée dans un disque de taille unitaire qui contient une ellipse qui limite son mouvement. Ce système est d'abord étudié numériquement puis analytiquement dans les cas spécifiques ou l'éllipse mène à des trajectoires intégrables analytiquement. Par exemple, dans le cas limite ou l'ellipse devient un cercle, le sytème est intégrable, mais dans les autres cas, une dynamique mixte apparaît entre un comportement analytique et un régime chaotique. Une analyse par diagramme de récurrence du régime chaotique est utilisée pour identifier les géométries critiques qui mènent à des dynamiques complètement chaotiques.

Subject : Models of Intermittent Particle Flow

Abstract:
Particle flows underlie many regulatable phenomena at multiple length scales, such as pedestrian traffic, ion channel flux and information flow. Tuning the system parameters produces a myriad of interesting and unexpected behaviour, notably intermittent dynamics. This thesis presents and analyses three distinct models systems motivated by these phenomena:

1) Analytical models of particulate flow through 1D single channels, as well as coupled and uncoupled channel bundles, with a limited carrying capacity. The stochastic dynamics is studied using queuing theory and regeneration techniques.

2) Finite sized, soft particles driven through a 2D channel, with a single or double constriction are studied using overdamped brownian dynamics simulation. Special conditions for intermittency, related to the formation of metastable structures, are observed. The geometrical origin of the effects are further explored and characterised in the near-ballistic regime.

3) The Iris Billiard, consisting of a freely moving point particle confined by a unit circle enclosing a central scattering ellipse in 2D is investigated numerically. When the ellipse degenerates to a circle, the system is integrable, otherwise it displays mixed dynamics. Recurrence analysis of the chaotic regime is applied to identify critical geometries that signal a transition to global chaos.